UNIVERSIDADE FEDERAL DE SANTA CATARINA
CENTRO TECNOLÓGICO
PROGRAMA DE PÓS-GRADUAÇÃO EM ENGENHARIA MECÂNICA

Eduardo Bader Dalfovo Mohr Alves

Coupled modeling of heat transfer and deformation of salt layers in hydrocarbon producing wells

Florianópolis
2021

Eduardo Bader Dalfovo Mohr Alves

Coupled modeling of heat transfer and deformation of salt layers in hydrocarbon producing wells

Dissertação submetida ao Programa de Pós-Graduação em Engenharia Mecânica da Universidade Federal de Santa Catarina para a obtenção do título de mestre em Engenharia Mecânica.
Supervisor:: Prof. Jader Riso Barbosa Jr., Ph.D.
Co-supervisor:: Prof. Eduardo Alberto Fancello, D.Sc.

Florianópolis
2021

Ficha de identificação da obra elaborada pelo autor,
através do Programa de Geração Automática da Biblioteca Universitária da UFSC.

Alves, Eduardo Bader Dalfovo Mohr
Coupled modeling of heat transfer and deformation of salt layers in hydrocarbon producing wells / Eduardo Bader Dalfovo Mohr Alves ; orientador, Jader Riso Barbosa Jr., coorientador, Eduardo Alberto Fancello, 2021.
262 p.

Dissertação (mestrado) - Universidade Federal de Santa Catarina, Centro Tecnológico, Programa de Pós-Graduação em Engenharia Mecânica, Florianópolis, 2021.

Inclui referências.

1. Engenharia Mecânica. 2. Transferência de Calor em Poços. 3. Aumento de Pressão Anular. 4. Fluência Salina. 5. Transformada de Laplace. I. Barbosa Jr., Jader Riso. II. Fancello, Eduardo Alberto. III. Universidade Federal de Santa Catarina. Programa de Pós-Graduação em Engenharia Mecânica. IV. Título.

Eduardo Bader Dalfovo Mohr Alves

Coupled modeling of heat transfer and deformation of salt layers in hydrocarbon producing wells

O presente trabalho em nível de Mestrado foi avaliado e aprovado por banca examinadora composta pelos seguintes membros:

Prof. Jader Riso Barbosa Jr., Ph.D.
Universidade Federal de Santa Catarina

Prof. Paulo de Tarso Rocha de Mendonça, Dr.
Universidade Federal de Santa Catarina

Prof. Marcus Vinícius Canhoto Alves, Dr.
Universidade do Estado de Santa Catarina

Certificamos que esta é a **versão original e final** do trabalho de conclusão que foi julgado adequado para obtenção do título de mestre em Engenharia Mecânica.

ICP-Edu
Documento assinado digitalmente
Paulo de Tarso Rocha de Mendonca
Data: 03/06/2021 22:53:43-0300
CPF: 149.822.691-49
Verifique as assinaturas em https://v.ufsc.br

Coordenação do Programa de Pós-Graduação

ICP-Edu
Documento assinado digitalmente
Jader Riso Barbosa Junior
Data: 31/05/2021 17:17:38-0300
CPF: 010.026.207-40
Verifique as assinaturas em https://v.ufsc.br

Prof. Jader Riso Barbosa Jr., Ph.D.
Supervisor:

Prof. Eduardo Alberto Fancello, D.Sc.
Co-supervisor:
Universidade Federal de Santa Catarina – UFSC

Florianópolis, 2021.

AGRADECIMENTOS

Agradeço inicialmente ao Prof. Jader Riso Barbosa Jr., não só pela oportunidade de estudar um assunto que tanto gosto, mas especialmente por toda atenção e tempo investidos na orientação deste trabalho.

Ao Prof. Eduardo Alberto Fancello por ter aceitado ajudar ao longo do trabalho, o que foi muito importante para a confecção desta dissertação.

À toda equipe do Polo. Em especial ao Arthur Pandolfo por todas as conversas e ensinamentos de Python ao longo do mestrado. Ao Ianto pela contribuição com simulações que fazem parte deste trabalho.

Também sou grato à Marcus Vinícius, Rafael Lima e André Vicente pela amizade e pausas para café que tornavam os dias muito melhores.

Gostaria de agradecer tanto ao professor Marcus Vinícius quanto ao professor Paulo de Tarso por todas as sugestões de melhorias e horas dedicadas na correção deste trabalho para aumentar a sua qualidade e clareza.

À Petrobras pelo suporte financeiro e pelos dados que permitiram os estudos que serão apresentados neste trabalho. Também à CAPES pelo suporte financeiro durante o mestrado.

Por fim, agradeço à meus pais, Mauriene e Wilhelm, por toda educação e apoio incondicional.

“The Universe is under no obligation
to make sense to you”
Neil deGrasse Tyson

RESUMO

O elevado investimento associado à construção de um poço de petróleo em alto mar é o principal motivo da busca contínua por processos e estruturas otimizados, a um custo cada vez menor. À medida que ambientes cada vez mais hostis são desbravados, como o pré-sal brasileiro, a segurança dos projetos torna-se tão importante quanto o custo, levando à necessidade de se desenvolver métodos de cálculo e projeto mais avançados. Dentre os principais riscos inerentes à produção em águas profundas, está o APB (*Annular Pressure Buildup*), que é aumento de pressão dos fluidos confinados nos anulares motivado pela expansão térmica devida à transferência de calor entre o fluido produzido e a formação rochosa. O APB deve ser considerado em todas as etapas do dimensionamento das estruturas do poço, havendo na literatura inúmeros trabalhos com enfoque em diferentes cenários. Nesta dissertação, ênfase é dada a dois mecanismos que geram APB em poços produtores do pre-sal brasileiro, a saber, transferência de calor e fluência salina. Para quantificar o primeiro, foi desenvolvida uma formulação inovadora híbrida baseada na transformada de Laplace com inversão numérica, que considera efeitos de capacidade térmica de componentes do poço e elimina a o uso de *funções de tempo* para acoplar termicamente o poço e a formação. O segundo mecanismo com potencial de geração de APB é a deformação de camadas de rochas evaporíticas por fluência no entorno dos poços, a qual pode reduzir consideravelmente o volume dos espaços anulares, agravando o aumento de pressão. Para modelar o fenômeno, foi desenvolvido um modelo numérico baseado no método de Elementos Finitos, posteriormente acoplado a um código *in-house* para cálculo de APB em poços produtores. A forma adotada para o acoplamento tira vantagem das novas abordagens, garantindo maior consistência física no resultado e menor custo computacional. Para validar os modelos, foram usadas três geometrias reais de poços produtores fornecidos pela Petrobras. Do primeiro poço, verificou-se que a nova formulação de transferência de calor tem desempenho semelhante aos de formulações tradicionais para altos números de Fourier (tempos longos), com desvio médio inferior a 1% (3.7 K) em relação à previsão de temperatura na cabeça do poço e 6% para a pressão. Na previsão do APB, desvios maiores são observados (cerca de 1.1 MPa em relação aos dados de campo), porém parte da discrepância pode ser atribuída à imprecisão dos dados de campo. No segundo poço, o modelo de transformada de Laplace se mostrou superior na previsão da transferência de calor para um poço em partida, atingindo um desvio médio abaixo de 1% (3.47 K) para a temperatura da cabeça contra 2.5% (8.67 K) do modelo tradicional. Para a pressão na cabeça do poço, ambas as formulações previram valores com desvio médio de 1.25%, aproximadamente. Um estudo de sensibilidade envolvendo as propriedades dos fluidos confinados dos anulares indicou que a variável mais importante para a modelagem do aumento de pressão é a densidade, afetando o problema de forma inversamente proporcional. No último poço analisado, a presença de uma camada de sal permitiu validar o modelo de deformação de rochas por fluência. Para a geometria avaliada, foi possível concluir que o sal afeta o segundo anular, aumentando sua pressão em 2.55 MPa acima do previsto pela abordagem tradicional, que não contempla a influência de efeitos térmicos na fluência do sal.

Palavras-chave: Transferência de Calor em Poços. Aumento de Pressão Anular. Fluência Salina. Transformada de Laplace. Método de Elementos Finitos

RESUMO EXPANDIDO

Introdução

O petróleo, como matéria prima, está entre as substâncias mais versáteis para desenvolvimento de produtos. Aplicado em quase todos os setores de produção em grande escala, seu consumo aumenta gradativamente, o que requer produções cada vez maiores. Nessa realidade, o mercado brasileiro de produção de petróleo passa por momento de transição, na qual maior parte da produção nacional vem dos campos do Pré-Sal. Em dados divulgados pela Petrobras, cerca de 1,5 milhões de barris de óleo bruto foram produzidos diariamente em 2018. Com campos de alta produtividade e de alta pressão, vazões maiores com óleo de qualidade superior torna a exploração destes reservatórios atrativa. Contudo, esses poços possuem questões que podem trazer grandes riscos às suas estruturas ao longo de suas vidas produtivas. Em especial, deve-se citar o *Annular Pressure Buildup* (APB) que consiste de um aumento de pressão nos anulares do poço em decorrência do aquecimento dos mesmos. O aumento de pressão ocorre devido a presença de fluidos aprisionados nessas regiões e que tentam expandir em função do aumento de temperatura durante a produção e caso esse fenômeno não seja levado em conta durante o projeto do poço, pode causar o colapso da estrutura. No contexto do o APB é ainda mais crítico, uma vez que camadas de sal podem deformar por meio de fluência, assim podendo reduzir o volume do espaço anular o que potencializa o aumento de pressão. Embora existam simuladores capazes de lidar com o APB térmico e com a deformação das camadas de sal, ainda existe uma grande lacuna quando se trata de um simulador que trate do problema de forma consistente e acoplada.

Objetivos

Os simuladores mais modernos de poços, de um modo geral, quando consideram a transferência de calor transiente na produção, tendem a necessitar de grande esforço computacional. Em paralelo, poucos trabalhos foram desenvolvidos para lidar com a deformação de camadas de sal no cenário de poços produtores. Com relação ao primeiro tópico, para contornar os altos custos computacionais, a maior parte dos simuladores usados para modelar o APB e a transferência de calor em poços usam abordagem que considera a transferência de calor em regime pseudo permanente. Essa abordagem, por mais que comprovadamente satisfatória para estimar o APB em longos tempos de operação gera resultados pouco satisfatórios para tempos curtos, assim um dos objetivos deste trabalho consiste em desenvolver nova abordagem para modelar a transferência de calor em poços de modo que seja possível reproduzir de forma mais correta a transferência de calor para tempos menores de produção. Além disso, busca-se então, desenvolver uma abordagem mais consistente para acoplar o fenômeno de transferência de calor com a deformação de camadas de sal em decorrência de fluência.

Metodologia

A simulação da transferência de calor em poços produtores é um tópico complexo

e altamente multidisciplinar, adicionado a isso a própria modelagem da fluência em camadas de sal fica claro que é necessário partir de alguma estrutura previamente desenvolvida. Assim usa-se como base para este trabalho programa desenvolvido previamente pelo grupo de pesquisa no laboratório Polo da UFSC. O pySAFE é a revisão mais moderna de uma família de programas capaz de lidar com a transferência de calor em poços produtores, bem como a simulação do APB em decorrência do aquecimento dos espaços anulares de poços, uma vez que tal programa já passou por extensas validações é um bom ponto de partida para desenvolvimento de modelos mais complexos. Assim, para lidar com a transferência de calor em tempos mais curtos, é adicionado ao pySAFE uma nova formulação desenvolvida na Transformada de Laplace. Esse modelo tem por intuito resolver a transferência de calor radial, incluindo os termos transientes nos anulares, de forma semi-analítica, para tanto são montadas equações de conservação baseadas na analogia de resistências e capacitâncias elétricas nos anulares do poço com condição de contorno externa (na parede com a formação) extraída da própria equação de condução de calor no meio semi-infinito cilíndrico. Nesse sistema de equações diferenciais resultante é aplicada a Transformada de Laplace, assim pode-se converter o sistema de equações diferenciais em um sistema de equações lineares que representam a solução analítica da transferência de calor no campo de Laplace. Para a inversão da solução será usada abordagem numérica baseada no *framework* de Abate-Whitt, com determinação dos nós de inversão pelo método de *Concentrated Matrix Exponential* (CME). Com relação à simulação acoplada com a fluência de camadas de sal, foi desenvolvido código baseado no Método de Elementos Finitos, esse código foi então acoplado ao pySAFE, usando a sua formulação para cálculo de APB para garantir consistência do acoplamento. Para validação dos novos modelos desenvolvidos foram usadas três poços reais produtores de hidrocarbonetos, esses três sendo fornecidos pela Petrobras e além de geometrias foram usados dados medidos nos próprios poços.

Resultados e Discussão

Dos três poços analisados, em apenas dois os dados de campo foram usados para validação dos modelos desenvolvidos. Nesses dois casos foram usados dados dos medidores de pressão e temperatura dentro do poço para avaliar a qualidade do novo modelo de transferência de calor apresentado. No caso, para o primeiro poço, os dados validaram que o novo modelo consegue reproduzir de forma muito satisfatória o comportamento da temperatura na cabeça do poço. Além disso, para este primeiro caso, esse novo modelo foi comparado com código comercial muito utilizado para modelar a transferência de calor em poços produtores, de um modo geral ficou claro que a nova formulação parece ser um meio termo entre modelos tradicionais pseudo permanentes e o código comercial. No segundo poço com dados já foi possível concluir de forma mais segura que a nova formulação consegue reproduzir melhor os dados de campo em comparação aos modelos tradicionais, levando o desvio relativo para os dados de campo de 2.2% (7.71 K) para 0.9% (3.27 K) em relação à temperatura média da cabeça do poço. Além disso, extensa análise de sensibilidade foi feita para avaliar os efeitos de incertezas dos modelos nos resultados das simulações, concluindo que ambos modelos usados para a transferência de calor conseguem reproduzir de forma satisfatória os dados de campo dentro da incerteza esperada. Por fim, para este mesmo poço, usando essa análise de sensibilidade pode-se confirmar que dentre os parâmet-

ros usados para simular o APB de poços, a densidade dos fluidos aprisionados é a propriedade mais importante em termos de APB final. Na última geometria estudada existe uma camada de sal exposta ao anular do poços, assim ela foi usada para valiar os efeitos de uma camada de sal. Uma vez simulada uma operação de trinta anos no poço, percebeu-se um aumento no APB de cerca de 2.55 MPa (15% de aumento em relação ao APB desconsiderando os efeitos de fluência), contudo, com base em parâmetros de segurança usados no trabalho, não se espera que a estrutura desse poço em específico esteja em risco. Por fim, foi feita análise inovadora aplicando os efeitos da expansão da camada de sal, em decorrência do aumento de temperatura da mesma, no APB, como para o caso estudado os efeitos foram quase imperceptíveis, propôs-se critério que pode ser usado para estimar se os efeitos de expansão térmicos do material podem afetar os estudos.

Considerações Finais

Esta dissertação foi desenvolvida com intuito de melhorar os modelos apresentados na literatura quanto à modelagem do APB em poços produtores do pré-sal. Para tanto foram desenvolvidos dois modelos inovadores, um relacionado à transferência de calor e outro à deformação de camadas de sal por meio de fluência, ambos sendo incluídos em programa já estabelecido na literatura (pySAFE). Uma vez desenvolvidos e implementados, ambos modelos foram usados em simulações de geometrias reais de poços produtores, sendo que o modelo de transferência de calor pôde ser validado contra dados de campo, o que deixou claro suas vantagens contra modelos tradicionais de transferência de calor. Embora não tenha sido possível validar o modelo de deformação de camadas de sal, os estudos apontaram que o modelo desenvolvido é capaz de lidar com cenários de poços produtores, indicando inclusive um aumento significativo no APB final previsto para o poço analisado.

Palavras-chave: Transferência de Calor em Poços. Aumento de Pressão Anular. Fluência Salina. Transformada de Laplace. Método de Elementos Finitos

ABSTRACT

The high investment associated with the construction of deep water oil wells is the main reason for the continuous search for optimized processes and structures, at increasingly lower costs. As more and more hostile environments are explored, such as the Brazilian pre-salt cluster, project safety becomes as important as cost, motivating the development of more advanced design and evaluation methods. APB (*Annular Pressure Buildup*) is among the main risks inherent to production in deep waters. It is defined as the increase in the pressure of the fluid confined in the concentric annuli due to thermal expansion resulting from the heat transfer between the produced fluid and the rock formation. APB has to be considered at all stages of well design, with numerous studies in the literature focusing on different scenarios. In this dissertation, emphasis is given to two mechanisms that generate APB in Brazilian pre-salt producing wells, namely, heat transfer and salt creep. To quantify the former, an innovative hybrid formulation based on the Laplace transform coupled with a numerical inversion algorithm was developed, which considers the thermal capacity of well components and eliminates the use of *time functions* to thermally couple the wellbore and the formation. The other mechanism with potential to generate APB is the deformation of evaporitic rock layers due to creep around the wells, which can considerably reduce the volume of the annular spaces, aggravating the pressure increase. To model the phenomenon, a numerical model was developed based on the Finite Element Method, which was later coupled with an *in-house* code for calculating APB in producer wells. The coupling takes advantage of the new numerical approaches, ensuring greater physical consistency in the result and lower computational cost. To validate the models, three real well geometries supplied by Petrobras were used. From the first well, it was found that the new heat transfer formulation performs similarly to traditional formulations for high Fourier numbers (long times), with an average deviation lower than 1 % (3.7 K) for the wellhead temperature and 6 % for the wellhead pressure. In the APB prediction, greater deviations are observed (about 1.1 MPa in relation to the field data). However, part of the discrepancy can be attributed to the inaccuracy of the field data. In the second well, the Laplace transform model proved to be superior in predicting the heat transfer during an extended well test, reaching an average deviation within 1% (3.47 K) of the wellhead temperature, against 2.5% (8.67 K) of the traditional model. For the pressure at the wellhead, both formulations predicted values with an average deviation of approximately 1.25%. A sensitivity analysis involving the properties of the confined fluids indicated that the most important variable for modeling the pressure increase is the density, which affects the problem in an inversely proportional manner. In the last well analyzed, the presence of a salt layer allowed the validation of the creep deformation model. For the evaluated geometry, it was possible to conclude that the salt affects the second annulus, increasing its pressure by 2.55 MPa above the prediction of the traditional approach, not considering the influence of thermal expansion on the salt creep.

Keywords: Heat Transfer on Wellbores. Annular Pressure Buildup. Salt Creep. Laplace Transform. Finite Element Method.

LIST OF FIGURES

LIST OF TABLES

LIST OF ABBREVIATIONS AND ACRONYMS

APB	Annular Pressure Buildup
API	American Petroleum Institute
CFD	Computational Fluid Dynamics
CME	Concentrated Matrix Exponential
EWT	Extended Well Tests
FEM	Finite Element Method
GLR	Gas to Liquid Ratio
HP/HT	High Pressure / High Temperature
KOP	Kick-off Point
MD	Measured Depth
MEG	MonoEthylene Glycol
PDG	Permanent Downhole Gauge
PT	Pressure Transducer
PVW	Principle of Virtual Works
pySAFE	Python Simulator of Annular Fluid Expansion
SAFE	Simulator of Annular Fluid Expansion
TOC	Top of Cement
TPT	Temperature/Pressure Transducer
TVD	True Vertical Depth
UFSC	Federal University of Santa Catarina
VIT	Vacuum-Insulated Tubing
WC	Water Cut

LIST OF SYMBOLS

Roman

A	Activation energy of material	[J/mol]
C_{Zhou}	Inclination parameter for Zhou correlation	[-]
$C_{\sigma\phi}$	Set of geometric parameters for Halal and Mitchel	[-]
$C_{\sigma r}$	Set of geometric parameters for Halal and Mitchel	[-]
$C_{\varepsilon\phi}$	Set of geometric parameters for Halal and Mitchel	[-]
C	Thermal capacitance	[J/mK]
E	Young's module	[Pa]
F_{Chen}	Intensifying term for the heat convection in Chen correlation	[-]
Fr	Froude number	[-]
G_{ov}	Overburden stress gradient	[ppg]
G	Shear modulus	[Pa]
H	Volumetric phase fraction	[-]
I_0	Modified Bessel function of first kind of 0th order	[-]
K_0	Modified Bessel function of second kind of 0th order	[-]
K_1	Modified Bessel function of second kind of 1th order	[-]
K	Bulk modulus	[Pa]
L	Well's length	[m]
L	Transitions parameters for Beggs and Brill two-phase correlation	[-]
M_0	Initial mass of the system	[kg]
M	Mass of a given annular	[kg]
N_L	Liquid adimensional parameter	[-]
N_{Gr}	Graetz's Number	[-]
N_{Ra}	Ramey's Number	[-]
N_{el}	Number of elements	[-]
N_{int}	Number of integration points	[-]
N_{sk}	Heat Skin Number	[-]
N	Number of nodes used in Abate-Whitt framework	[-]
Pr	Prandtl number	[-]
P	Pressure	[Pa]
Q'	Heat transfer rate per unit length	[$\mathrm{W\,m^{-1}}$]
R_{gas}	Universal gas constant	[J/molK]
Ra	Rayleigh number	[-]
Res	General scalar residual function	[-]
Re	Reynolds number	[-]
R	General resistance term	[$\mathrm{m\,K\,W^{-1}}$]
T	Temperature	[K]

U	Equivalent thermal conductance	$[\mathrm{W\,m^{-1}\,K^{-1}}]$
V	Volume	$[\mathrm{m^3}]$
W	Weights for Gauss-Legendre integration	[-]
X_{int}	Integration nodes for Gauss-Legendre	[-]
X_{tt}	Martinelli parameter	[-]
Z_{top}	True vertical depth on the top of a salt layer	[m]
Z	Vertical depth	[m]
$\boldsymbol{B}$	Derivative of shape functions	[-]
$\boldsymbol{D}$	Derivative operator	[-]
$\boldsymbol{F_{ext}}$	Internal forces vector	[N]
$\boldsymbol{F_{int}}$	Internal forces vector	[N]
$\boldsymbol{N}$	Normal flow direction for creep	[-]
$\boldsymbol{Res}$	Residua for balance equations	[N]
$\boldsymbol{S}$	Deviatoric stress tensor	[Pa]
$\boldsymbol{U}$	Discrete displacement field	[m]
$\mathbf{I}$	Identity tensor	
$\boldsymbol{b}$	Body force vector	[N]
$\boldsymbol{f}$	Nodal force in a given element	[N]
$\boldsymbol{t}$	External stress	[Pa]
$\boldsymbol{u}$	Displacement field	[m]
$\dot{V}$	Volume flow rate	$[\mathrm{m^3\,s^{-1}}]$
$\dot{m}$	Mass flux	$[\mathrm{kg/m^{2s}}]$
γ	Creep amplitude	[-]
$\mathbb{I}$	Fourth rank identity tensor	[-]
$\mathbb{P}$	Projection tensor	[-]
$\mathscr{A}$	Assembly operator	[-]
$\mathscr{L}$	Laplace transform operator	[-]
$\mathscr{N}$	Shape functions	[-]
$\overline{T}$	Temperature profile in Laplace domain	[-]
$\bar{f}$	Generic function under Laplace transform	[-]
dev	Deviatoric operator	[-]
tr	Trace operator	[-]
c_p	Specific heat capacity	[J/kgK]
c	Flow correlation parameters for Beggs and Brill correlation	[-]
d_T	Production tubing inner diameter	[m]
$f(t)$	Time function	[-]
f	Moody friction factor	[-]
f	Generic function	[-]

g	Gravity acceleration	[m s^{-2}]
h_c	Heat transfer coefficient for convection	[W/m^{2}K]
h_r	Heat transfer coefficient for radiation	[W/m^{2}K]
h	Specific enthalpy	[J kg^{-1}]
k	Thermal conductivity	[W/mK]
n	Creep law parameter	[-]
p	Volumetric stress tension	[Pa]
q	Effective stress	[Pa]
r	Radial direction	[m]
s	Time variable in time domain	[-]
s	Stretching factor	[-]
t	Time	[s]
v	Fluid flow velocity	[m s^{-1}]
x_g	Quality	[-]
z	Axial direction of the well associated with Measured Depth	[m]
y	Auxiliary variable useful for constitutive model	[-]
Greek		
$\Delta\sigma_z$	Variation in hoop stress	[Pa]
$\Delta\sigma_z$	Variation in radial stress	[Pa]
$\Delta\sigma_z$	Variation in axial stress	[Pa]
$\Delta\varepsilon_\phi$	Hoop deformation	[-]
Γ_0	Auxiliary variable for constitutive relationship	[-]
Γ_1	Auxiliary variable for constitutive relationship	[-]
Ω	Salt domain	[-]
α_{fm}	Thermal diffusivity of the formation	[m s^{-2}]
β_{lin}	Linear thermal expansivity	[K]
β	Thermal expansivity	[K^{-1}]
$\boldsymbol{\sigma}$	Stress tensor	[Pa]
$\boldsymbol{\varepsilon_{cr}}$	Creep strain tensor	[-]
$\boldsymbol{\varepsilon_{el}}$	Elastic strain tensor	[-]
$\boldsymbol{\varepsilon_{th}}$	Thermal strain tensor	[-]
$\boldsymbol{\varepsilon}$	Total strain tensor	[-]
χ_1	Stretching parameter 1	[-]
χ_2	Stretching parameter 2	[-]
$\dot{\gamma}$	Creep rate	[s^{-1}]
ϵ	Pipe roughness	[m]
ϵ	Surface emissivity	[-]
η^*	Original grid before stretching	[-]

η	Parametric direction of element domain	[-]
κ	Fluid compressibility	[Pa^{-1}]
λ	No-slip volumetric phase fraction	[-]
λ	Nodes for Abate-Whitt framework	[-]
μ	Dynamic viscosity	[$m^2\,s^{-1}$]
ν	Poisson coefficient	[-]
ω_{welb}	Cheng's ratio of capacitance	[-]
ω	Weights for Abate-Whitt framework	[-]
ϕ	Tangential direction	[-]
ρ	Fluid specific mass	[$kg\,m^{-3}$]
σ_L	Surface tension	[$N\,m^{-1}$]
σ_h	horizontal component of stress	[Pa]
σ_{SB}	Stefan-Boltzmann constant	[W/m^{2K}]
σ_{ov}	Overburden stress	[Pa]
τ	Fourier time	[-]
θ	Tubing inclination with respect to the vertical	[°]
ϱ	Cross-Correlation coefficient	[-]
ξ	Parametric direction of element domain	[-]

Subscripts

0	Initial state
D	Dimensionless variable
El	Element index
Int	Solid interface
ann	Annular space
bot	Deepest point of a fluid column for example top of a cementation layer
cas	Casing
cem	Cement
cond	Related to conduction
conv	Related to convection
fm	Formation
g	Gas phase
inn	Inner material interface
i	Radial index for thermal system
j	Integration node index particular to a given element
k	Index for Abate-Whitt inversion algorithm
l	Liquid phase
l	l'th iteration of Newton Algorithm

m	Mixture
n	Index for time discretization
out	Outer material interface
pf	Production fluid
rad	Related to radiation
ref	Reference state for creep law calibration
tub	Production Tubing
ns	No-slip
s	Slip

Superscripts

T	Transpose
tr	Trial step of predictor-corrector algorithm

CONTENTS

1 INTRODUCTION

Large-scale oil production began when the famous Drake well in Cherrytree Township, Pennsylvania, produced for the first time in 1859; that well was only 21-m deep and estimated to have produced 800 to 1200 gallons of oil per day (between 19.05 and 28.57 bbl/d) (BAKER, 1979). The concept of using casings was introduced in that well to ensure structural integrity of its walls, as previous attempts suffered from collapse of unconsolidated shallow walls.

Unconsolidated regions were the main reason why casings were used for the first time. Nowadays, however, casings serve multiple purposes. First, to balance the tendency of weaker layers to collapse into the well, the most common drilling practice is to balance the pressure on the wellbore walls by controlling the density of the drilling fluid. This creates a high pressure environment which holds the formation in place. However, this practice has a limitation related to the strength of the rocks; when increasing the density of the fluid to accommodate deeper layers, fractures may appear in the shallower regions. Therefore, to avoid damage in the upper regions of the well, casings are added to isolate the different depths of the wellbore, enabling the use of heavier fluids without fracturing the shallower regions.

The use of casings allowed deeper drilling, and such structures are still used in every well drilled nowadays. The drilling process is usually described in terms of the stages used to reach a given oil reservoir. These stages are somewhat similar to each other, so a basic explanation of a standard stage suffices to understand the phenomena to be presented later.

Drilling occurs when a drilling bit is lowered inside the drilling column to remove material from the formation. The column is simply a long section of tubes connecting the drill bit and the platform. Drill bits work by either cutting or smashing the formation, however, they always require the use *drilling muds* (LAKE, 2006). These suspensions flow through the column and are ejected from the drilling bit. As it leaves the column, the drilling mud rises through annular spaces formed during previous (upper) drilling stages. As such, every new stage must be smaller in diameter than the previous one to prevent jamming of the drilling column inside the wellbore walls.

Once the drilling of a stage is completed, a casing must be lowered. To accommodate the weight of the drilling mud in shallower regions, the drilling column is taken out of the well and replaced by a casing. To firmly lock it in place, cement slurry is injected in the annular space. This, however, does not mean that the entire volume of the annulus will be cemented. Due to cost or even structural requirements, the annulus is filled only partially with the cement slurry. Consequently, a certain amount of drilling mud is left in place, from the top of the cement layer up to the wellhead. At each stage, as a new casing is lowered into the well, the steel tubes are settled by sealing

the annular spaces from previous stages, trapping the drilling mud inside the cavities formed.

The drilling stages follows the so-called operation window, which is a region comprised between the geomechanical gradients under which the well integrity is guaranteed. Figure 1 presents an example of a drilling operation window considering the staging from the well head to the bottom, where the depth of each stage is determined by the vertical lines. Notice that, once the specified depth is reached, the drilling bit diameter is changed; Figure 2 shows a sequence of the most common completion styles for a production well.

Figure 1 – Scheme of casing designs from the well head down to the bottom

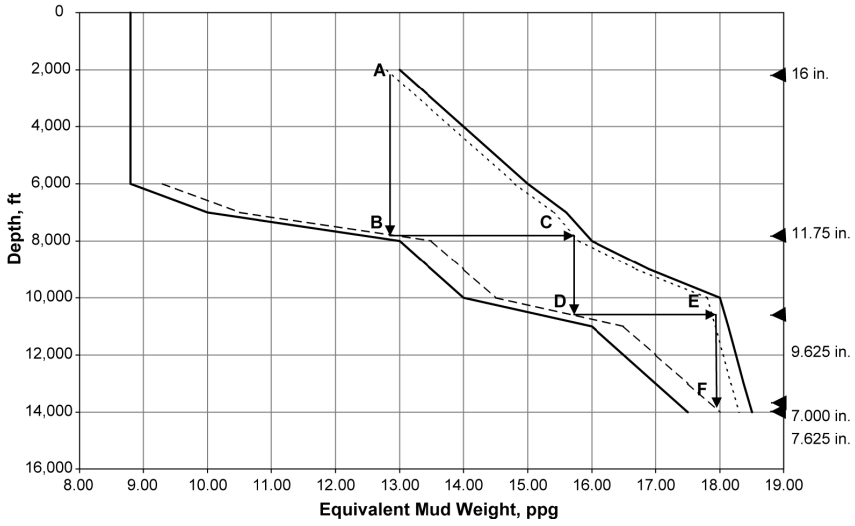

Source: Lake (2006)

Figure 2 – Sequences of drilling diameters adopted for different stages

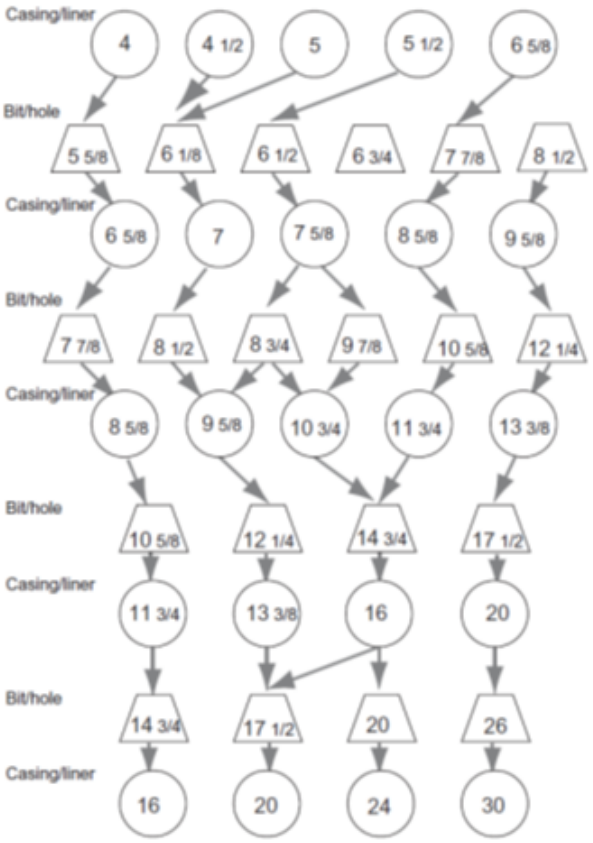

Source: Byrom (2015)

At the end of drilling, the well is ready for completion, which is a different stage compared to the previous ones since, at this step, the tubing lowered into the column is not cemented in place. Rather, it is held by the wellhead and secured via a set of packers which seal its annular space against the nearest casing (the so-called production casing). This annular space is usually only sealed at the bottom, leaving it accessible from the wellhead, which is important since many operations require access to the outside of the production column. Moreover, the innermost annulus can be used to operate the well with artificial lift methods, such as gas lift (GUO; LYONS; GHALAMBOR, 2007). This annulus is filled with the so-called completion fluid which, contrary to drilling muds, does not contain suspended solid particles.

After drilling and completing the well with multiple casings of different diameters, it acquires the typical inverted periscope configuration, as shown in Figure 3. It is important to emphasize the presence of concentric annular cavities containing the fluids trapped during the stages described above. The thermal behavior of such fluids during well production, and their influence on the structural behavior of solid components of the well (e.g., casing, cement) and formation, are the focus of the present work.

Figure 3 – A typical well geometry

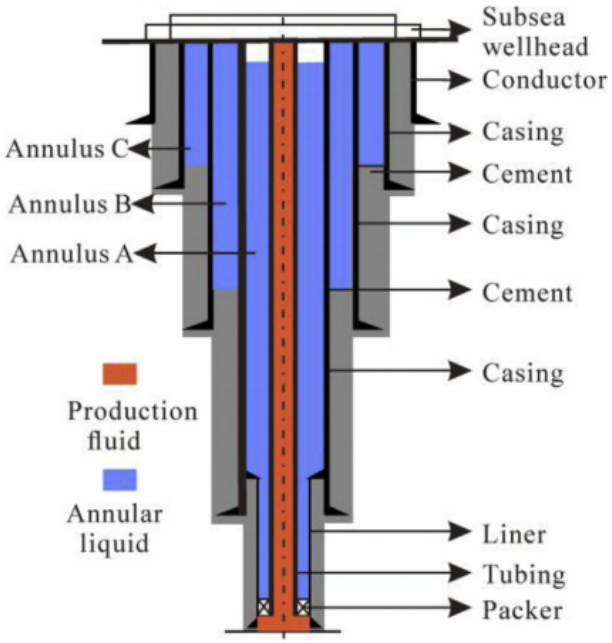

Source: Zhang, Guan, et al. (2019)

The above described procedures and the evolution of casing and tubing design, drilling and completion technologies enabled the construction of deeper wells capable of reaching reservoirs of increasingly higher pressures. This contributed to a significant growth in production from increasingly challenging scenarios. Particularly hazardous conditions are encountered in pre-salt wells, which are drilled in ultra deep waters (at sea depths greater than 3000 m). Production from pre-salt oil fields will remain strategically important for Brazil, even when the impact of the COVID-19 Pandemic is considered. Petrobras' Strategic Plan for 2021-2025 forecasts a growth in production reaching 3.3 million barrels per day, of which 80% are expected to come from pre-salt wells (PETROBRAS, 2020).

One of the important precautions to be taken during well design is the handling of Annular Pressure Buildup (APB), a thermally-driven phenomenon thought to be responsible for the collapse of deepwater producer wells in the Gulf of Mexico (BRADFORD et al., 2004; ELLIS et al., 2004; GOSCH et al., 2002; PATTILLO; COCALES; MOREY, 2006; PATTILLO; SATHUVALLI, et al., 2007). APB is a direct consequence of the thermal expansion of drilling and completion fluids trapped within the annular cavities formed by the casings. Since this expansion is somewhat contained by the casings, the fluid pressure adds to the mechanical loads on the wellbore structure.

The heating of the annular spaces is due to a geothermal gradient generated by the hot magma below the earth's crust, this gradient usually has a average value around $25\,\mathrm{K\,km^{-1}}$, however it may vary depending on the region drilled (RENNER, 2007). As the heated hydrocarbons rise from deeper regions, they exchange heat with shallower,

colder regions, increasing the temperature of the casings and drilling/completion fluid trapped in the annuli.

A direct consequence of this phenomenon is illustrated in Figure 4, which shows a photograph of one of the casings from the Pompano A-31 well in the Gulf of Mexico. According to Pattillo, Cocales, and Morey (2006), there is strong evidence that the observed collapse was related to APB. Similarly, Figure 5 shows another case of collapse in a production well, this time located at the Peace River region (BROWN; KENNY; SLAGMULDER, 2016). In the latter case, the production casing broke and wrapped itself around the production tube, an event which can potentially affect the production of the well. Generally, the collapse of internal casings are more easily detected since the innermost annulus is better instrumented than the outer ones, and any failure connected to them can directly compromise the well flow rate.

Figure 4 – Failure of the 16” casing in the Pompano A-31 well.

Source: Pattillo, Cocales, and Morey (2006)

Figure 5 – Collapsed production casing in a producing well.

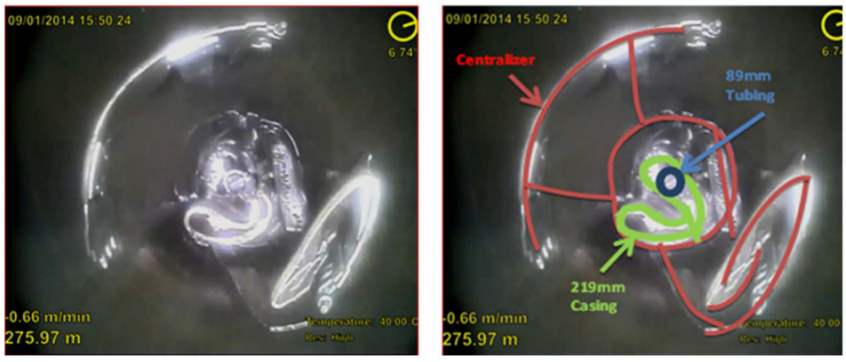

Source: Brown, Kenny, and Slagmulder (2016)

Brazilian pre-salt wells generally produce from reservoirs sealed by evaporitic rocks. But this is not exclusive to Brazil; in fact, about 90% of the world oil reservoirs are sealed by evaporative rocks (JENYON, 1986). However, in the case of the Brazilian pre-salt, the evaporitic rock layers are long, reaching more than one kilometer in length. Also, the sealant rock present in the pre-salt rock formation has specific mechanical

properties that pose some risks to both drilling and well operations (TAHERI et al., 2020; AGOSTINI; ALMEIDA, et al., 2019).

In addition to APB, which is already a concern in deepwater wells, pre-Salt wells are subject to creep of the sealant salt layers. These can potentiate the increase in pressure in these wells, leading to an additional risk, which, if not accounted for during well design, may result in the collapse of the casings and production tube.

Casing design, as demonstrated by the significant number of accidents reported over the years, is an major crucial step on Petroleum Exploration and Production. However, some industry standards make it easy fro such accidents to occur. Byrom (2015) describes the basic procedure for estimating the loads on a given casing, it is based on the standards by AER (2009), here it is presented that a safety factor of 1.0 is acceptable for the collapse strength of a designed casing. Cases such as the one faced by a production well by PETROBRAS may lead the loads of a given project to lower for terms not originally considered. The reason for such a low safety factor is related to the API criteria used to determine the yield limit of casings, in this standard the yield is pretty conservative, so this safety factor can accommodate extra loads in casings (API, 2018). The cause of such failure is the rapid cooling during a acidification to increase permeability at the reservoir, this rapid cooling was not predicted on standard simulators. This lead the company to change the basic procedure for design of its wells (MOREIRA et al., 2020).

The development of new tools to assist the correct design is of upmost importance, since it allows for better predictions of the loads to which the wellbore structure will be presented and as a consequence a greater safety of project. However there is a perceptible gap on development of programs for coupled simulation of the thermally driven APB and the resulting increase in pressure due to salt displacement. So it is clear there is a great interest in programs which can predict the behavior of heat exchange in oil wells which can deal with many different scenarios. Specially for the case of pre-salt wells which hold large commercial interest in Brazil. So this works aims to improve the development of tools useful for design of well structures, assuring integrity on the context of APB including the presence of salt surrounding the well. The proposed tool are based on previous programs used to model APB.

1.1 GENERAL OBJECTIVE

The objective of this thesis is to propose new calculation methods to quantify thermal and structural phenomena in petroleum wells subjected to creep deformation of salt layers. The models, which combine analytical and numerical methods, such as Laplace Transforms and the Finite Element Method, are applied to realistic petroleum production scenarios, with a particular emphasis on the prediction of APB.

The models are compared with field data, commercial software and other in-

house numerical models in order to demonstrate their capabilities and limitations.

1.2 THESIS STRUCTURE

To achieve this general objective, this thesis is divided into 6 chapters, counting this brief introduction. Chapter 2 presents the state-of-the-art in APB modeling on production wells, including the complete mathematical formulation of a standard program used to model APB used in the literature. Chapter 3 presents a new mathematical formulation developed to better represent the heat transfer in shorter simulations of APB. Chapter 4 will present a complete mathematical formulation based on Finite Element Method (FEM) used to model creep on salt layer. This formulation also contains a coupling scheme, used to allow for its influence on APB. On chapter 5 a set of studies are performed to analyze the validity of the developed models and to better understand the phenomenon. For such there are three main studies, the first one using a well already analyzed on Barcelos (2017), after that a well at its starting life, during the Extended Well Tests (EWT). Lastly a well with a salt layer is used to validate the new creep model used to estimate the displacement of salt layers. On the last chapter of the master thesis, chapter 6, the conclusion of the thesis, as well as, proposals of futures works are presented.

2 STATE OF THE ART

Annular Pressure Buildup (APB) and heat transfer phenomena in oil wells have been widely studied in the literature. The purpose of this chapter is to review the state of the art on these subjects, with a focus on pre-salt wells where the issue of salt creep is often a concern. After presenting some basic definitions in section 2.1, section 2.2 presents a detailed review of wellbore heat transfer modelling. Section 2.3 points to some basic works on the wellbore structural deformation. Section 2.4 shows the models used to predict APB in wells. Section 2.5 presents the contributions in the literature on salt creep deformation with focus on oil wells. Section 2.6 presents a set of works which led to the development of a strong numerical formulation to model APB, followed by section 2.7 where the final iteration of the simulation program which is the basis of this thesis. Section 2.8 brings the objectives to be tackled in this thesis.

2.1 BASIC DEFINITIONS

Figure 6 presents a general well geometry (BARCELOS, 2017), where the *y* axis represent the Measured Depth (MD) of the well and the *x* axis is the radial distance with respect to the center line (symmetry axis). Different components of the well structure (e.g., casings, drilling mud, completion fluid) are shown according to the definitions presented in the previous chapter. The right-hand side of the figure presents the lithology of the formation around the well. This is an important aspect of thermal modelling, due to the influence of the rock physical properties on the heat flow and temperature distribution. As mentioned above, fluid flow takes place through the production tube, whose diameter may vary slightly with respect to depth.

Figure 6 – Schematic geometry of a well

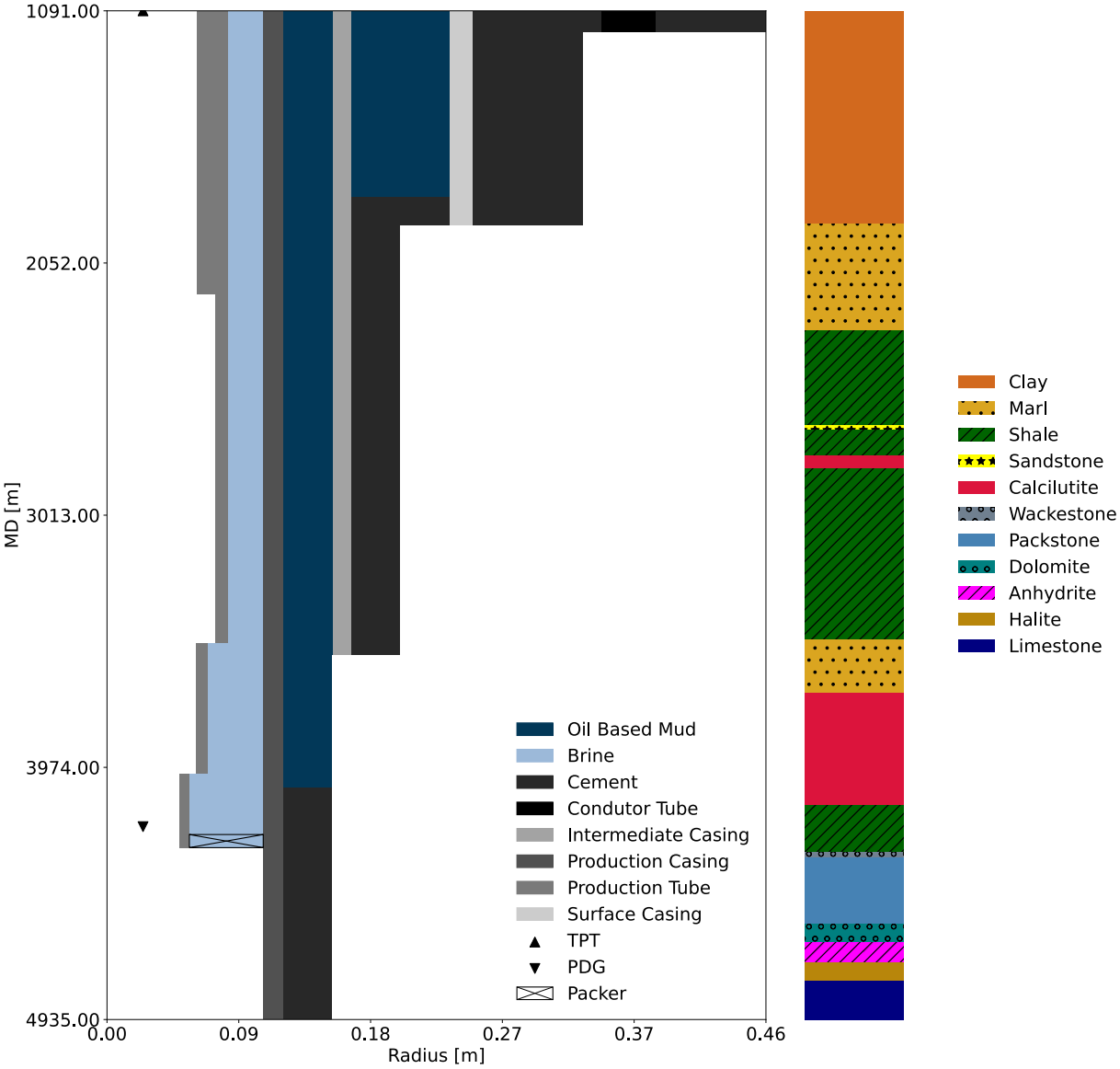

The standard nomenclature adopted in the petroleum industry and is used in Figure 6: the outermost casing is the *conductor tube*, next to it is the *surface casing* and a sequence of *intermediate casings*, which are not found in every well. Finally, inside the production casing lies the production tube.

As most wells have some degree of inclination, at least two definitions of well depth arise. The MD follows the inclination of the well and is equal to the length of an imaginary cable lowered inside the well. On the other hand, the True Vertical Depth (TVD) is the theoretical line which crosses the center of the planet and perpendicularly reaches the wellhead. In other words, the TVD is the projection of the well onto the vertical. Figure 7 presents the the inclination of the well presented in Figure 6 as a function of MD and the relation between TVD and MD.

Figure 7 – Inclination as a function of MD and relationship between MD and TVD for the well of Figure 6.

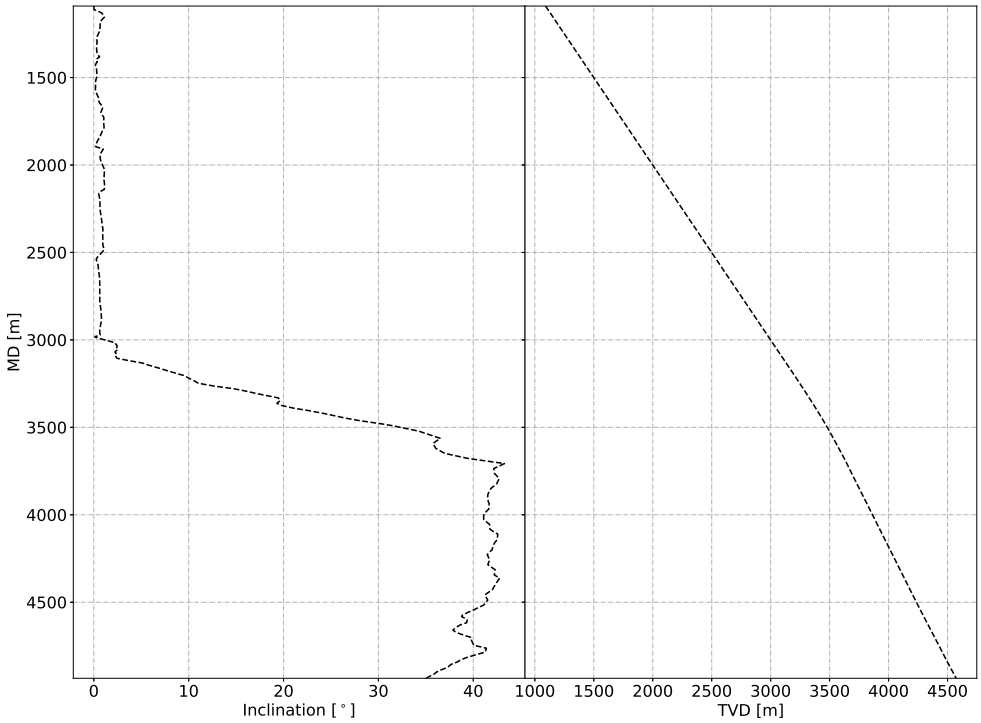

Notice that, at a depth of 3000 m, the so-called Kick-off Point (KOP), the well starts to deviate from the vertical. It is always important to distinguish between MD and TVD, since some variables are reported in terms of the former (e.g., well components) and others are defined as function of the latter (e.g., formation lithology). In the present thesis, all plots use MD as the standard depth, however, for all geometries, the conversion to TVD are presented in Appendix B.

As mentioned before, the annular spaces are filled with either brine or oil based mud. The innermost annulus (annulus A) is filled with brine that is contained by a *packer*, which is a coupling tool that seals the bottom of the annulus. The top of this annulus (wellhead) is equipped with a set of valves which can be used as a pressure relief or as a port for other operations. At the wellhead, there is also a Pressure Transducer (PT), responsible for measuring the fluid pressure inside the innermost annulus. This is the main source of data for validating models to predict APB, as only this annular space is instrumented for pressure. In the other annuli (annulus B and C, the intermediate and the outermost, respectively) of Figure 6, the oil based mud fills the space between the Top of Cement (TOC) and the wellhead.

The main sources of field data from the well are the Permanent Downhole Gauge (PDG) and Temperature/Pressure Transducer (TPT). In the typical well of Figure 6, the PDG is located near the bottom of the production tube to measure the pressure and temperature as close as possible to the reservoir. Meanwhile, the TPT is located on

the wellhead, where it records the pressure the and temperature of the produced fluid leaving the well. One of the main problems associated with this measurement is the fact that the transducers are close to the sea bed, giving rise to large uncertainties due to the high temperature gradients. Nevertheless, the PDG and TPT often provide the only data against which wellbore heat transfer models can be validated.

The well flow rate is perhaps the only relevant measurement performed remotely. The produced fluid flow rate is measured at the platform, downstream of the separation tank which, as the name entails, is used to separate the gas, oil and water by action of gravity. A schematic diagram of a complete petroleum production system is shown in Figure 8, the separator is located at the surface and measurements of flow are made for each phase independently. As the production line and tank have a large volume, often a significant time delay exists before a flow structure that has passed through the wellbore is detected downstream of the separator. This is an important issue to be dealt with in strongly transient flows.

Figure 8 – Schematic representation of a simple oil producing system

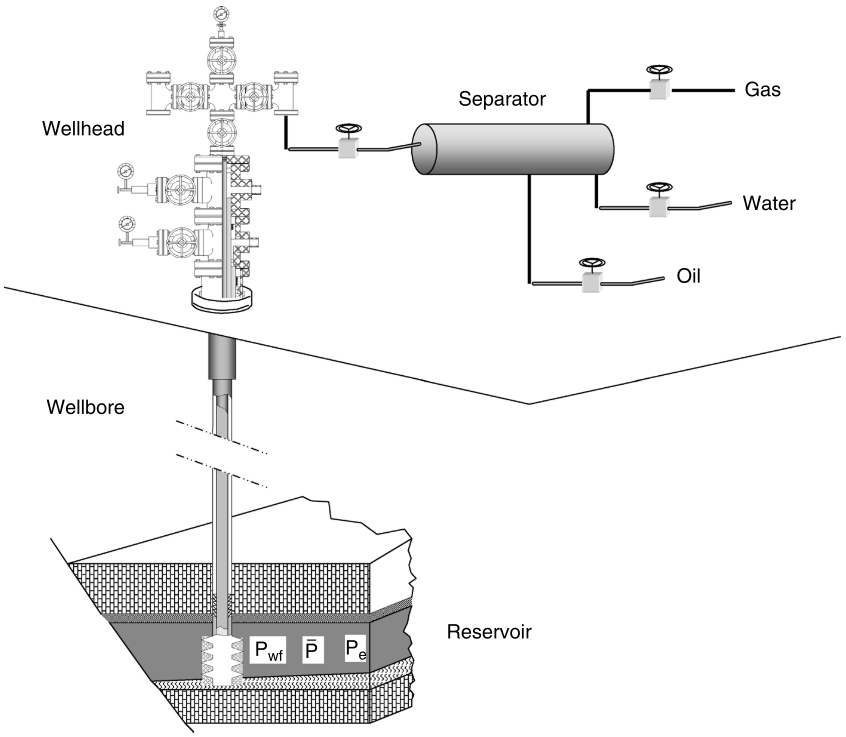

Source: Guo, Lyons, and Ghalambor (2007)

Once the measurements of the oil and gas flow rates are made, the produced fluid ratios can be defined. The Gas to Liquid Ratio (GLR) is the ratio of the gas to the total liquid produced at the standard condition (this condition is defined by the American Petroleum Institute (API) as 60°F and 14.7psia). Another important ratio is the Water Cut (WC), which is defined as the ratio of the water to the oil flow rate at the standard

condition. With these ratios, it is possible to describe the flow in terms of only the oil flow rate at the standard condition..

2.2 WELLBORE HEAT TRANSFER

Since APB is a thermally driven problem, accurate modelling of heat transfer phenomena in wellbores is of utmost importance to estimate the temperature field in well components, including the fluids trapped in the annular regions and the surrounding rock formation. Scientific studies related to heat transfer in wells began to emerge around the 1950's, as authors began to realize its importance in oil recovery techniques, such as hot fluid injection in reservoirs (BIRD et al., 1954). Ramey (1962) advanced a model that is accepted nowadays as the basis of most works dealing with heat transfer in wells.

In what follows, Ramey's approach to solving the heat transfer in injection and production wells is discussed in detail. The works that extended his approach to incorporate additional phenomena and solve more complex scenarios are also reviewed.

2.2.1 Ramey's formulation

2.2.1.1 Assumptions and energy balance

The main assumptions adopted by Ramey (1962) are as follows:

1. The rock formation is treated as a semi-infinite solid;
2. The thermal capacitance of the wellbore is negligible when compared to that of the formation;
3. Momentum and energy balances in the wellbore can be solved via one-dimensional steady-state equations in the axial direction;
4. The heat transfer between the wellbore and the formation is one-dimensional in the radial direction.

The above assumptions are justified by the aspect ratio of wellbores, since the axial and radial dimensions are, respectively, of the order of a few kilometers and under a meter. Therefore, mass, momentum and energy balances in the well can be formulated in one-dimensional form without a perceivable loss in accuracy. Also, in most practical situations, the advection time scale (i.e., the characteristic time associated with the fluid flow through the wellbore) is much shorter than the time scale associated with the change in boundary conditions (i.e., at the reservoir or at the bottom of the well). Thus, it is reasonable to adopt a pseudo steady-state approach in which the

dependence on time is considered in the boundary conditions and closure relationships for the radial heat transfer.

The well is surrounded by the rock formation that acts, from a heat transfer perspective, as a semi-infinite medium. As such, given the radial length scales and physical properties of the well components and rock formation, the time scale of the problem as a whole is dictated by the transient heat transfer within the rock formation.

In order to calculate the rate of heat transfer from the formation to the production fluid (or vice-versa in the case of oil production), an equivalent thermal conductance (the reciprocal of an overall thermal resistance) can be defined, considering the multiple radial layers between the flowing fluid and the interface between the well and the formation:

$$Q' = 2\pi r_{\text{tub}} U \left(T_{\text{fm,Int}} - T_{\text{pf}} \right) \tag{1}$$

where Q' is the heat transfer rate per unit length, r_{tub} is the inner radius of production tube, U is the overall heat transfer coefficient, $T_{\text{fm,Int}}$ is the temperature at the interface between the wellbore and the formation, T_{pf} is the bulk temperature of the production fluid.

The energy balance in the production fluid, according to Ramey (1962), was written as:

$$\frac{\partial h_{\text{pf}}}{\partial z} - g + v\frac{\partial v}{\partial z} = \frac{Q'}{\dot{m}} \tag{2}$$

where h_{pf} the specific enthalpy of the produced (or injected) fluid, v is the mass average flow velocity, $\dot{m}$ is the mass flux (mass flow rate per unit cross-sectional area) and z is the depth (MD).

By assuming steady state in the wellbore and transient heat transfer in the formation, Ramey (1962) resolved the energy conservation for single-phase flow with a single overall thermal conductance, neglecting the friction term. He derived two analytical expressions for the one-dimensional longitudinal temperature profile: one for (incompressible) liquids and another for (ideal) gases, which corresponded to attempts to model field operations such as water and superheated steam injection, respectively.

Equation 1 was used to couple the formation heat transfer problem and the wellbore thermal network via the interface temperature, $T_{\text{fm,Int}}$. As mentioned previously, Ramey (1962) treated the formation as a semi-infinite medium. Although both the heat transfer rate per unit length, Q', and $T_{\text{fm,Int}}$ are time dependent, Ramey (1962) *assumed* a constant heat flux boundary condition at the wellbore-formation interface to solve the transient heat flow in the formation. By doing so, simpler (but intrinsically less accurate) expressions can be derived for the variation of $T_{\text{fm,Int}}$ with respect to time, which can be plugged into Equation 1 to determine the heat transfer rate per unit length

to be used in the energy balance, Equation 2. The formation heat transfer problem, as solved by Ramey (1962), is discussed next.

2.2.1.2 Formation heat transfer

Ramey (1962) assumed a predominately radial heat transfer in the formation. Therefore, disregarding the longitudinal heat transfer term, the formation heat conduction equation becomes:

$$\frac{\partial^2 T_{\text{fm}}}{\partial r^2} + \frac{1}{r}\frac{\partial T_{\text{fm}}}{\partial r} = \frac{1}{\alpha_{fm}}\frac{\partial T_{\text{fm}}}{\partial t} \tag{3}$$

where T_{fm} is the formation temperature and α_{fm} its thermal diffusivity. It is important to emphasize that this model does not consider explicitly the presence of fluids in the pores of the rock formation. However, its effects can be considered implicitly in the thermal diffusivity.

The boundary conditions consider the presence of an undisturbed geothermal gradient, which is a function of depth only. Also, continuity of temperature and heat flux are guaranteed at the interface between the well and the formation. Thus:

$$\begin{cases} T_{\text{fm}}(r, t=0) = T_{\text{fm},0} & \text{(4a)} \\ \lim\limits_{r\to\infty} T_{\text{fm}}(r,t) = T_{\text{fm},0} & \text{(4b)} \\ T_{\text{fm}}(r = r_{\text{fm}}, t) = T_{\text{Int,fm}} & \text{(4c)} \\ Q' = -2\pi k_{\text{fm}} r \left.\dfrac{\partial T_{\text{fm}}}{\partial r}\right|_{r=r_{\text{fm}}} & \text{(4d)} \end{cases}$$

where $T_{\text{fm},0}$ is the initial (undisturbed) formation temperature (derived from the geothermal gradient) and r_{fm} is the radius of the well-formation interface.

Note that both Equation 4c and Equation 4d are necessary, since $T_{\text{Int,fm}}$ is, *a priori*, unknown. Ramey (1962) used Equation 4d as a boundary condition, assuming a constant heat flux to obtain an approximate closed form solution to Equation 3, which was solved together with the wellbore steady-state thermal network to determine both Q' and $T_{\text{Int,fm}}$ that satisfy the energy conservation in the radial direction.

The above equations can be simplified by introducing the following dimensionless groups:

$$\begin{cases} \tau = \dfrac{\alpha_{fm} t}{r_{\text{fm}}^2} & \text{(5a)} \\ r_{\text{D}} = \dfrac{r}{r_{\text{fm}}} & \text{(5b)} \\ T_{\text{D,fm}} = \dfrac{T_{\text{fm}} - T_{\text{fm},0}}{T_{\text{fm},0}} & \text{(5c)} \\ Q'_{\text{D}} = \dfrac{Q'}{k_{\text{fm}} T_{\text{fm},0}} & \text{(5d)} \end{cases}$$

Equation 5a is the Fourier time (or the Fourier number), which is defined as the ratio of characteristic scales associated with the diffusive transport rate ($\alpha_{fm}/r_{\text{fm}}^2$) and thermal storage rate ($1/t$). Thus, a large value of τ indicates a faster heat propagation through the medium. In dimensionless form, the formation thermal model becomes:

$$\begin{cases} \dfrac{\partial^2 T_{\text{D,fm}}}{\partial r_{\text{D}}^2} + \dfrac{1}{r_{\text{D}}} \dfrac{\partial T_{\text{D,fm}}}{\partial r_{\text{D}}} = \dfrac{\partial T_{\text{D,fm}}}{\partial \tau} & \text{(6a)} \\ T_{\text{D,fm}}(r_{\text{D}}, \tau = 0) = 0 & \text{(6b)} \\ \lim\limits_{r_{\text{D}} \to \infty} T_{\text{D,fm}}(r_{\text{D}}, \tau) = 0 & \text{(6c)} \\ Q'_{\text{D}} = -2\pi r_{\text{D}} \left. \dfrac{\partial T_{\text{D,fm}}}{\partial r_{\text{D}}} \right|_{r_{\text{D}}=1} & \text{(6d)} \end{cases}$$

In order to solve the above system of equations for a constant Q'_{D}, Ramey (1962) adopted a procedure similar to that of Van Everdingen and Hurst (1949) for the hydraulic diffusion problem using Laplace transforms. In terms of the dimensional temperature, the analytical solution is given by:

$$T_{\text{fm}}(r_{\text{D}}, \tau) = T_{\text{fm},0} + \frac{Q'}{2\pi k_{fm}} \mathscr{L}^{-1} \left\{ \frac{K_0\left(r_{\text{D}}\sqrt{s}\right)}{s\sqrt{s} K_1\left(\sqrt{s}\right)} \right\} \tag{7}$$

where K_0 and K_1 are the modified Bessel functions of the second kind, $\mathscr{L}$ is the Laplace transform operator and s is the transformed variable in the Laplace domain (time in this case).

Since there is no known analytical inversion for the Laplace transform in Equation 7, numerical inversions must be sought or, in Ramey's case, approximate expressions can be derived such that:

$$f(t) \approx \mathscr{L}^{-1} \left\{ \frac{K_0\left(\sqrt{s}\right)}{s\sqrt{s} K_1\left(\sqrt{s}\right)} \right\} \tag{8}$$

where $f(t)$ is a simplified expression which approximates the inverse transform over a particular time range. For instance, Ramey (1962) proposed a log-linear expression that fits the actual profile for large Fourier times (LEE; ROLLINS; SPIVEY, 2003):

$$f(t) = -0.290 + \ln\left(\frac{r_{\text{fm}}}{2\sqrt{\alpha_{fm}t}}\right) \tag{9}$$

Therefore, to provide closure for solving the wellbore energy balance, the above expression is used in conjunction with Equation 7 for $r_{\text{D}} = 1$ and Equation 1 to determine Q'_{D} and $T_{\text{Int,fm}}$ at a given depth.

2.2.2 Works based on Ramey's approach

The work by Ramey (1962) has several limitations and simplifications which were tackled by other authors in subsequent works dealing with injection and production operations. Satter (1965) generalized Ramey's energy balance to handle vapor condensation, since understanding how the vapor mass quality changes with depth is essential to design superheated steam injection operations. The formulation was identical to that of Ramey (1962) up to the depth at which the fluid begins to condense. A new expression was proposed to calculate the vapor quality from that point on. Again, friction was disregarded, resulting in an expression for the vapor quality that does not depend on the potential energy.

To include friction effects, Durrant and Thambynayagam (1986) solved the momentum and energy balances for near-critical steam injection using a numerical method (marching procedure). Ramey (1962) assumed that the properties used in the calculation of the heat exchange rate between the wellbore and the surrounding media were independent of temperature and pressure (hence independent of depth). Conversely, Durrant and Thambynayagam (1986) took advantage of the marching procedure to add variable properties (functions of temperature and pressure) which were calculated at different depths. Although the formulation was numerically robust, the computational cost was considered high for the time, so the method was replaced by simpler formulations (HASAN; KABIR, 1991). By using the marching procedure, the heat flux had to be computed at each depth, a procedure that is similar to most modern algorithms.

To cope with the computational limitations of the time, Sagar, Doty, and Schmidt (1991) developed a model for multiphase production wells, which included the Joule-Thomson and friction effects in a correlation that could be applied directly in the energy balance equation. This correlation was derived from field data and allowed the deduction of an analytical expression for the axial temperature distribution similar to that of Ramey (1962). This model allowed simulation of multiphase flows in the wellbore, however, it still assumed that the properties used to determine the heat transfer rate were independent of temperature.

Hasan and Kabir (1991) used a more robust formulation to further develop Ramey's time functions. Numerical inversion was used to better approximate Equation 8 using two expressions. The obtained time function, one of the most used in the

literature, is defined by:

$$f(t) = \begin{cases} 1.1281\sqrt{\frac{t\alpha_{fm}}{r_{\text{fm}}^2}}\left(1-0.3\sqrt{\frac{t\alpha_{fm}}{r_{\text{fm}}^2}}\right), & \text{if } \frac{t\alpha_{fm}}{r_{\text{fm}}^2} \leq 1.5 \\ \left[0.4063+0.5\ln\left(\frac{t\alpha_{fm}}{r_{\text{fm}}^2}\right)\right]\left(1+\frac{0.6r_{\text{fm}}^2}{\alpha_{fm}t}\right), & \text{otherwise} \end{cases} \tag{10}$$

Chiu, Thakur, et al. (1991) considered the effect of well inclination in the momentum and energy balances. Their formulation was similar to that of Durrant and Thambynayagam (1986) in that a coupled numerical solution of the conservation equations was proposed via a marching scheme. The frictional pressure gradient was calculated using the Beggs and Brill (1973) correlation. The effect of variable fluid injection rates was investigated, thus allowing comparisons with several real wells. For such cases, it was shown that assuming a constant wellhead flow rate may lead to unsatisfactory heat loss predictions.

Alves, Alhanati, and Shoham (1992) proposed a complete model applicable to production wells, which included the effects of well inclination, frictional pressure gradient and Joule-Thomson coefficient in the energy equation written in terms of temperature. Physical properties were calculated via the Black-Oil correlations.

Most models developed so far disregard buoyancy-induced fluid motion and assume a purely conductive thermal resistance in the sealed annuli. In order to estimate whether such approach is precise, Hasan and Kabir (1994) compared the effects of different heat transfer phenomena when considering convection in the annulus. By doing so, they refined the use of an equivalent thermal network (considering different heat transfer modes) as the basis for calculating the equivalent conductance used in Equation 1. They concluded that considering convection in the annulus is important to properly compute the temperature profile in a production well.

One aspect not previously considered by the other models is the ability to deal with a sequence of different well operations, such as periodically stopping and restarting production. An intrinsic problem of such predictions is that, for shorter times (small Fourier numbers), the modeling assumptions lead to a poor agreement with field data. To alleviate this problem, Hasan, Ameen, and Wang (1996) applied methods based on the superposition principle to deal with a succession of trasient-like problems. This approach consists of solving the heat transfer in a sequence of small time steps, using Duhamel's principle to better capture transient nature of the heat transfer problem. By doing so, a complete transient solution to Equation 3 was emulated using the time function proposed in Hasan and Kabir (1991) (Equation 10).

To facilitate understanding of the approach described above, Figure 9 illustrates the superposition treatment of a continuous generic heat transfer function using a stepwise function of equally spaced, constant heat flow, time intervals. Notice that a finer discretization in regions of steeper descent would yield more precise solutions.

Also, in this case of an exponential decay, the final approximation is closer to the actual function.

Figure 9 – Superposition principle using a stepwise functions to represent the actual heat transfer rate.

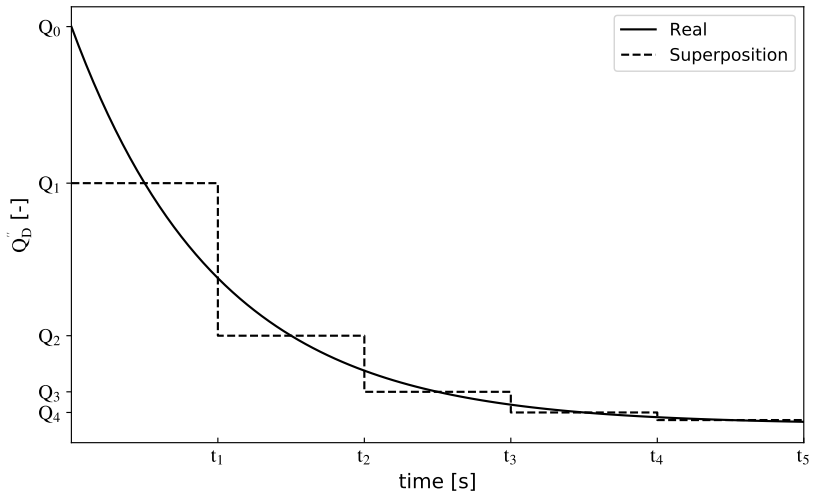

Hagoort (2004) proposed a graphical method to determine the validity of the constant heat flux boundary condition to solve the transient heat transfer in the wellbore-formation system. He established that, for Fourier times above 10, Ramey's assumptions are valid. Hagoort (2004) also determined that the heat transfer is ruled by tree dimensionless numbers: Ramey number (coined by the author), Graetz number and the thermal skin factor, defined by:

$$N_{Ra} = \frac{2\pi k_{\text{fm}} L \rho_{\text{pf}}}{c_{p\text{pf}} \dot{V}} \tag{11}$$

$$N_{Gr} = \frac{k_{\text{fm}} L}{r_{\text{fm}}^2 v} \tag{12}$$

$$N_{sk} = \frac{U r_{\text{fm}}}{k_{\text{fm}}} \tag{13}$$

The physical meaning behing the Ramey's number (N_{Ra}) is related to the ratio of heat loss to the formation by the heat advected up the tube. Larger Ramey number points to a higher temperature difference from the bottom to the wellhead.

The Graetz's number arises from the ratio of the characteristic time for the formation and the characteristic time for the convection in the wellbore. It is usually used to estimate if a flow profile is completely developed, in the wellbore scenario it can be used to evaluate if the assumption of negligible accumulation is valid in the annuli.

The dimensionless heat transfer coefficient (reciprocal of the skin number), defined by Equation 13, represents the ratio of conduction in the formation to the near

wellbore heat transfer. Large values of N_{sk} represents little resistance near the borehole.

When applied in the context of short transients, Hagoort (2004) observed a tendency of Ramey's assumptions to over-predict the wellhead temperature in a production scenario. He also proposed a new time function based on a different approach that tries to mimic the behavior of transient interface heat flux instead of approximating Equation 8. By doing so, a new expression better suited for shorter times is reached as follows:

$$f(t) = \begin{cases} \frac{1}{\sqrt{\pi\tau}} + 0.5 - \frac{0.79526}{4}\sqrt{\frac{\tau}{\pi}}, & \text{if } \tau \leq 1.0 \\ -0.0012[\ln(\tau)]^3 + 0.0249[\ln(\tau)]^2 + 0.3083\ln(\tau) + 1.0504, & \text{if } \tau \leq 10^5 \\ 0.5\ln\left(\frac{4\tau}{\gamma}\right) \end{cases} \tag{14}$$

where γ is the exponential of the Euler-Mascheroni constant (≈ 1.7810724).

Another work which aimed to improve the solution for small Fourier times, while still using Ramey's assumptions, was proposed by Cheng et al. (2011). In order to better estimate the temperature of steam during injection, the authors defined a new time function that depends on the ratio of thermal capacity of the formation and the radial thermal capacity of the wellbore.

$$\omega_{welb} = \frac{(\rho c_p)_{\text{fm}}}{(\rho c_p)_{welb}} \tag{15}$$

where $(\rho c_p)_{welb}$ is the sum of all radial thermal capcity in a given layer of wellbore (adding all tubings, cement and fluids presents in the depth). $(\rho c_p)_{\text{fm}}$ is the formation thermal heat capacity defined as:

$$(\rho c_p)_{\text{fm}} = \frac{k_{\text{fm}}}{\alpha_{fm}} \tag{16}$$

By doing so, a time function was created to calculate the transient heating of the annulus by considering part of the energy from the steam that is stored in each annulus as follows:

$$f(t) = \ln\left(2\sqrt{\tau}\right) - \frac{e}{2} + \frac{1}{4\tau}\left[1 + e + \left(1 - \frac{1}{\omega_{welb}}\right)\ln(4\tau)\right] \tag{17}$$

where e is the Euler constant.

The results were compared with Ramey's time function and with the superposition principle approach of Hasan, Ameen, and Wang (1996), with the proposed solution lying between the two. The authors also pointed out that Ramey's assumptions are valid after 7 days.

2.2.3 Other works

Due to the limitations of Ramey's assumptions, many authors proposed different ways to model heat transfer in wellbores. Bahonar, Azaiez, and Chen (2010) were the first to verify the classical assumptions against more complex formulations by developing multiple models. The first of such models is a two-dimensional heat transfer model of the formation. Later, a one-dimensional numerical model of the formation with a full discretization of the domain, i.e., without the use of time functions, was investigated. After that, the thermal capacity of the annuli and casings was considered. Finally, these three models were compared to the original formulation of Ramey (1962), using multiple time functions.

The main result was that for time frames over a week, the classical assumptions hold true, except near the top and bottom regions of the formation, where two-dimensional approaches may prove necessary, even for longer times, due to the heat transfer with the sea bed and reservoir. Besides that, it was shown that for longer times, the Ramey (1962) time function gave more accurate results than other time functions, such as that of Hasan and Kabir (1991). For shorter times, a two-dimensional transient approach is necessary for greater accuracy, however, it comes with a high computational cost. This was a great limitation of this type of formulation before the present decade. Bahonar, Azaiez, and Chen (2010) used field data from a steam injection well to validate their analysis.

Nian et al. (2014) also investigated wellbore thermal capacitance effects during steam injection. They also point out that, for most cases, even after 3 days of operation, Ramey's assumptions can be valid. However, for shorter times, capacitance effects cannot be neglected.

A particular operation which requires high precision temperature predictions is Underbalanced Drilling. In this operation, the well is most susceptible to suffering from *kicks* which, if not dealt with properly, may lead to a blowout of the well. In order to better understand the thermal phenomena in this scenario, Mou Yang et al. (2015) developed a complete two-dimensional simulator which takes into account the transient terms in the momentum and energy balance equations. Since the relevant phenomena occur at time scales smaller than days, models based on Ramey's assumptions cannot be applied. The proposed model demonstrated good accuracy against field data, with deviations smaller than 2.13%. The model of Hasan and Kabir (1994) presented a relative error of 4.06%. Since the basic heat transfer phenomena involved in drilling and oil production are similar, the formulation of Mou Yang et al. (2015) can be easily adapted to production applications. As most of the heat exchange during drilling takes place over short periods of time, more robust approaches should be used. In general, the models for fluid circulation during drilling and kick prevention are very close to the state-of-the-art thermal models (LI; LIU; LI, 2015; LI; YANG, et al., 2016; XU et al.,

2018; ABDELHAFIZ; HEGELE; OPPELT, 2020).

You, Rahnema, and McMillan (2016) developed a complete two-dimensional model to predict the heat transfer in a cyclic-injection steam well and a geothermal well. The model was more precise than the one by Ramey (1962), especially near the tube inlet, where the deviations between the models were more perceptible. Also, there were differences with respect to the Hagoort (2004) time function, but these were somewhat smaller which, in itself, is an important result since, for most scenarios, the elevated computational cost of two-dimensional models may still not be worth the small gain in precision. Figure 10 shows the comparison of the two time functions and the two-dimensional model of You, Rahnema, and McMillan (2016). It is clear that for Fourier times above 10, all three models converges to the same solution.

Figure 10 – Comparison of three different formation heat transfer model.

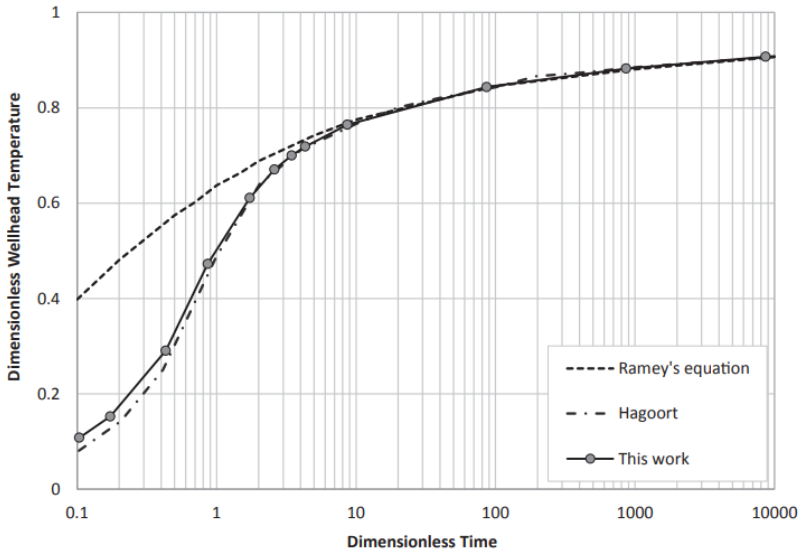

Source: You, Rahnema, and McMillan (2016)

Supercritical CO_2 injection as an enhanced oil recovery technique is receiving increased attention for its environmental contribution (carbon capture). Since this operation involves cooling of the well, Yi et al. (2018) proposed a complete formulation to deal with the heat transfer in the wellbore, considering the thermodynamics of the injected fluid. The model was implemented using fully a implicit finite-difference method to predict the temperature and pressure in the injection string so that the CO_2 reaches the supercritical state at well bottom. However, two basic inconsistencies were found in the energy balance equation derived in their work. First, the authors presented a wrong expression for the Joule-Thomson effect, which may lead to wrong predictions of expansion and compression effects of the CO_2. Second, viscous dissipation effects were incorrectly modeled as heat conduction between two adjoining semi-infinite bodies, namely the injected fluid and the tubing wall.

Zhang, Guan, et al. (2019) argued that the discontinuities present in traditional one-dimensional heat transfer models may lead to poor APB predictions, which demands the development of more advanced formulations. Regarding the thermal simulation only, Hu et al. (2020) compared the results from traditional approaches to a complete CFD simulation of a geothermal well using the commercial software Comsol™ (COMSOL, 2018). It was concluded that, for engineering applications, due to computational cost, most of the state-of-the art simulators may not be ready for large scale application.

In recent years, the application of complete transient analysis gained interest in the design of wellbores. Moreira et al. (2020) presented the case of a pre-salt cluster well that collapsed during acidification. This operation, which involves cooling of the wellbore and is deemed harmless by steady-state simulators, when analyzed via fully transient approaches, needs to be carefully designed so that the pressure difference between neighboring annuli caused by unsteady heat transfer due to cold fluid injection does not pose a risk of well collapse. Agostini, Júnior, et al. (2020) extended the analysis by discussing APB mitigation procedures applicable to different well configurations.

2.3 WELLBORE STRUCTURAL MODELING

In addition to the heat transfer in the wellbore, in order to properly model APB in oil producing wells, it is also necessary to model the structural deformation. As a consequence of temperature variations and fluid expansion within the annuli, the solid materials deform, thus changing the volumes of the confined spaces which, in turn, affect the pressure behavior of the fluid.

The calculation of the stress state in the wellbore structure is a two-step process. First, the initial design requires the calculation of the stresses during installation. This is done via simple force balances and considers the weights of the drilling fluids in order to estimate the pressures on the walls of the casings (BYROM, 2015). The second part, which is directly affected by the wellbore heat transfer, consists of evaluating the stress condition due to heating of the concentric annuli.

To deal with the second step, most works either use simplified models or commercial software to compute the stress state as well as deformation of the solids. In the realm of simplified models, the main contributions can be divided into works which consider the casings as single strings (and do not deal with the radial contact between neighboring elements) or multi-string simulators. Goodman and Halal (1993) indicated that the use of single-string models can generate poor results for the stress in the casings so more advanced models are necessary. To correct this problem, and to include thermal expansion terms to couple the structural simulation with APB simulation, Halal and Mitchell (1994) presented a multi-string formulation that includes the thermal expansion in the casings.

The basic idea behind the latter model is to use the solutions proposed in Timoshenko and Goodier (1970) for thick wall tubes, based on the assumption of plane stress in a axissymmetric grid. The model is defined such that there is continuity both in stress and deformation between solid interfaces in direct contact. To achieve this, a set of equations for “bundled” solids is created, which can be solved in a coupled manner as each solid interacts withits neighbor. The complete mathematical formulation of this model will be detailed further in Section 2.7.3.1 of the present work.

The approach by Halal and Mitchell (1994) proved to be robust and sufficiently general for application in complex geometries. However, more recent studies considered the axial deformation as a result of the displacement of the wellhead. This approach captures volume changes that traditional one-dimensional models cannot quantify. An example of the latter models is the work of Liu et al. (2014) in which an axial displacement of approximately 0.15 m is reported.

2.4 APB COMPUTATION

The first major work to explore the physics of APB was presented by Oudeman and Bacarreza (1995). Drilling mud and completion fluid thermodynamics was used to write a basic equation to estimate the annulus pressure increase as follows:

$$\Delta P_{\text{ann}} = \left.\frac{\partial P_{\text{ann}}}{\partial M_{\text{ann}}}\right|_{V,T} \Delta M_{\text{ann}} + \left.\frac{\partial P_{\text{ann}}}{\partial V_{\text{ann}}}\right|_{M,T} \Delta V_{\text{ann}} + \left.\frac{\partial P_{\text{ann}}}{\partial T}\right|_{M,V} \Delta T \tag{18}$$

where M_{ann} is the mass of fluid and V_{ann} is the volume of each annulus. This equation represents the three main contributions to APB. The first term is related to mass leakage of fluid, which may occur due to fractures in the formation or intentional venting. The second is due to volume variation. Normally this opposes APB as a result of elastic deformation of casings and uncemented formation. The last and dominant term relates the pressure buildup to a variation in average temperature. As highlighted by Oudeman and Bacarreza (1995), Equation 18 is a linearization of a differential expression of the pressure in the annulus, and is applicable only to small pressure increments.

Since the partial derivatives used in Equation 18 can be related to thermodynamic coefficients, it can be rewritten as:

$$\Delta P_{\text{ann}} = \frac{\Delta V_{\text{ann,l}}}{\kappa V_{\text{ann,l}}} - \frac{\Delta V_{\text{ann}}}{\kappa V_{\text{ann,0}}} + \frac{\beta \Delta T}{\kappa} \tag{19}$$

where, β and κ are the expansivity and isothermal compressibility of the fluid filling the annulus. $V_{\text{ann,0}}$ is the initial volume of the annular space and $V_{\text{ann,l}}$ is the fluid volume. The last two terms are different: the first one represents the volume variation of the annular space, while the second one represents the volume of fluid leaked from

the annulus. Oudeman and Bacarreza (1995) applied this model to an instrumented producing well during transient testing and obtained good results against field data.

The consequences of APB became notorious after the work of Moe, George Robert; Erpelding (2000), who outlined the main contributing well design factors and operating conditions, which are common to most newer offshore wells and can lead to significant pressure increases in sealed annuli:

1. Great water depths, resulting in colder installations;
2. Deep reservoirs, resulting in hotter produced fluids;
3. Large flow rates, resulting in a high thermal capacity fluid stream.

Moe, George Robert; Erpelding (2000) also presented some of the first mitigation techniques used to reduce APB (i.e. use of crushable foam to allow the expansion of the trapped fluid without significant increase in pressure). However, it was also stated that APB is an inherent problem of oil production and even with mitigation techniques it is not possible to completely prevent APB, so it is crucial to predict its magnitude during the well design stage.

Bradford et al. (2004) reported the catastrophic failure of the production tie-back of the Marlin A-2 well in the Gulf of Mexico. Several scenarios were compared and a conclusion was reached that APB was directly related to the failure. Using Equation 19, Ellis et al. (2004) investigated mitigation techniques to be used in the remaining Marlin wells. During several test scenarios, the the use of Vacuum-Insulated Tubing (VIT) was suggested to reduce heat transfer and fluid expansion in the annuli. Also, new concepts involving a N_2 filled annulus were discussed, which provided good thermal insulation and compressibility to reduce the risk of APB failure.

Oudeman and Kerem (2004) further improved the model of Oudeman and Bacarreza (1995), and pointed out that the temperature term of Equation 19 can be responsible for about 80% of the APB. In a sealed annulus, the deformation term is responsible for the rest. Also, using field data, they confirmed that the formulation is precise up to an increase of 40 ℃. From this point on, it starts to overestimate the APB; the use of water properties to simulate the drilling mud was attributed as the cause of this deviation.

By collecting all previously proposed APB models, Sathuvalli, Payne, et al. (2005) advanced a formulation for computing the pressure increment. The models were compared with field data and new mitigation techniques were discussed. After a thorough investigation, Pattillo, Cocales, and Morey (2006) concluded that APB was the cause of the collapse of a casing during drilling of the Pompano A-31 well. This was the first reported case of APB-related catastrophic failure during drilling. The authors used thermal modeling tools with Finite Element Method (FEM) computational programs to analyse the effects of pressure variation in the annulus during drilling. They concluded

that, even with all specifications satisfied for the well, the APB was sufficient to collapse one of the casings, trapping the drilling column. One of the most important conclusions from Pattillo, Cocales, and Morey (2006) was the fact that thermal effects can be crucial in every scenario of well design, further motivating the study of APB and its consequences.

Hasan, Izgec, and Kabir (2009) developed a fully transient approach to predict the temperature in each annuli. In their calculation of the APB, the volume deformation contribution was disregarded and the temperature change contribution was averaged with respect to the volume of each differential control volume, considering the mass filling each annulus and its density. The final expression for the APB is given by:

$$\Delta P_{\text{ann}} = \frac{\sum_{vol} \left(M_{vol}/\rho_{vol}^2\right) \left(\frac{\partial \rho}{\partial T}\Big|_P\right) \Delta T - \Delta V_{\text{ann,l}}}{\sum \left(M_{vol}/\rho_{vol}^2\right) \left(\frac{\partial \rho}{\partial P}\Big|_T\right)} \tag{20}$$

where M_{vol} is the mass contained in each individual control volume used in the discrete grid and ρ_{vol} is the density of the fluid calculated in each volume. This approach leads to an algebraic ("pressure vessel-like") treatment of the annulus, with all thermal properties averaged based on the discrete grid used.

Also, Hasan, Izgec, and Kabir (2009) used the fully transient analysis coupled with a reservoir simulator. It was concluded that more robust transient analyses are important when flow rates can vary drastically. In such cases, the higher computational cost may be justified.

Jin Yang et al. (2013) proposed a new iterative approach for estimating APB, which uses the volume variation of the annulus with a purely radial deformation scheme to calculate the total volume variation of the annulus and the APB. For its relative simplicity and small deviations with respect to field data (within 7.27%), this iterative approach is used in some commercial simulators.

Dong and Chen (2017) performed a complete analysis of APB mitigation methods (see Figure 11), while discussing the benefits of each mitigation technique. Under explored APB mitigation techniques, such as the use of better insulation fluids, were indicated. This work is only one of many to tackle the mitigation methods, which is a topic of high interest (FERREIRA; SANTOS; VANZAN, 2012; SANTOS et al., 2015; SATHUVALLI; PILKO, et al., 2016).

Figure 11 – APB Mitigation strategies and techniques

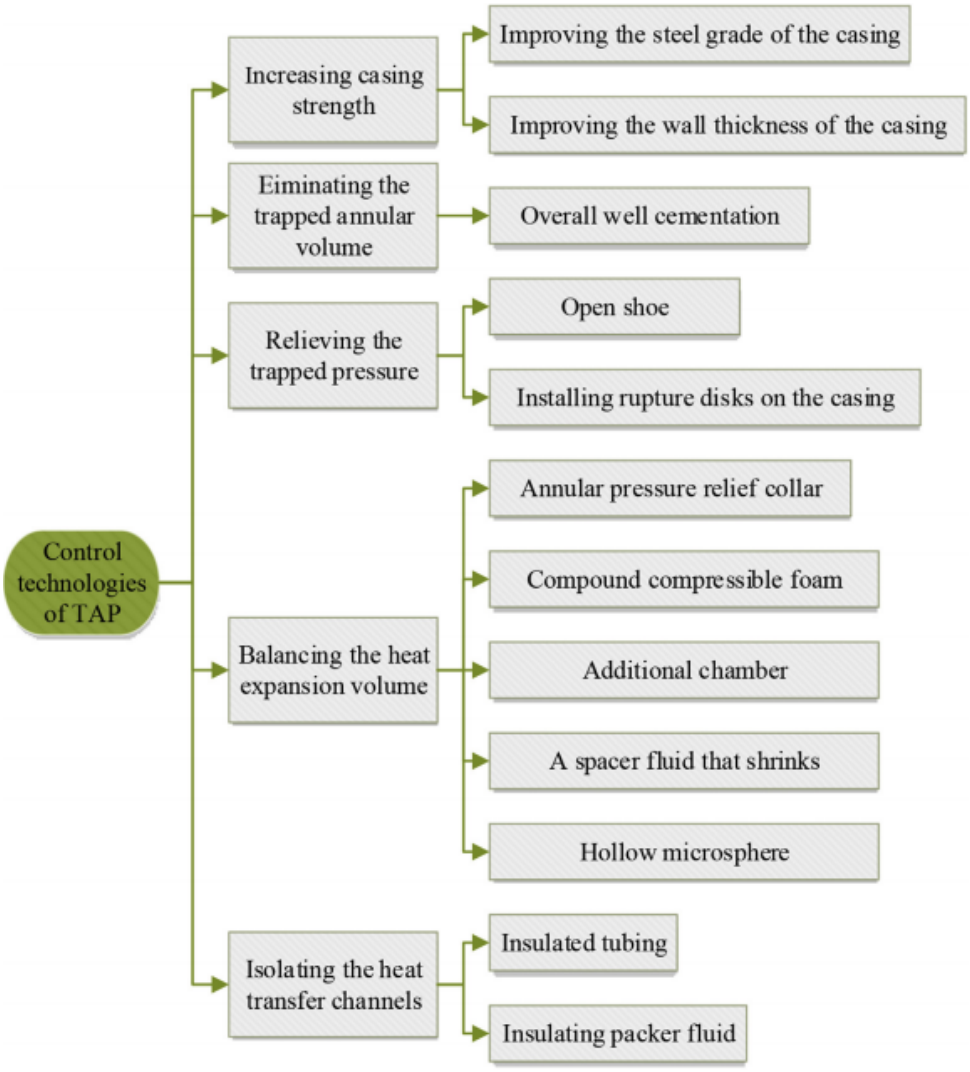

Source: Dong and Chen (2017)

Even with all the development from previous decades, the literature still lacks models and simulators with the capacity do deal with all aspects related to APB and its mitigation methods. This statement is corroborated by studies such as that of Zhang, Guan, et al. (2019), who recently reviewed the APB mitigation strategies and the advantages and limitations of several modeling schemes. For example, the one-dimensional methods (based on Ramey's assumptions) generate discontinuous temperature profiles in the annuli, leading to a poor representation of the final pressure increase. Also, by not considering the dependence of the thermophysical properties with respect to temperature, most models under predict the heat exchange, and therefore, the APB.

2.5 SALT CREEP IN WELLBORES

According to Halal and Mitchell (1994) the thermo-elastic deformation of the wellbore structure is an important factor of APB, which may contribute to as much as 20% of the increase in pressure in a sealed annulus (OUDEMAN; KEREM, 2004). However, in certain scenarios, other mechanisms need to be taken into account, such as plastic deformation phenomena, fracture propagation, deformation of unconsolidated rocks and creep (FJAER et al., 2008).

Creep (or cold flow) is the time-dependent inelastic deformation of a material subjected to a constant load (JAEGER; COOK; ZIMMERMAN, 2007). It is highly important in well engineering, as most oil reservoirs are trapped by evaporitic sealant rocks (JENYON, 1986), which are known to suffer from creep. Even after long periods of time (of the order of decades), extra stresses in the casings due to creep of the rock formation may still be significant.

Studies on creep started in the 1830's (ALMEIDA, 2016), but the main contributions to the understanding of the phenomenon of creep in rocks emerged with Griggs (1940) (JAEGER; COOK; ZIMMERMAN, 2007). It is now known that creep occurs in three main stages; in the primary stage (also called transient), the deformation decelerates rapidly over time. After this initial stage, in the secondary (or stationary, or steady-state) stage, the creep rate becomes constant for a long period of time. Finally, there comes a point where the crystalline structure of the material cannot resist large deformations and the creep rate varies more sharply until the point where a failure occurs. This last stage is called tertiary. The stages are shown in Figure 12, which represents the axial strain as a function of time for a uniaxial, constant stress test. In general, the primary and secondary deformations are not considered plastic, but tertiary deformations exhibit a kind of viscoplastic deformation (MUNSON, 1997).

Figure 12 – Creep stages for a strain versus time diagram at constant stress

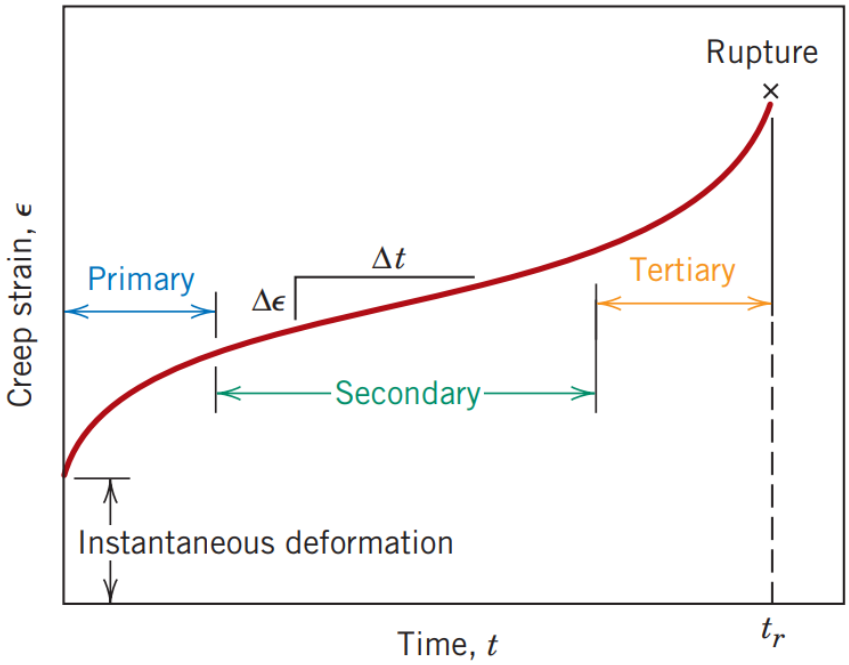

Source: Callister (2007)

The first study to pinpoint the basic mechanisms of creep in salt rocks was published by Munson (1979), whose main result is the map of Figure 13, which shows the distinct physical mechanisms ruling creep strain for salt crystals with grains of 3mm in size. The map shows the creep regimes as a function of temperature and dimensionless stress. On this map, the solid lines represent transitions determined by experimental data and the dashed lines result from the application of constitutive equations. The author points that these transitions are not discrete but continuous, so in regions near the boundaries more than one mechanism is possible.

Figure 13 – Salt creep mechanism map

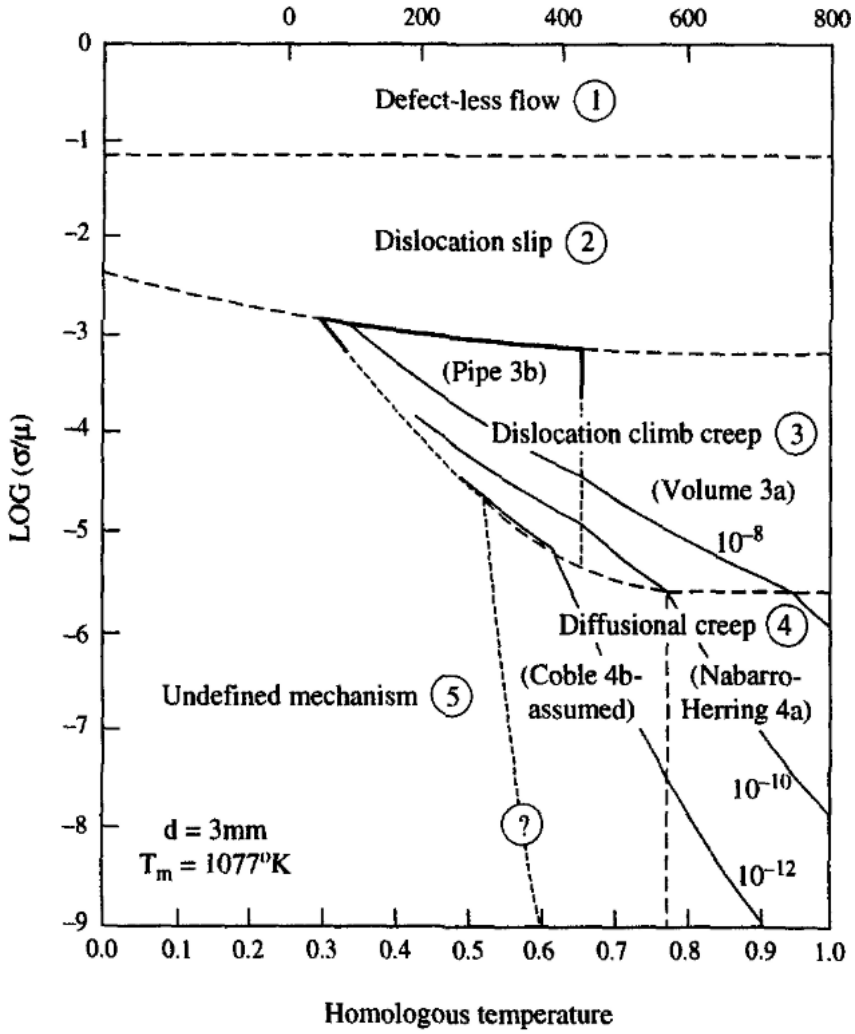

Source: Munson (1979)

As shown in Figure 13, there are five main underlying mechanisms involved in the creep of salt rocks. These are as follows:

1. **Defectless Flow**: This mechanism occurs only under large stresses, normally of magnitude greater than 1/20 of the shear modulus of the material. In this mechanism, a theoretical value of infinite creep rate is achieved in a crystalline structure free of defects;

2. **Dislocation Glide**: For salts with cubic arrangement, dislocation within the layers are common. In this mechanism, hardening occurs as the glide deformation intersects with obstacles to the flow;

3. **Dislocation Climb Creep**: This regime is experimentally determined as the result of equilibrium between the dislocation climb mechanism and polygonization of the salt crystals, leading to a steady-state creep rate. This mechanism is expected

to rule the second stage of creep and is divided into two inner regions with the transition between them related to the diffusion of Cl^- (defined by temperature). This mechanism occurs only under low stresses;

4. **Diffusional Creep**: This mechanism is found in many different materials and is related to changes in shape of grains by selective material transport;

5. **Undefined Mechanism**: This last mechanism is the most complex, as there was no known theoretical natural phenomena governing the deformation in this regime. Together with **Dislocation Climb Creep**, it is expected to be found in excavation conditions (such as well drilling). More recent studies pointed out that this mechanism is related to dissolution effects due to the increase of solubility at the contact points between grains, which only occurs under high pressures (MAIA C et al., 2005).

The transition mechanisms presented by Munson (1979) led to a better understanding of creep in salt layers, which are key to the development of constitutive models. For instance, Munson and Dawson (1979) proposed a unified mechanistic model that takes into account the **Dislocation Glide**, **Dislocation Climb Creep** and **Undefined Mechanism** regimes. These three mechanisms are the ones leading to the steady-state creep expected to be found in long term deformations resulting from geomechanical loads. Based on additional experimental data and on the work by Munson and Dawson (1979), Carter et al. (1993) developed a new constitutive model based for the transient regions. It was pointed out that, with respect to the creep mechanisms, elastic and plastic deformations can normally be disregarded over time. Two equations were proposed to model the steady-state creep replacing this term in the Munson's expression. The authors suggested that, during steady-state, the microestructural development is ruled by subgrain formation. This new formulation with two expressions delimited by the effective stress was latter adopted by other authors.

Munson (1997) revisited previously used databases and the model developed before (MUNSON, 1979), and proposed a revised model to unify the elastic and inelastic deformations (including plasticity, which was separated from the other inelastic terms by Carter et al. (1993), and later eliminated). This *Multimechanism-Deformation* constitutive model considers the same three mechanism studied previously in Munson and Dawson (1979), while adopting the considerations of Fossum et al. (1988) to convert uniaxial formulation into multiaxial ones. The constitutive equation was based on the Tresca criterion, which was chosen since the Von Mises criterion would lead to a difference of a factor of 2 in the models proposed.

The constitutive equation was based on the Tresca criterion. In comparison with the more common Von Mises criterion, the former was chosen based on its greater

accuracy against experimental data. A pure shear criterion, such as Von Mises', would result in a creep response, which may be unacceptable in certain circumstances.

Carcione, Helle, and Gangi (2006) analysed the stability of boreholes when drilling trough salt layers. Using a simplified viscoelastic model (Burger's) to represent creep and a plane stress model, an expression was presented, which capable of estimating the ideal weight of mud to be used when drilling regions prone to salt creep.

Based on the Multimechanism-Deformation model, Maia C et al. (2005) studied the displacement of salt layers surrounding wellbores, with a focus on drilling operations in the Campos Basin. Data from samples taken directly from the field were used to calibrate a new constitutive equation for steady-state creep given by:

$$\dot{\gamma} = \begin{cases} \dot{\gamma}_{\text{ref}} \left(\frac{q}{q_{\text{ref}}}\right)^{n_1} \exp\left(\frac{A}{R_{gas} T_{\text{ref}}} - \frac{A}{R_{gas} T}\right), & \text{if } q \leq q_{\text{ref}} \\ \dot{\gamma}_{\text{ref}} \left(\frac{q}{q_{\text{ref}}}\right)^{n_2} \exp\left(\frac{A}{R_{gas} T_{\text{ref}}} - \frac{A}{R_{gas} T}\right), & \text{otherwise} \end{cases} \tag{21}$$

where $\dot{\gamma}$ is the creep rate, q is the effective stress, n_1 and n_2 are empirical parameters, A is the activation energy of the rock and R_{gas} is the universal gas constant. The constitutive relation was calibrated for three of the most common rock types in the Brazilian Campos Basin pre-salt cluster, as shown in Figure 14.

Figure 14 – Graphical representation of the Creep Law

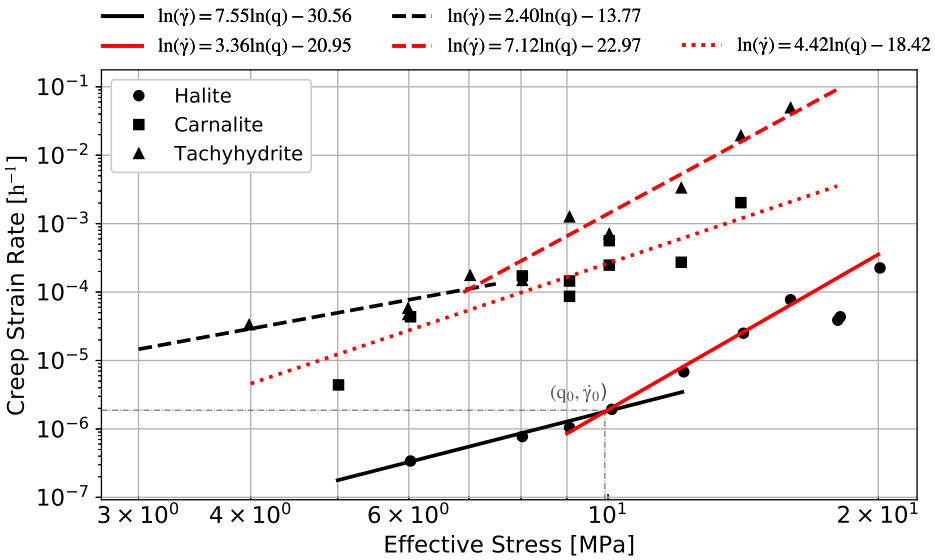

Source: Adapted from Poiate, Maia, and Falcao (2006)

Using a Finite Element Method (FEM) package, Poiate, Maia, and Falcao (2006) expanded the above described creep law to model the displacement of salt layers in the pre-salt cluster. The model was used to evaluate two drilling/completion plans for a well, and estimate the optimal mud weight and ideal cementing strategies.

Regarding the risks related to drilling salt layers, Zhang, Standifird, and Lenamond (2008) analysed the failure of a casing in what was at the time the world's deepest well, located in the Gulf of Mexico. A complete study of every possible scenario faced during the perforation was presented, as well as points which could benefit from FEM modelling during casing design, taking into account the effects of creep of rock layers. The use of these methods can ensure integrity of the wellbore reducing cost of construction and operation.

Similar problems were analyzed by Mackay et al. (2008), who developed a new transient, power-law formulation considering hardening effects. A FEM model was developed to study the closure of salt rocks around wellbores, using 2-D and 3-D models to assess the speed at which the closure would occur as a function of the mud weight used during drilling. An important result was the size of the affected formation region around wellbore. For the case studied, distances of 20 times the inner formation radius (from the center line) are sufficient for the effects not to be felt, which is an important result to estimate the size of computational grids.

Some authors modeled salt displacement treating the salt rock as a fluid instead of a solid. For example, Garibotti (2014) solved the Navier-Stokes equations with some constitutive terms for the in-situ stresses. This formulation was solved via the EBFVM (Element Based Finite Volume method) for small Weissenberg numbers to study possible scnearios of sideways displacement of salt domes, which could bend a wellbore as the rock moves. The model was not compared with real field data, so it is not possible to verify its accuracy. However, it is know that sideways motion of salt domes can be extremely dangerous, as presented in Wang and Samuel (2016).

The first work to try to model the APB considering creep deformation of salt layers was proposed by Melo et al. (2015). The thermal contribution to APB was disregarded, and only the effects of volume variation of the annular space were considered. Comparisons involving the effects of different mud weights were carried out.

Almeida (2016) considered both thermal effects and salt creep in the APB calculation in a hydrocarbon producing well. A commercial FEM software was used to model the deformation of the salt layer in an axisymmetric geometry and, in parallel, another commercial software was used to model the thermal effects. Both programs were coupled externally by scripts and executed via command line. The APB was calculated using the expression of Oudeman and Bacarreza (1995) with corrections made by adding mass in the annular spaces to account for the displaced mass due to the fluidity of the Salt layer. This added mass is purely virtual, since the coupling of both models was not performed implicitly. The case under study consisted of a long salt layer (Halite) exposed (i.e., with previous drilling stages not cemented up to the casing shoe, leading to contact of the salt and drilling mud) to the second annulus. When considering creep, the pressure increase was reduced by more than 10%. For the proposed scenario, the

salt would open instead of close around the well, increasing the annular volume and reducing the APB.

In the same year, Perez (2016) used the program developed by Poiate, Maia, and Falcao (2006) to model the deformation of salt rocks in a production well. An in-house code was developed to simulate the thermal APB, which was later coupled to results for the salt creep contribution APB. Among the main results, a variation of over 1800 psi (12.41 MPa) was detected in the annulus in contact with the salt layer. In addition, contrary to what normally occurs in APB calculations, for this well, the effect of the volume variation, largely due to salt creep, contributes to about 40% of the total APB.

Agostini, Almeida, et al. (2019) used the formulation proposed in Almeida (2016) to estimate the pressure variation in operations involving cooling of the annuli. The simulation procedure was somewhat different due to periods without heat transfer, followed by injection cooling, ending in a stop period where the annular eventually warms up to the initial condition. This formulation was used to study APB mitigation techniques, showing the importance of the simulator beyond estimating structural loads on casings.

Taheri et al. (2020) reported a real case of well collapse in Iran, in which the failure to consider the flow of the salt layer led to a reduction of the safety coefficients from 3.03 to 1.02 for this well, indicating that creep may have been the main responsible for the collapse. To model the phenomenon, a simple power-law calibrated for halite samples from the Gachsaran formation was used. Note, however, that the cause of this collapse was not the APB but the salt closure itself.

2.6 THE SAFE FAMILY OF SIMULATORS

At the Polo Research Laboratories at UFSC, studies on APB were carried out in hydrocarbon producing wells. From these studies, the Simulator of Annular Fluid Expansion (SAFE) model was developed based, mainly, on the classical assumptions of Ramey (1962) for pseudo steady-state in the wellbore and time functions to model heat transfer in the rock formation.

The first version of the model was developed by Hafemann (2015), and implemented in Matlab™(MATLAB, 2010) using the on the equation of Oudeman and Bacarreza (1995) to estimate APB. Compositional models were used to calculate the properties of all fluids in the wellbore, allowing a thermodynamically consistent formulation, but at the price of a higher computational cost. Only vertical multiphase flow models were implemented, limiting the application of the program to wells with small deviations from the vertical. Based on the 4^{th} order Runge-Kutta algorithm with varying steps, the simulator used pre-allocated geometries to calculate the terms for the marching procedure. In addition, the Halal and Mitchell (1994) model for thermo-elastic deformations was implemented for the casings walls and formation. Despite the encour-

aging results against limited field data, some discrepancies were detected in the APB predictions due to discontinuities in the pressure profiles in the anulli. The discontinuities were caused by the application of the Oudeman and Bacarreza (1995) expression at each individual control volume. This way, the pressure increase was computed locally instead of being an overall quantity associated with the annulus as a whole. This lack of physical consistency in the results did not compromise the results related to the thermal behavior, and was corrected in later works.

Barcelos (2017) improved the SAFE program by making it more consistent and robust. Multiphase flow models for inclined tubes (BEGGS; BRILL, 1973) allowed the program to be applied to a wider range of producing wells. In addition, a new approach was proposed for calculating the APB in which an average density and temperature is calculated for each annulus, enabling the calculation of the increase in average annular pressure, i.e., a unique value of APB for the entire annulus. This physically consistent approach was validated with field data and commercial software, demonstrating a good ability to estimate the pressure increase in real wells. Another contribution was the capacity to deal with *separation collars*, which are layers of fluids existing in complex cementations. Finally, to reduce the computational cost, the author proposed a new way to calculate the thermophysical properties of the wellbore fluids using tables for interpolation that were previously generated using the same thermodynamic property software.

Ferreira (2017) developed new models to simulate heat transfer in wells completed with Vacuum-Insulated Tubing (VIT). The VIT is a thermal isolation equipment which is used as the production tube in regions of the well where heat transfer is not desired, to achieve such isolation two distinct tubes (which fits within each other) are welded together and a vacuum is made in the gap left between the tubes. The model consisted of a two-dimensional equivalent thermal resistance network to represent the heat flow in the VIT, while considering the non-linearities arising from thermal radiation in the evacuated section of the casing. The model was validated with experimental data and was compared with result from a Computational Fluid Dynamics (CFD) software. Ferreira (2017) also developed a new time function aiming at modeling shorter times with greater precision. The results were encouraging, considering the exisiting deviations with respect to field data.

Despite the efforts from Barcelos (2017) and Ferreira (2017) to reduce the computational costs of the early versions of the SAFE simulator, the processing time was still prohibitive. With the specific intention of cutting down the computational time to a few seconds, a totally new numerical approach to solving the governing equations using the Python (ROSSUM; DRAKE, 2009) language was proposed by Veiga et al. (2020). The governing equations solved in the latest version of the simulator will be presented in detail in Section 2.7. From a numerical perspective, the use of adaptive stepping

solvers was replaced by a more conventional 4^{th}-order Runge-Kutta method with fixed steps. This permits pre-allocation of meshes and geometry information, resulting in greater numerical performance and physical consistency.

This extra physical consistency is related to vertical interfaces of materials. When simulating via adaptive stepping schemes, it is possible to cross an interface without solving its vicinity, this could lead to a poor representation of the temperature profile in the annulus. By pre-allocating the meshes it is possible to ensure a greater refinement near this regions, thus leading to a better representation of temperature at the annuli.

2.7 THE PYSAFE FORMULATION

Since one of the main objectives of the present thesis is to advance more general models to account for the effects of salt creep and wellbore thermal capacitance on the APB, the basic formulation of the Python Simulator of Annular Fluid Expansion (pySAFE) code, upon which those new features will be constructed, is described in detail.

2.7.1 Hydrodynamic model

Inside the well, the flow will be single-phase if the local pressure is above the bubble-point pressure of the produced oil at the local temperature. Therefore, it is important for the hydrodynamic model to handle both single-phase and multiphase flow regimes (GUO; LYONS; GHALAMBOR, 2007).

2.7.1.1 Single Phase Flow

By using Rameys's assumptions of pseudo steady-state, one-dimensional flow, the mass conservation of the flowing fluid in the well is given by:

$$\frac{\partial \rho v}{\partial z} = 0 \tag{22}$$

where ρ is mass density, v is the flow velocity and z is the axial distance, i.e., the MD.

Figure 15 presents the forces acting on a differential control volume. By neglecting the flow acceleration (advection), which is negligible for single-phase liquid flows and two-phase flows with mild variations of liquid holdup and cross-section area (production tube diameter), the momentum conservation written in terms of the pressure gradient for pseudo steady-state is given by:

Figure 15 – Force balance in a control volume

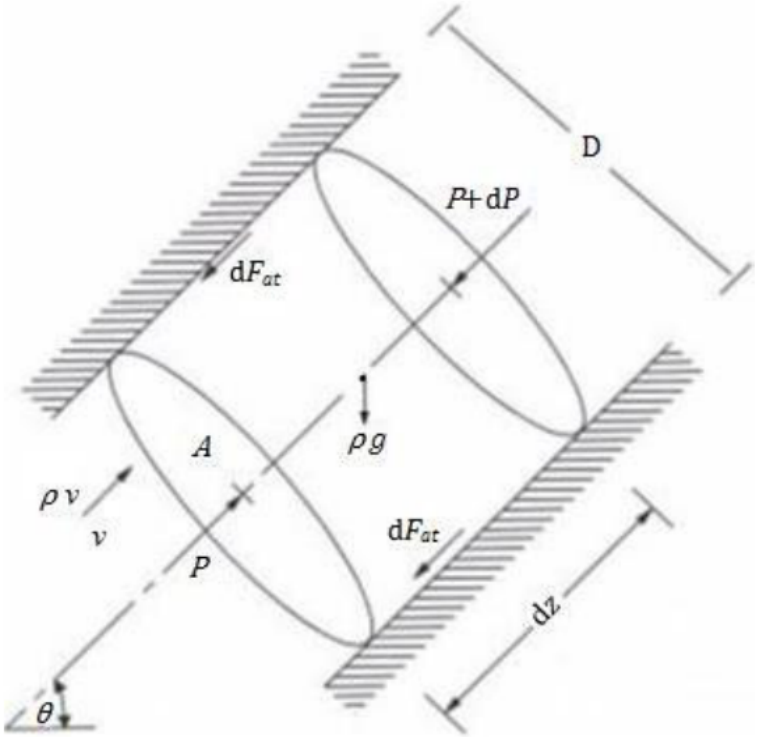

Source: Barcelos (2017)

$$\frac{\partial P_{\text{pf}}}{\partial z} = f\frac{\rho v|v|}{2d_T} + \rho g \sin(\theta) \tag{23}$$

where P_{pf} is the pressure of the produced fluid, f is the friction factor, d_T is the inner diameter of the production tube, g is the acceleration of gravity and θ is the inclination of the tube with the vertical.

In single-phase flow, the friction factor correlation due to Colebrook (1939) was adopted for its good precision for a wide range of Reynolds numbers:

$$\frac{1}{\sqrt{f}} = -2\log\left(\frac{\epsilon}{3.7d_T} + \frac{2.51}{Re\sqrt{f}}\right) \tag{24}$$

where ϵ is the pipe roughness and Re is the Reynolds number which, for single-phase flow is defined as $Re = \rho d_T v/\mu$. As in Barcelos (2017), ϵ was assumed equal to 15 µm. Equation 24 was solved via the Newton-Raphson method, with the derivative taken analytically.

2.7.1.2 Multi Phase Flow

Multiphase flows occur when the local pressure is lower than the bubble-point pressure at the local temperature of the produced fluid. With the pseudo steady-state assumptions of Ramey (1962), negligible flow acceleration and the Brill and Beggs

(1991) flow pattern-based approach to model the two-phase friction factor and mass densities, the one-dimensional momentum equation is given by:

$$\frac{\partial P_{\text{pf}}}{\partial z} = \frac{f_s \rho_{ns} v_{\text{m}}}{2 d_T} + \rho_s \sin(\theta) \tag{25}$$

where the subscript *s* represents variables which consider slip between the phases. Variables with the subscript *ns* assume ideal (no-slip) hydrodynamic model. The no-slip density is defined as:

$$\rho_{ns} = \lambda_{\text{l}} \rho_{\text{l}} + (1 - \lambda_{\text{l}}) \rho_{\text{g}} \tag{26}$$

where λ_{l} is the no-slip liquid volumetric fraction defined as the ratio of the liquid to the total flow volume flow rate:

$$\lambda_{\text{l}} = \frac{\dot{V}_{\text{l}}}{\dot{V}_{\text{l}} + \dot{V}_{\text{g}}} \tag{27}$$

The slip density is defined as:

$$\rho_s = H_{\text{l}} \rho_{\text{l}} + (1 - H_{\text{l}}) \rho_{\text{g}} \tag{28}$$

where H_{l} is the liquid holdup, which represents the fraction of a given volume occupied by the liquid. It is calculated via a set of flow-pattern dependent correlations based the following criteria:

$$\begin{cases} \text{Segregated}, & \text{if } \lambda_{\text{l}} < 0.01 \text{and } Fr < L_1 & \text{(29a)} \\ \text{Segregated}, & \text{if } \lambda_{\text{l}} \geq 0.01 \text{and } Fr < L_2 & \text{(29b)} \\ \text{Transition}, & \text{if } \lambda_{\text{l}} \geq 0.01 \text{and } L_2 \leq Fr \leq L_3 & \text{(29c)} \\ \text{Intermitent}, & \text{if } 0.01 \leq \lambda_{\text{l}} < 0.4 \text{and } L_3 \leq Fr \leq L_1 & \text{(29d)} \\ \text{Intermitent}, & \text{if } \lambda_{\text{l}} \geq 0.4 \text{and } L_3 \leq Fr \leq L_4 & \text{(29e)} \\ \text{Distributed}, & \text{if } \lambda_{\text{l}} < 0.4 \text{and } L_1 \geq Fr & \text{(29f)} \\ \text{Distributed}, & \text{if } \lambda_{\text{l}} \geq 0.4 \text{and } Fr \geq L_4 & \text{(29g)} \end{cases}$$

The Froude number and the empirical factors are defined as (BRILL; BEGGS, 1991):

$$\begin{cases} Fr = \dfrac{v_{\text{m}}^2}{g d_T} & \text{(30a)} \\ L_1 = 316 \lambda_{\text{l}}^{0.302} & \text{(30b)} \\ L_2 = 0.0009252 \lambda_{\text{l}}^{-2.4684} & \text{(30c)} \\ L_3 = 0.10 \lambda_{\text{l}}^{-1.4516} & \text{(30d)} \\ L_4 = 0.5 \lambda_{\text{l}}^{-6.738} & \text{(30e)} \end{cases}$$

It is important to mention that the above parameters and flow patterns are defined for horizontal flow, so the first step of the model is to estimate an equivalent horizontal flow condition that is later corrected to the desired inclination. The horizontal liquid holdup is estimated by the following correlation:

$$H_l(\theta = 0) = \frac{c_1 \lambda^{c_2}}{Fr^{c_3}} \tag{31}$$

where the coefficients for each flow pattern are obtained from Table 2.

Table 2 – Horizontal parameters for Brill and Beggs (1991)

Flow Patter	c_1	c_2	c_3
Segregated	0.980	0.4846	0.0868
Intermitent	0.845	0.5351	0.0173
Distributed	1.065	0.5824	0.0609

The liquid holdup for a given inclination θ is given by:

$$H_l(\theta) = H_l(\theta = 90°)\, c_4 \tag{32}$$

where:

$$c_4 = 1 + c_5 \left[\sin(1.8\theta) - \frac{1}{3}\sin^3(1.8\theta) \right] \tag{33}$$

$$c_5 = (1 - \lambda_l) \ln\left(c_6 \lambda_l^{c_7} N_L{}^{c_8} Fr^{c_9} \right) \tag{34}$$

and N_L is a dimensionless parameter defined as:

$$N_L = \frac{\dot{m}_l}{\rho_l} \sqrt[4]{\frac{\rho_l}{g\sigma_L}} \tag{35}$$

The coefficients in Equation 34 are presented in Table 3.

Table 3 – Parameters for c_5 Brill and Beggs (1991)

Flow Patter	c_6	c_7	c_8	c_9
Segregated	0.011	-3.7680	3.5390	-1.6140
Intermitent	2.960	0.3050	0.4473	0.0978
Distributed	-	-	-	-
Downhill flow	4.700	-0.3692	0.1244	-0.5056

Note that for distributed flow the method requires no correction and, therefore, $c_4 = 1$.

For the transition flow regime situated between the segregated and intermittent flow regimes, the procedure consists of linearly interpolating the result for these two flow patterns. Therefore:

$$H_{l,Trans}(\theta) = c_{10} H_{l,Seg}(\theta) + (1 - c_{10}) H_{l,Int}(\theta) \tag{36}$$

where c_{10} is defined by:

$$c_{10} = \frac{L_3 - Fr}{L_3 - L_2} \tag{37}$$

To determine the two-phase friction factor, the Colebrook (1939) correlation is used with the no-slip Reynolds number defined as:

$$Re_{ns} = \frac{\rho_{ns} v_m d_T}{\mu_{ns}} \tag{38}$$

The friction factor is given by:

$$f_s = f_{ns} \exp(c_{11}) \tag{39}$$

where

$$c_{11} = \frac{\ln(c_{12})}{-0.0523 + 3.182\ln(c_{12}) - 0.8725\ln(c_{12})^2 + 0.01853\ln(c_{12})^4} \tag{40}$$

and:

$$c_{12} = \frac{\lambda_l}{H_l^2} \tag{41}$$

Since Equation 40 is discontinuous (around $c_{12} \approx 1.01665$), the following definition must be used if $1 \leq c_{11} \leq 1.2$:

$$c_{11} = \ln(2.2 c_{12} - 1.2) \tag{42}$$

This correlation also has a criterion to ensure a maximum pressure gradient even for the scenarios where slip may lead to smaller gradients. Therefore, the values of the liquid hold-up must obey the following condition $H_l \geq \lambda_l$.

2.7.2 Thermal Modeling

The approach to resolve the heat transfer within the well consists of writing the energy conservation equation for pseudo steady-state. As with the momentum equation, the kinetic energy term is neglected. Thus the energy balance writtent in terms of the enthalpy of the production fluid is given by:

$$\frac{\partial h_{pf}}{\partial z} = \frac{Q'}{\dot{m}} - g\sin(\theta) \tag{43}$$

where Q' is the heat transfer rate per unit length and $\dot{m}$ is the mass flux (mass flow rate per unit cross sectional area). Pressure and enthalpy are the dependent variables, which is advantageous to simulate flows with phase change, since both variables change continuously with depth.

To calculate the heat transfer rate per unit length, an equivalent thermal network is used. In order to assemble the equations, Figure 16 can be used as an example of geometry to be modeled.

Figure 16 – Arbitrary well section

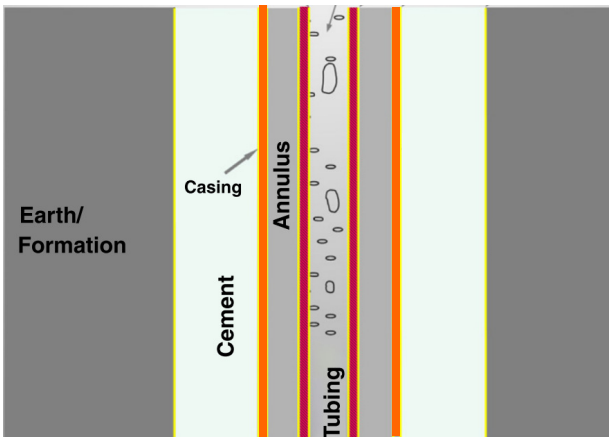

Source: Adapted from Hasan and Kabir (2012)

This geometry has the fluid flowing inside the production tubing, the steel casing, the fluid that completes the first annular, a steel layer from the casing of the first annular and a layer of cement before the interface with the formation. Figure 17 shows the resulting resistance circuit for this scenario.

Figure 17 – Equivalent thermal resistors for specified scenario

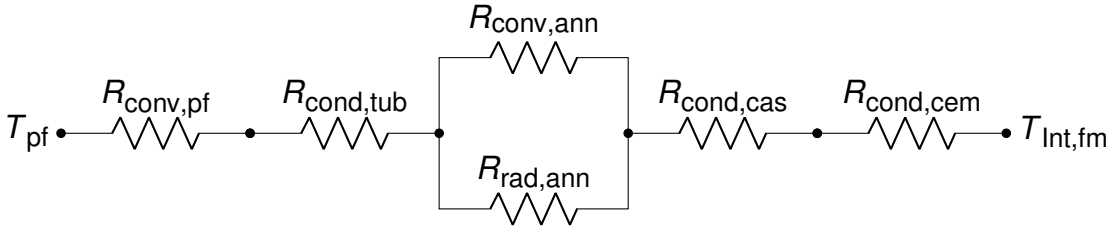

Source: Adapted from Barcelos (2017)

Here, all forms of heat transfer that will be considered in the problem are present. For the solid regions of the well, heat exchange by conduction will be considered. For the fluid regions, two scenarios are considered, when forced fluid flow is present, radiation is negligible and the thermal resistance is calculated from forced convection models. For stagnant fluids in the sealed annuli, the resistance is calculated from natural convection and radiation contributions, which act in parallel. The driving potential is the difference between Tpf and $T_{Int,fm}$.

A brief description of the individual thermal resistances is presented next.

2.7.2.1 Conduction Resistance

The conduction resistance is applicable to the solid components of the well, such as the steel casings and cement. For these materials, the properties are considered independent of pressure and temperature. The conduction resistance, in $\mathrm{m\,K\,W^{-1}}$, is given by:

$$R_{\text{cond}} = \frac{\pi}{2k} \ln\left(\frac{r_{\text{out}}}{r_{\text{inn}}}\right) \tag{44}$$

where k is the thermal conductivity of the solid, and r_{inn} and r_{out} are, respectively, the internal and external radii of the solid interfaces with other materials.

2.7.2.2 Forced Convection in the Production Tubing

In the production tubing, the thermal resistance ($\mathrm{m\,K\,W^{-1}}$) is determined as:

$$R_{\text{conv}} = \frac{1}{2\pi r_{\text{out}} h_c} \tag{45}$$

where h_c is the heat transfer coefficient for forced convection. For single-phase flow, this is computed via the Sieder and Tate (1936) correlation for turbulent flow:

$$h_c = \frac{0.023 k_l}{d_T} Re_l^{0.8} Pr_l^{\frac{1}{3}} \left(\frac{\mu_l}{\mu_w}\right)^{0.14} \tag{46}$$

where the subscript *l* stand for the bulk liquid properties, while the subscript *w* is related to the viscosity calculated at the wall temperature.

For multiphase flow in the production tube, the Chen (1966) correlation for convective boiling is used, disregarding the nucleated boiling term. Thus:

$$h_c = \frac{0.023 k_l}{d_T} Re_l^{0.8} Pr_l^{0.4} F_{Chen} \tag{47}$$

In this equation, the liquid terms are calculated assuming that the liquid occupies the entire cross section of the tube. The two-phase enhancement factor, F_{Chen}, is given by:

$$F_{Chen} = \begin{cases} 1, & \text{if } X_{tt}^{-1} \leq 0.1 \\ 2.35(0.213 + X_{tt})^{0.736}, & \text{otherwise} \end{cases} \tag{48}$$

where X_{tt} is the Martinelli parameter defined as:

$$X_{tt} = \left(\frac{1-x_g}{x_g}\right)^{0.9} \left(\frac{\rho_g}{\rho_l}\right)^{0.5} \left(\frac{\mu_l}{\mu_g}\right)^{0.1} \tag{49}$$

2.7.2.3 Annular thermal resistance

In the annular cavities, the main heat transfer mechanisms are natural convection and radiation. Since they are independent of each other, the equivalent resistance of the annulus, R_{ann}, is given by:

$$R_{\text{ann}} = \frac{1}{\frac{1}{R_{\text{conv}}} + \frac{1}{R_{\text{rad}}}} \tag{50}$$

where R_{rad} is the radiation resistance computed as:

$$R_{\text{rad}} = \frac{1}{2\pi r_{\text{out}} h_r} \tag{51}$$

in terms of a radiation transfer coefficient as follows (HASAN; KABIR, 1994):

$$h_r = \frac{\sigma_{SB}(T_{\text{inn}} + T_{\text{out}})\left(T_{\text{inn}}^2 + T_{\text{out}}^2\right)}{\frac{1}{\epsilon_{\text{inn}}} + \frac{r_{\text{inn}}}{r_{\text{out}}}\left(\frac{1}{\epsilon_{\text{out}}} - 1\right)} \tag{52}$$

where σ_{SB} is the Stefan-Boltzmann constant and the variables ϵ_{inn} and ϵ_{out} are the emissivities of the inner and outer surfaces of the annular, respectively, assumed equal to 0.68.

R_{conv} is the natural convection thermal resistances, which is also defined by Equation 45. As in Barcelos (2017), the Zhou (2013) correlation will be used to determine the heat transfer coefficient in the annulus. However, a small modification to the coefficient was made for numerical reasons. Originally the correlation is given by:

$$h_c = \begin{cases} \dfrac{k}{r_{\text{inn}} \ln\left(\frac{r_{\text{out}}}{r_{\text{inn}}}\right)}, & \text{if } Ra \leq 6000 \\ \dfrac{0.13 k Ra^{0.25}}{r_{\text{inn}} \ln\left(\frac{r_{\text{out}}}{r_{\text{inn}}}\right)}, & \text{if } 6000 < Ra \leq 5 \times 10^4 \\ \dfrac{C_{Zhou} k Ra^{\frac{1}{3}} Pr^{0.074}}{r_{\text{inn}} \ln\left(\frac{r_{\text{out}}}{r_{\text{inn}}}\right)}, & \text{if } 5 \times 10^4 < Ra \leq 7.17 \times 10^8 \end{cases} \tag{53}$$

where C_{Zhou} is a model constant that is related to the pipe slope, Ra is the Rayleigh number defined by:

$$Ra = \frac{g\beta\rho c_p (r_{\text{out}} - r_{\text{inn}})^3 (T_{\text{out}} - T_{\text{inn}})}{\mu k} \tag{54}$$

where β is the thermal expansivity of the fluid and c_p the specific heat capacity.

In Veiga et al. (2020), a change in the correlation of Zhou (2013) was proposed to deal with numerical instability issues due to discontinuities in the correlation. This small change consists of using 4^{th}-order polynomials to connect the discontinuities of the correlation. That is, for Ra between 4000 and 8000, and between 4×10^4 and 6×10^4, the solution of the correlation is achived via a 4^{th}-order interpolation limited

by the values of the correlation and its derivative with relation of *Ra*. This guarantees continuity of the function and its derivative throughout the problem domain.

2.7.3 APB computing program

This section describes the structural deformation and APB models implemented in the context of the pySAFE framework.

2.7.3.1 Multi-String structural deformation

In order to model the deformation of the casings and formation due to pressure variation and heating of the annulus, Halal and Mitchell (1994) proposed a model based on a multi-string approach which couples the axial contribution of stress to the radial deformation of each material.

The basic idea of this method is to solve for each solid interface the radial displacement such that:

$$\Delta r_{\mathrm{i}} = r_{\mathrm{i}} \Delta \varepsilon_{\phi} \tag{55}$$

where $\Delta \varepsilon_{\phi}$ is the variation in hoop strain. This term can be calculated by assuming linear thermal-elasticity calculated by:

$$\Delta \varepsilon_{\phi} = \frac{\Delta \sigma_z - \nu \left(\Delta \sigma_z + \Delta \sigma_z \right)}{E} + \beta_{lin} \Delta T \tag{56}$$

where $\Delta \sigma_z$, $\Delta \sigma_z$ and $\Delta \sigma_z$ are the difference in the principal stress components from the initial state. β_{lin} is the linear thermal expansion coefficient and ΔT is the variation in temperature from the undisturbed formation. ν is the Poisson coefficient and E is the Young's modulus.

The difference in stress components are computed via:

$$\Delta \sigma_z = C_{\sigma r 1} \Delta P_{\mathrm{inn}} + C_{\sigma r 2} \Delta P_{\mathrm{out}} \tag{57}$$

and

$$\Delta \sigma_z = C_{\sigma \phi 1} \Delta P_{\mathrm{inn}} + C_{\sigma \phi 2} \Delta P_{\mathrm{out}} \tag{58}$$

where ΔP_{inn} is the variation in pressure from the inner surface of a given solid, ΔP_{out} is the outer variation and both coefficients $C_{\sigma r}$ and $C_{\sigma \phi}$ are related to the geometry, defined by:

$$C_{\sigma r 1} = \frac{r_{\mathrm{inn}}^2 - r_{\mathrm{inn}}^2 r_{\mathrm{out}}^2 / r^2}{r_{\mathrm{out}}^2 - r_{\mathrm{inn}}^2} \tag{59}$$

$$C_{\sigma r2} = \frac{r_{\text{inn}}^2 r_{\text{out}}^2/r^2 - r_{\text{out}}^2}{r_{\text{out}}^2 - r_{\text{inn}}^2} \tag{60}$$

$$C_{\sigma\phi1} = \frac{r_{\text{inn}}^2 + r_{\text{inn}}^2 r_{\text{out}}^2/r^2}{r_{\text{out}}^2 - r_{\text{inn}}^2} \tag{61}$$

$$C_{\sigma\phi2} = \frac{r_{\text{inn}}^2 r_{\text{out}}^2/r^2 + r_{\text{out}}^2}{r_{\text{inn}}^2 - r_{\text{out}}^2} \tag{62}$$

These terms can be used to rearrange Equation 56 such that:

$$\Delta\varepsilon_\phi = C_{\varepsilon\phi1}\Delta P_{\text{inn}} + C_{\varepsilon\phi2}\Delta P_{\text{out}} + C_{\varepsilon\phi3} \tag{63}$$

where:

$$C_{\varepsilon\phi1} = \frac{C_{\sigma\phi1} - \nu C_{\sigma r1}}{E} \tag{64}$$

$$C_{\varepsilon\phi2} = \frac{C_{\sigma\phi2} - \nu C_{\sigma r2}}{E} \tag{65}$$

$$C_{\varepsilon\phi3} = \beta_{lin}\Delta T - \frac{\nu\Delta\sigma_z}{E} \tag{66}$$

$\Delta\sigma_z$ can be treated through two different approaches related to the boundary conditions of the solid material. If it is free to elongate, i.e., non cemented section, then $\Delta\sigma_z = 0$. If it is next to the cement, than it is calculated by:

$$\Delta\sigma_z = 2\nu\frac{r_{\text{inn}}^2(\Delta P_{\text{inn}} - \Delta z\Delta\rho_{\text{inn}}) - r_{\text{out}}^2(\Delta P_{\text{out}} - \Delta z\Delta\rho_{\text{out}})}{r_{\text{out}}^2 - r_{\text{inn}}^2} - E\beta_{lin}\Delta T \tag{67}$$

If two or more solids share a common boundary, then a linear system is written, which allows for continuity of both stress and strain at the interfaces.

The outer boundary condition of this linear system is the strain of the formation boundary, which can be calculated individually for the scenario of a rock exposed to the annulus, or can be included into the linear system based on the formulation previously presented. This strain is calculated by:

$$\Delta\varepsilon_{\phi\text{fm,Int}} = \Delta P_{\text{inn}}\frac{1+\nu_{\text{fm}}}{E_{\text{fm}}} \tag{68}$$

This formulation can be applied at each simulated time for each radial layer where the radial thermal system is solved. By doing so, a profile of vertical displacements for the casings and formation can be computed. This method, when used to estimate the variation in deformation from a initial state, does not predict variations with respect to the *actual* initial condition of production (time 0), but compares the deformation

with respect to an undeformed, i.e., equivalent to the condition at the surface. The deformation resulting from the installation process in the wellbore is not taken into account by this model.

2.7.3.2 APB Calculation

The geometry of the annuli and the fluid properties are inputs to the APB model. The geothermal gradient for each well is also known, therefore, it is assumed that the well always starts from a condition of thermal equilibrium with the formation. In order to determine the pressure profile within each annulus, it is necessary to assume that the fluids are stagnant, therefore, the initial pressure will obey the hydrostatic profile.

For each annular space, a pair of differential equations can be written: one for the mass that occupies the given space and another for the hydrostatic pressure, that is:

$$\frac{\partial P_{\text{ann}}}{\partial z} = \rho g \sin(\theta) \tag{69}$$

$$\frac{\partial M}{\partial z} = \pi \rho \left(r_{\text{out}}^2 - r_{\text{inn}}^2 \right) \tag{70}$$

With these equations, Veiga et al. (2020) proposed an alternative method for calculating APB, which is currently implemented in pySAFE. In this method, the equations are integrated from the wellhead to the bottom of each annulus in a marching procedure to determine the pressure and mass distributions in each annulus.

Having started at the bottom of the annulus with an arbitrary value of the local pressure, the following residuum is calculated and used in a convergence criterion to determine the APB:

$$Res(P_{\text{bot}}) = M_0 - M(P_{\text{bot}}) \tag{71}$$

where M_0 is the initial mass of fluid in each annulus (calculated as an input from the initial temperature and hydrostatic pressure) and P_{bot} is the pressure at the deepest point of each annulus.

The algorithmic APB calculation procedure of Veiga et al. (2020) consists of solving this nonlinear problem by changing the bottom-hole pressure of each annulus until the density profile (considering the structural deformations) results in a final mass that is equal to the initial mass of the system.

For that purpose, the root function in the optimization module of the SCIPY library is used, more specifically the “hybrid” method (VIRTANEN et al., 2020), which showed the robustness of converging even in cases where pressure estimates are far from the actual root of Equation 71.

2.7.3.3 Thermodynamic library

To resolve the entire physical phenomenon, it is necessary to estimate the thermodynamic properties of many fluids for different pressure and temperature conditions. However, some of the fluids are difficult to model, such as the oil produced or the mud that occupies some of the annuli, for which general equations of state are not yet available.

In general, the composition of actual oils are provided from field data up to the C_{20+} groups. However, for the other components, such information is not known. Therefore, different approaches are used to model each type of fluid.

In order to predict fluids properties, the software Multiflash^{TM} (INFOCHEM/KBC, 2019) is used. This program has a vast library of components that can be used to model fluids, especially the library of organic groups, even allowing complete compositional modeling of the produced oil.

Due to the large computational cost of solving the equations of state during the simulation, a simplified approach was used in which thermodynamic tables are previously generated for all the fluids which are found in wells, with a wide range of pressure, temperature and enthalpy. It is possible to interpolate the properties for all points of interest without great losses in precision and with reduced computational cost.

2.7.4 Algorithmic approach for solving the APB

As demonstrated along the present section, in order to estimate the APB in oil producing wells using the pySAFE model, many smaller numerical problems must be solved. Some of the most important algorithms and methods used are presented next.

First, the marching algorithm uses explicit methods, so that at each point the enthalpy and pressure of the fluid in the production tube are known without the need of extra iterations. For this purpose, the fourth-order Runge-Kutta method with fixed steps (an explicit high-order method) was used (PRESS et al., 2007). Also, the possibility of mesh pre-allocation enables the creation of a much more versatile code to deal with the complex geometry of a well.

2.8 SPECIFIC OBJECTIVES

The present chapter introduced the state of the art in modelling heat transfer phenomena in wellbores, emphasizing the prediction of APB in oil producing wells and salt creep. In order to address some of the gaps encountered in the literature, the following specific objectives are proposed:

1. Develop a new model for thermal phenomena and APB in wells valid for large and small values of Fourier number, which takes into account the thermal capacity of

the wellbore components and the heat transfer in the formation without relying on *ad hoc* time functions to describe the thermal interaction between the wellbore and the formation;

2. Compare this new formulation with existing methods (e.g., the pySAFE code and commercial software) and field data in order to pinpoint its advantages and drawbacks in terms of physical consistency, accuracy and computational time;

3. Develop a complete modelling framework to predict creep strain in salt layers based on the calibrated constitutive equation of Maia C et al. (2005) and on a new non-linear FEM-based algorithm;

4. Propose a new method for coupling the creep strain and heat transfer models in order to precisely evaluate the impact of thermal effects (such as thermal expansion and creep rate temperature dependence) on APB in pre-salt wells;

5. Apply the new formulation to an actual pre-salt well to quantify the APB over an extended period of time.

3 HYBRID TRANSIENT HEAT TRANSFER MODEL

The traditional pseudo steady-state approaches based on Ramey's assumptions are fairly accurate at predicting the wellbore heat transfer behavior for long times (large Fourier numbers), as verified against field data. However, for small Fourier numbers, non-physical behavior has been observed and reported (HAFEMANN, 2015; BARCELOS, 2017), which can be attributed to the lack of modeling of the thermal capacities of wellbore components. This led, for instance, to the over prediction of APB at earlier times (i.e., at the onset of production).

This chapter presents a new model for heat transfer in wellbores which incorporates thermal capacitance effects in the wellbore, while maintaining most features of the pySAFE model for its robustness and computational speed.

The proposed hybrid transient formulation is based on the use of Laplace Transformation. This is one of the Integral Transformations which have the characteristic of mapping a function from its original functional space into a transformed version of it, while retaining information of the original function. By transforming the domain studied it is possible to convert Differential Equations into algebraic equations which can be solved with simpler methods. Mainly, when transforming differential equations, it is possible to embed into the transformed expression some boundary conditions, reducing considerably the amount of calculation required to solve the equation (BEERENDS et al., 2003).

For this thesis the traditional unilateral Laplace transform is defined as (BOYCE; DIPRIMA; MEADE, 2017):

$$\mathscr{L}\{f(t)\} = \int_0^\infty f(t)\, e^{-st} dt \tag{72}$$

where f is a generic function, t is the original time domain of the function and s is the transformed variable in Laplace domain (also refereed as complex-valued Laplace variable).

The notation which will be used in this thesis to infer that a function is represented in the Laplace domain will be:

$$\bar{f}(s) = \mathscr{L}\{f(t)\} \tag{73}$$

where $\bar{f}$ is the transformed version of f.

3.1 GEOMETRY AND ASSUMPTIONS

To introduce the problem geometry, Figure 18 presents the general structure of a well completed with two annuli filled with drilling mud/completion fluid and another cemented up to the wellhead. As the proposed model uses most formulations previously

presented, the radii of the interfaces of material are highlighted and will be used in the expressions to come. The rectangular region (red contour) near the bottom of the well will be used later to illustrate the derivation of the model equations.

Figure 18 – Schematic diagram of the well

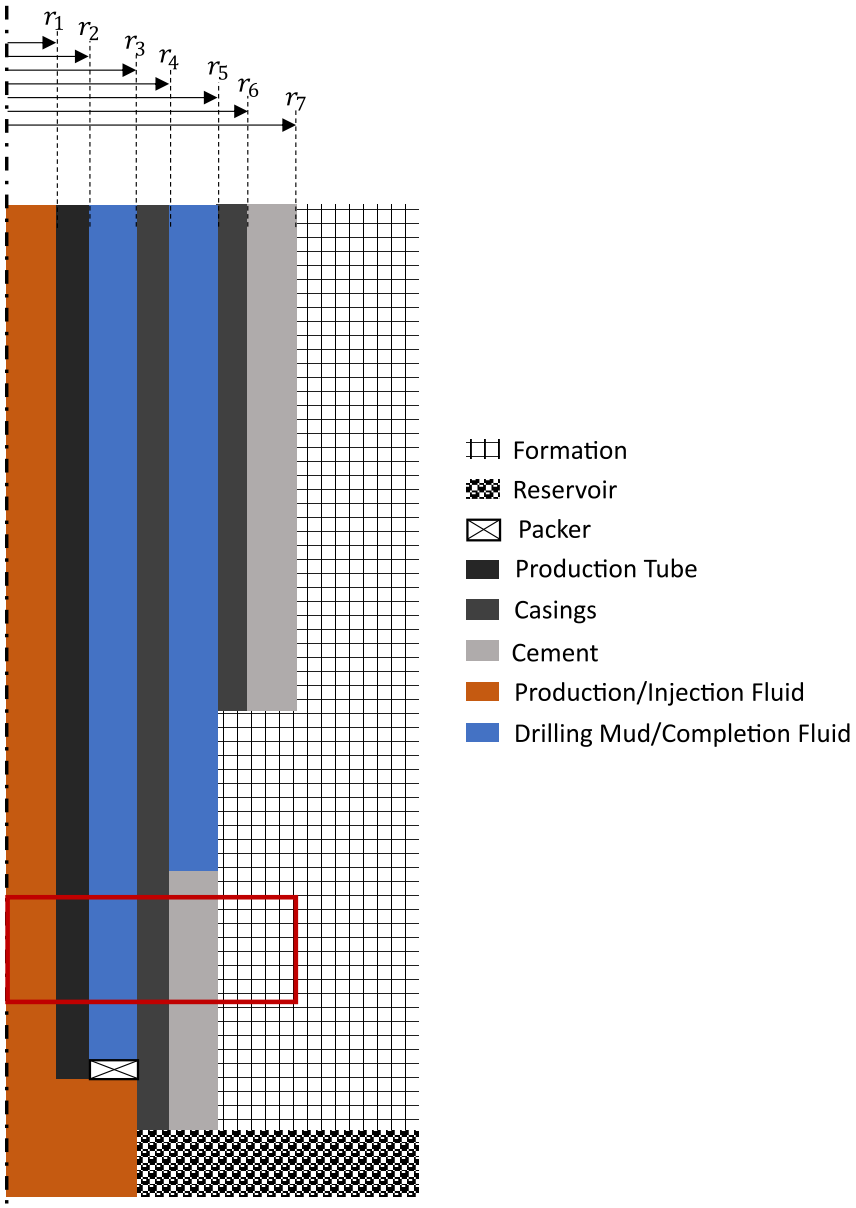

The main assumptions of the new model, some of which still based on Ramey's considerations, are as follows:

1. The rock formation is treated as a semi-infinite solid;
2. The thermal capacitance of the production fluid is neglected;
3. Momentum and energy balances in the wellbore can be solved via one-dimensional steady-state equations in the axial direction;

4. The heat transfer between the wellbore and the formation is one-dimensional in the radial direction.

Notice that, compared to the original assumptions, only the second item is different, as it considers that the thermal capacity of the fluids trapped in the annuli and the solid materials affect the heat transfer. In the production fluid, this term is still disregarded as the characteristic time fluid advection time scale is much smaller than the one associated with the change of the boundary conditions. In other words, for the production fluid it is assumed that:

$$C_{\text{pf}} \frac{\partial T_{\text{pf}}}{\partial t} \approx 0 \tag{74}$$

where C_{pf} is the thermal capacitance of the production fluid.

3.2 GOVERNING EQUATIONS

By disregarding the transient and kinetic energy terms of the momentum and energy equations for the production/injection fluid, the pseudo steady-state equations are identical to those in the original pySAFE formulation (Equations 25 and 43) repeated here for convenience:

$$\frac{\partial P_{\text{pf}}}{\partial z} = \frac{f_s \rho_{ns} v_{\text{m}}}{2 d_T} + \rho_s \sin(\theta) \tag{75}$$

$$\frac{\partial h_{\text{pf}}}{\partial z} = \frac{Q'}{\dot{m}} - g \sin(\theta) \tag{76}$$

where the variables are used as defined before, except for Q', which is no longer uniform in the radial direction. Therefore, the main difference between the hybrid formulation proposed here and the original method lies in the way in which the heat transfer rate per unit length *at the production tubing wall* is calculated.

In the original formulation, the heat transfer rate was computed neglecting the thermal capacity of the wellbore, assuming a prescribed temperature of the bulk production fluid. In the present model, only the thermal capacity of the production fluid is neglected, while those of the other components are considered as presented in the schematic diagram of Figure 19 for the red contour region of Figure 18.

Figure 19 – Equivalent resistances and capacitances of the thermal network

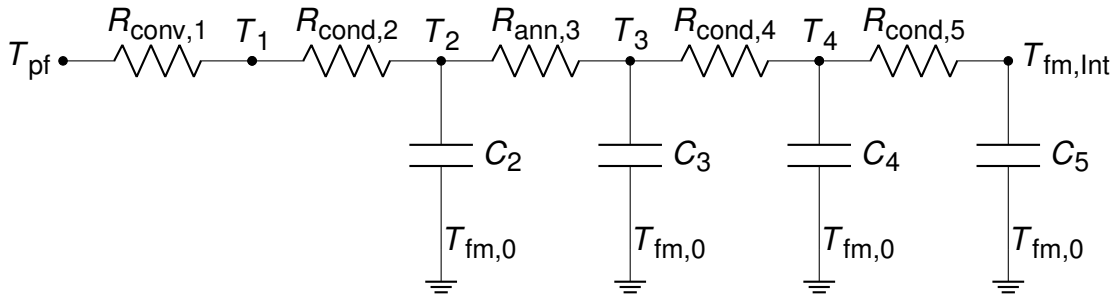

In the present model, the conduction, convection and radiation thermal resistances are the same ones presented in Section 2.7.2. However, for the sake of calculating the heat flow per unit length through the resistances, while assigning a thermal capacitance to a node associated with the center of the layer, the temperatures at the interfaces between are assumed to be close to the average temperature in each material (ISHIZUKA et al., 2011), a assumption that is supported by the long aspect ratio of the wellbore.

In order to mathematically describe any thermal network, including the one presented in Figure 19, a particular way to represent the energy balance through the components of the wellbore has been devised. Figure 20 illustrates the nomenclature consisting of subscripts $i-1, i, i+1$ and so on to represent the interfaces and the bulk of each material. With this discretization it is possible to generalize the thermal system for as many materials presents at the same slice dz.

Figure 20 – Index definition

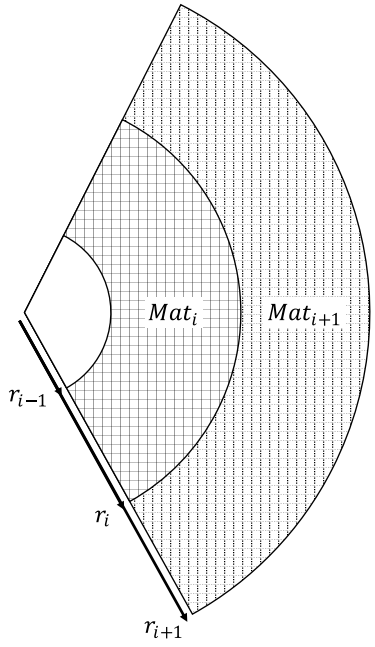

The energy balance between two adjacent domains (materials) is shown in Figure 21. So for a general node with transient heat transfer rate the energy equation

can be written such that:

Figure 21 – General Energy balance between two materials considering the thermal capacitance

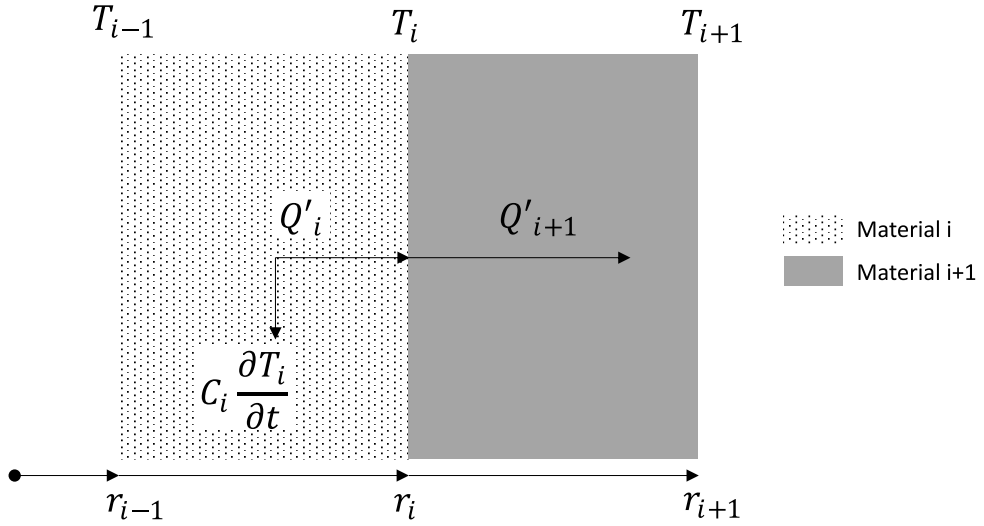

$$C_{\mathrm{i}} \frac{\partial T_{\mathrm{i}}}{\partial t} = Q'_{\mathrm{i}} - Q'_{\mathrm{i+1}} \tag{77}$$

where C_{i} and Q'_{i} are the capacitance and heat transfer rate per unit of length for a given i-th thermal node given, respectively, by:

$$C_{\mathrm{i}} = \pi \rho c_p \left(r_{\mathrm{i}}^2 - r_{\mathrm{i-1}}^2 \right) \tag{78}$$

and

$$Q'_{\mathrm{i}} = \frac{T_{\mathrm{i}} - T_{\mathrm{i-1}}}{R_{\mathrm{i}}} \tag{79}$$

Thus, in terms of the individual resistances and capacitance, the energy balance becomes:

$$R_{\mathrm{i}} R_{\mathrm{i+1}} C_{\mathrm{i}} \frac{\partial T_{\mathrm{i}}}{\partial t} + (R_{\mathrm{i}} + R_{\mathrm{i+1}})\, T_{\mathrm{i}} = R_{\mathrm{i+1}}\, T_{\mathrm{i-1}} + R_{\mathrm{i}}\, T_{\mathrm{i+1}} \tag{80}$$

As mentioned before, at the innermost node of the thermal network (production/injection node), a prescribed temperature is assumed. Therefore:

$$T_{i=0} = T_{\mathrm{pf}} \tag{81}$$

Also, the energy balance between the production fluid and the production tube) shown in Figure 22 does not consider the thermal capacitance of the former. Thus:

Figure 22 – Energy balance at the vicinity of the production fluid

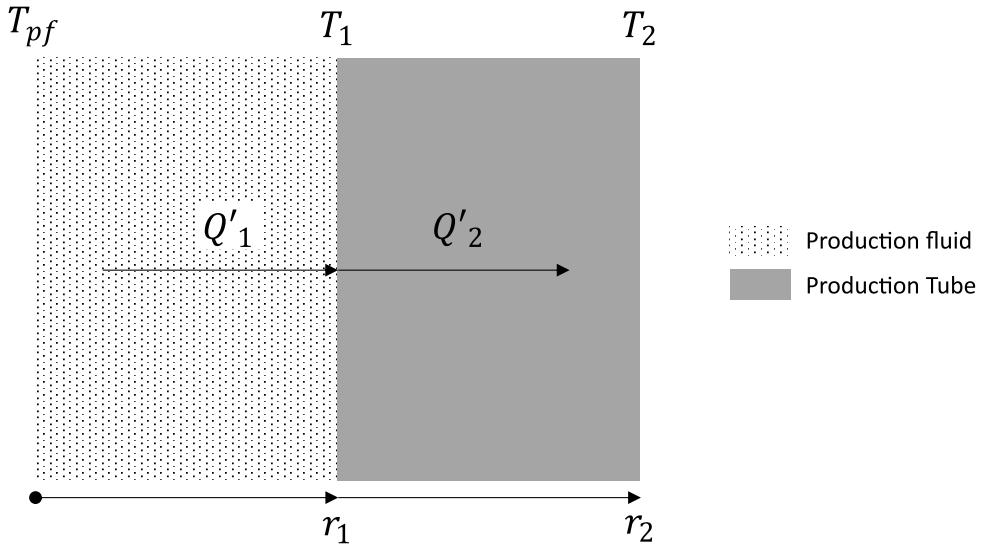

$$Q'_1 - Q'_2 = 0 \tag{82}$$

which, when applying the thermal circuit analogy becomes:

$$(R_1 + R_2)\, T_1 = R_2 T_0 + R_1 T_2 \tag{83}$$

For the intermediary nodes of the thermal network, Equation 80 is valid. At the interface between the wellbore and the formation, the energy balance illustrated in Figure 23 is implemented.

Figure 23 – Energy balance at the interface between the wellbore and the formation

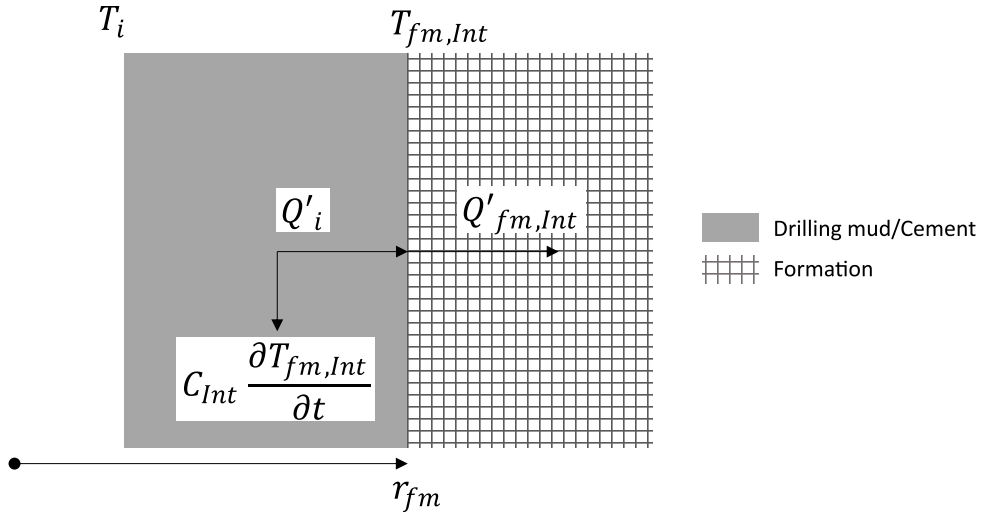

For that last node, the energy balance is solved assuming that the heat transfer rate per unit length to the formation is computed via the solution for the semi-infinite medium which is the formation. Thus:

$$C_{\mathrm{i}} \frac{\partial T_{\mathrm{fm,Int}}}{\partial t} = Q'_{\mathrm{i}} - Q'_{\mathrm{fm,Int}} \tag{84}$$

where:

$$Q'_{\mathrm{fm,Int}} = -2\pi k_{\mathrm{fm}} r \left. \frac{\partial T_{\mathrm{fm}}}{\partial r} \right|_{r=r_{\mathrm{fm}}} \tag{85}$$

In order to determine the first derivative of the formation temperature at the interface, the following semi-infinite medium heat transfer problem needs to be solved:

$$\begin{cases} \dfrac{\partial^2 T_{\mathrm{fm}}}{\partial r^2} + \dfrac{1}{r} \dfrac{\partial T_{\mathrm{fm}}}{\partial r} = \dfrac{1}{\alpha_{fm}} \dfrac{\partial T_{\mathrm{fm}}}{\partial t} & \text{(86a)} \\ T_{\mathrm{fm}}(r, t=0) = T_{\mathrm{fm},0} & \text{(86b)} \\ \lim\limits_{r \to \infty} T_{\mathrm{fm}}(r, t) = T_{\mathrm{fm},0} & \text{(86c)} \\ T_{\mathrm{fm}}(r = r_{\mathrm{fm}}, t) = T_{\mathrm{Int,fm}} & \text{(86d)} \end{cases}$$

By assuming constant properties in the formation and in the radial thermal network, the system composed of differential equations becomes linear, and one can take advantage of the semi-infinite medium solution proposed by Van Everdingen and Hurst (1949) to calculate the temperature and heat flow distributions in the entire domain, including the interface with the production fluid. In this method, the Laplace method was used to transform a differential equation written in the time domain into an algebraic equation in the Laplace domain. As explained previously, Ramey (1962) applied this method only to the formation to obtain the temperature of the interface with the wellbore, assuming a constant heat flux at the interface. However, it is possible to apply the transformation to all equations and, by doing so, the system of linear differential equations changes into an algebraic linear system which can be solved in Laplace's domain.

3.3 SOLUTION METHOD

Instead of the traditional approach of linearizing the time derivatives, the hybrid method proposed here leads to a time continuous solution, which does not require discretization of the time domain, thereby reducing the computational cost. The approach is similar to the so-called Laplace Transform/Finite Difference Method presented by Chen and Chen (1988).

The basic idea of the hybrid method is to apply the Laplace transform to spatially discretized equations via the finite difference method. This is done to solve the heat transfer using much simpler equations in the Laplace domain. The nature of this method allows the solution of the problem to be continuous over time.

The first step of the wellbore heat transfer solution is the determination of the formation temperature profile. The complete solution procedure is presented in Appendix A. In terms of the dimensionless group presented previously, Equations 5a-5d, the dimensionless temperature profile is given by:

$$\overline{T}_{\mathrm{D,fm}}(r_{\mathrm{D}},s)=\frac{\overline{T}_{\mathrm{D,Int}}K_0\left(r_{\mathrm{D}}\sqrt{s}\right)}{K_0\left(\sqrt{s}\right)} \tag{87}$$

Before calculating the derivative of the above expression needed in the interfacial boundary condition, it is important to further develop the equations for the intermediate nodes, so that they are all written in terms of the same dimensionless parameters formulated in terms of the formation properties. The choice of using the formation as the basis for this step is the fact that it dominates the transient heat transfer. By applying those groups to the set of equations for the inner nodes the system of differential equations becomes:

$$\begin{cases} T_{\mathrm{D,i}}=T_{\mathrm{D,pf}} & \text{i=0} \quad (88a)\\ \left(R_{\mathrm{i}}+R_{\mathrm{i+1}}\right)T_{\mathrm{D,i}}=R_{\mathrm{i+1}}T_{\mathrm{D,i-1}}+R_{\mathrm{i}}T_{\mathrm{D,i+1}} & \text{if i=1} \quad (88b)\\ C_iR_i\dfrac{\alpha_{fm}}{r_{\mathrm{fm}}^2}\dfrac{\partial T_{\mathrm{D,i}}}{\partial\tau}=-T_{\mathrm{D,i}}+T_{\mathrm{D,i-1}}-2\pi k_{fm}R_i\left.\dfrac{\partial T_{\mathrm{D,fm}}}{\partial r_{\mathrm{D}}}\right|_{r_{\mathrm{D}}=1} & \text{if i=Int} \quad (88c)\\ \left(R_{\mathrm{i}}R_{\mathrm{i+1}}C_{\mathrm{i}}\dfrac{\alpha_{fm}}{r_{\mathrm{fm}}^2}s+R_{\mathrm{i}}+R_{\mathrm{i+1}}\right)T_{\mathrm{D,i}}-R_{\mathrm{i}}T_{\mathrm{D,i+1}}-R_{\mathrm{i+1}}T_{\mathrm{D,i-1}}=0 & \text{otherwise} \quad (88d)\end{cases}$$

By applying the Laplace transform on this set of linear differential equations, one can find:

$$\begin{cases} \overline{T}_{\mathrm{D,i}}=\dfrac{T_{\mathrm{D,pf}}}{s} & \text{i=0} \quad (89a)\\ \left(R_{\mathrm{i}}+R_{\mathrm{i+1}}\right)\overline{T}_{\mathrm{D,i}}-R_{\mathrm{i}}\overline{T}_{\mathrm{D,i+1}}-R_{\mathrm{i+1}}\overline{T}_{\mathrm{D,i-1}}=0 & \text{if i=1} \quad (89b)\\ \left[R_{\mathrm{i}}C_{\mathrm{i}}\dfrac{\alpha_{fm}}{r_{\mathrm{fm}}^2}s+1\right]\overline{T}_{\mathrm{D,i}}-\overline{T}_{\mathrm{D,i-1}}+2\pi k_{fm}R_{\mathrm{i}}\left.\dfrac{\partial\overline{T}_{\mathrm{D,fm}}}{\partial r_{\mathrm{D}}}\right|_{r_{\mathrm{D}}=1}=0 & \text{if i=Int} \quad (89c)\\ \left(R_{\mathrm{i}}R_{\mathrm{i+1}}C_{\mathrm{i}}\dfrac{\alpha_{fm}}{r_{\mathrm{fm}}^2}s+R_{\mathrm{i}}+R_{\mathrm{i+1}}\right)T_{\mathrm{D,i}}-R_{\mathrm{i}}T_{\mathrm{D,i+1}}-R_{\mathrm{i+1}}T_{\mathrm{D,i-1}}=0 & \text{otherwise} \quad (89d)\end{cases}$$

Notice that in Equation 89c the derivative of the temperature profile at the wellbore interface is required, which can be calculated analytically from Equation 87, therefore the final form of the thermal network for the new model becomes:

$$\begin{cases} \overline{T}_{\mathrm{D,i}} = \dfrac{T_{\mathrm{D,pf}}}{s} & \text{i=0} \quad (90a) \\ (R_{\mathrm{i}} + R_{\mathrm{i+1}})\,\overline{T}_{\mathrm{D,i}} - R_{\mathrm{i}}\overline{T}_{\mathrm{D,i+1}} - R_{\mathrm{i+1}}\overline{T}_{\mathrm{D,i-1}} = 0 & \text{if i=1} \quad (90b) \\ \left[R_{\mathrm{i}} C_{\mathrm{i}} \dfrac{\alpha_{fm}}{r_{\mathrm{fm}}^2} s + \dfrac{2\pi k_{fm} R_{\mathrm{i}} \sqrt{s} K_1\left(\sqrt{s}\right)}{K_0\left(\sqrt{s}\right)} + 1 \right] \overline{T}_{\mathrm{D,i}} - \overline{T}_{\mathrm{D,i-1}} = 0 & \text{if i=Int} \quad (90c) \\ \left(R_{\mathrm{i}} R_{\mathrm{i+1}} C_{\mathrm{i}} \dfrac{\alpha_{fm}}{r_{\mathrm{fm}}^2} s + R_{\mathrm{i}} + R_{\mathrm{i+1}} \right) \overline{T}_{\mathrm{D,i}} - R_{\mathrm{i}}\overline{T}_{\mathrm{D,i+1}} - R_{\mathrm{i+1}}\overline{T}_{\mathrm{D,i-1}} = 0 & \text{otherwise} \quad (90d) \end{cases}$$

It is important to emphasize that, by computing the derivative of Equation 87 analytically while using the temperature of the formation interface as a boundary condition, this set of equations couples the heat transfer directly via the coefficients in Equation 90c. The main advantage of doing this is the consistency acquired by the method. The formulations based on Ramey's method, on the other hand, assume a constant heat flux at the interface between the wellbore and the formation.

The new system of equations considers both the transient heat transfer in the formation and the correct behavior of the temperature at the interface. Simultaneously, the proposed method allows for the addition of the thermal capacitance of the wellbore materials. Finally, by assembling the governing equations in the Laplace domain, the differential equations become a simple linear system, which can be solved directly as a function of the Laplace domain variable (s).

3.4 INVERSION ALGORITHM

In order to invert the solution found in the Laplace domain, many algorithms have been developed. One of the most widely known is that of Stehfest (1970) for its high efficiency and simplicity. In general, the most efficient inversion algorithms are those in the unified framework of Abate-Whitt (ABATE; WHITT, 2006), which consists of finding values of ω and λ that satisfy the following relationship:

$$f(t) \approx \frac{1}{t} \sum_{\mathrm{k=0}}^{N} \omega_{\mathrm{k}} \bar{f}\left(\frac{\lambda_{\mathrm{k}}}{t}\right) \quad (91)$$

where λ is a set of nodes used in the inversion algorithm, while ω are weight parameters. Many methods have been developed to determine this set of variables. Among them, the most important ones are the Euler method, which is based on a discrete Fourier transform algorithm, the Talbot method, which approximates the solution to the Bromwich integral, and the Gaver-Stehfest method (ABATE; WHITT, 2006).

The main drawback of the above mentioned methods is that the order of magnitude of ω grows very quickly, so that for large values of N, double precision arithmetic does not reach the required precision. For example, with the Gaver-Stehfest algorithm,

for *N* greater than 22, the associated numerical error is similar in magnitude to the inverted function itself. In the present work, an inversion method that does not suffer from this problem was chosen so that more inversion nodes can be used to achieve the desired precision.

A more recent method that meets the above mentioned precision requirement is the so-called Concentrated Matrix Exponential (CME) method presented by Horváth et al. (2020). Although the method is comparatively more difficult regarding the determination of the values of λ and ω, the authors made the framework parameters for large sets of *N* available on a public repository (HORVÁTH, 2019). A particular aspect of this method is that it requires more complex computation, which can be dealt with the NUMPY library (WALT; COLBERT; VAROQUAUX, 2011). The method of Horváth et al. (2020) can be safely applied with more than 1000 nodes without the risk of the inversion divergence due to numerical errors, even when using normal floating point arithmetics.

One step in implementation that is relevant to the application of the method is the fact that Equation 91 was implemented by using a dot product operator. The advantage of doing so is the increase in performance of the inversion step. This is achieved by vectorizing the code and allowing for faster multiplication of the terms. Since the dot operator can be expanded to higher order functions, it can be applied directly to the set of vectors resulting from the linear system solved for the radial network. This approach is written as:

$$f(t) \approx \frac{1}{t}\boldsymbol{\omega} \cdot \bar{f}\left(\frac{\boldsymbol{\lambda}}{t}\right) \tag{92}$$

where $\boldsymbol{\omega}$ and $\boldsymbol{\lambda}$ are the representations of weights and nodes in a first rank tensor. Note that as $\bar{f}$ is a generic representation of any function this equation is generalized to most types of functions, for example, in the thermal network a set of temperatures will be the final result of each calculation. For this example the result of $\bar{f}\left(\frac{\boldsymbol{\lambda}}{t}\right)$ will be a second rank tensor.

It is important to emphasize that the CME approach has a computational cost higher than the traditional methods, since for each node of the inversion algorithm it is necessary to assemble and solve the linear system presented in Equations 90a-90d. However, the method still has a lower computational cost than solving the heat transfer by linearization or other marching methods.

At this point, it is also important to emphasize the advantages of using this novel Laplace transform approach for solving heat transfer in wellbores. Even though many classical books, that deals with diffusion, may present an “analytical” solution to the semi-infinite solids heat transfer, such expressions are usually expressed in terms of integrals and power series which limits the precision of the solution and increase the computation required to find the temperature at the formation. Besides that, in essence

these solutions reproduces the same expressions as the one in Laplace domain. The point in using the numerical inversion is to simplify the effort in the inversion step without any detriment, as even the so called “analytical” solutions would yield only good enough expressions with accuracy limited to the approach used to compute the integral present in the expression. Besides that, the use of analytical solutions for the formation would lead to a harder coupling procedure for the wellbore. In general the transient terms would have to be solved by approximating the derivatives, which would involve marching schemes or other standard approaches for dealing with such terms. The solution, by means of the Laplace transform, deals with this problem directly, as the transformation procedure allows for the direct solution of the derivative terms in the Laplace domain. So, as it is clear, the use of the numerical inversion yields a more consistent solution without any loses in relation to other methods for solving transient heat transfer in wellbores.

3.5 DIFFERENCES BETWEEN THE HYBRID METHOD AND THE CONVENTIONAL APPROACHES

Compared to traditional approaches for solving the wellbore heat transfer, especially those implemented in the pySAFE program, the proposed hybrid method offers a number of advantages, as will be made clear along the text below.

When using time functions, the traditional approaches assemble the thermal system once and solve it in order to estimate the temperatures at all interfaces. Then, the heat transfer rate per unit length is estimated by applying Equation 1 to the solution of the thermal system. With this value for the heat transfer rate per unit length it is possible to re-assemble the thermal network updating the values of the thermal resistances and the result of the temperature at the wellbore interface (by updating the heat transfer to the formation). As this procedure is repeated until convergence is achieved for the temperatures at all nodes and for the heat transfer rate, several iterations may be required to properly estimate the behavior of the temperature in the thermal nodes. On the other hand, the new Laplace method follows a different approach since it does not need to iterate the heat transfer with the formation.

With the values of capacitance and resistance determined for each node of the thermal system, the inversion framework can be initiated. Therefore, many linear systems must be assembled for different values of solution nodes (λ). This adds an extra computational cost as more linear systems need to be assembled and solved. However, by reducing the number of iterations needed to solve the thermal network, the computational cost does not increase proportionally with the extra nodes in the formation algorithm. Iterations are still used to update resistances and capacitances as the temperatures are updated, but the influence of the temperature in these variables is mostly through the physical properties, so the overall number of iterations to reach

convergence is small.

The new procedure for solving the derivatives in the producing well is presented in Figure 24. It should be mentioned that there is great similarity between the solution procedures adopted for the pseudo steady-state approach (section 2.7) and Laplace methods in this regard.

Figure 24 – Procedure for solving the derivatives

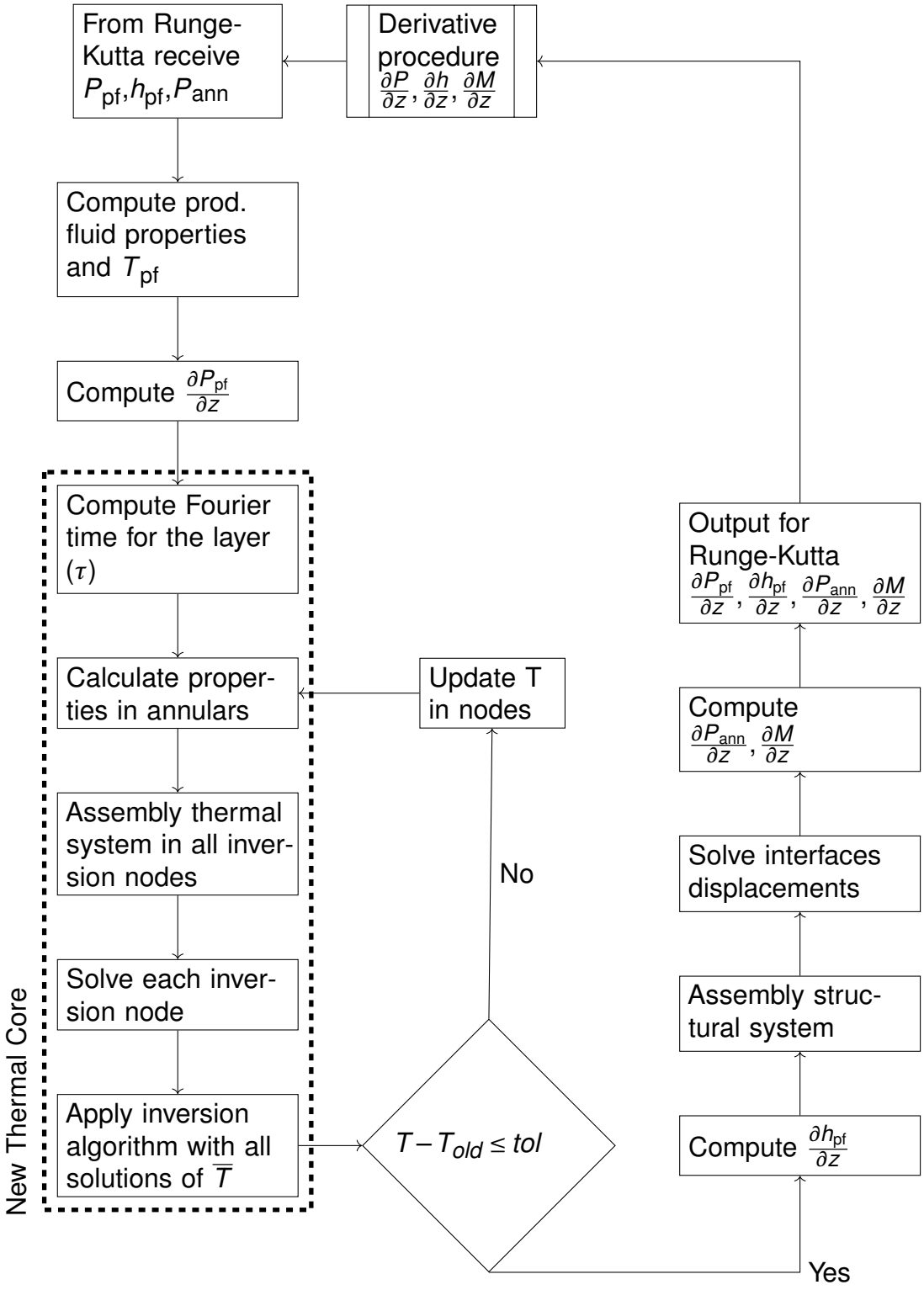

The differences in the new numerical core are highlighted, with one additional step in comparison with the traditional approach (inversion step). However, the remainder of the solver remains the same.

3.6 SOLUTION OF THE TEMPERATURE IN THE FORMATION

One important aspect which motivated the development of the new wellbore heat transfer calculation method is the ability to model the temperature in the formation. The normal approach of using time functions does not allow temperatures beyond the wellbore-formation interface to be computed.

In the hybrid approach, a procedural step has to be added to the thermal solver whenever the temperature profile in the formation is required. First, it is important to reiterate that Equation 87 is the exact solution of the temperature in the formation. However, to obtain the exact solution in functional form, $\overline{T}_{D,Int}$ must be known. This function is only assembled during the solution of the linear system, so one may think that solving the entire thermal network for each point in the formation is required. However, it is possible to take advantage from the Abate-Whitt framework to reduce the computational cost.

By storing the values of $\overline{T}_{D,Int}$ at the inversion nodes, it is possible to apply the inversion framework directly in Equation 87 by substituting the value of $\overline{T}_{D,Int}$ in the Laplace domain. In dimensionless form, the solution of the formation temperature profile can be written as:

$$\overline{T}_D(r_D,\tau) \approx \frac{1}{\tau}\sum_{k=0}^{N}\omega_k \frac{\overline{T}_{D,Int,k} K_0\left(r_D\sqrt{\frac{\lambda_k}{\tau}}\right)}{K_0\left(\sqrt{\frac{\lambda_k}{\tau}}\right)} \tag{93}$$

where $\overline{T}_{D,Int,k}$ is the interface temperature computed at each k-th step of the inversion in the thermal network system.

As the thermal model communicates with the rest of the program by means of interpolators, it is possible to write the temperatures $\overline{T}_{D,Int,k}$ in a vector which can be interpolated for application in different layers. As will be discussed in the Results (chapter 5), this approach managed to predict the interpolated behavior without problems, however, in the particular case of heat transfer in salt layers, in regions near the cemented layer (large resistance layers), the interpolations led to certain oscillations as a consequence of the one-dimensional approach used to solve the heat balance. To minimize such problems, the interpolator used for these scenarios was a simple previous value, where the value of $\overline{T}_{D,Int,k}$ is taken from the closest integration node of the Runge-Kutta step located above the studied section. This issue will be discussed in further detail in chapter 5.

This represents another computational advantage of the Laplace based model in relation to other advanced heat transfer models, such those by Bahonar, Azaiez, and Chen (2010) and You, Rahnema, and McMillan (2016). Since these models require discretization of the formation, their computational cost are strongly correlated to the need for higher precision. Conversely, in the present method, by using a sufficient

number of inversion nodes, the temperature profile is able to match the exact solution of the problem using smaller linear systems, at a reduced computational cost.

The procedure described above is used in the structural model for the salt layers proposed in the present thesis and described in detail in chapter 4. In this problem, the temperature profile in the salt layer is a determining factor related to creep and wellbore closure.

4 SALT CREEP MODEL

In order to model the deformation of the salt layers around producing wells, the same general strategy used in Almeida (2016) was adopted, i.e., modeling the creep related displacement using a FEM framework to deal with the inelastic material behavior. Almeida (2016) performed his simulation using a FEM commercial software, however, this approach prevents the detailed knowledge about how the problem is actually modeled and solved.

The following chapter has the objective to explain the mathematical model used to simulate the displacement of salt layers susceptible to creep. For that, section 4.1 explains the geomechanical aspects of the problem, section 4.2 describes the constitutive formulation used for the salt rock, section 4.3 deals with the aspects related to the FEM program used to model the displacement and, lastly, section 4.4 explains the algorithmic approach used to couple the thermal solver with the salt displacement model.

4.1 ROCK MECHANICS

Salt creep is known to affect APB in regions where the salt layers are exposed directly to the annulus. Therefore, the applicability of the model presented here is limited to non-cemented salt layers. Figure 25 presents a typical well geometry, similar to the one which illustrated the hybrid Laplace model, containing an non-cemented salt layer between Z_0 and Z_1. An intrinsic assumption of the present model is that the mechanics of cemented regions does not affect the displacement in non-cemented regions (ALMEIDA, 2016).

Figure 25 – Schematic diagram of a well containing a non-cemented salt layer

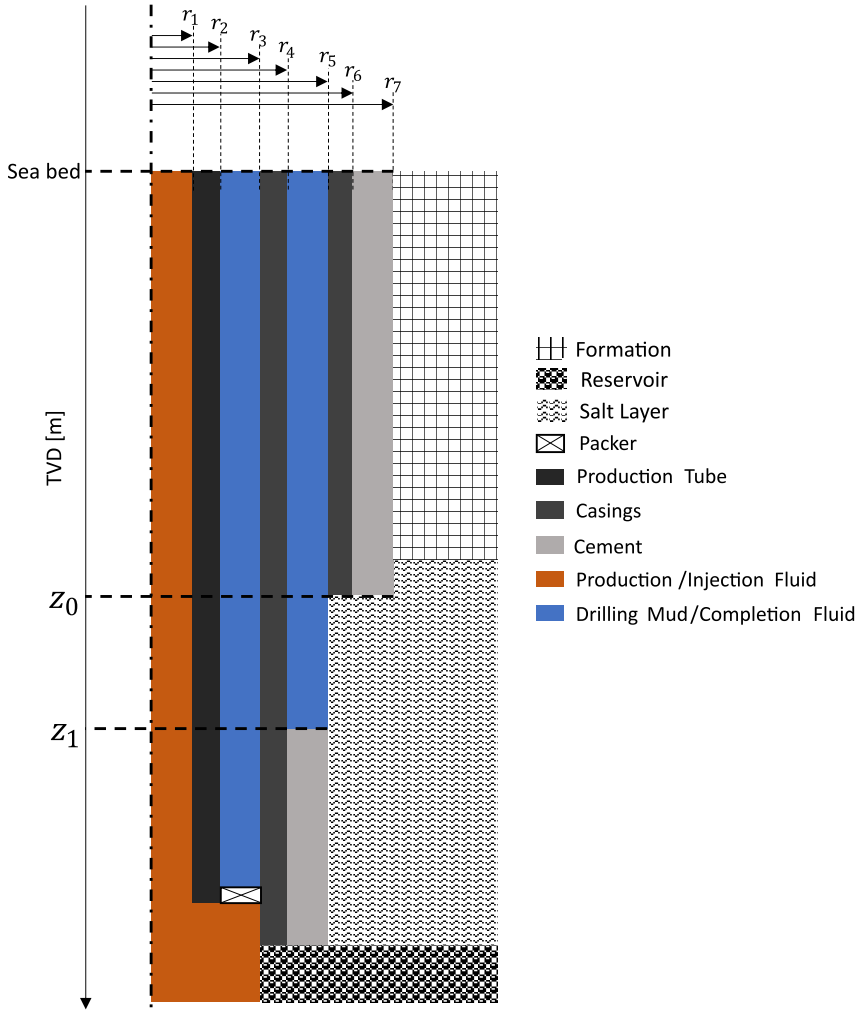

An important aspect of the model is that salt layers are treated as a *normal* formation layer (particularly from the point of view of the heat transfer), but which are subject to creep. Thus, the model developed here should be general enough to only be activated in the neighborhood of an annulus. Also it must be capable to automatically detect regions in salt layers which can suffer from creep.

In order to determine the creep intensity in a particular salt layer, it is necessary to estimate the stress condition within the rock. To do so, differential equations for the mechanical balance (strong formulation) can be written as:

$$\begin{cases} \nabla \cdot \boldsymbol{\sigma} + \boldsymbol{b} = \mathbf{0} & \text{if } r,Z \in \Omega \quad (94a) \\ \boldsymbol{\sigma}\mathbf{n} = \boldsymbol{t} & \text{if } r,Z \in \partial\Omega_t \quad (94b) \\ \boldsymbol{u} = \boldsymbol{u}_b & \text{if } r,Z \in \partial\Omega_U \quad (94c) \end{cases}$$

In the above set of equations, $\boldsymbol{\sigma}$ is the Cauchy stress tensor, $\boldsymbol{b}$ is the body force, $\mathbf{n}$ is the unit normal vector associated with the surface where the normal force $\boldsymbol{t}$ is applied. $\boldsymbol{u}$ is the displacement field and $\boldsymbol{u}_b$ is the displacement prescribed in certain boundaries.

As most drilling in salt rocks is done in the vertical direction, axial symmetry is assumed and, therefore, the positions within the salt layer are described exclusively by r and Z, which is directly related to the TVD which, in this case, coincides with the MD.

As the coordinate system is defined, the domain is split into three main regions. The inner volume of the salt layer is delimited by Ω. The boundaries of this domain are $\partial\Omega_t$, where normal loads are applied to the wall, and $\partial\Omega_U$ where displacements are imposed in the domain.

In terms of the geomechanical balance during drilling, different approaches are possible. Here, an approach similar to those of Fjaer et al. (2008) and Almeida (2016) was adopted. These approaches are based on the concepts of overburden stress and overburden gradient. The first one is defined as the weight which the rock formation exerts on itself and subsequent layers, similar to pressure of a column of fluid. The second one is the gradient of the stress variable, which is usually represented as a type of density that can directly represent the stress state of the rock as a function of depth. This relation is given by:

$$\sigma_{ov} = 1174.74 G_{ov} Z \tag{95}$$

where G_{ov} is the overburden gradient given in pounds per gallon, which are the units commonly adopted by the industry. σ_{ov} is the overburden stress, in Pa. The constant 1174.74 is the combination of the gravitational acceleration and a unit conversion factor (ALMEIDA, 2016).

This relationship proves to be very important in geomechanics, because it relates parameters in the vertical direction, where the greatest stresses are found (FJAER et al., 2008). Knowing that the stress state of the rock is described by an orthogonal representation of three components, relationships exist to determine the radial stresses acting on the well.

As the creep deformation model is developed to deal with vertical wells considering homogeneous rocks, it is assumed that the both horizontal components of stresses will have a similar modulus. As a result, an axisymmetric model can be used to model the state of stress and deformation of the rock.

For the more specific case of elastic deformations of rocks, a traditional approach to treat the stress state in regions further away from the well is to consider that the horizontal stress must be such that the deformation decays over long distances. This condition can be achieved as long as the following relationship between the overload stress and the horizontal stress for long distances from the well is satisfied:

$$\sigma_h = \frac{\nu}{1-\nu}\sigma_{ov} \tag{96}$$

where ν is the Poisson's ratio of the rock. Once this relationship between the vertical and radial stresses is applied, the stress state is known. Once the well is drilled, the

inner boundary condition (stress) becomes the pressure imposed by the annulus.

Assuming pure elastic deformation, the stress condition given by Equation 96 is equivalent to a zero displacement far away from the well, $\boldsymbol{u}_r = 0$, (FJAER et al., 2008). In order to expand this mechanical balance to other deformation mechanisms, it is possible to apply the outer stress from Warplnskl (1989), which takes into account history effects from viscoelastic and thermal deformations and, by doing so, it can maintain balance on the outer boundary even when multiple mechanism are modelled simultaneously. The problem in using the traditional geomechanical elastic boundary condition, given by Equation 96, is that when non-elastic deformations reach the outer boundary, the mechanical balance is no longer satisfied. To avoid this problem, it is possible to write an equivalent outer boundary condition that satisfies the mechanical balance by imposing a zero displacement far from the well. Almeida (2016) indicates that a distance of 10 radii is sufficient to properly represent the deformation for creep. However, due to the addition of other deformation mechanisms (namely thermo-elasticity), a distance of 100 radii is used in the present study. Figure 26 shows graphically the boundary conditions which are used. At the inner wall, the pressure from the annulus, at the top, the overburden stress and, at bottom and outer walls, a slip condition is used, fixing at zero the displacement in the normal direction.

Figure 26 – Boundary conditions used in the salt creep model

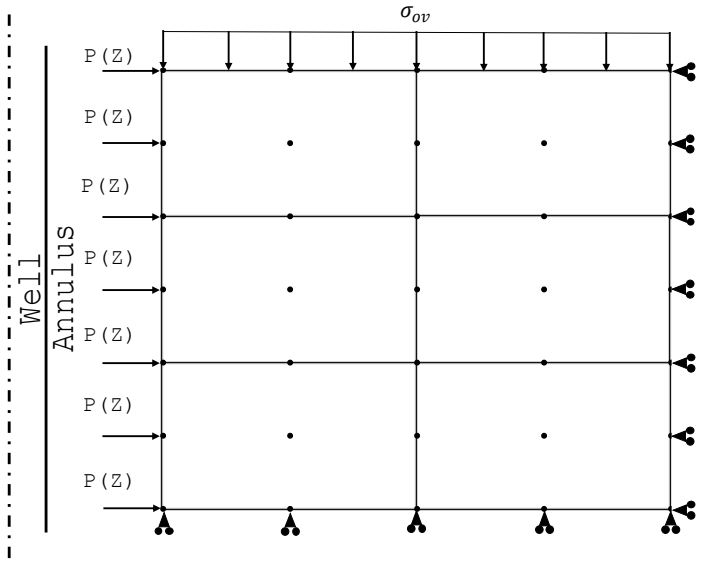

At this point, it is already possible to define the initial stress distribution in the rock. This is limited only to the initial stress field, without addressing the creep related strain and how the stress will behave over time. For that, it is necessary to describe the constitutive model used in the salt rock formation.

4.2 CONSTITUTIVE MODEL

The basic constitutive model consists of modeling the deformation using a viscoelastic approach. In that, the total deformation is composed of three main contributions: the elastic deformation itself, thermal expansion associated with the heating of the rock and the creep. The sum of all contributions to the strain of the material is written as:

$$\boldsymbol{\varepsilon} = \boldsymbol{\varepsilon_{el}} + \boldsymbol{\varepsilon_{th}} + \boldsymbol{\varepsilon_{cr}} \tag{97}$$

where $\boldsymbol{\varepsilon}$ is the strain tensor, and the subscripts "el", "th" and "cr" denote the elastic effect, thermal expansion and creep, respectively.

Constitutive models relate the stress state and the history of deformation suffered by a material point. In the salt rock formation investigated in the present work, the creep strain rate is modelled via the creep law proposed by Maia C et al. (2005). This model relates the state of stress, more specifically a measure of it called effective stress, to the instantaneous creep strain rate amplitude. It should be clear that a time dependence is implied in this relationship, that is, to model the salt deformation, an incremental model is required, similar to those used for plastic and viscoplastic deformation of materials.

In general, the state of stress is solved at each instant of time so that it is possible to estimate the rate at which the deformation occurs. Mendonça and Fancello (2019) explain this approach for plastic materials, while de Souza Neto, Peri, and Owen (2008) describe a more detailed procedure to create codes for solving plasticity and viscoplasticity with FEM. Naumenko (2006) addresses this issue in the context of creep at high temperatures. In the present scenario of modeling salt layers, an incremental model with an implicit time integration approach was used.

To describe this approach, it is first necessary to define the creep law, as described in Maia C et al. (2005):

$$\dot{\gamma} = \begin{cases} \dot{\gamma}_{\text{ref}} \left(\frac{q}{q_{\text{ref}}}\right)^{n_1} \exp\left(\frac{A}{R_{gas} T_{\text{ref}}} - \frac{A}{R_{gas} T}\right), & \text{if } q \leq q_{\text{ref}} \\ \dot{\gamma}_{\text{ref}} \left(\frac{q}{q_{\text{ref}}}\right)^{n_2} \exp\left(\frac{A}{R_{gas} T_{\text{ref}}} - \frac{A}{R_{gas} T}\right), & \text{otherwise} \end{cases} \tag{98}$$

where $\dot{\gamma}$ is the creep rate, q is the effective stress, n_1 and n_2 are empirical parameters, A is the activation energy of the rock and R_{gas} is the universal gas constant. $\dot{\gamma}_{\text{ref}}$ and q_{ref} are experimentally calibrated. An important thing to note is that the effective stress is originally calculated using the Tresca criterion in Maia C et al. (2005), however, for some applications, like that of Almeida (2016), the von Mises' criterion was used. As demonstrated by Oliveira (2016), for many scenarios, both criteria tend to generate similar results. Therefore, the Von Mises' criterion was used in the present formulation to model the salt layer. The identification of the material parameters for this equation was already shown in Figure 14.

The main variable of the constitutive model is the creep amplitude. This variable is responsible for the history of creep deformation in the material. It is defined by:

$$\gamma = \int_0^t \dot{\gamma} dt \tag{99}$$

As the creep rate depends on the instantaneous stress state of the material, the integral is cumbersome and difficult to use. Getting around this problem involves describing the time domain in terms of discrete points using the implicit Euler method. For this approach the creep amplitude for a t_{n+1} timestep is described by:

$$\gamma_{n+1} = \gamma_n + \Delta t_{n+1} \dot{\gamma}(t_{n+1}) \tag{100}$$

The main consequence of using discrete timesteps for the creep amplitude is that the remaining variables of the constitutive model should be modeled accordingly. Every term in Equation 97 now must be described using this same approach. However, the only term which will actually depends on time history is the creep strain, which is described by:

$$\boldsymbol{\varepsilon_{cr}}_{n+1} = (\gamma_{n+1} - \gamma_n) \boldsymbol{N}_{n+1} + \boldsymbol{\varepsilon_{cr}}_n \tag{101}$$

where the second order tensor $\boldsymbol{N}_{n+1}$ defines the direction of creep flow, which is co-linear to the deviatoric stress (this variable will be better explained when describing the trial step of the constitutive model).

The stress tensor is conveniently separated into deviatoric and volumetric contributions:

$$\boldsymbol{\sigma} = \boldsymbol{S} + p\mathbf{I} \tag{102}$$

where $\boldsymbol{\sigma}$ is the total stress tensor, $\boldsymbol{S}$ is the deviatoric stress tensor, p is the volumetric stress contribution and $\mathbf{I}$ is the identity tensor.

These stress contributions can be calculated from the isotropic elastic model as follows:

$$\boldsymbol{S} = 2G\boldsymbol{\varepsilon_{el}}^{dev} \tag{103}$$

and:

$$p = K\mathrm{tr}(\boldsymbol{\varepsilon_{el}} - \beta_{lin}\Delta T\mathbf{I}) \tag{104}$$

In these two equations, $\boldsymbol{\varepsilon_{el}}^{dev}$ is the elastic deviatoric strain tensor, G is the shear modulus and K is the bulk module of the material. tr is the trace operator which, in this case, is being applied to the elastic strain tensor and thermal expansion term.

The latter is defined as the product of the thermal linear expansion coefficient (β_{lin}) and the temperature difference from the initial condition.

As explained before, the Euler's implicit method (incremental approach) was chosen to model creep deformation. Because of this, the strain at time t_{n+1} needs to be resolved iteratively with the stress.

This iterative process consists of applying the predictor-corrector algorithm (MENDONÇA; FANCELLO, 2019), which is a trial-and-error approach that tests different sets of stresses and deformations until all equations of the constitutive model are satisfied at the end of the time . The first hypothesis is of a purely thermo-elastic behavior. Thus, it is possible to define the set of variables of the first "trial" step of the algorithm as follows:

$$\begin{cases} \boldsymbol{\varepsilon_{el}}^{\text{tr}}_{\text{n+1}} = \boldsymbol{\varepsilon}_{\text{n+1}} - \boldsymbol{\varepsilon_{cr}}_{\text{n}} & \text{(105a)} \\ \boldsymbol{S}^{\text{tr}}_{\text{n+1}} = 2G\text{dev}\left(\boldsymbol{\varepsilon_{el}}^{\text{tr}}_{\text{n+1}}\right) & \text{(105b)} \\ p^{\text{tr}}_{\text{n+1}} = K\text{tr}\left(\boldsymbol{\varepsilon_{el}}^{\text{tr}}_{\text{n+1}} - \beta_{lin}\Delta T_{\text{n+1}}\mathbf{I}\right) & \text{(105c)} \\ \boldsymbol{N}^{\text{tr}}_{\text{n+1}} = \sqrt{\frac{3}{2}}\frac{\boldsymbol{S}^{\text{tr}}_{\text{n+1}}}{\|\boldsymbol{S}^{\text{tr}}_{\text{n+1}}\|} & \text{(105d)} \end{cases}$$

Some interesting results can be obtained from these equations. First, the initial test consists of assuming that creep does not occur in the updated time step. However, as the contribution of the creep is found in the deviatoric strain, the volumetric stress term will not change as the algorithm finds the total creep which occurs in this time step. In addition, due to the option of using the von Mises criterion to model the effective stress, the creep direction calculated in the first step will already be collinear with the final direction (MENDONÇA; FANCELLO, 2019). Therefore, these two variables will not need to be recalculated during the algorithmic procedure.

To write the algorithm that calculates the creep strain. the following residual function is defined:

$$Res(\gamma_{\text{n+1}}) = \gamma_{\text{n}} - \gamma_{\text{n+1}} + \Delta t_{\text{n+1}}\dot{\gamma}_{\text{n+1}} \tag{106}$$

The creep rate $\dot{\gamma}_{\text{n+1}}$ depends on the effective stress at time n+1 given by:

$$q_{\text{n+1}} = q^{\text{tr}}_{\text{n+1}} - 3G(\gamma_{\text{n+1}} - \gamma_{\text{n}}) \tag{107}$$

where the trial effective stress $q^{\text{tr}}_{\text{n+1}}$ is defined by:

$$q^{\text{tr}}_{\text{n+1}} = \sqrt{\frac{3}{2}}\|\boldsymbol{S}^{\text{tr}}_{\text{n+1}}\| \tag{108}$$

Therefore, by combining Equation 98 with the last 3 equations, one can write the residual equation used to determine γ_{n+1} value which satisfies the algorithm as follows:

$$Res(\gamma_{n+1}) = \begin{cases} \gamma_n - \gamma_{n+1} + \Delta t_{n+1}\dot{\gamma}_{ref}\left[\frac{q_{n+1}}{q_{ref}}\right]^{n_1} \exp\left(\frac{A}{R_{gas}T_{ref}} - \frac{A}{R_{gas}T}\right), & \text{if } q_{n+1} \leq q_{ref} \\ \gamma_n - \gamma_{n+1} + \Delta t_{n+1}\dot{\gamma}_{ref}\left[\frac{q_{n+1}}{q_{ref}}\right]^{n_2} \exp\left(\frac{A}{R_{gas}T_{ref}} - \frac{A}{R_{gas}T}\right), & \text{otherwise} \end{cases} \tag{109}$$

The above equation was solved with the *rtsolve* solver (PRESS et al., 2007), which is a hybrid of the Newthon-Rapshon and bisection methods. As a result, it has great numerical performance while guaranteeing that a root is found, as long as it exists within the search interval. To delimit such an interval, the extreme conditions that can occur with the creep rate are taken into account.

First, it is known that the creep amplitude cannot decrease from one step of time to the next, so one of the limits for the root search will be the creep amplitude of the previous step. The other extreme considers a state that is able to zero the creep rate, which must occur for times that are long enough to bring the effective stress to close to a zero. Thus, Equation 107 provides the other limit of the search interval. This region is described as:

$$\gamma_n \leq \gamma_{n+1} \leq \gamma_n + \frac{q^{tr}_{n+1}}{3G} \tag{110}$$

Thus, it is already possible to determine the value of γ_{n+1} that satisfies the condition of local stress. With this value, one can update the other strain variables and advance the algorithm.

Another issue that the constitutive model needs to address the derivative of the stress tensor in relation to the strain tensor. This is important to solve the deformation field that satisfies the mechanical balance of the material. The derivation of this tensor is relatively long so it will be described in the Appendix A. However, once the necessary operations are done, it is possible to write that:

$$\frac{\partial \boldsymbol{\sigma}_{n+1}}{\partial \boldsymbol{\varepsilon}_{n+1}} = 2G\left[1 - \frac{3G(\gamma_{n+1} - \gamma_n)}{q^{tr}_{n+1}}\right]\mathbb{P} - 6G^2\left[\frac{\gamma_{n+1} - \gamma_n}{q^{tr}_{n+1}} - \frac{\Gamma_1}{\Gamma_0 + 3G\Gamma_1}\right]\frac{\boldsymbol{S}_{n+1} \otimes \boldsymbol{S}_{n+1}}{\|\boldsymbol{S}_{n+1}\|^2} + K(\mathbf{I} \otimes \mathbf{I}) \tag{111}$$

where $\mathbb{P}$ is the projection tensor, and Γ_0 and Γ_1 are auxiliary variables defined as:

$$\Gamma_0 = \frac{\exp\left(\frac{A}{R_{gas}T_{ref}} - \frac{A}{R_{gas}T}\right)}{\Delta t_{n+1}\dot{\gamma}_{ref}} \tag{112}$$

and:

$$\Gamma_1 = \frac{n}{q_{ref}}\left[\frac{q^{tr}_{n+1} - 3G(\gamma_{n+1} - \gamma_n)}{q_{ref}}\right]^{n-1} \tag{113}$$

Finally, to update the stress once the algorithm converged, it is possible to write the following expression:

$$\boldsymbol{\sigma}_{n+1} = \boldsymbol{S}^{tr}_{n+1} - 2G(\gamma_{n+1} - \gamma_n)\boldsymbol{N}_{n+1} + p_{n+1}\mathbf{I} \tag{114}$$

With that, the constitutive model is complete. The next section deals with the FEM model developed to resolve the salt creep around the well.

4.3 FINITE ELEMENT METHOD

The FEM method is used to find an approximate solution of the partial differential equations of the problem. In the present case the main variable is the displacement field u that in the axissimetric formulation is written as:

$$\boldsymbol{u} = \begin{Bmatrix} u_r(r,Z) \\ u_\phi = 0 \\ u_Z(r,Z) \end{Bmatrix} \tag{115}$$

Small deformations were considered, so the linearized deformation hypothesis was used. From this, it is possible to write the strain in terms of the displacement as follows:

$$\boldsymbol{\varepsilon} = \frac{\boldsymbol{D}\boldsymbol{u} + \left(\boldsymbol{D}\boldsymbol{u}^{\mathsf{T}}\right)}{2} \tag{116}$$

where $\boldsymbol{D}$ is the derivative operator, which for the axisymmetric geometry is defined as:

$$\boldsymbol{D} = \begin{bmatrix} \frac{\partial}{\partial r} & 0 \\ \frac{1}{r} & 0 \\ 0 & \frac{\partial}{\partial Z} \\ \frac{\partial}{\partial Z} & \frac{\partial}{\partial r} \end{bmatrix} \tag{117}$$

To facilitate the computational implementation of the method, from this point on, Voigt's notation is used to describe the stresses and deformations. Thus:

$$\boldsymbol{\varepsilon} = \begin{bmatrix} \varepsilon_{rr} \\ \varepsilon_{\phi\phi} \\ \varepsilon_{ZZ} \\ \gamma_{rZ} = 2\varepsilon_{rZ} \end{bmatrix} \tag{118}$$

Using this notation, it becomes possible to write the strain by directly applying the derivative operator to the displacement field:

$$\boldsymbol{\varepsilon}(r,Z) = \boldsymbol{D}\boldsymbol{u}(r,Z) \tag{119}$$

The FEM is based on the idea of proposing an approximate solution based on shape functions $\mathcal{N}(r,Z)$ modulated by parameters $\boldsymbol{U}$.

$$\boldsymbol{u}(r,Z) = \mathcal{N}(r,Z)\,\boldsymbol{U} \tag{120}$$

where $\mathcal{N}$ are the shape functions used and $\boldsymbol{U}$ is a vector with all nodal displacements.

It is important to clarify that a shape function interpolates information (displacement, stress and any other variable) within each element. Thus a shape function is only valid within the element it describes. Besides that, these functions must comply with certain properties. Firstly, to obey the characteristic presented previously, it must be non-zero only within its element. Also, they must follow a Kroenecker delta behavior within its nodes. In other words, the shape function, when described as a function of each individual node, must be equal to zero when applied in neighbor nodes within the same element (FISH; BELYTSCHKO, 2007). As this thesis will use a quadratic element of type Lagrangian, Figure 27 presents an example of a 1-D shape function for a quadratic element.

Figure 27 – One dimensional quadratic shape function

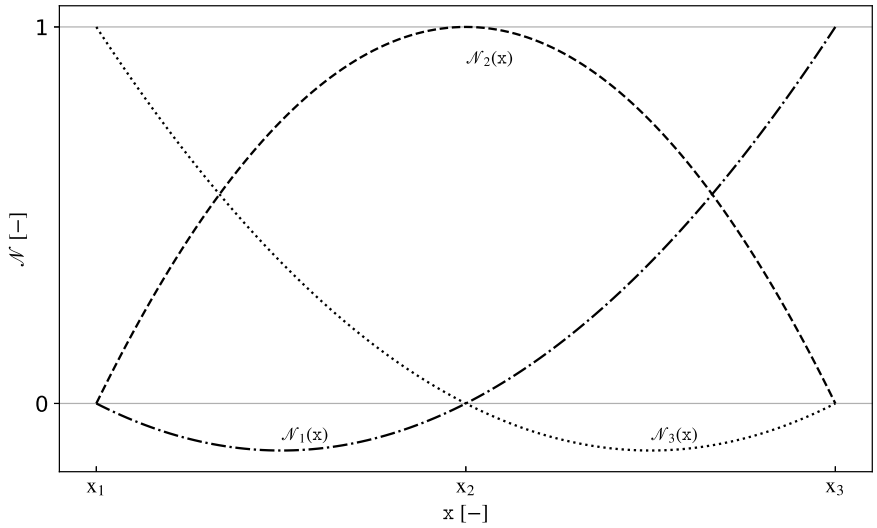

To calculate the strain field using the shape functions, one can write:

$$\boldsymbol{\varepsilon}(r,Z) = \boldsymbol{B}(r,Z)\,\boldsymbol{U} \tag{121}$$

where:

$$\boldsymbol{B}(r,Z) = \boldsymbol{D}\mathcal{N}(r,Z) \tag{122}$$

The complete description of the shape functions used, as well as the procedure for how to calculate their derivatives is described in the Appendix A. From this point on,

these terms can be used in the Principle of Virtual Works (PVW) so that it is possible to set up a balance equation based on the sum of the internal and external forces so that:

$$\boldsymbol{Res}_{\mathrm{n+1}}\left(\boldsymbol{U}_{\mathrm{n+1}}\right) = \boldsymbol{F_{int}}_{\mathrm{n+1}} - \boldsymbol{F_{ext}}_{\mathrm{n+1}} \tag{123}$$

where the forces vectors are described by:

$$\boldsymbol{F_{int}}_{\mathrm{n+1}} = \int_{\Omega} 2\pi r \boldsymbol{B}^{\mathsf{T}} \boldsymbol{\sigma}_{\mathrm{n+1}}\left(\boldsymbol{U}_{\mathrm{n+1}}\right) d\Omega \tag{124}$$

and:

$$\boldsymbol{F_{ext}}_{\mathrm{n+1}} = \int_{\Omega} 2\pi r \mathscr{N}^{\mathsf{T}} \boldsymbol{b} d\Omega + \int_{\partial\Omega} 2\pi r \mathscr{N}^{\mathsf{T}} \boldsymbol{t}_{\mathrm{n+1}} d\partial\Omega \tag{125}$$

where Ω is the domain studied, the salt layer, $\partial\Omega$ are the boundary surfaces where boundary stresses, $\boldsymbol{t}$, are applied. $\boldsymbol{b}$ is the body force tensor which, in the present case, will depend on the overburden gradient in the region of interest. The procedure for calculating this term will be better explained below.

Note that, in the above equations, there are integrals to be solved over the entire domain. However, as part of the developed formulation, it is possible to segment these integrals with respect to the individual elements. Thus, the so-called *Assembly routines* are created, and for the vector of internal forces this is written by:

$$\boldsymbol{F_{int}}_{\mathrm{n+1}} = \mathscr{A}_{k}^{N_{el}} \int_{\Omega_{\mathrm{El}}} 2\pi r \boldsymbol{B}_{\mathrm{El}}^{\mathsf{T}} \boldsymbol{\sigma}_{\mathrm{n+1,El}}\left(\boldsymbol{U}_{\mathrm{n+1,El}}\right) d\Omega_{\mathrm{El}} \tag{126}$$

where $\mathscr{A}$ is the assembly operator, N_{el} is the total number of elements used to describe the domain, Ω_{El} is the individual subset of the entire domain delimited by an element.

Even with this spatial division, it is not yet possible to perform integration (Equation 126) in an analytical way. For this purpose, numerical integration techniques can be used. The traditional approach adopted here involves the application of the Gauss-Legendre quadrature technique. In this method, the integration can be approximated as:

$$\boldsymbol{F_{int}}_{\mathrm{n+1}} \approx \mathscr{A}_{\mathrm{El}}^{N_{el}} \sum_{\mathrm{j}}^{N_{int}} 2\pi r\left(X_{int,\mathrm{j}}\right) \boldsymbol{B}^{\mathsf{T}}\left(X_{int,\mathrm{j}}\right) \boldsymbol{\sigma}_{n+1,\mathrm{El,j}} W\left(X_{int,\mathrm{j}}\right) \tag{127}$$

where N_{int} is the number of integration points in any given element, X_{int} are the positions of these integration points in relation to the domain and W are the weights used in the integration procedure.

Something not mentioned yet is that for every node in the domain, there will be two degrees of freedom which are related to the displacement of the node. So, the nodes are responsible for storing information of displacement. The resulting stress and remaining variables of the model, which are required in the integration procedure, are

stored in the integration points. In the post processing of the results, both grids (solution and integration node grids) are used to store information.

In the literature, FEM has been applied using a mesh of linear quadrilateral elements (ALMEIDA, 2016). In order to propose a small improvement in the solution of displacements in rocks susceptible to creep, a mesh of bi-quadratic elements is used in the present work. These elements have Lagrangian interpolators calculated using 9 nodes and are further explained in Appendix A. As these are of a higher order, 9 integration nodes are also used for each element. Along with the description of the element, a review of the weights and positions of the integration nodes is presented next.

The elements have an internal indexing system used to identify the nodes contained internally. This indexing system follows the scheme presented in Figure 28:

Figure 28 – Indexation of a given element

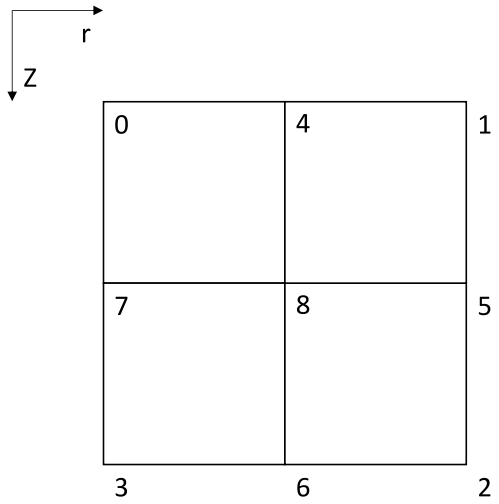

Every element is comprised of 9 nodes, following a clockwise convention, however it points downward to match the vertical direction of the TVD.

At this point, the basic formulation for estimating the deformation within the domain is complete. However, one must be able to compute both the body forces and forces applied at the boundaries of the salt layer. To complete the formulation both terms will be described starting with the former.

It is important to explain how the overburden gradient data is provided. For it is a variable of great importance in the construction of wells, known at different depths, it is possible to linearly interpolate this variable in the region of interest. Going back to Equation 95, one can write the term $\boldsymbol{b}$ by the equation:

$$\boldsymbol{b}(r,Z) = \begin{bmatrix} 0 \\ 1174.74 \left[Z \left. \frac{\partial G_{ov}}{\partial Z} \right|_Z + G_{ov}(Z) \right] \end{bmatrix} \tag{128}$$

With this equation, it is possible to calculate the terms necessary to compute the body force in the vector of external forces.

For the boundary conditions of both pressure at the inner wall and stress at the top of the salt column, the equations are simpler, allowing the use of analytical expressions to reduce the computational cost.

For the nodes located at the top of the salt column, using the notation shown in Figure 28, it is possible to calculate the force that each node will be subjected to due to the weight of the rock column above the salt. Since this load is evenly distributed, these nodal forces are described by:

$$\boldsymbol{f}_{\mathrm{El},0} = \frac{1174.74 G_{ov} Z_{top} \pi \left(r_{\mathrm{El},1} - r_{\mathrm{El},0}\right)}{3} \begin{bmatrix} 0 \\ r_{\mathrm{El},0} \end{bmatrix} \tag{129}$$

$$\boldsymbol{f}_{\mathrm{El},1} = \frac{1174.74 G_{ov} Z_{top} \pi \left(r_{\mathrm{El},1} - r_{\mathrm{El},0}\right)}{3} \begin{bmatrix} 0 \\ r_{\mathrm{El},1} \end{bmatrix} \tag{130}$$

$$\boldsymbol{f}_{\mathrm{El},4} = \frac{1174.74 G_{ov} Z_{top} \pi \left(r_{\mathrm{El},1} - r_{\mathrm{El},0}\right)}{3} \begin{bmatrix} 0 \\ 4 r_{\mathrm{El},4} \end{bmatrix} \tag{131}$$

In this set of equations, $\boldsymbol{f}_{\mathrm{El},i}$ represents the nodal forces of the element El, the second subscript represents the node of the element in question. It is important to emphasize that this operation must be repeated for all elements located at the top of the salt column, and must be followed by the Assembly process in the vector of external nodal forces. Similar to the indexers used in terms of force, the radii shown are related to the positions of the same nodes.

It is important to distinguish the difference between the inner walls and the top of the salt layer in terms of the boundary conditions. In this case, the pressure that is applied to the wall is dependent on the depth. As a consequence, it is not possible to apply an equally distributed stress condition. In addition, the relationship between the fluid pressure and the depth may be non-linear, as the annular can be filled with more than one fluid, thus making it necessary to consider these factors. For this purpose, one can take advantage of the elements' own shape functions. In this case, it is considered that the pressure at the wall of the salt layer can be approximated by the same shape functions that are used to describe the displacement field. From this, the force vectors in the contour nodes can be written by:

$$\boldsymbol{f}_{\mathrm{El},0} = \frac{\pi r_{\mathrm{fm}} \left(Z_{\mathrm{El},3} - Z_{\mathrm{El},0}\right)}{15} \begin{bmatrix} 4P\left(Z_{\mathrm{El},0}\right) - P\left(Z_{\mathrm{El},3}\right) + 2P\left(Z_{\mathrm{El},7}\right) \\ 0 \end{bmatrix} \tag{132}$$

$$\boldsymbol{f}_{\mathrm{El},7} = \frac{2\pi r_{\mathrm{fm}} \left(Z_{\mathrm{El},3} - Z_{\mathrm{El},0}\right)}{15} \begin{bmatrix} P\left(Z_{\mathrm{El},0}\right) + P\left(Z_{\mathrm{El},3}\right) + 8P\left(Z_{\mathrm{El},7}\right) \\ 0 \end{bmatrix} \tag{133}$$

$$\boldsymbol{f}_{\mathrm{El},3} = \frac{\pi r_{\mathrm{fm}} \left(Z_{\mathrm{El},3} - Z_{\mathrm{El},0}\right)}{15} \begin{bmatrix} -P\left(Z_{\mathrm{El},0}\right) + 4P\left(Z_{\mathrm{El},3}\right) + 2P\left(Z_{\mathrm{El},7}\right) \\ 0 \end{bmatrix} \tag{134}$$

where P is the pressure provided by the solution of the pressure profile in the annulus at each given depth of the solution nodes.

For the other boundaries of the domain it is assumed that the salt layer does not deform in the directions normal to the faces (ALMEIDA, 2016). In other words, for points far from the well, or at the base of the study region, a prescribed zero offset is applied.

At this point the formulation to describe the balance equations is ready, however, it takes the displacement field as an input. In order to find the displacement field that satisfies the balance, the residue must be zeroed. The approach chosen to solve this problem is the application of Newton's method to solve the residual equations. So the algorithm is written so that:

$$\left.\frac{\partial \boldsymbol{Res}}{\partial \boldsymbol{U}_{\mathrm{n+1}}}\right|_{\mathrm{l}} \delta \boldsymbol{U}_{\mathrm{n+1,l+1}} = -\boldsymbol{Res}\left(\boldsymbol{U}_{\mathrm{n+1,l}}\right) \tag{135}$$

where l is the index of Newton's method iterations and $\delta \boldsymbol{U}_{n+1,\mathrm{l+1}}$ is the increment calculated for the method step. The greatest difficulty for its implementation is the calculation of the residue derivatives with respect to the displacement. However, assuming that displacements affect only the terms related to the internal forces it is possible to write that:

$$\frac{\partial \boldsymbol{Res}}{\partial \boldsymbol{U}_{\mathrm{n+1}}} = \int_{\Omega} \boldsymbol{B}^{\mathrm{T}} \frac{\partial \boldsymbol{\sigma}_{\mathrm{n+1}}}{\partial \boldsymbol{\varepsilon}_{\mathrm{n+1}}} \frac{\partial \boldsymbol{\varepsilon}_{\mathrm{n+1}}}{\partial \boldsymbol{U}_{\mathrm{n+1}}} d\Omega \tag{136}$$

Considering that the stress derivative term with respect to strain is provided by the material's constitutive model of Equation 111 and using the definition of $\boldsymbol{B}$, this equation simplifies to:

$$\frac{\partial \boldsymbol{Res}}{\partial \boldsymbol{U}_{\mathrm{n+1}}} = \int_{\Omega} \boldsymbol{B}^{\mathrm{T}} \frac{\partial \boldsymbol{\sigma}_{\mathrm{n+1}}}{\partial \boldsymbol{\varepsilon}_{\mathrm{n+1}}} \boldsymbol{B} d\Omega \tag{137}$$

This integral is also approximated with the Gauss-Legendre method, so the terms required are computed in the same integration points.

To evaluate the convergence of the method, two techniques are used. The first one directly involves the Residua Tensor norm. The second one involves making the product of the incremental displacements with the calculated forces. This is called the energy criterion and will be used due to the large dimension of the problem, since convergence by the residue norm could be difficult to achieve. Although this can somewhat reduce the numerical precision of the algorithm, it is hoped that this issue will not be important in the final solution. A step-by-step description of the solution framework will be provided below.

4.4 COUPLING WITH WELLBORE HEAT TRANSFER MODEL

In order to allow the two programs to work together and solve the APB model coupled with the creep deformation, it is possible to take advantage of the structure provided by the iterations of the mass conservation in the annulus.

First, it is important to emphasize that the coupling starts even before running the thermal simulation. As the program needs to detect the layers susceptible to creep automatically, the coupling starts as soon as the model input files are read. To detect the layers subjected to creep, the creep parameters are used as additional data for the structural models. If only elastic data are passed, the creep module is not activated. Once the layers of interest are identified, it is necessary to consider which of these are actually going to experience creep.

For that, the results presented in Almeida (2016) can be used. It was concluded that cemented layers have less potential to undergo creep, so once the positions of the cement layers in the well are detected, it is necessary to make a lateral assessment for the presence of this material. If cement is detected in contact with layers of salt, some actions must be taken. If one region is defined as unable to creep, the model of Halal and Mitchell (1994) is used as the standard deformation solver.

For scenarios in which the entire salt layer is cemented, the algorithm removes it from the list of regions of interest. However, it is possible that the layer is cemented only in a certain region. If this is the case, the code must detect which sections of the layer will be in contact with fluids in the annulus, then edit the list of regions of interest.

Once the zones to be modeled using FEM have been determined, the code moves on to the meshing step of the salt layer. As the geometry of the well is generally very complex, the meshes of the salt rock formation are generated independently of the meshes of the well. In this way, refining the mesh in the vertical direction becomes simpler and makes it unnecessary to add extra nodes to the numerical solution of the problem.

The numerical mesh will be addressed in detail later in the thesis (chapter 5). However, it can be anticipated that the elements are distributed in a non-uniform way so as to increase their concentration near the boundary with the annulus. As pointed out by Almeida (2016), the most important phenomena take place in this region, so to capture them with greater precision, a mesh spaced geometrically in the radial direction was generated. Thus, the radial dimension of the elements increase at a constant rate one moves away from the well interface. In the vertical direction, a uniform spacing is used.

Regarding the dimensions of the domain, the vertical size is dictated by the lengths/depth of the salt layer. For the radial direction, many studies have been performed to determine the outer limit of the mesh that should be used so that the non-displacement approach is accurate. Almeida (2016) pointed out that a distance of about

10 internal radii is sufficient to model the creep of salt layers. In the present study, as a conservative measure, the non-displacement condition is applied at a distance of 100 radii, so longer times can be analyzed without worrying about wall effects being affected by this approach.

Since the salt creep and thermal meshes do not coincide with each other, interpolators are required to transfer information between the models. In the case of the thermal solver, it already returns its solution through interpolators, both for thermal information and for pressure fields. Thus, for both temperatures and pressures on the inner walls, the salt model will use the most recent solutions obtained during the iterations of mass convergence. On the other hand, as the FEM method consists of the application of large interpolators in the form of the shape functions, which are used to provide the displacements of the well wall to the thermal solver.

Once meshes and initial boundary conditions are initialized, the first step of the creep solver consists of calculating the initial displacement of the pure elastic deformation for the drilling scenario. Since this elastic displacement occurs instantly as the well is being drilled, creep does not affect it, so only the elastic contribution of the model is used, forcing the creep amplitude to remain equal to zero for the initial condition. This information is provided for the thermal solver and a new calculation for the initial mass of the system is performed to establish a new initial condition for the simulation.

Regarding the iterative procedure to obtain the solution, one can take advantage of the iterations of the mass conservation convergence. As the solution of the creep problem requires the solution of several depths simultaneously, it cannot be solved in a similar way to the well via a marching procedure. So the models were run one after the other, starting with the thermal system solution. Once the pressure and temperature fields are resolved for the entire well, the interpolators of these variables are used to compute the force vectors and assemble Equation 123 to be solved in the mechanical balance. In the first iteration, every time the creep model is called, it is checked whether the current step is large enough using the residual vector standard criterion. If in the first iteration, the norm of the residua is sufficiently small, the Newton algorithm flags the solution as converged and returns the input value for the deformation without further iterations. Otherwise, it is iterated by the Newton method until convergence is reached by the energy criterion. Once the convergence is achieved, the interpolators for the displacement of the wall will be provided for the thermal model for recalculation of the annulus cross section area.

The two models iterate until the mass conservation is achieved for each time interval. The annular pressure is updated with each iteration and the displacement interpolation will adjust accordingly.

Lastly, it should be mentioned that to model the temperature field within the

salt layer, there are two major approaches, one developed for the traditional (pseudo steady-state) model and another for the hybrid (thermal capacitance) model for the wellbore. In the former, Equation 7 is used to model the temperature in the integration nodes with the heat flow entering as one of the interpolated parameters of the well. In the latter, the transient profile of the wall itself is passed interpolated as a function of the Laplace time to apply the inversion using the transient formation model. This way, the consistency between the models is maintained, making it possible to maintain a reduced computational cost without having to solve the heat transfer again in the formation.

5 RESULTS

This chapter presents all the results of the simulations performed to validate and further evaluate the models developed. These results are separated based on the simulated geometries, *i.e.*, three real well geometries to test all aspects of the models. Each section contains the results corresponding to each well geometry with exception of the last one which discuss the results.

Some of the geometries are not ideal for testing both thermal models and the salt displacement model. Therefore, the first two sections will focus on the validation of the new Laplace based model, comparing its results with the traditional pseudo steady-state model as well as with commercial software for heat transfer in wells. In two of these cases, the results are also compared with field data in order to determine the applicability and significance of the models. This is also useful to further validate the new formulation used for determining the APB.

Finally, the last well of the chapter contains a real well geometry with a salt layer, and the results of the salt displacement model will be discussed there.

The last section contains a brief discussions of the main results found in the chapter.

As many comparisons of numerical performance of the proposed methods will be performed it is important to present the machine used in all simulations. In Every study presented a simple notebook equipped with an Intel i7-6700HQ processor with base clock at 2.60GHz and 16 GB of Ram was used. As by the nature of the problem, parallelism would be complicated to achieve with good performance, therefore, every individual simulation was performed with single thread.

5.1 VERTICAL WELL

The vertical well used for validating the mathematical models is the same shown by both Hafemann (2015) and Barcelos (2017). This well is under a sea depth of 1394 m and has only one production zone located between the depths of 4390 m to 4564 m. Being an almost vertical well (with very small deviations reported in the field data), no distinction is made between TVD and MD, and only the latter is reported in the figures. The complete geometry of the well, as well as the basic characteristics of the fluids are presented in Appendix B. Figure 29 describes the wellbore geometry and the surrounding lithology.

Figure 29 – Vertical well geometry

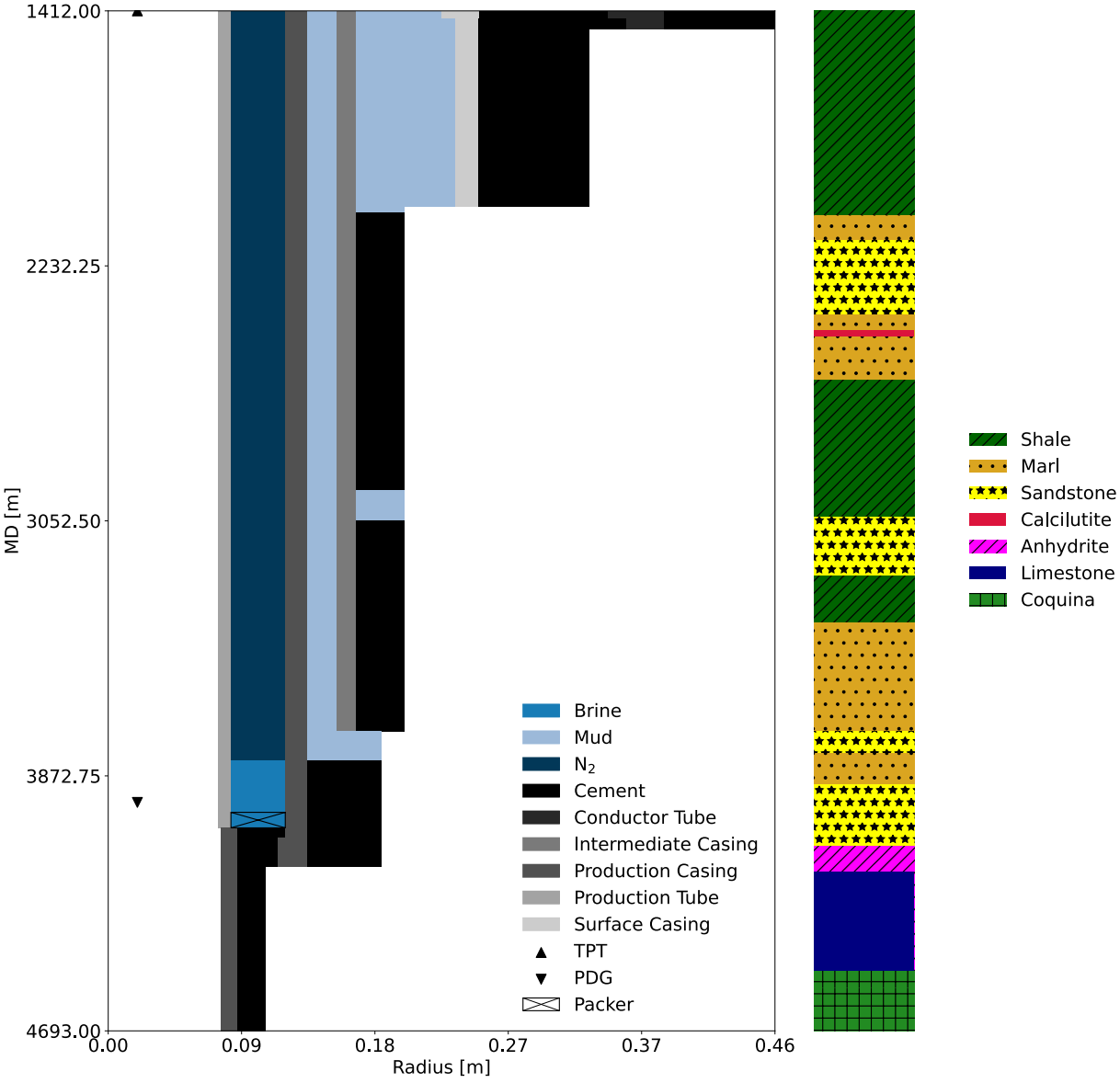

It is important to mention some characteristics of this wellbore that make the present study a little more complex. First, annulus A (the innermost annulus) is filled with two completion fluids, nitrogen and brine. This is so because of gas lift operations intended for that well. The presence of a gas significantly changes the behavior of APB, first because the gas is highly compressible, reducing the potential of a large scale APB. In addition, as the annular deformation models will change the cross section of this space, the interface level will move as a consequence. Another characteristic of this well is the presence of a *spacer fluid* separating two layers of cement, this is a volume of fluid that separates two cemented regions external to the intermediate casing. As this small region is isolated from the others, it behaves like an extra annulus, so the same APB modelling procedure is adopted.

In addition to these two characteristics, it should be noted that this well passes through a small layer of evaporitic rock (salt) in the form of anhydrite. As this layer is

cemented it will not be useful for applying the creep model, however, it still affects the thermal model marginally. It turns out that these types of rocks have greater thermal diffusivity than the other rocks, therefore, the geothermal gradient will suffer noticeable deviation in this region. In addition, higher heat transfer rates through these depths should be expected.

To confirm this statement about the geothermal gradient, Figure 30 presents the initial temperature profile of the well. This information was collected during drilling and will be the initial condition for the thermal simulation of this well.

Figure 30 – Geothermal profile of the vertical well

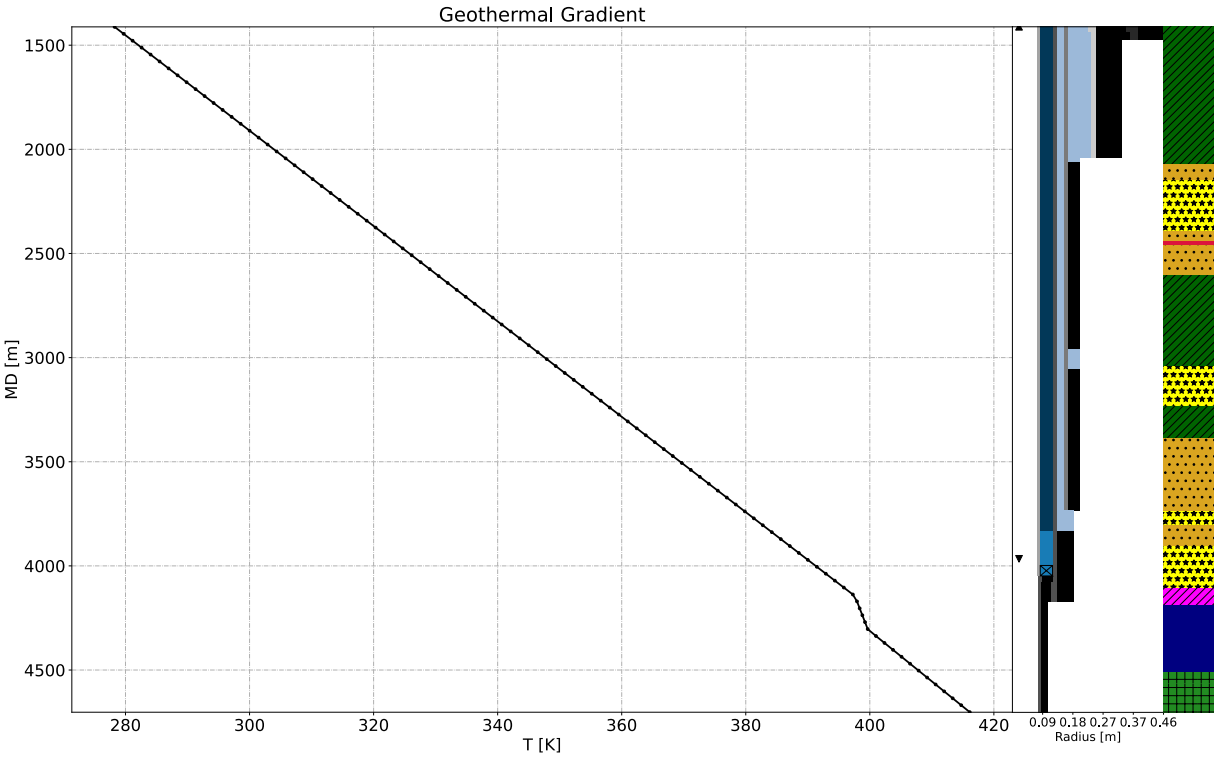

As can be seen, the initial temperature profile undergoes a noticeable deviation around the anhydrite. Below this region, the gradient returns to the initial value detected at shallower depths.

As this is the first well to be discussed in this chapter, it is important to highlight the importance of the lithological structure on the thermal results. Data on rock properties were obtained from several sources in the literature (FJAER et al., 2008; ALMEIDA, 2016; BARCELOS, 2017), so all properties used for all the wells are presented in a table at Appendix C.

Regarding the fluids that complete the annuli, in annulus A, as previously mentioned, there is both nitrogen and brine. Annulus B, C and SF are filled with drilling mud. To determine the thermophysical properties of these fluids, an approach similar to that of Barcelos (2017) was used, which consisted of adopting a compositional formulation based on the external software package (INFOCHEM/KBC, 2019). To reduce the com-

putational cost, the property package was run beforehand, and the calculated property data were were organized in the form of lookup tables for interpolation.

The drilling mud is the most complicated fluid to be modeled. As recommended by Barcelos (2017), it is assumed that its properties are similar to those of a 50% wt. glycerin/water solution. The brine is modeled as an aqueous solution of NaCl, with a mass fraction concentration that matches the density at standard condition (BOURGOYNE JR. et al., 1991). As for the produced oil, the molar composition is provided in Appendix B, which is used as an input to the property software package to generate the thermodynamic tables.

The input data for the model were obtained in a few different ways. First for the pressure and temperature data, sensors kept inside the well, either PDG, TPT or PT, were used. From these meters, instantaneous values are known throughout the production time. On the other hand, the flow data are known only as averages over time, especially for the time interval used for the study. Therefore, for the flow, a single, constant value will be assumed.

In order to validate the models, it is still necessary to explain some limitations faced due to the production history. Figure 31 shows the data provided by TPT throughout the production. It is clear that this well goes through many short production intervals, something that complicates the analysis using the pseudo steady-state model. Because of this, the region selected for the previous studies is the one highlighted in red (BARCELOS, 2017). This is far from ideal from a thermal modeling point of view because, as the well has been in production for more than 90 days, the formation is likely to be already heated, which can certainly influence the final results. This aspect must be taken into account when comparing the models.

Figure 31 – TPT data since start of production

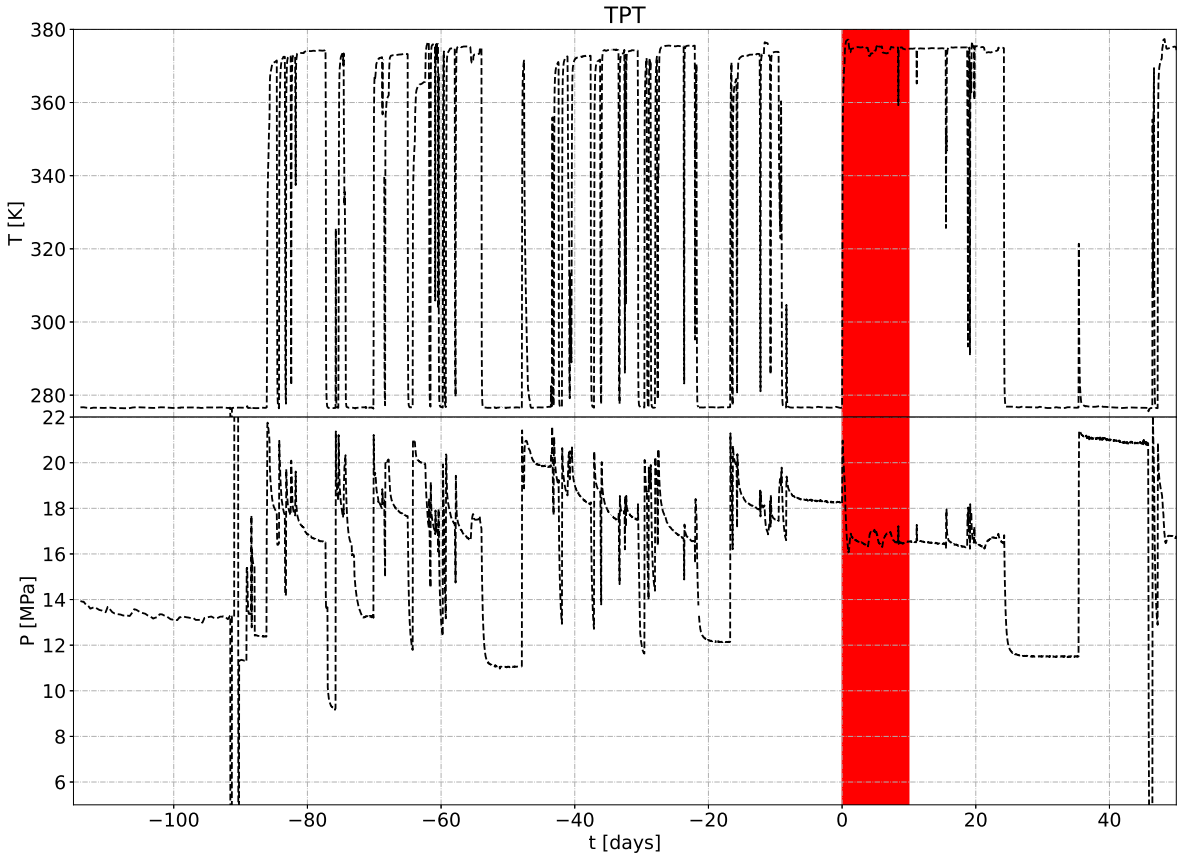

Other important sensors are located at the PDG, situated at a depth of 3958.15 m to measure the pressure and temperature inside the production column. The data of this meter remain restricted to a smaller period of time, indicating measurement failure in other instants. Thus, Figure 32 presents the data from the PDG with the region marked representing the 10 days interval used for the simulations.

Figure 32 – PDG data for vertical well

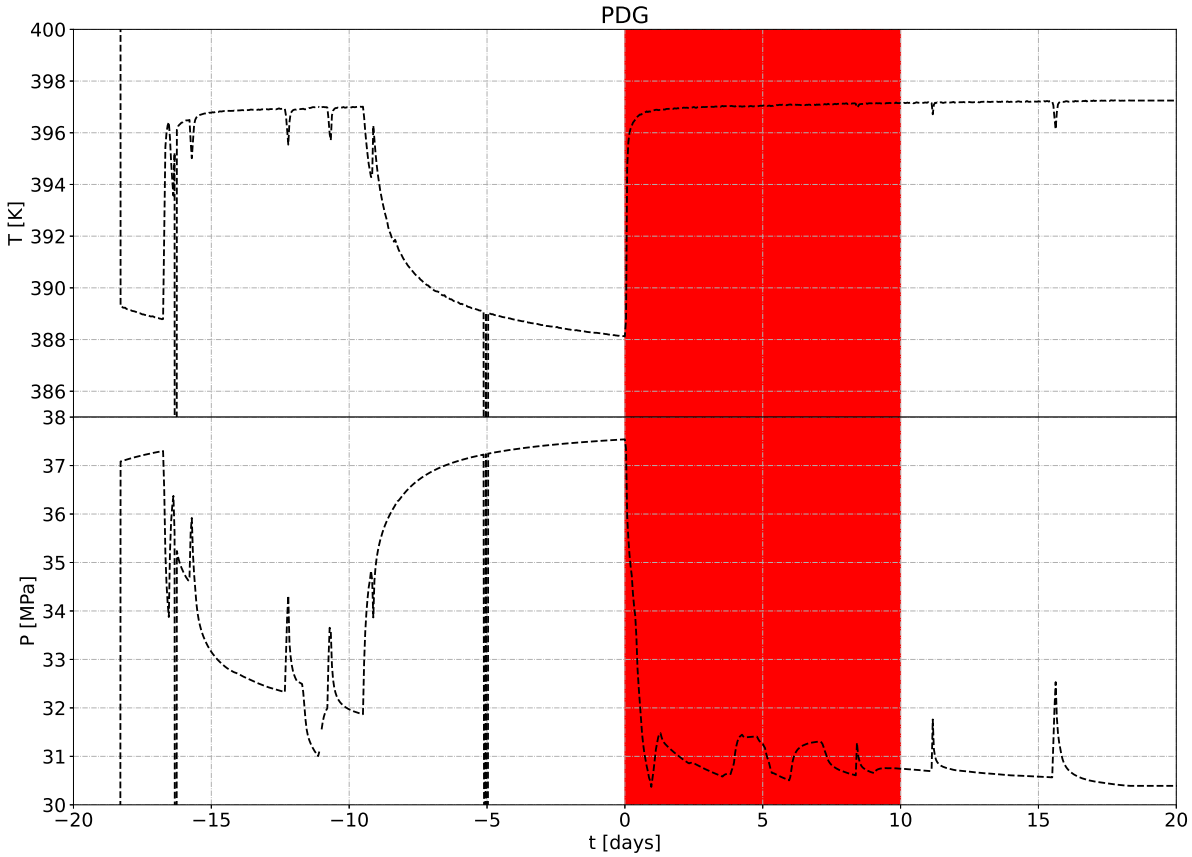

Figure 32 corroborates the idea that all the production intervals prior to the 10-day window (red zone) still affect this new “start” of the well. This is justified by the fact that the temperature profile has not stabilized at the geothermal gradient after a period of approximately 10 days without production ($t = -10$ to 0 days). Thus, it is reasonable to assume that, when the new flow restarts, the production fluid flow will cross regions that are still warm. Because of this, the results obtained when simulating shorter production times should be treated as approximations and will probably have a slower response than the field data.

Figure 33 represents the region of study (10-day window) and the input data (at the PDG) for the thermal model. The time intervals are spaced every 6 hours starting from the point defined as 0 hours of production. This starting point comprises the first point in the production region to register a pressure fluctuation in the PDG meter. This interval will continue until 10 days of production are completed, thus having a region that includes the transition to pseudo steady-state in the annuli. The symbols are the actual input data points used in the simulation. Their values were calculated by interpolating the data measured in the field.

Figure 33 – PDG inputs for models: pressure and temperature as a function of time for a production time of 10 days.

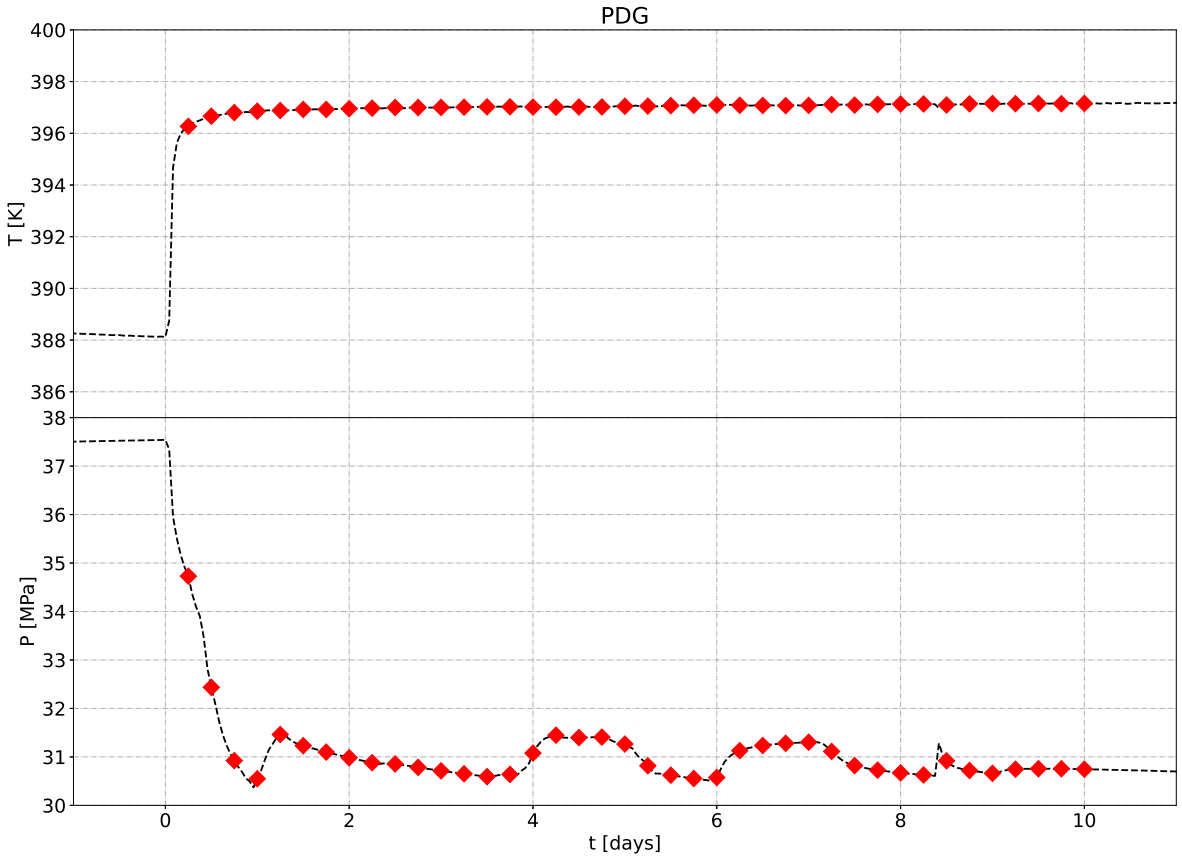

Regarding the hydrodynamic model, a constant flow rate of 1501 $m^3\,d^{-1}$ is assumed, which represents an average for the production region. In addition, a GLR of 211 $m^3\,m^{-3}$ is assumed. The Beggs and Brill (1973) correlation was used to model the multiphase flow within the production column. As for the wellbore heat transfer, for comparison purposes, the time function of Hasan and Kabir (1991) was used.

Before discussing the results, a brief verification of the convergence of the Laplace method as a function of the number of nodes used in the inversion algorithm is presented. Using the input parameters discussed above, for a simulated production time of 6 hours, the APB calculated in the three annuli are compared to check their convergence. The criterion used to determine if the number of nodes is sufficient is to double the number of nodes and check the absolute relative deviation from the previous test. The number of nodes is considered suitable if the relative deviation from the previous test for all annuli is lower than 1%. Figure 34 shows the results of this test, demonstrating that the convergence is already reached with 16 nodes in the CME inversion method.

Figure 34 – Convergence test for Laplace model in the Vertical well (production time of 6 h)

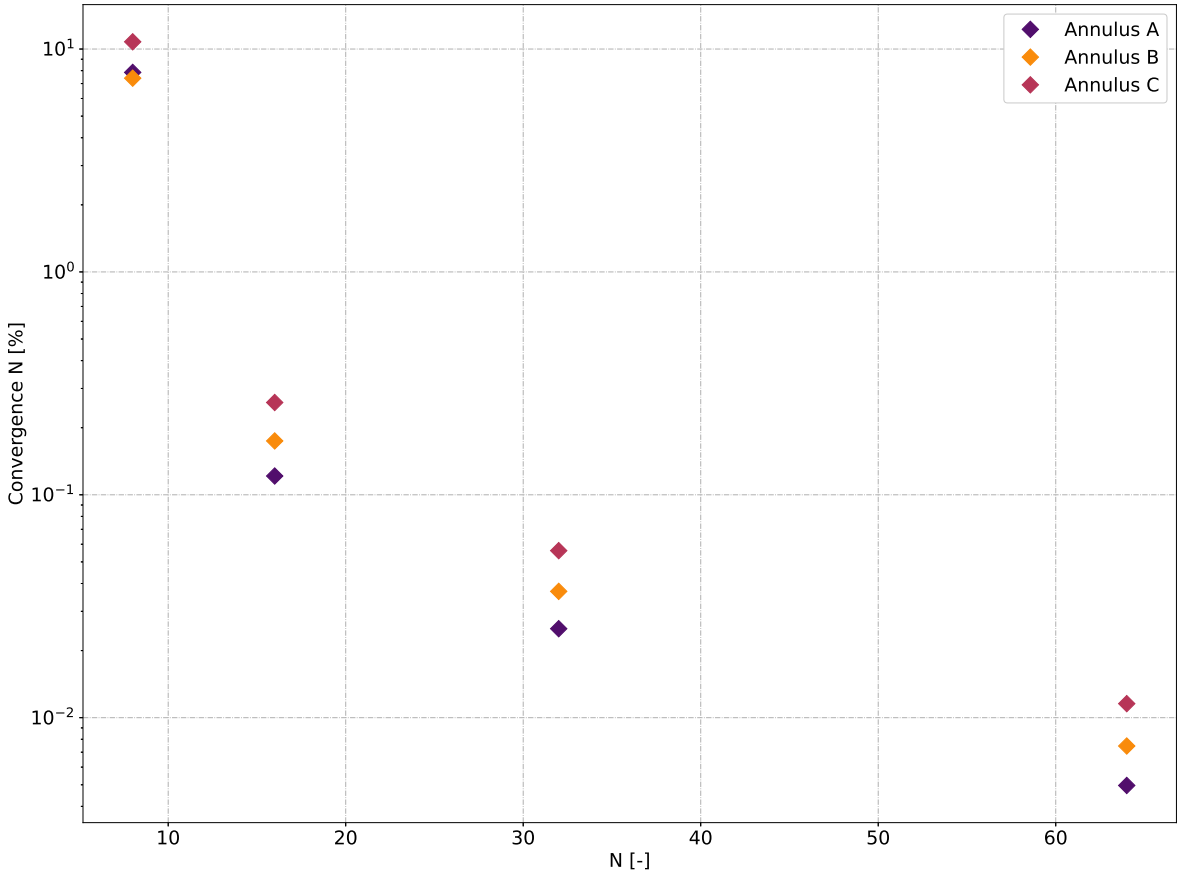

The number of 16 nodes means that the thermal systems must be solved 16 times for each point in the Z direction (marching procedure), resulting in a somewhat higher computational cost. The standard pseudo steady-state model runs the 6-hour production simulation in 6 seconds, while the Laplace model increases this time to 16 seconds. Although it is almost 3 times slower, the overall computational cost of the hybrid Laplace method cannot be considered high (in absolute terms), especially when the extra information added to the solution is taken into account. So, for the remainder of this section, 16 nodes are considered as the ideal precision for the simulation.

5.1.1 Validation of the Laplace model

With the number of nodes in the inversion algorithm properly determined, it is possible to evaluate the performance of the models with respect to the field data. For a production time of 10 days, using the same input data as before, both models (pseudo steady-state and Hybrid Laplace) numerically converged for all 40 simulated intervals. Figure 35 shows a comparison between the field data and thermal models in terms of the temperature and pressure at the TPT.

Figure 35 – Comparison of temperature and pressure from proposed models and field data at TPT

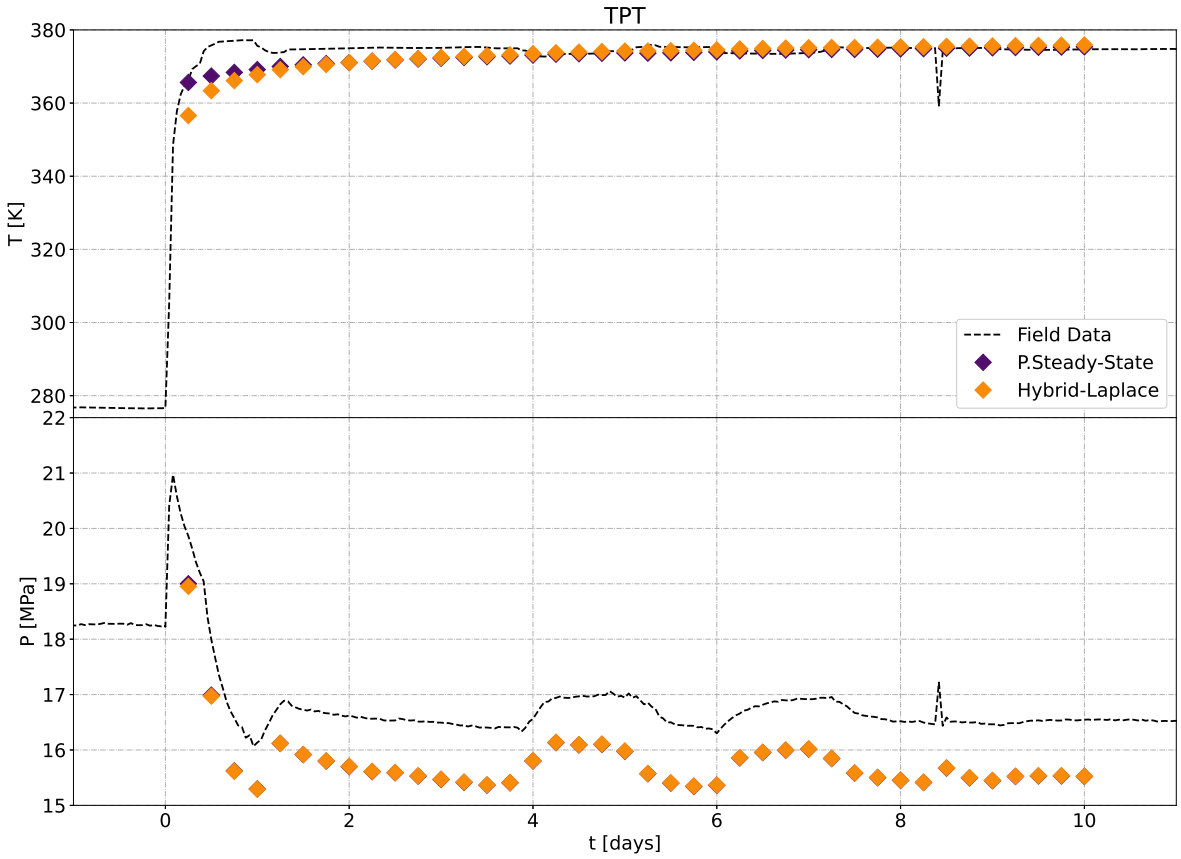

Both models provide a good fit of the field data and, for the wellhead temperature, two phenomena described previously were actually observed. The heating of the fluid occurred very quickly, something that seems to indicate that the annuli were still warm at the beginning of the simulation. In addition, as a characteristic of the models, the Laplace model heats up more slowly when compared to the traditional pseudo steady-state model. Note that the fluctuations of the bottom-hole pressure are almost directly transported to the wellhead.

Figure 36 shows the numerical deviation with respect to the field data, so it is easier to visualize in which regions each model performs better.

Figure 36 – Deviations from TPT temperature and pressure and predicted results from simulations

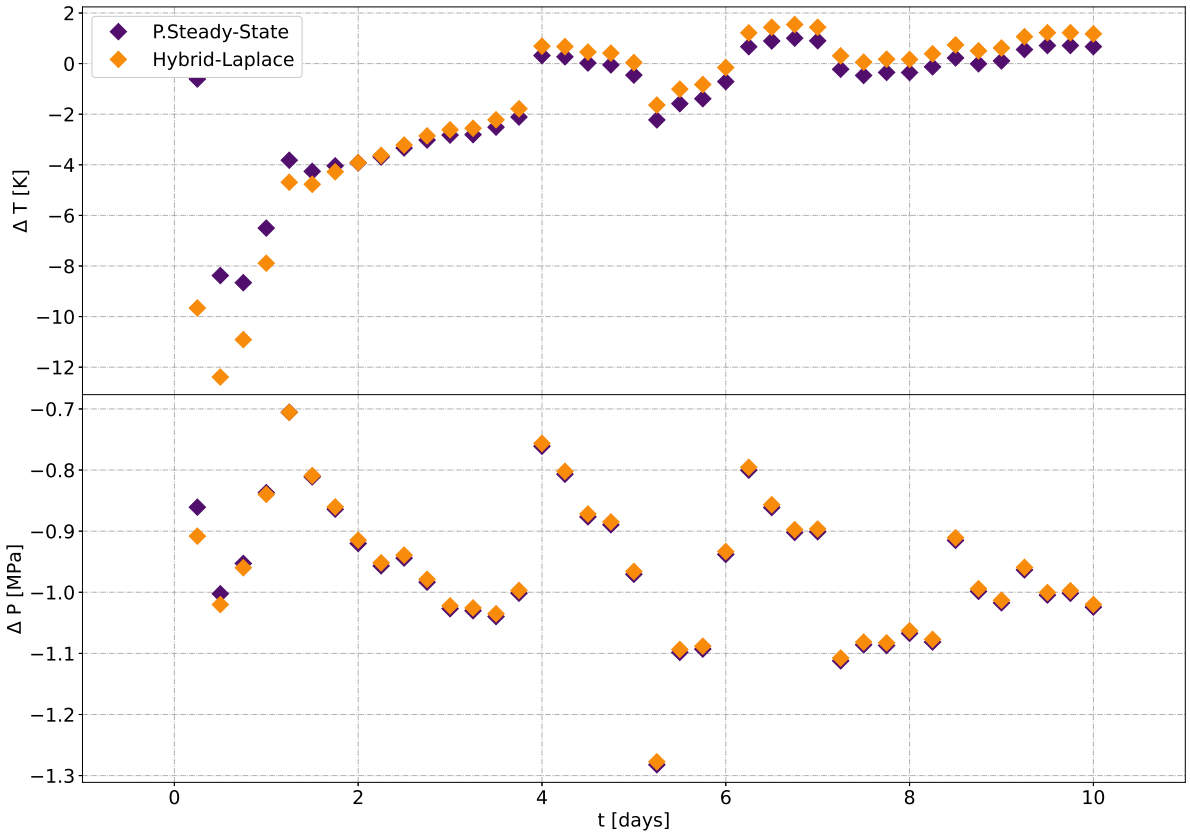

This figure shows that both models perform in a very similar manner. After a poor start, especially the Laplace model, which deviates by 12.38 K at 12 hours of production, the differences fall quickly, fluctuating around 2 K for production times greater than 3 days. As for the pressure behavior, although the trend is well picked up, there seems to be a more or less fixed bias of around 1 MPa with respect to the field data, which can be explained by the choice of correlations for the multiphase flow frictional pressure gradient and liquid holdup.

After 10 days of production, both models achieve good accuracy when compared with the field data, with the pseudo steady-state model having a deviation of 0.67 K, while the Hybrid-Laplace model differs from the field data within 1.17 K. This result alone may point to a greater accuracy of the standard model. However, it is important to consider that there are many unknowns which could lead to imprecise results, so it is not possible to determine only by these results which model captures better the wellbore thermal behavior of heat.

A simple statistical analysis can be performed to provide the magnitude of the deviations expected for each model. Figure 37 presents the Absolute Average Deviation from the the field data. It shows the same trend detected before, both models have

great accuracy when compared to the field data, with the standard pseudo steady-state model appearing to outperform the Laplace model by a small margin. Note that this result point to a good accuracy, providing expected deviations of less than 1% (in relation to the average temperature of the TPT, this corresponds to approximately 3.7 K) for the wellhead temperatures and 6% in the wellhead pressures.

Figure 37 – Average Absolute Deviation from simulations and TPT data for vertical well

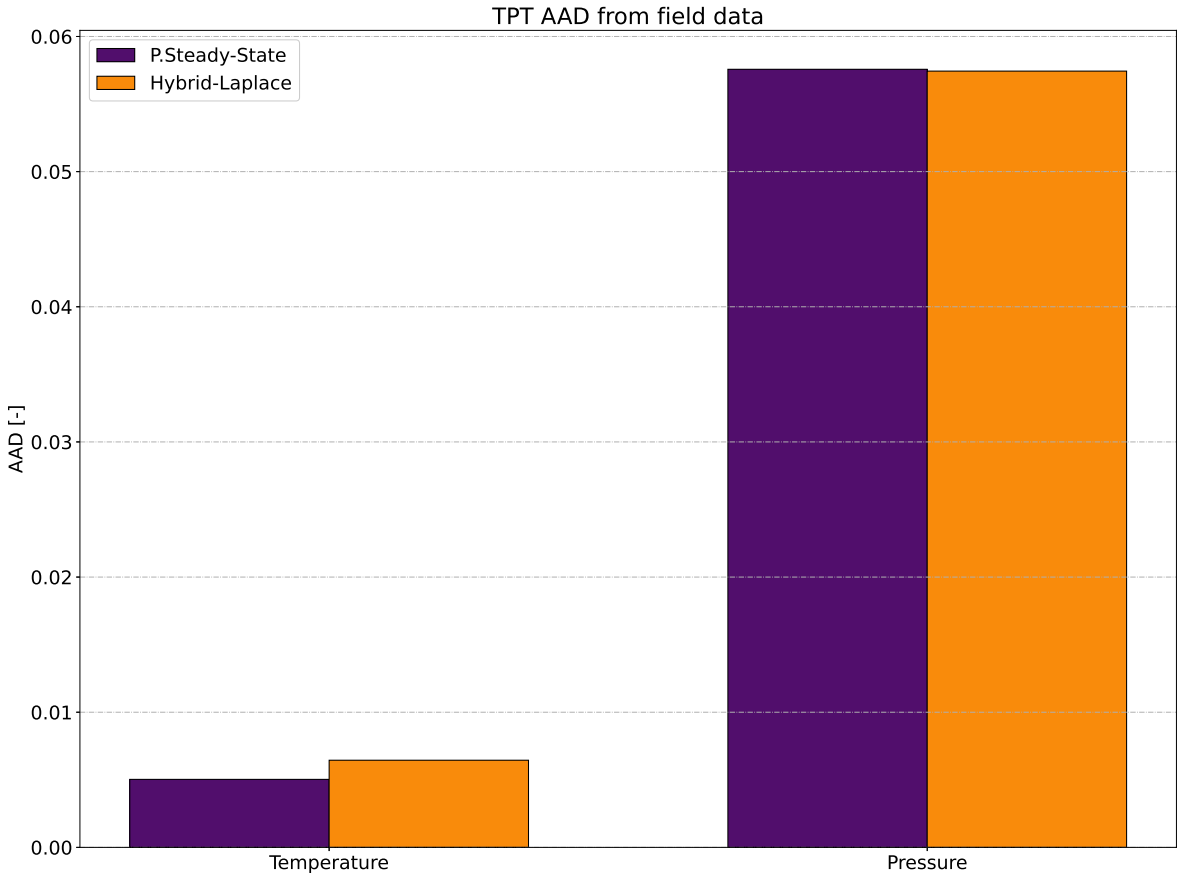

Up to this point, the results presented refer to the TPT located at the wellhead. To better understand the behavior of both models when predicting the heat transfer in wells, it is important to compare the temperature profiles predicted by the models. By doing so, it may be possible to find explanations for the behavior observed previously. For that, Figure 38 shows the temperature profile in the vertical well for 6 hours of production. Additionally, Figure 39 shows the profile for 1 day of production. At this point, the models are expected to present closer results than at 6 hours since, for longer times, the Hybrid-Laplace model should converge to the standard, pseudo steady-state, model.

Figure 38 – Temperature profile predicted by heat transfer models for 6 hours of production

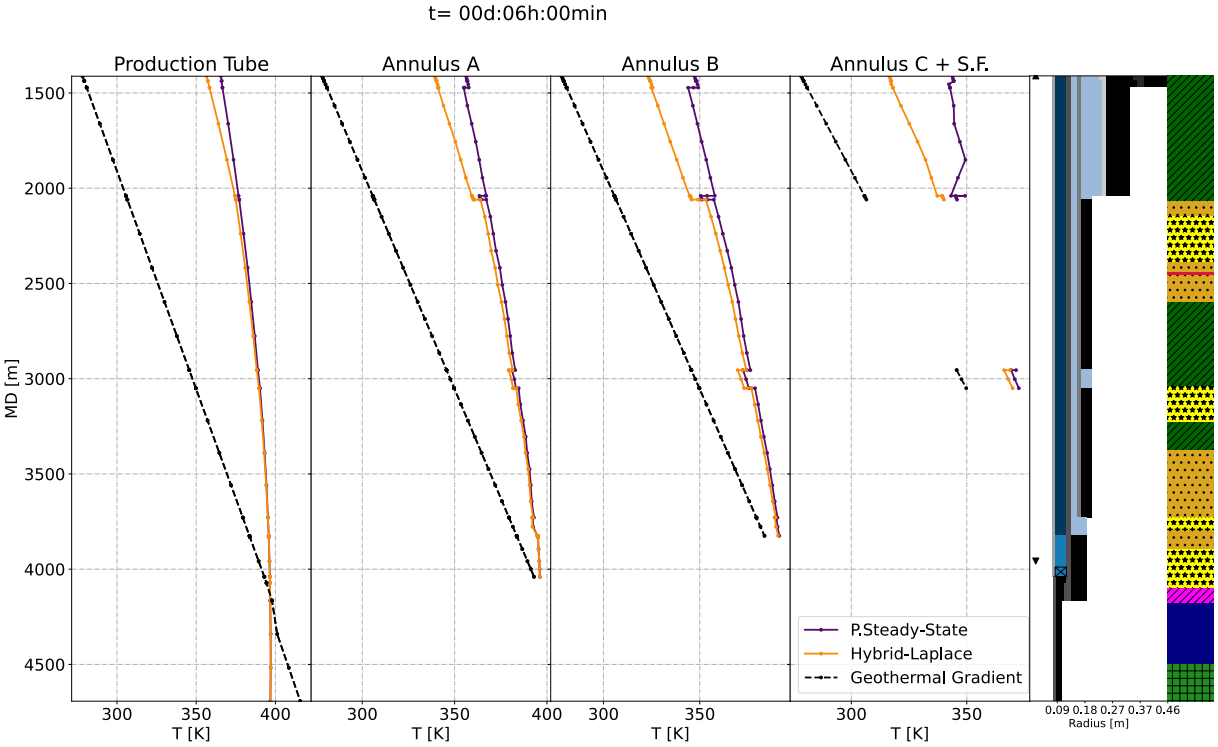

Figure 39 – Temperature profile predicted by heat transfer models for one day of production

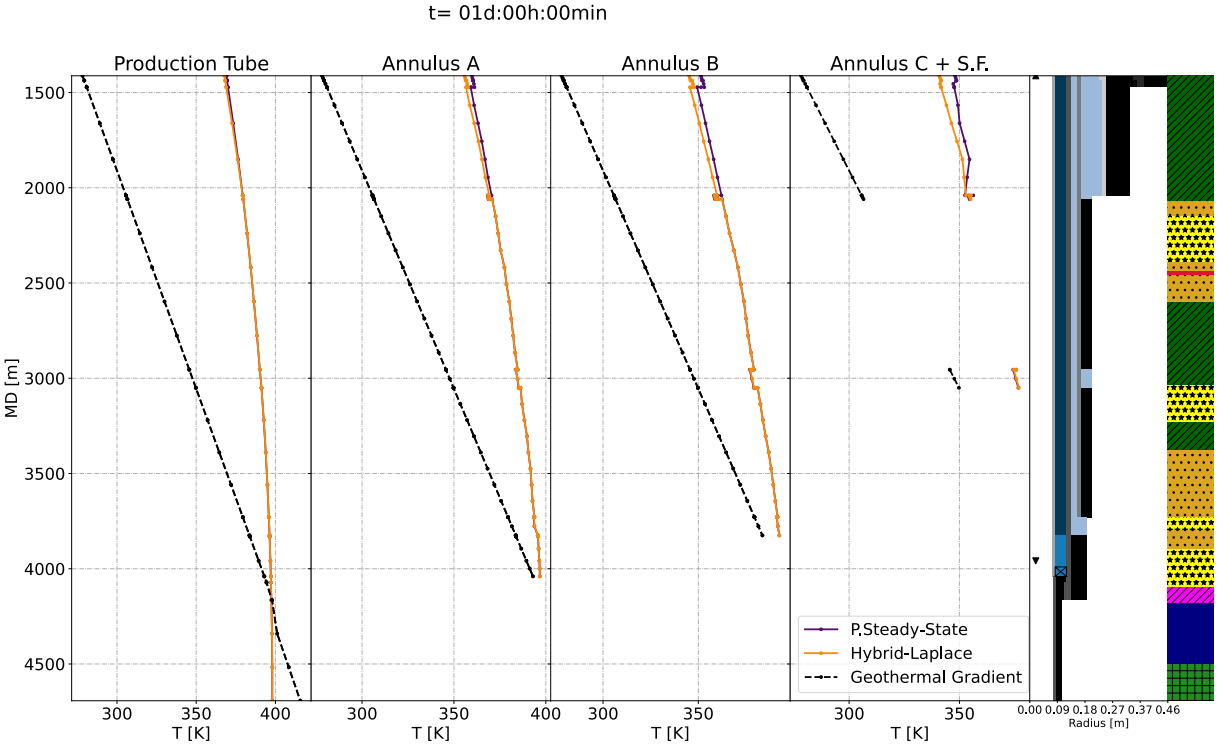

By comparing these two figures, some important points become clear. First, since both models are essentially one-dimensional, changes in material properties or

the presence of shallower annuli are registered in the form of discontinuities of the temperature profiles. Another important aspect is the high influence of cementation on thermal resistance systems. As the cement has a low thermal conductivity, the heat transfer is minimized in the layers adjacent to them. This effect becomes even more prominent when analyzing the region between 2955 m and 3050 m, that is, the region containing the Spacer Fluid. The presence of this fluid layer drastically affects the other annuli.

Comparing the models, a greater difference in temperature is noticeable for the time of 6 hours, and this difference is felt more strongly in the outermost annuli. Such behavior is consistent with the nature of the problem since the heat source is the fluid that flows inside the well, so it is to be expected that the outer annuli take longer to heat up. Table 4 shows the difference between the average temperatures of the models for each annulus at different simulation times.

Table 4 – Average temperature difference predicted from pseudo steady-state and Hybrid-Laplace at each annulus for certain simulated times

	Annulus A	Annulus B	Annulus C	Spacer Fluid
6 hours	4.65K	8.09K	18.83K	2.79K
1 day	0.72K	1.37K	3.96K	-0.21K
5 days	-0.30K	-0.44K	-0.44K	-0.69K
10 days	-0.32K	-0.52K	-0.82K	-0.57K

Table 4 also shows that, already for a production time of one day, the annulus closest to the production column already responds quite similarly for the Laplace model and the pseudo steady-state model. Furthermore, it is confirmed that, for real geometries, the Laplace model achieves higher temperatures than the traditional model.

Figure 40 – Total heat loss from produced fluid in the vertical well for both proposed models

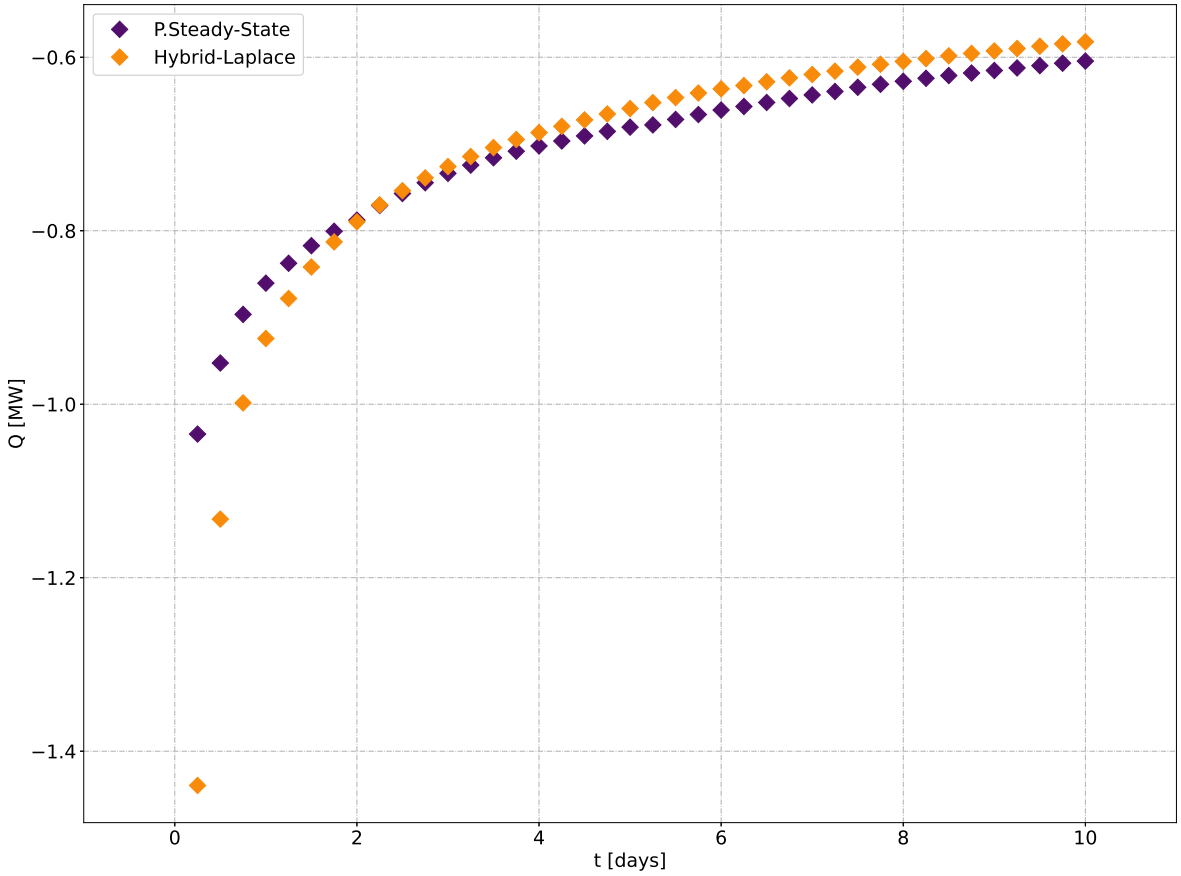

Figure 40 offers a possible explanation for this phenomenon of higher temperatures predicted by the Laplace model, as it shows the total heat transfer rate from the flowing fluid to the producing tube. This transfer rate is calculated as the integral of the heat transfer rate per unit of length in the vertical direction. As can be seen, the heat transfer between the models starts with a difference of 0.40 MW, approximately 40%.

Unlike the pseudo steady-state model, the Laplace model carries some temporal information about the heat transfer. Thus, although it starts with a slower temperature growth in the annuli, the formation responds more quickly than the pseudo steady-state model. This is due to the higher heat transfer rates at the initial moments of production. Thus, the formation undergoes a greater temperature increase for the same simulated time, which leads to a greater temperature increase in the annulus.

Figure 41 shows the temperature profile for 10 days of production. It becomes evident that both models give very close results in all regions of the wellbore. This is promising because it demonstrates consistency at longer times, when capacitance effects in the wellbore are less important, and the pseudo steady-state model is known to provide accurate results.

Figure 41 – Temperature profiles in the vertical well after 10 days of production

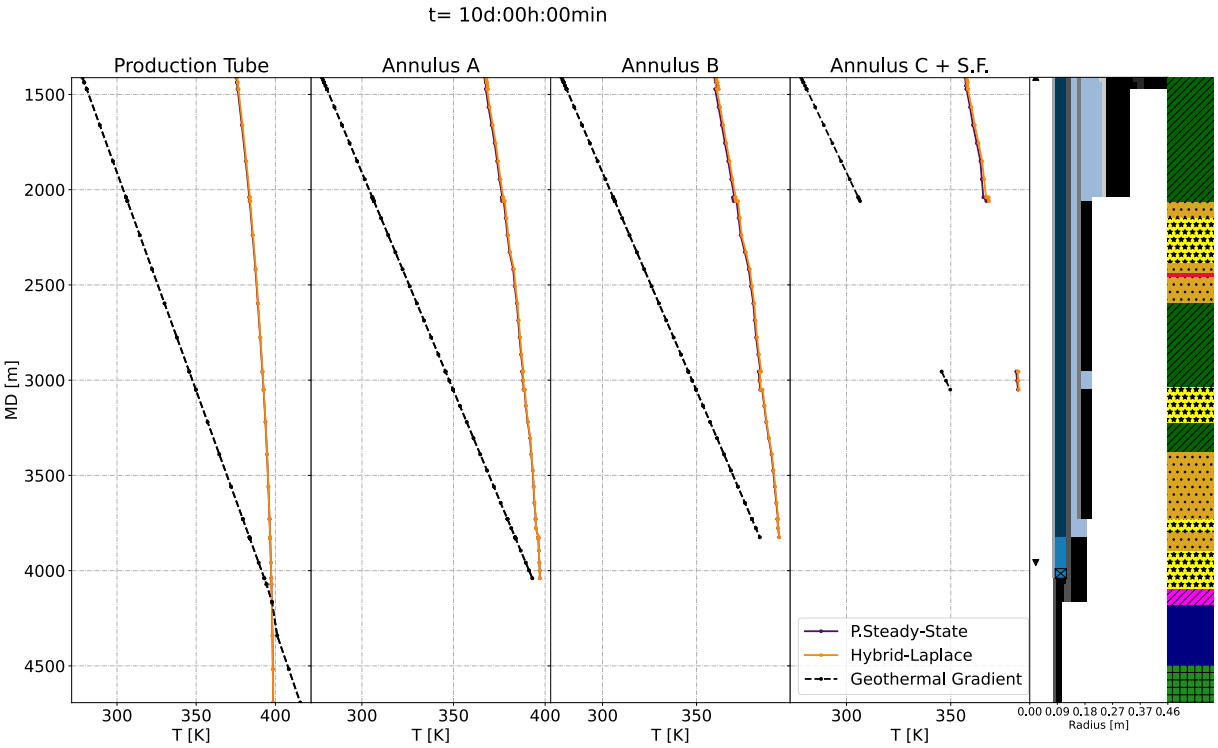

Despite the similar temperature profiles, the different heating curves exhibited by each model directly affect the behavior of the fluid pressure inside each annulus and, hence, the APB. As explained in Section 2.7.3.2, the reported value of the APB corresponds to the highest value of the APB temporal profile for a given annulus. In addition, it is calculated taking the initial hydrostatic pressure in each annulus as a reference (since the APB is, effectively, a pressure difference). For annulus A, due to the presence of N_2 pressurizing the internal volume, the reference is the wellhead pressure at the end of the well completion. Thus, the initial pressure of annulus A is calculated using the hydrostatic column, starting from a prescribed value at the wellhead obtained from the completion report of the well (3200 psi or 22.06 MPa).

Figure 42 – APB predicted with pseudo steady-state and Hybrid-Laplace for vertical well

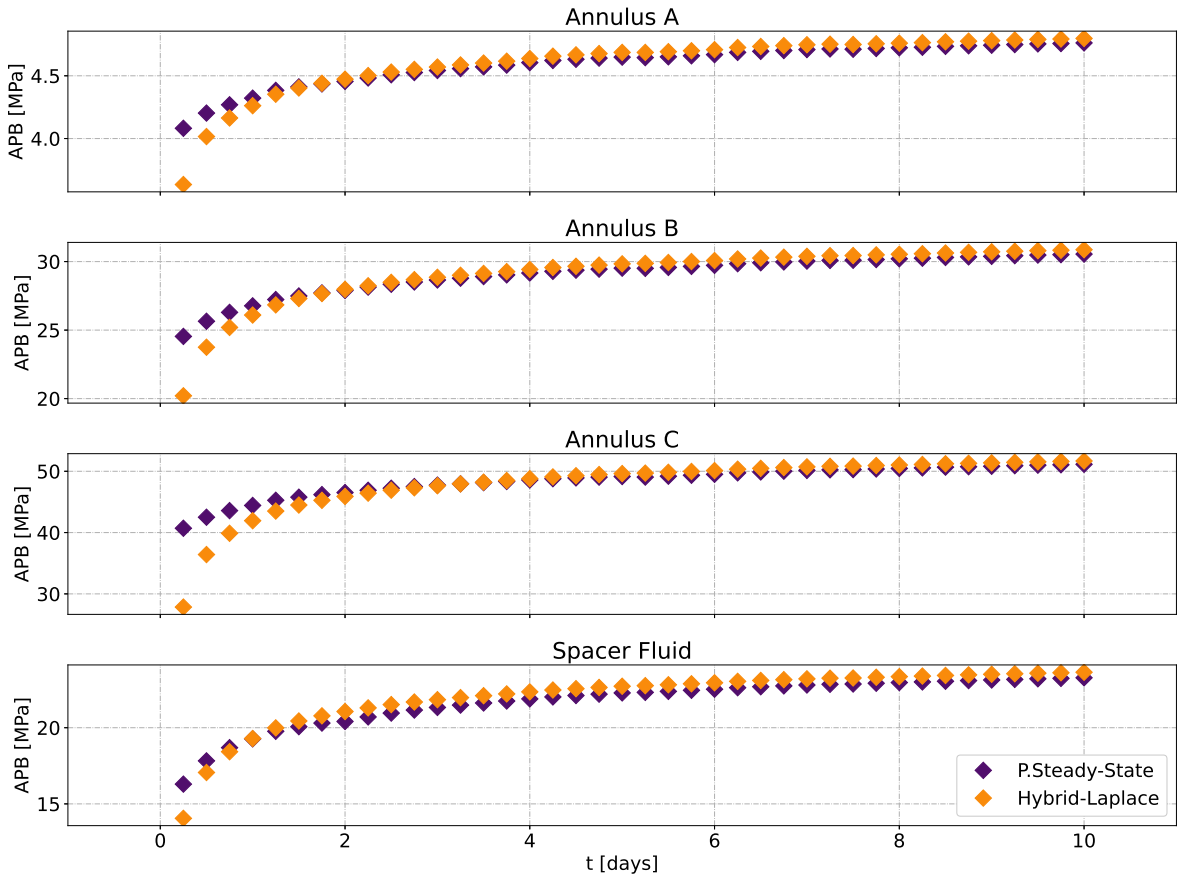

Figure 42 shows the evolution of the APB at each annulus according to both models. As expected, the APB increases faster for the pseudo steady-state model, a phenomenon that is more noticeable in annular C because it is the furthest away from the well. This difference in APB reaches 12.86 MPa at 6 hours in annulus C. The figure also shows that the presence of N_2 in annular A causes the APB to be much smaller than in the other annuli. In addition, because the Spacer Fluid is located at a greater depth, it undergoes less heating and therefore has an APB smaller than annulus A and B.

Figure 43 presents the APB predictions by both models compared with the pressure field data gathered by the PT located at the wellhead of annulus A.

Figure 43 – Comparison of pressure at the top of Annulus A from field data and numerical models for the vertical well

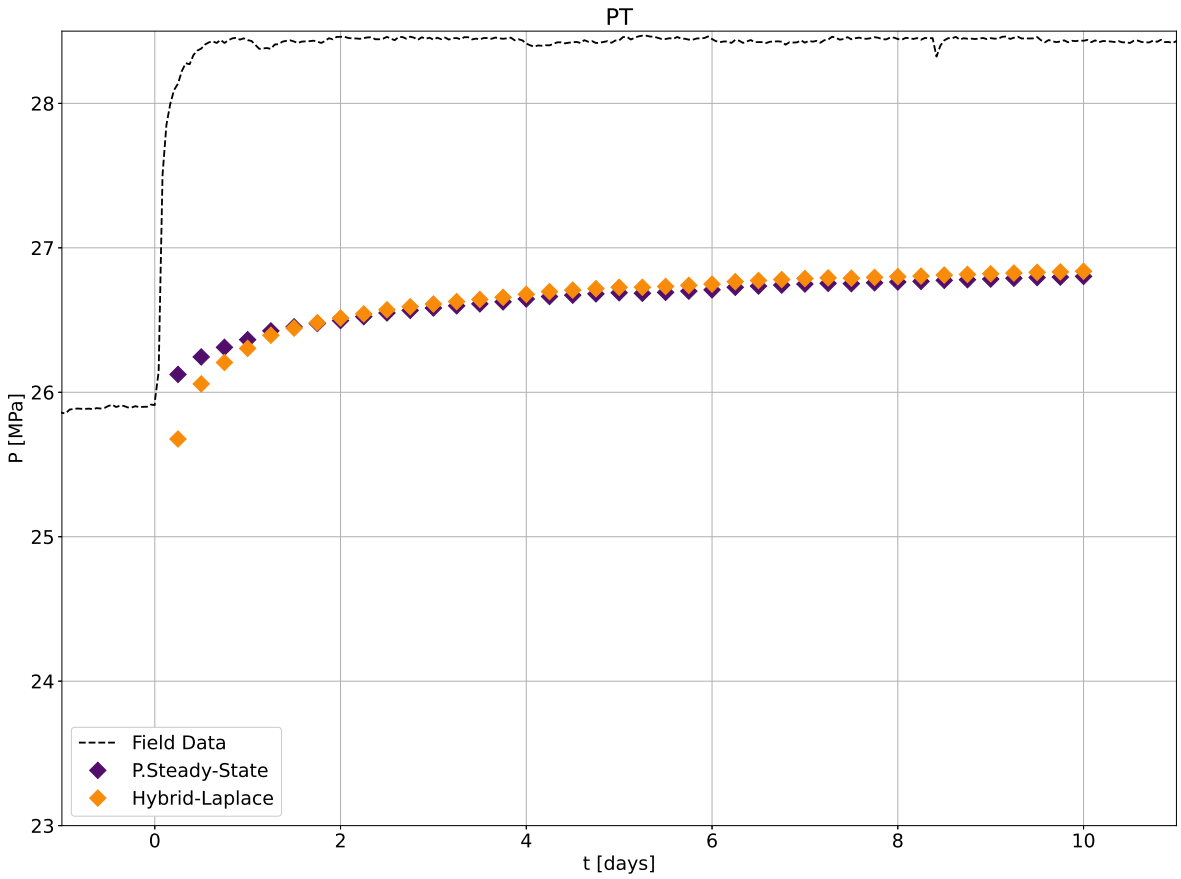

Clearly, both models show considerable deviations with respect to the final pressure of the annulus. Nevertheless, this may have more to do with the initial condition obtained from the completion report (22.06 MPa or 3200 psi) and with the fact that the well spent a lot of time in production than with the poor performance of the models.

Thus, one possibility would be to try to determine the initial condition based on the values measured at the sensor, which differs from the value in the completion report. Once this is done, the field data for APB is taken from the difference of pressure measured from this new reference state. Using the provided field data, the APB for Annulus A is estimated to be around 5.9 MPa at the 10^{th} day of production. Both proposed models predict lower values for the increase in pressure, with the pseudo steady-state predicting 4.76 MPa and the Hybrid-Laplace 4.80 MPa.

One possible explanation for such behavior is the fact that the program does not consider initial deformations, as mentioned in Section 2.3. This makes sense since the temperature predictions are in good agreement with the field data. Since annulus A is filled with N_2, the outer annuli would compress it reducing the total volume and increasing the potential for APB. Adding this term to the program used would require great effort and since this is not the focus of this work, it will be left as a recommendation

for future works.

In the method adopted for computing APB (using the mass conservation), it is not possible to estimate the individual contributions of each term in the pressure increase, as was done in Barcelos (2017). However, it is possible to verify the behavior of the volume variation and analyse how it is affected by the heating of the annuli. Figure 44 presents this variation for each annulus.

Figure 44 – Variation in volume predicted at each annulus during production for vertical well

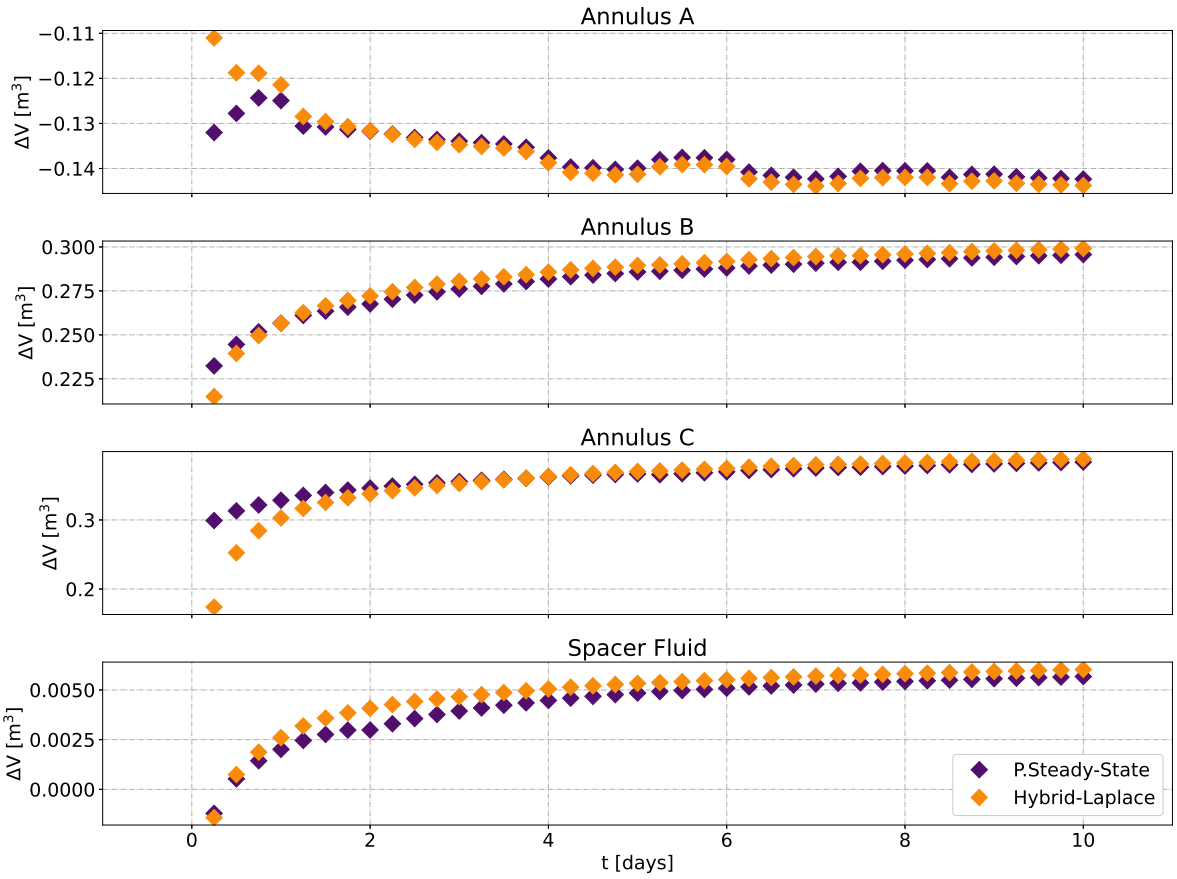

The initial volume of each annulus was 63.26 m^3 for annulus A, 48.27 m^3 for annulus B, 55.38 m^3 for annulus C and there are 3.71 m^3 of Spacer Fluid. As can be seen, the volume variation in annuli B, C and the Spacer Fluid increases with the heating. Meanwhile, for annulus A, due to the presence of the compressible N_2, the volume of the annulus decrease as a consequence of the expansion of annulus B. Also, as the increase in pressure is smaller in this annulus, it is possible to perceive that variations in pressure of the production string are being felt in the volume of the first annulus, up to the point that the behavior of the volume variation is similar to the pressure in Figure 33.

As demonstrated in Hafemann (2015) and confirmed later in Barcelos (2017), the deformation model of Halal and Mitchell (1994) has a strong connection to the

heat transfer solution resulting from the thermal expansion of solid materials. Thus, an important analysis for the Laplace model will be to compare the strain of the casing walls with the pseudo steady-state model. Thus, Figure 45 shows the strain of annulus walls for the time 6 hours.

Figure 45 – Strain profile predicted by both models for vertical well at 6 hours of production

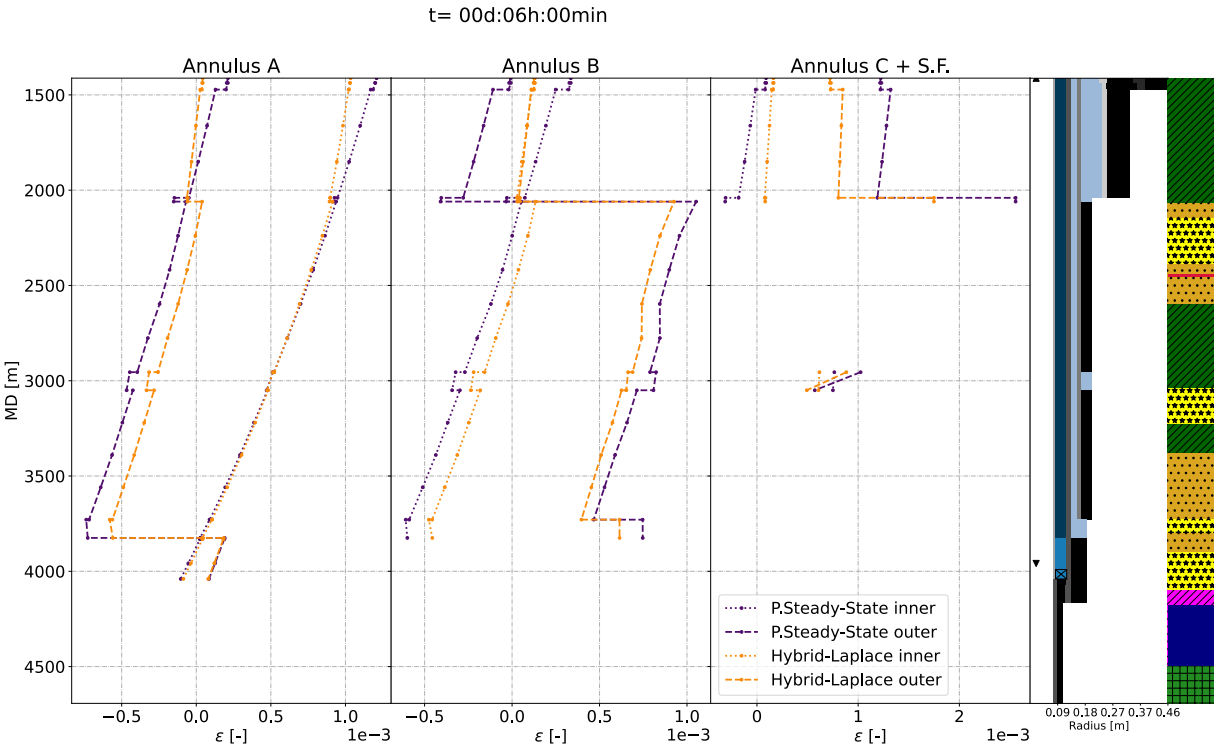

Figure 45 confirms the idea that the strain is closely linked to the heat flow that passes through each layer. A very interesting result that is noticeable in this figure is the presence of the capacitance terms acting on annulus A, where strains of the external interface of the production tube are quite similar when comparing the two models but, on the other hand, the strain of the inner wall of the production casing behave differently. The magnitude of the strain is not as intense for the Laplace model when compared to the pseudo steady-state model. This difference becomes even more pronounced in the other annuli, where the capacitances are more significant. Figure 46 shows these same strains after 10 days of production. Here, as the thermal results for each model get closer, the strains also follow the same trend.

Figure 46 – Strain profiles predicted by both models for vertical well at 10 days of production

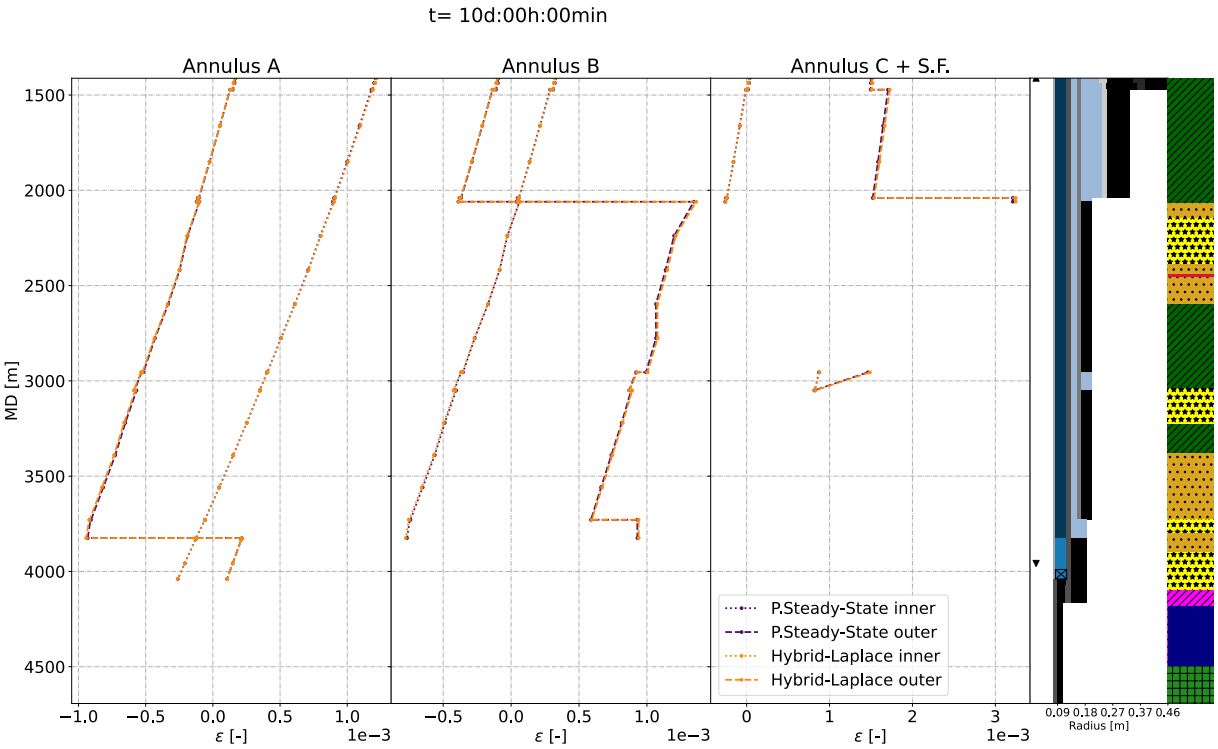

According to the API standards, the maximum strain limit of a given tube is 5% (ENGINEERING, 1983), so it is clear from both figures that the casings do not appear to be in a hazardous condition. For there to be certainty about this, a study for longer times should be carried out to contemplate greater increases in temperature and pressure, however, at first these casings do not present a risk of collapse.

Based on the models presented so far, it is clear that the Laplace model has the ability to at least respond as well as traditional models of heat transfer in wells, keeping computational cost low and including new capacitive terms to try to model shorter times better. However, there is still significant uncertainty associated with the inputs used for the simulation. Barcelos (2017) performed studies to estimate this uncertainties, but there are still some topics which could be further investigated. Thus, the aim of the following section is to address the uncertainties associated with both the time simulated and the oil flow rate used.

5.1.2 Sensitivity analysis

To evaluate the effect of the production flow rate on the thermal model results, the same 10 days of production were used with both models, varying the production flow rate up to 60% in relation to the default case. Thus, the temperature results at the wellhead are compared at different times for both models.

Figure 47 shows the impact of the hydrocarbon flow rate on wellhead temperature for the pseudo steady-state model. It demonstrates that even small variations in

flow rates, around 5%, would result in changes of wellhead temperature of 1 K. This already raises the question that a different flow rate could lead to a finer adjustment in relation to the field data. Furthermore, something interesting to note here is that for shorter times the flow effects will be more drastic than for longer times. This is so because for longer times the formation will be approaching equilibrium with the well, reducing the contribution of the flow to the heat transfer. Another interesting aspect is that the flow reduction seems to affect heat transfer more than its increase.

Figure 47 – Wellhead temperature sensitivity to the flow rate for the pseudo steady-state model in the vertical well at specific times

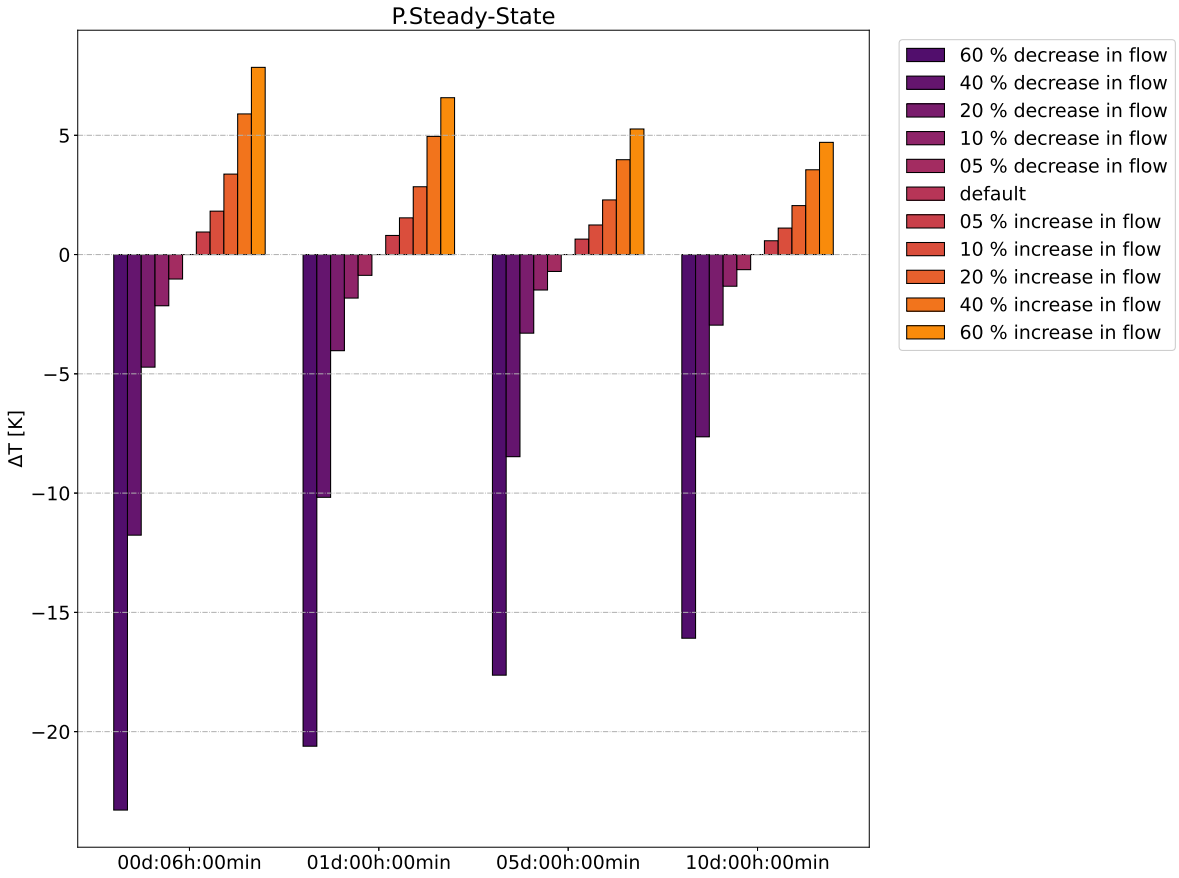

On the other hand, Figure 48 presents the same analysis by applying the flow variation to the Laplace model, thus allowing a comparison of which model would be more sensitive to the effects of flow inaccuracies. It demonstrates that the temperature behavior in the wellhead follows the same pattern perceived for the pseudo steady-state model. However, the effect seems to be potentiated, especially for shorter times. A 5% variation of the flow rate can lead to a variation of 1.5 K, going so far as to vary more than 28 K for a 60% reduction in flow, this variation seems to be affected by flow reduction more than the increase. In terms of agreement for longer times, the effects of flow rate becomes similar for both models reaching differences between the models as low as 0.1 K for a period of 10 days.

Figure 48 – Wellhead temperature sensitivity to the flow rate for the Hybrid-Laplace model in the vertical well at specific times

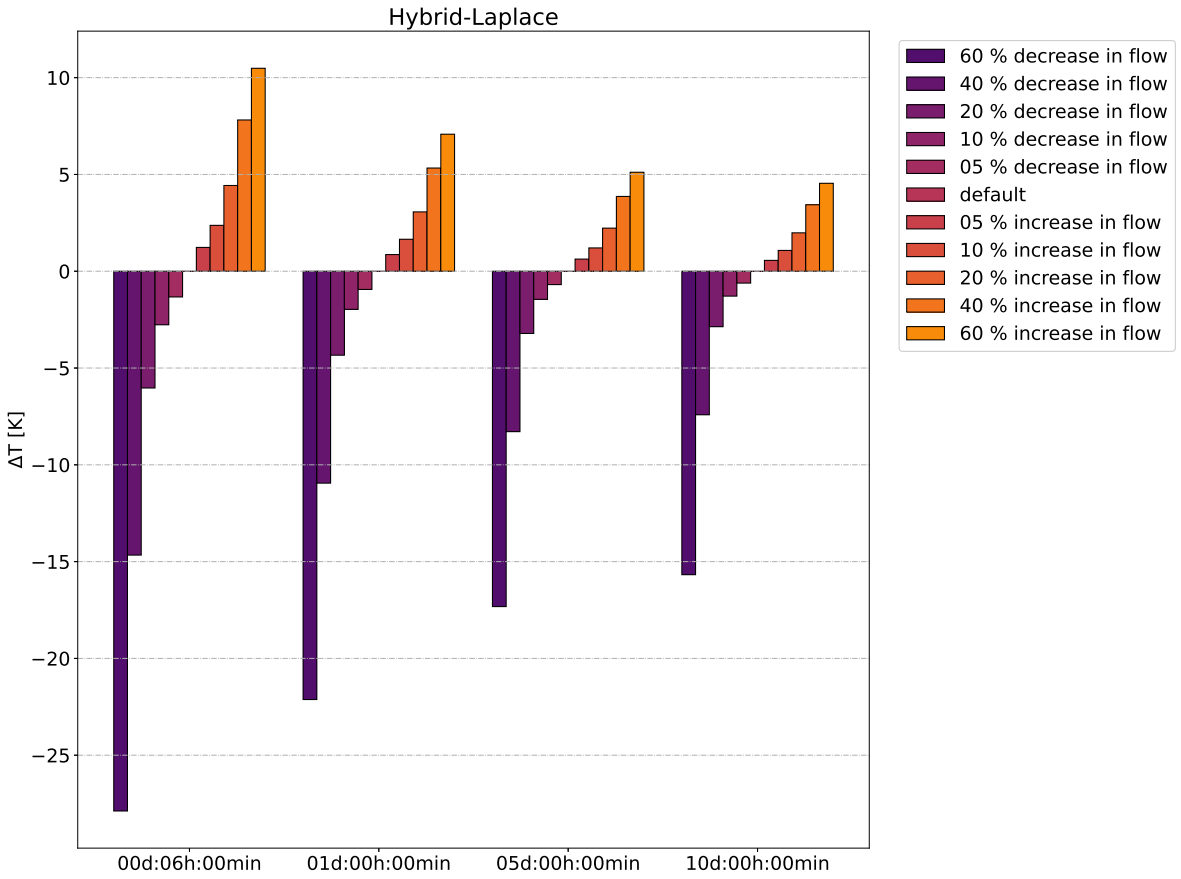

This conclusions make it hard to attest which model is better suited to model even longer times since, as shown, even small flow rate fluctuations can lead to differences in wellhead temperature greater than the original deviation to the field data.

Another possible source of error for the proposed study is the fact that the well spent about 90 days in production before the 10-day interest interval. To test how much this can affect the final results, the field data from the TPT are compared with the model predictions. The simulated flow rate is the same as used in the original simulations. It is known that because the well experienced several production interruptions, one possible procedure would be to adopt a flow rate lower than the one used. However, as one does not known how much the well produced in the 90-day period, varying the fluid flow rate in order to reduce the deviation between the solution and the field data would defeat the purpose of this study.

Figure 49 shows the comparison between the results for 90 days of operation. The natural consequence of using longer simulation times is a greater heating of the fluid produced. As the flow variation was not taken into account and the well goes through a stoppage period just before this interval, the results end up adjusting worse to the field data.

Figure 49 – Comparison of previous simulations and 90 days of production consideration in the wellhead temperature and pressure for vertical well

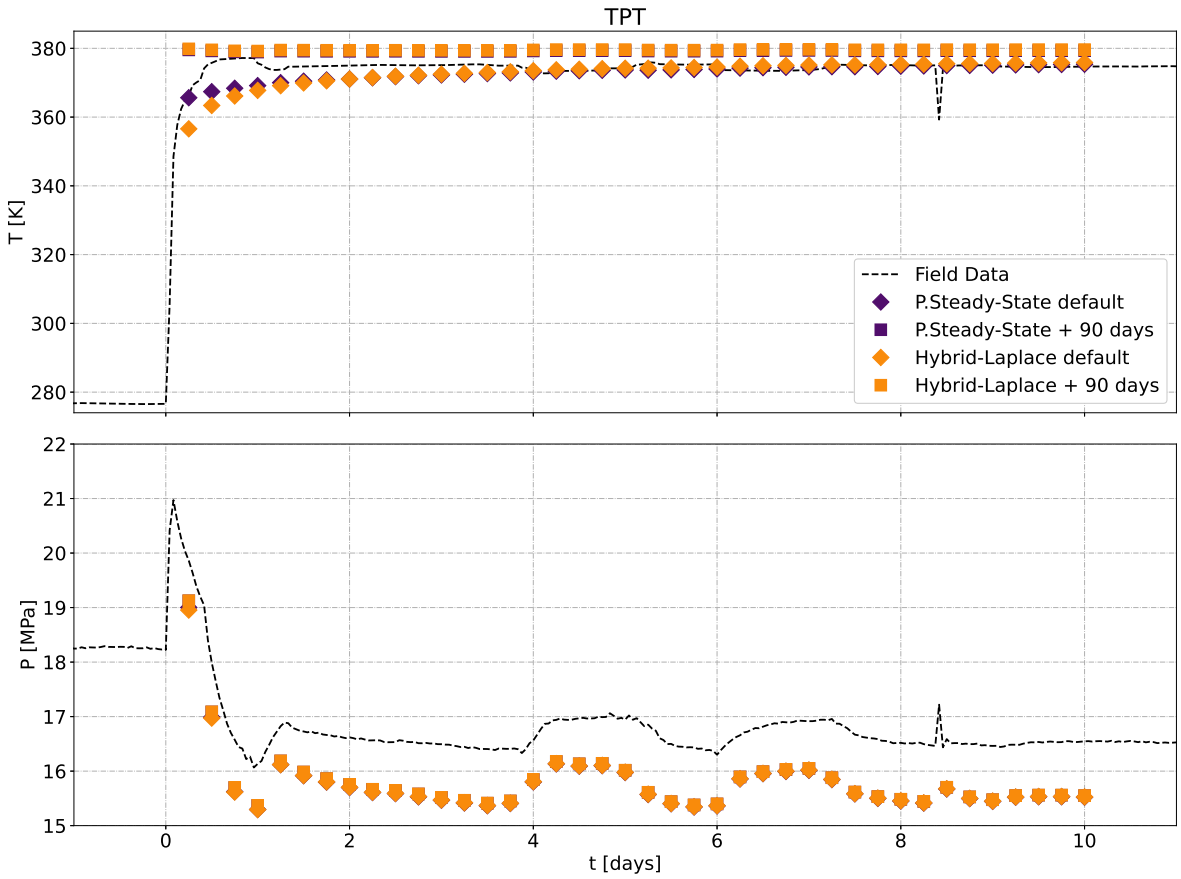

When compared to the result of the PT sensor, shown in Figure 50, it is clear that the effect of those additional few degrees in temperature significantly impacts the pressure increase. The APB calculated for the pseudo steady-state model went to 5.03 MPa while for the Laplace model it went to 5.05 MPa. These are values closer to those seen in the field, however, as they were obtained at the expense of extending the production time to 90 days, which is not what took place in reality. For this reason, they should be taken with care.

Figure 50 – Comparison between the previous simulations with a 90-day production condition: pressure at top of Annulus A for vertical well

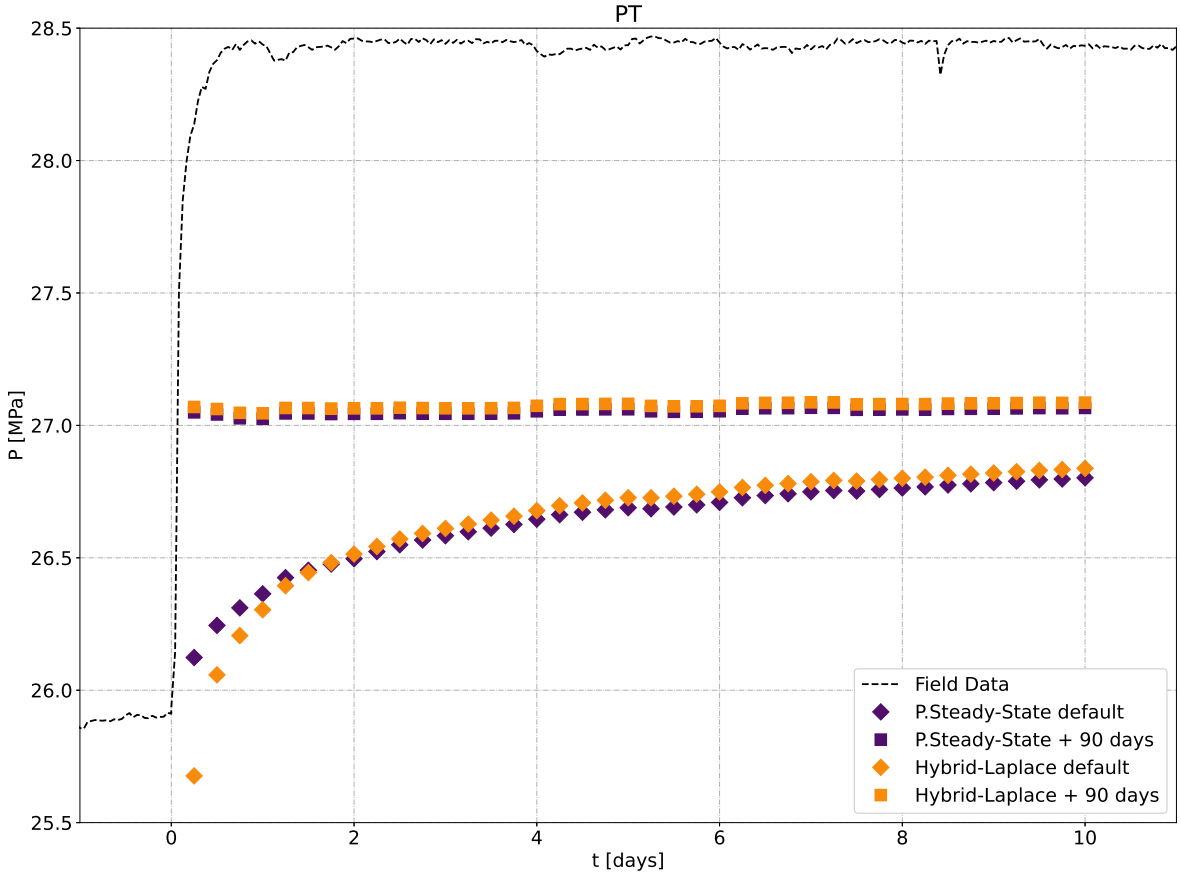

As can be seen, there are some variables that affect be accuracy of the models, so it is fair to state that the heat transfer models are able to predict the correct behavior of the well with reasonable accuracy. Regarding APB, there is still a significant deviation and further studies should be conducted to determine a cause with better precision.

5.1.3 Comparison with commercial software

Figure 51 shows the comparison of the simulation results including the simulations made with a commercial software for casing design (industry gold standard). The first with 1 day of production and the other at 10 days. This figure shows that for 10 days of production all models converge to what is virtually the same answer. For the first day of simulation, it is clear that the Laplace model appears as a middle ground between the commercial software (which supposedly solves the two-dimensional transient heat transfer) and the traditional pseudo steady-state models.

Figure 51 – Comparison between the proposed models and field data with a commercial software: wellhead temperature for vertical well at first and 10th day of production

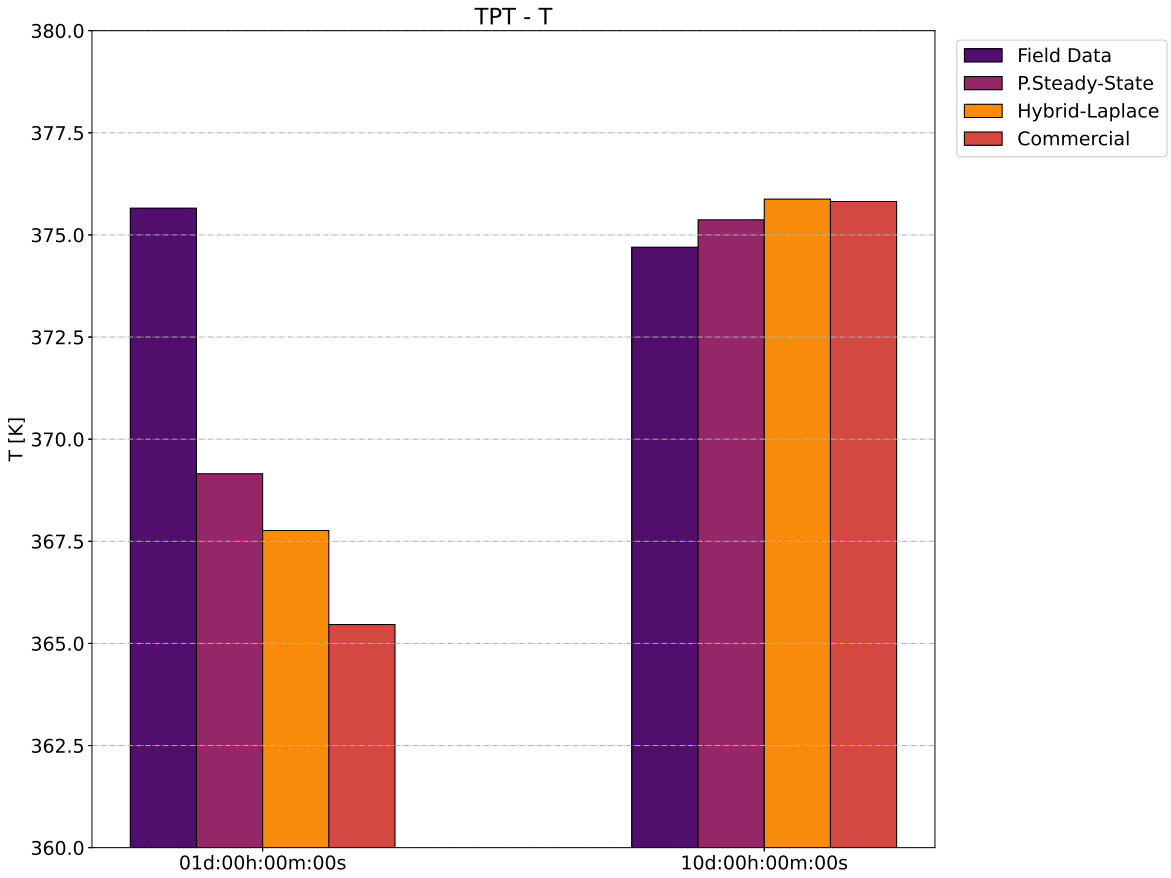

This claim that the Laplace model is a middle ground between the two approaches is corroborated by Figure 52. It shows the behavior of the temperature profile after one day of production. For this period, the transient term still affects annuli, especially at depths that contain annulus C. In these regions, it is clear that the Laplace model appears between commercial software and the pseudo steady-state model.

Figure 52 – Temperature profiles including commercial software for 1 day of production for the vertical well

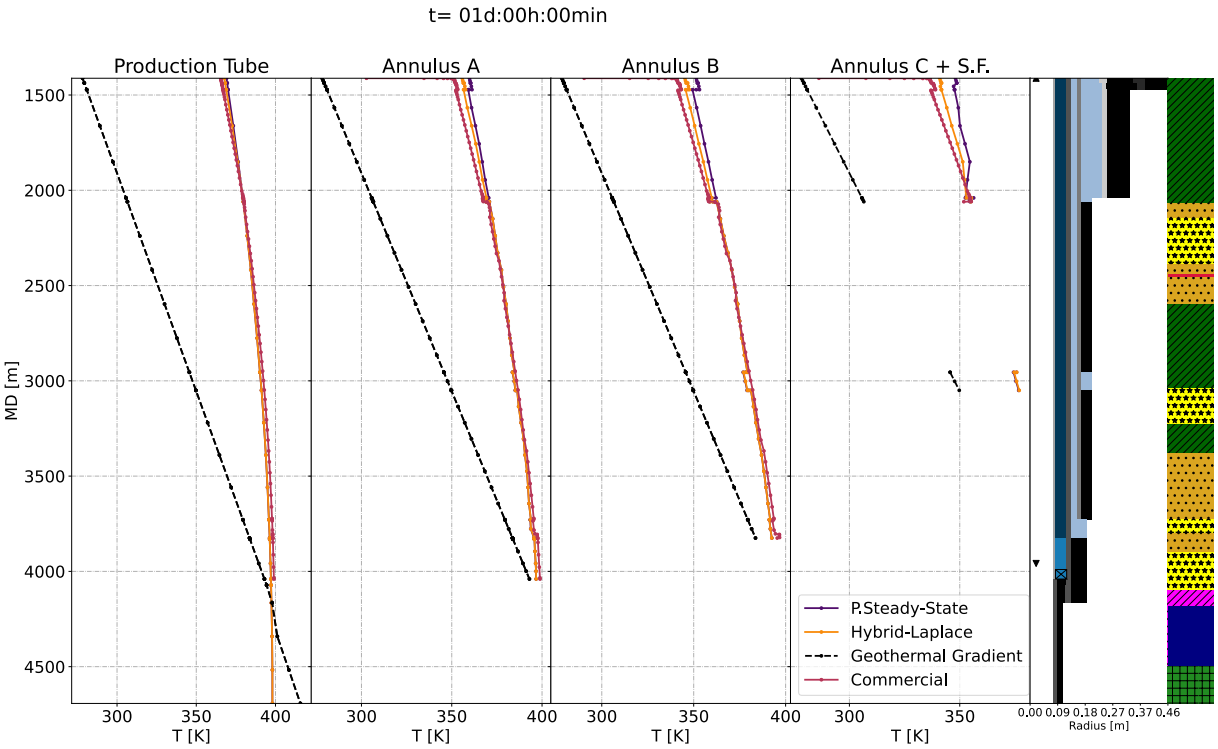

The comparison with a commercial software is useful for other aspects, Figure 53 reaffirms two ideas, first that all models converge to the same result in 10 days. More than that, it also confirms that these 10 days are in fact enough to validate the pseudo steady-state behavior of the wellbore. Clearly, the two transient models converge to the same solution as the pseudo steady-state program.

Figure 53 – Temperature profiles including commercial software for 10 days of production for the vertical well

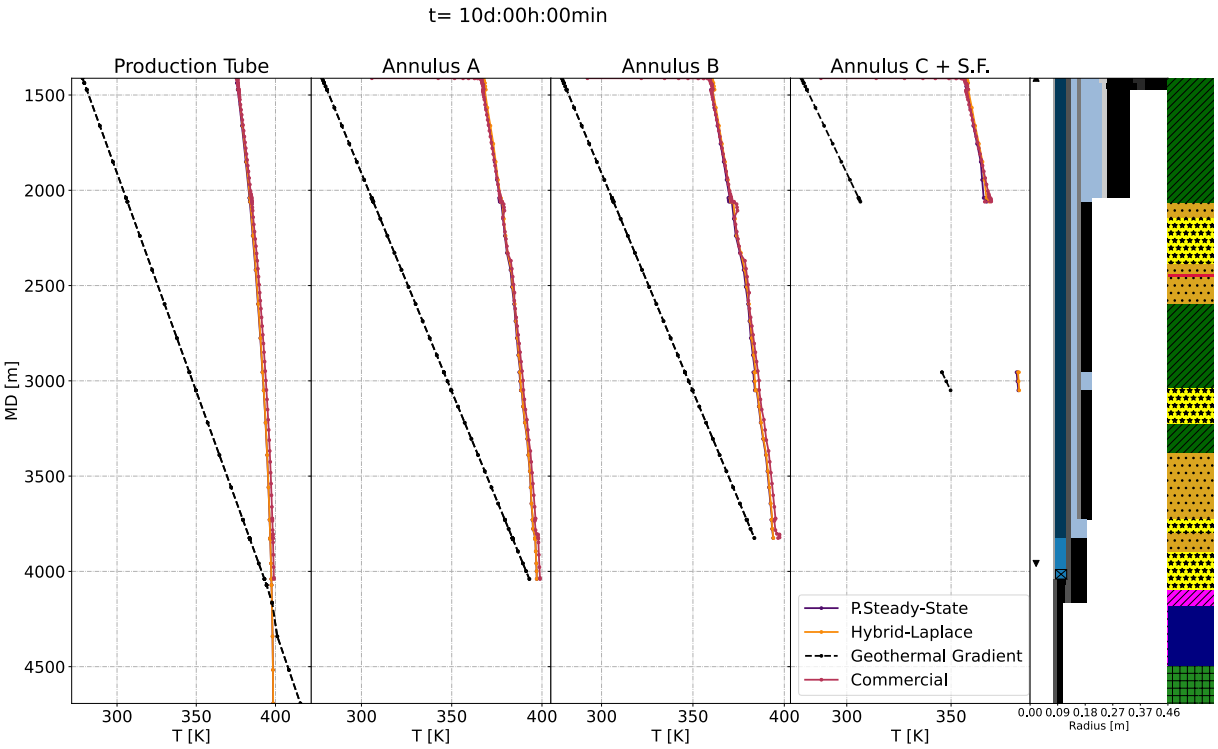

The results seem to be a little different between the models when the calculation of APB is considered. It is not certain how the commercial code calculates this parameter. However, its results are certainly different from those obtained by the models presented in the work. Figure 54 shows the behavior of the APB for the well annuli.

Figure 54 – APB in vertical well, comparison with commercial code

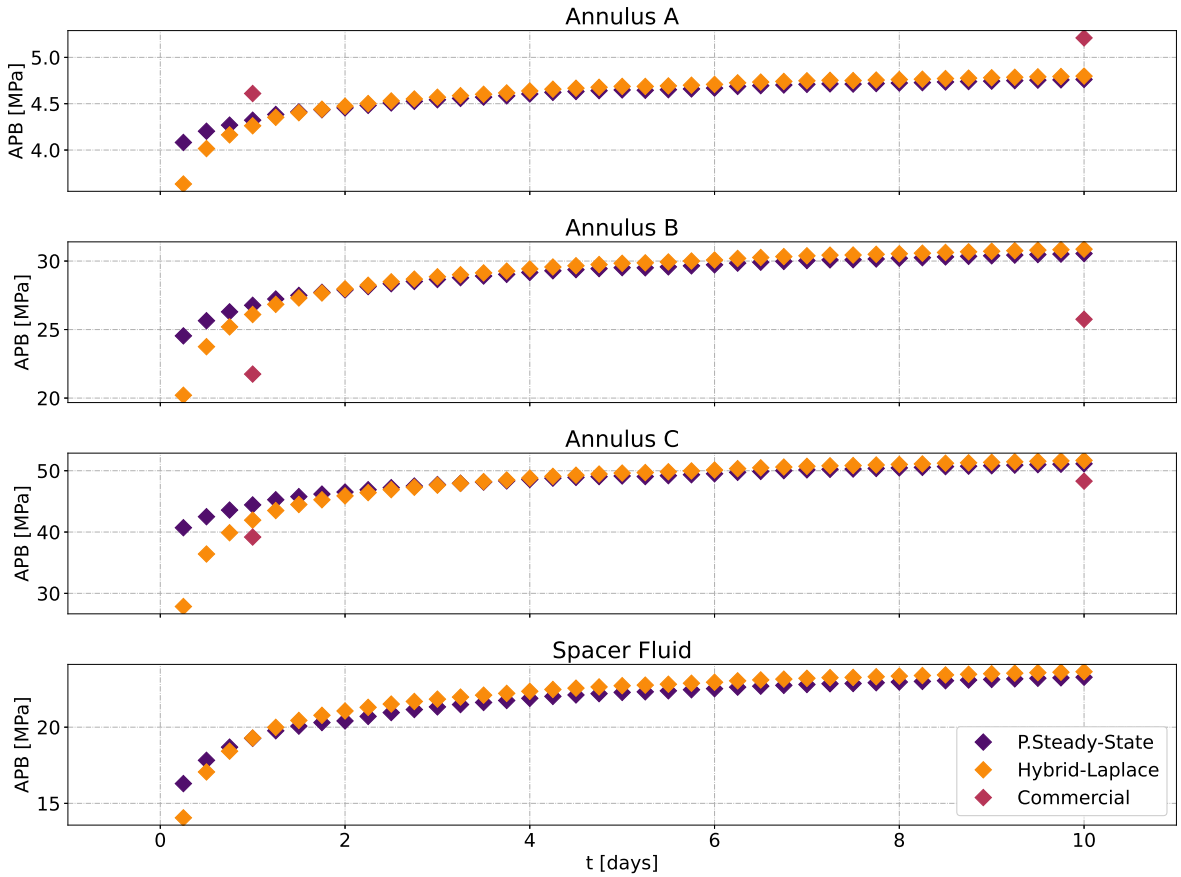

It is somewhat counter intuitive that despite finding lower values of temperature increase, the commercial software calculates greater values of APB. For 10 days of production, the commercial software returns an APB of 5.21 MPa, which is closer to the field data than the other models. Such a difference does not have a clear explanation, since the software is a “black box”, without much information on how to compute the thermal APB and its volumetric contributions.

Another issue regarding the commercial code is that the pressure increase in annulus A is greater but, on the other hand, the APB in the other annuli are reduced. This may seem inconsistent, but it is actually an expected result since an increase in pressure in an annulus causes deformation in the casings. Therefore, it is expected that the increase in volume in an annular space will occur at the expanse of the neighboring annulus.

5.1.4 Summary of results

The results obtained with the vertical well are important in the context of model validation. First, it is possible to state that the new formulation for calculating the heat transfer coupled with the APB, as proposed in Veiga et al. (2020), achieves a performance similar to that obtained in Barcelos (2017). In addition, it was possible to confirm

that the new heat transfer model based on Laplace transforms obtained an excellent performance for longer times, remaining close to the results obtained by the pseudo steady-state model.

Unfortunately, these data have not yet allowed validation of the accuracy of the Hybrid-Laplace at short time because the well has been producing for a long time. In addition, there are a lot of uncertainties in the problem to attest that one model shows a superior behavior to the other. To try to circumvent this problem, a brief sensitivity analysis was made with respect to the well flow rate. This analysis served to corroborate the idea that small temperature variations can occur with variations in flow.

Other than that, when compared to commercial software, it is clear that the Laplace model behaves as a middle ground between more complex models and the traditional ones used to model heat transfer in oil producing wells. Taking into account that the computational cost of this new approach has remained low, this model shows promising behavior.

The following case should be beneficial for determining which model behaves better since it evaluates a well subjected to an extended well test (EWT).

5.2 EXTENDED WELL TEST (EWT)

This section contains the thermal analysis of a well in Extended Well Tests (EWT). It is more relevant for analysis of shorter time periods, since wells in EWT are at the start of their production life, thus leading to a formation which is not affected by previous productions. Also, extra field data were collected for this particular well, allowing for better analysis.

The EWT consists of a pre-operation period in which the well is put to the test to evaluate its productivity and completion. During this period, it produces as if in normal production operation, however, all of its production is analyzed isolated from other wells.

Similarly to the vertical well presented in the previous section, this is an offshore well at a water depth of 2501 m. Figure 55 shows the geometry of this well and some of its main characteristics. First, as recommended by the well operator, one assumes that the well is surrounded only by shale. Although this is rarely the case for a real well, no data were available on the specific lithology.

Also, it is assumed that all annuli are filled with brines of different densities, once again as a consequence of lack of data for the type of muds used during drilling. Since the only information provided was the standard density of the fluids, these data were used to estimate their respective salt concentrations. For the production fluid, similarly to the vertical well, the composition used to model the fluid is presented in Appendix B.

Figure 55 – Geometry of well in EWT

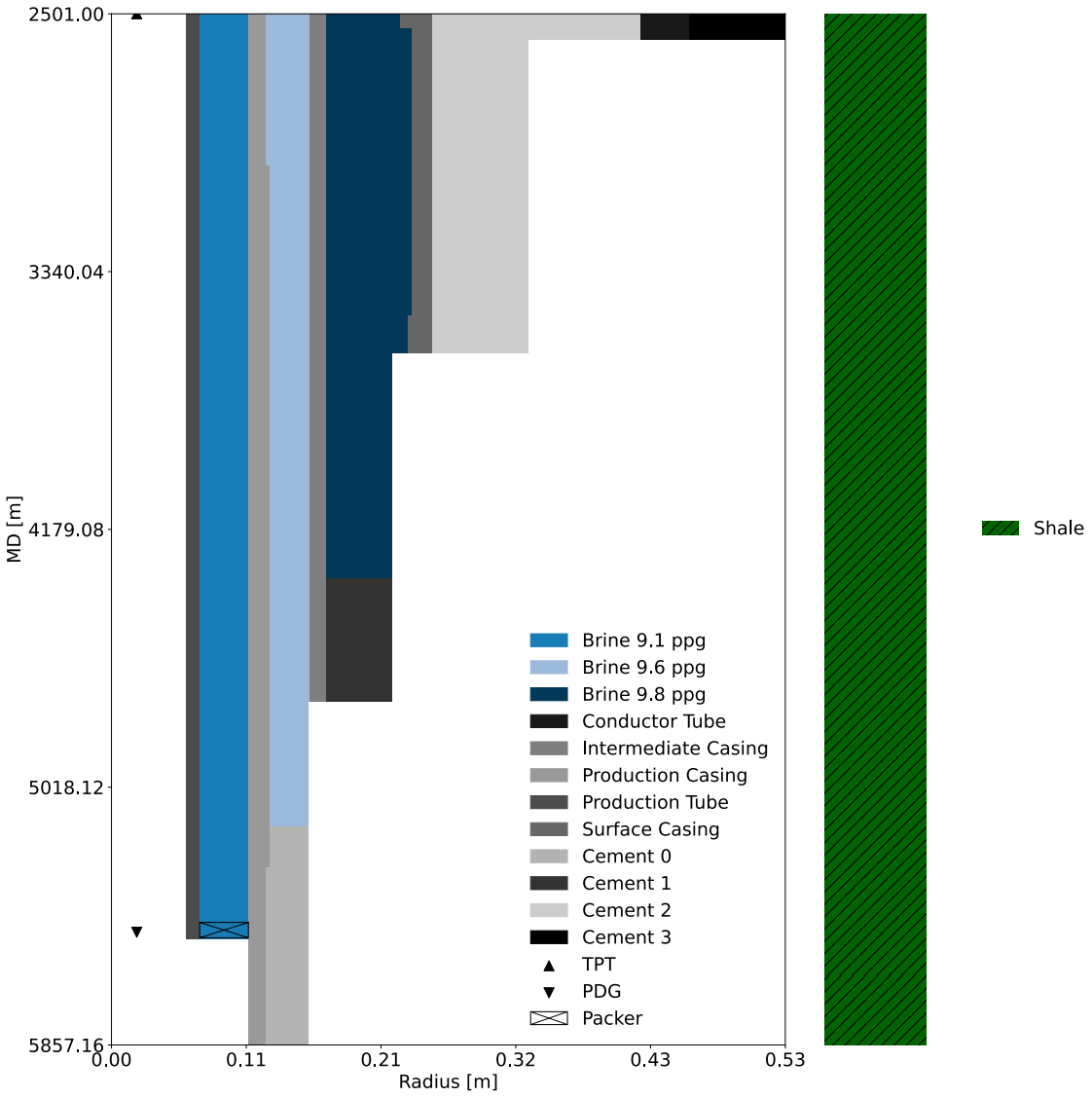

This well, unlike the previous one, is inclined with KOP at 4909 m and the production zone is positioned at an approximate angle of 20° angle.

As no salt layer was crossed during drilling, the geothermal gradient of this well (see Figure 56) does not present any deviation, starting at 277.15 K at sea depth and 375.15 K at the bottomhole (5857.16 m).

Figure 56 – Geothermal gradient of the EWT well

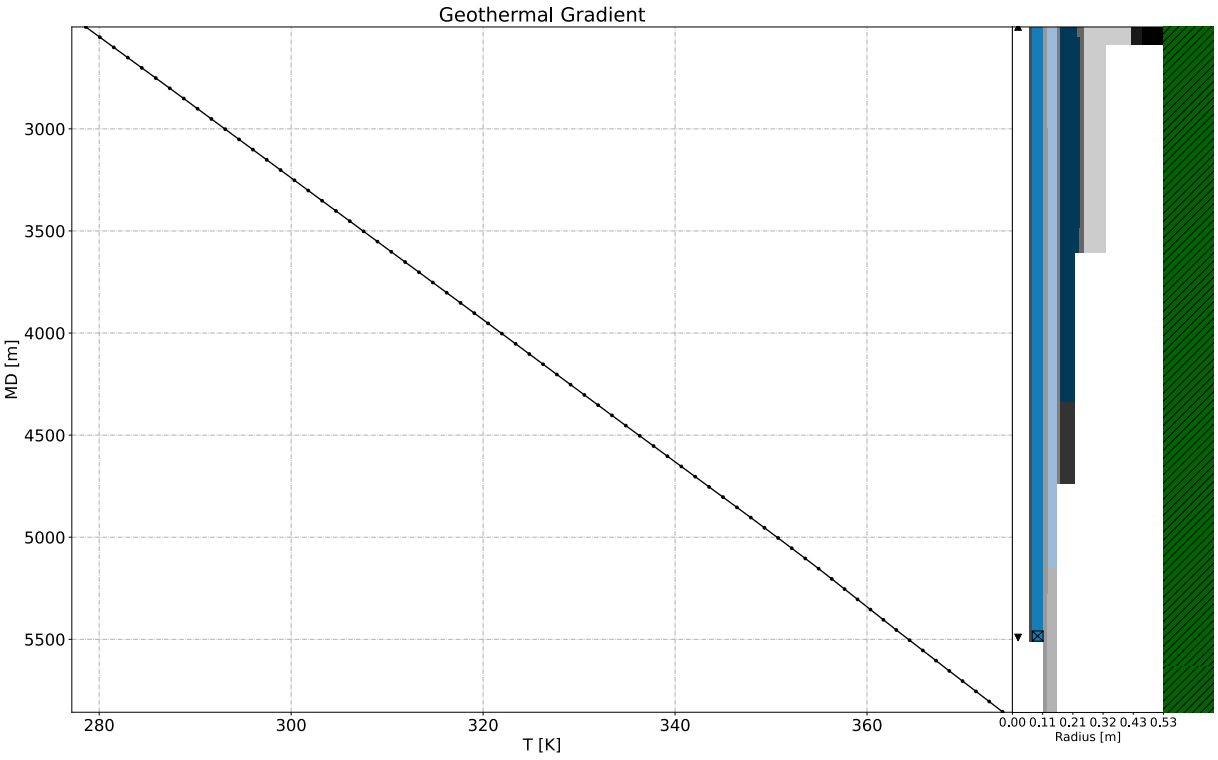

As previously mentioned, the data provided for this well allow for more complete analyses. Figure 57 presents the models inputs, namely the pressure and temperature data from the PDG and the flow rate as a function of time.

Figure 57 – Volumetric flow rate, PDG pressure and temperature for EWT well

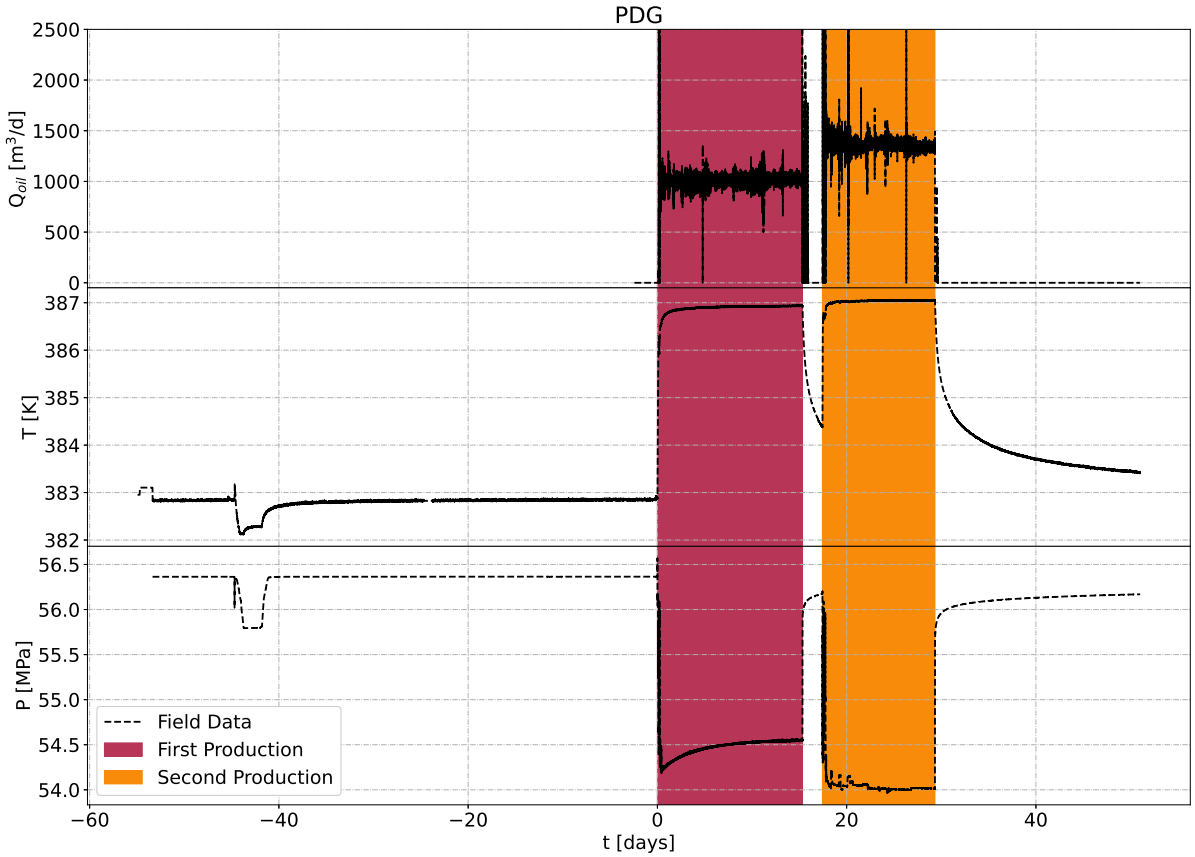

Note that this well has two production periods in the interval shown, as highlighted in the figure. The first region in particular has greater potential for the thermal analysis as is the first time that this well enters into production.

Figure 57 also shows that at the start of each production interval the flow rate suffers from large fluctuations. However, the well seems to operate close to an average of 1000 $m^3\,d^{-1}$ for the first 15 days. Than it undergoes a period of 2 days without production retaking it with an average of 1430 $m^3\,d^{-1}$ for the next 12 days of production.

Although it may seem trivial to use this data directly as the input of the models, some considerations were taken into account. First, regarding the synchronization of the different variables of the field data, it is important to explain that the exact position of the flow meter used is not known. Therefore, it is not possible to guarantee that the data presented for the PDG was registered at the same time as the flow rate (i.e., zero time lag). Also, there is no information whether or not the production lines and the separator tank were filled prior to the production, which could lead to loss of some information as the lines would act as an intermediate storage volume for the produced oil.

Figure 58 corroborates this idea when the first 12 hours of the first production period are analyzed in detail. It becomes clear that the flow rate measurements are delayed in relation to the PDG data.

Figure 58 – Flow rate, temperature and pressure at PDG in the first 12 hours

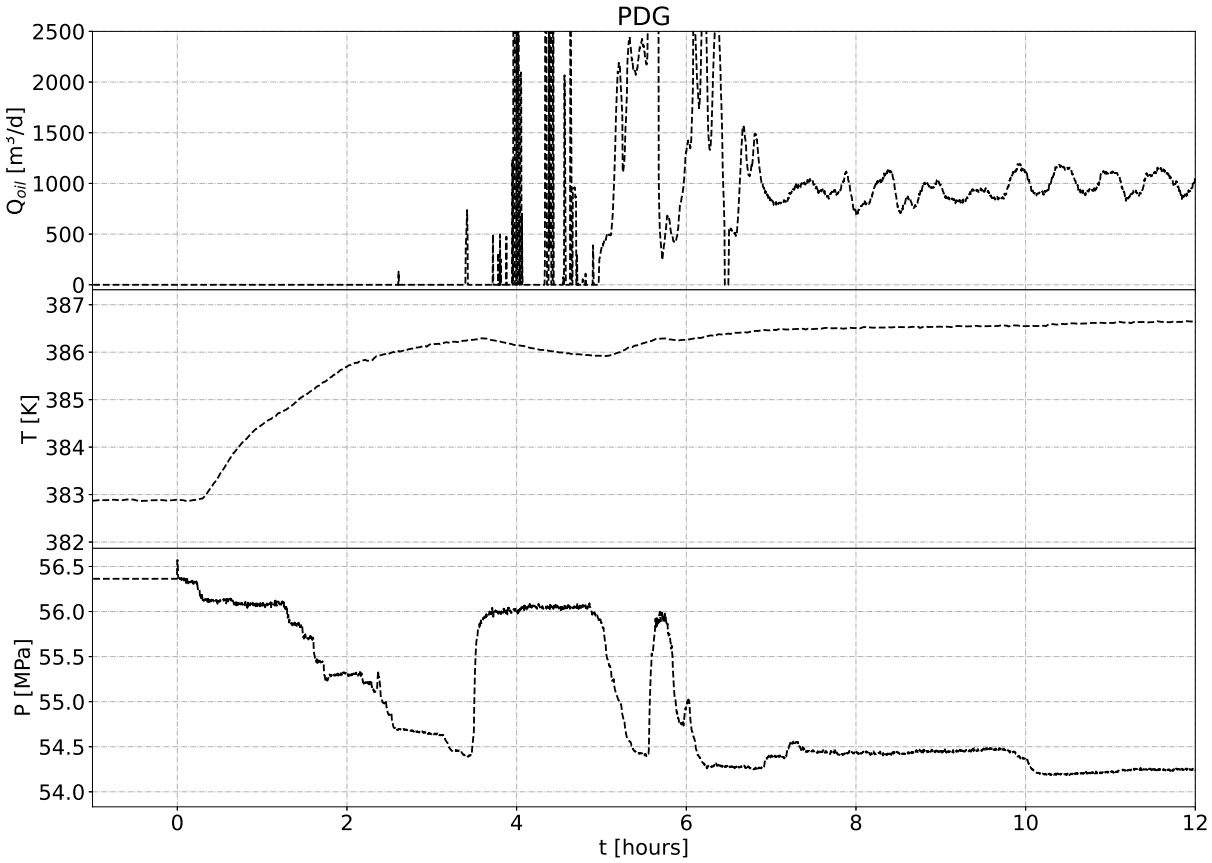

Since there is a clear indication that the meters are not registering the same events at a given time (i.e., there is a time lag due to a significant physical distance between the flow meter and the PDG), one sensor position must be taken as a reference. In this case, the PDG pressure is assumed as the reference variable, so all delays are measured in relation to its time frame.

To determine the delay in the measured data, a simple procedure involving cross-correlation of the data can be used. The idea behind such procedure is to find values of lag in data which maximizes the cross-correlation coefficient (IFEACHOR; JERVIS, 1993) described by:

$$\varrho(m) = \frac{r_{fg}(m)}{\sqrt{r_{ff}(0)\, r_{gg}(0)}} \tag{138}$$

where ϱ is the cross-correlation coefficient of each offset (lag) m. r_{fg} represents the cross-correlation of time series (f, g) sampled using the same frequency. With this, it is possible to determine the value of m which maximizes the cross-correlation for a set of experimental data, such as the ones provided.

When analysing the data, it was detected that the first production interval has a higher noise which could make it more difficult to estimate the delay. Thus, to avoid

such problem the second production interval will be used to apply the cross correlation. Figure 59 shows this time period.

Figure 59 – Flow rate, temperature and pressure at PDG in the second production interval

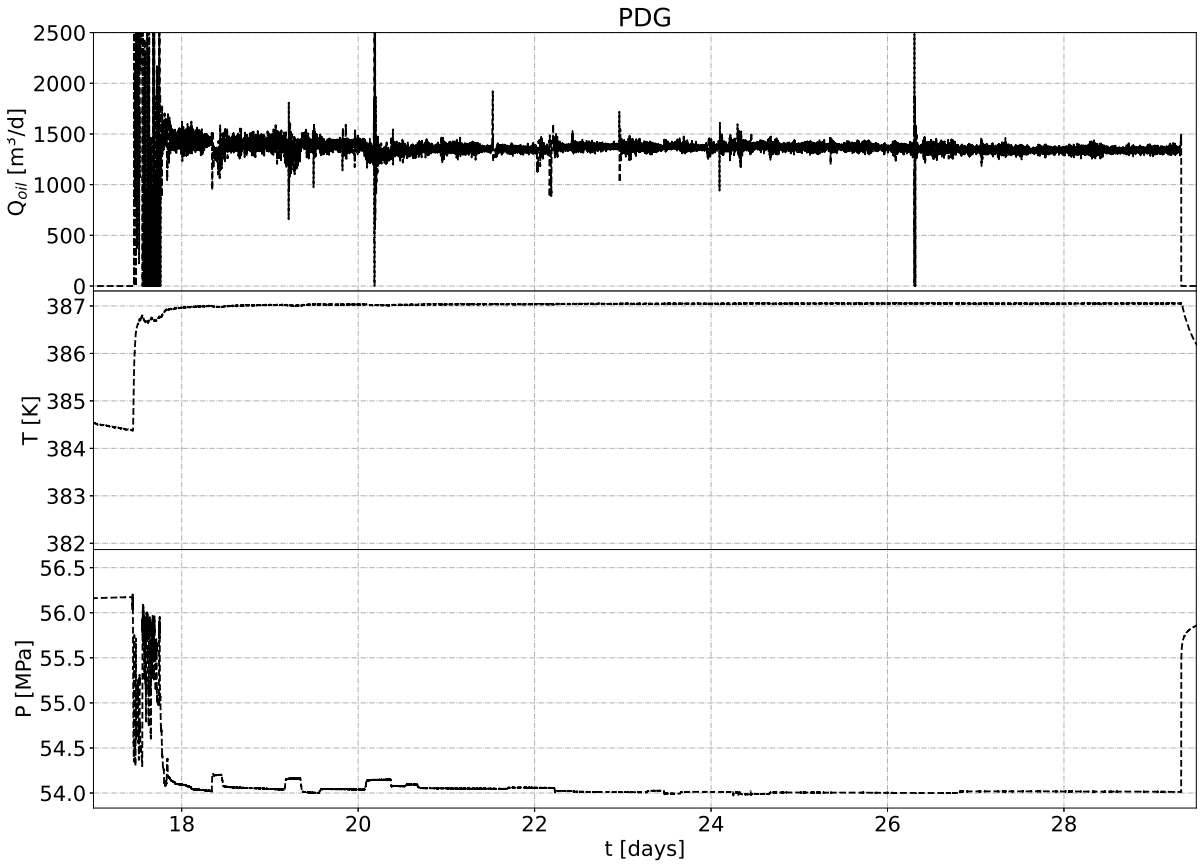

This data still have some problems for the application of the cross-correlation. First, the data sampling was not evenly spaced, nor are they taken at the same sampling frequency for different variables. To apply the cross correlation, both data must have the same dimensions and preferably have been lightly filtered to avoid inaccuracies due to noise.

In order to correct the data, first a sampling scheme using linear interpolation was used. As a consequence the data series are evenly spaced and are taken at the same time. This new data set is then filtered using a convolution with the Bohman window (HARRIS, 1978).

In summary, the procedure of using the cross-correlation for determining the lag in this problem consists in creating linear interpolations such that it is possible to create a evenly distributed sampling. To this interpolators, a simple filtering is applied, by using a convolution with the Bohman window. Than, these filtered functions are used to sample sufficient points in order to apply Equation 138 and determine the offset in

the data (which can be converted to lag) that results in maximum cross-correlation in data.

Figure 60 presents the data for the second interval including the filtered data which will be used in the cross-correlation.

Figure 60 – Filtered data used in the cross-correlation procedure

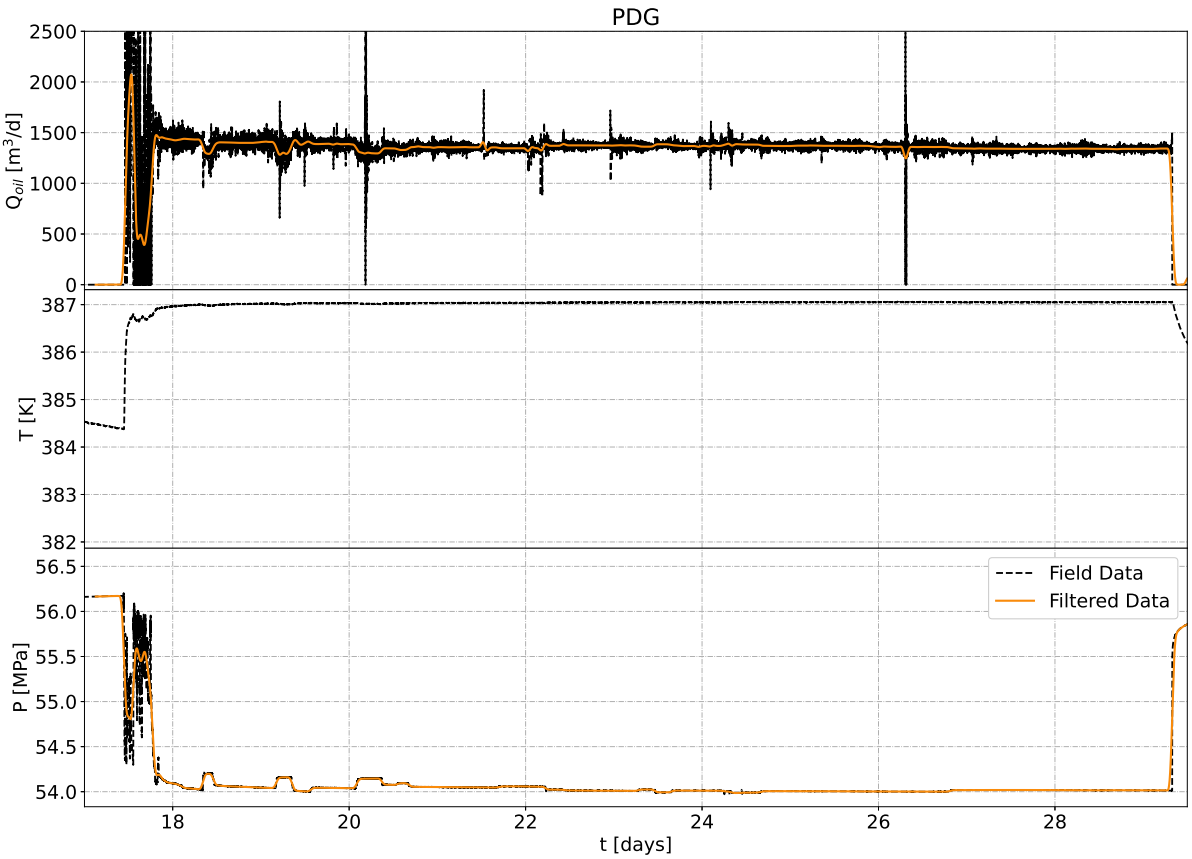

Using Equation 138, it was possible to establish that the maximum correlation coefficient was detected with a lag of 28 minutes in the measured flow (ϱ=0.97). When analysing Figure 58, it is clear that this delay is not sufficient to accommodate the visual differences associated with the initial production. Also, there are clear plateaus of constant pressure which are not identified in the flow rate. This serves as an indication that there were issues with the actual flow rate measurement, so an adjustment of the data may be required for the first couple hours of production. Therefore, besides the application of a time lag to improve the synchronization, for shorter times, a set of extrapolations were used to fill the data up to the start of the measurements at the PDG

Since this well has actual data for the flow rate, an alternative for modeling the heat transfer is also proposed. Contrary to what was done by Hafemann (2015) and Barcelos (2017), where a single average flow rate was used to model every simulated time, here, as the temporal data is available, an average flow rate function will be used instead. A direct consequence of this will be a better representation of the temperature

in the TPT for the second production interval at the expense of accurately calculating the pressure, as this variable is related to smaller time-scales.

To better understand the phenomena present in this well, extra points were used in the simulation. Thus, for the first 6 hours of production a simulation will be carried every 15 minutes. Following that, until 15 days of production (first production interval), the time spacing from each simulation will be of 6 hours. No simulation is executed during the interval without production, however, in the second interval, from 18 to 29 days, a 12-hour spacing will be used. So, in total, 104 individual simulations were performed in each analysis. Figure 61 presents the points used as inputs for the simulations.

Figure 61 – Input points for flow rate, temperature and pressure in PDG for both production intervals

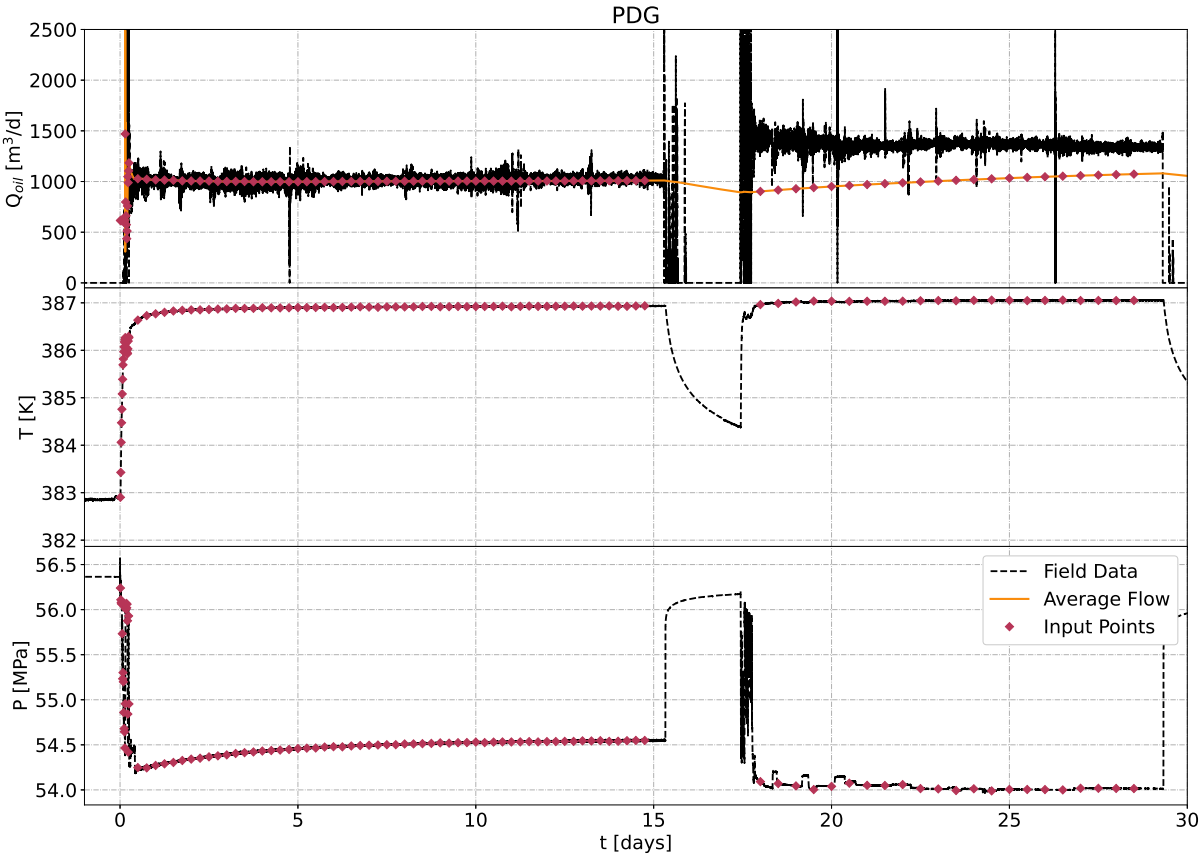

As mentioned previously, there is a region at the start of the production where the data for flow rate is lacking. Therefore, a simple extrapolation can be used to approximate the data in this region. For that, a threshold of 615 $m^3\,d^{-1}$ is used. This threshold serves the purpose of ensuring higher flow rates at the start of production in order to avoid instabilities detected in the mass conservation algorithm. Such a topic will be discussed further when analysing the results. Figure 62 presents the input values with greater detail in this starting region.

Figure 62 – Input points for flow rate, temperature and pressure in PDG for the first 12 hours of production

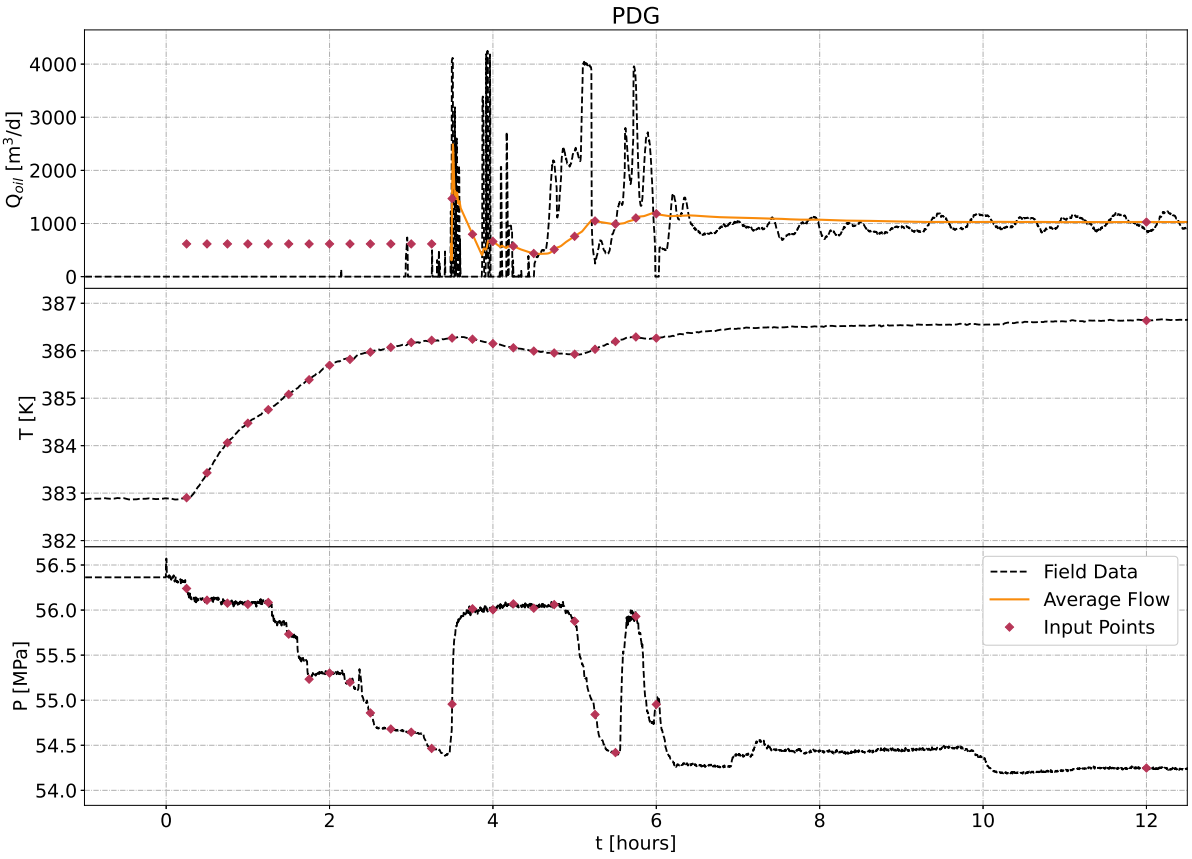

To ensure synchronization of the PDG with the TPT data, the same cross correlation procedure was applied. The study will be omitted as it did not detect any significant delay in the data, due to this fact no delay is assumed for the TPT. Figure 63 presents the data from wellhead at the TPT.

Figure 63 – TPT temperature and pressure data for EWT well

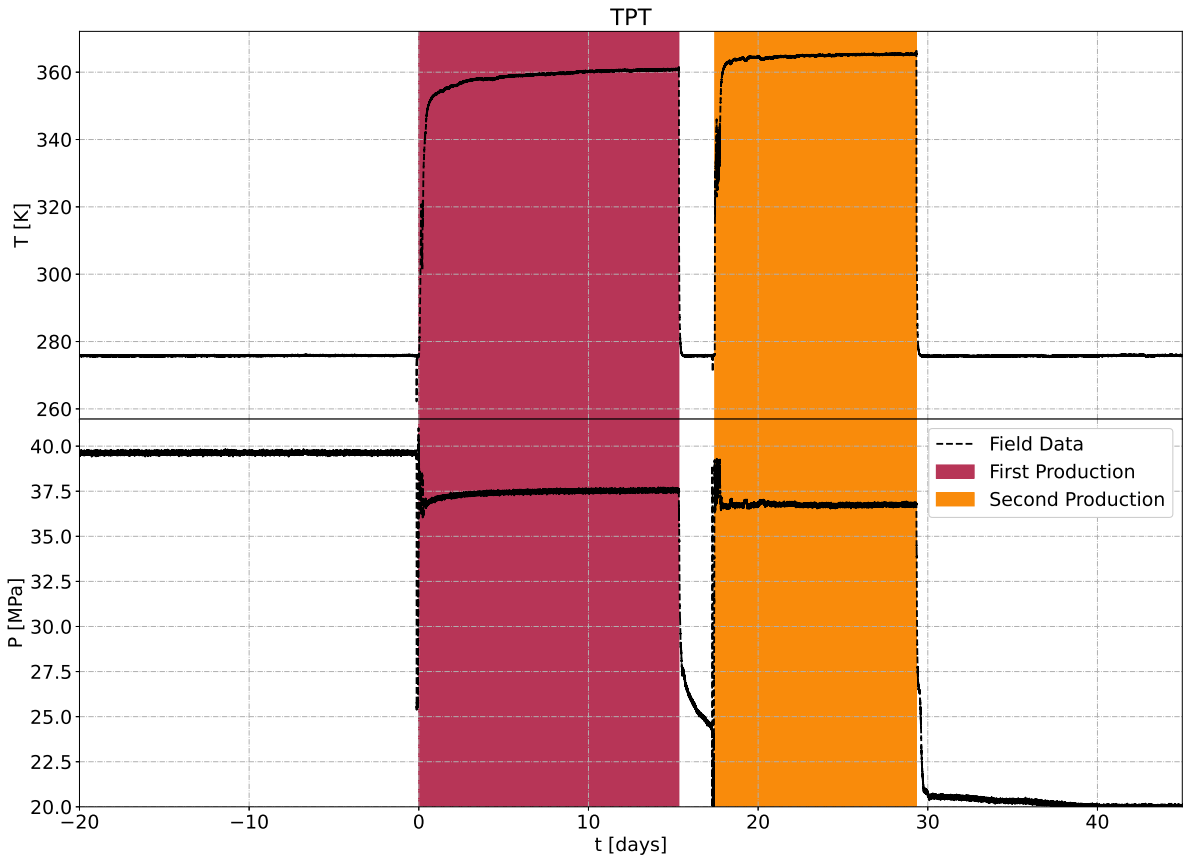

Contrary to what occurred in the vertical well, the studies in this well are focused mainly at predicting the temperature at the wellhead (TPT). The reason for that is the fact that the first annulus of this well was left ventilated, i.e. opened to the platform. As a consequence, any fluid expansion due to heating would be able to escape at the top of the annulus, so no APB was detected in this well. In other words, it is not possible to validate the APB estimation via mass conservation for this well.

5.2.1 Validation of Thermal models

The validation of both the traditional pseudo steady-state and the Hybrid-Laplace is performed in a similar manner to what was done in the vertical well. First, all the 104 points were simulated using both models and the predicted wellhead temperature and pressure are compared with TPT field data. Figure 64 shows this comparison.

Figure 64 – Comparison of TPT temperature and pressure with predicted results from proposed models in EWT well

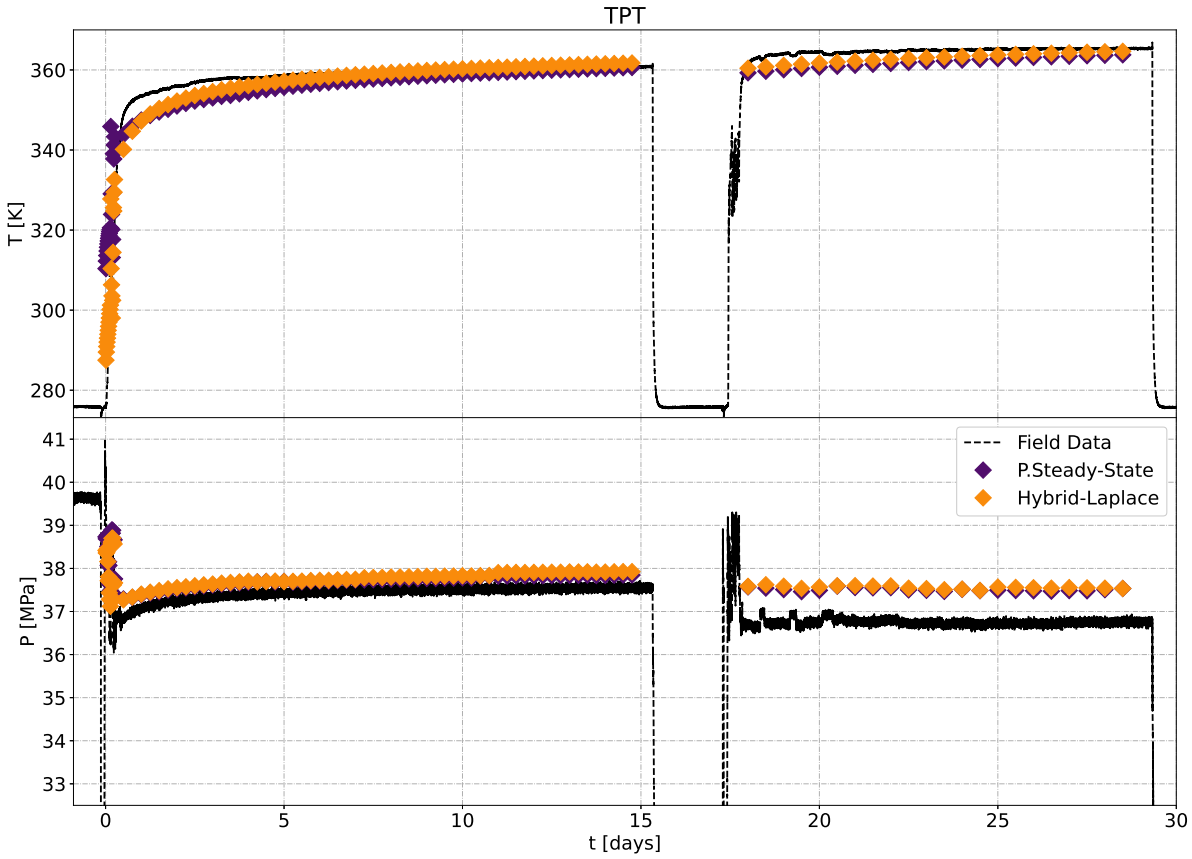

Both methods achieved good results when comparing to the TPT. However, there are three main regions which can be analysed independently. After the first 12 hours of production, and prior to 15 days, both models agreed with good accuracy with the field data. Especially after the first day, the Hybrid-Laplace managed to outperform the traditional pseudo steady-state method. This behavior, however, changes by the end of the first production interval, where the Laplace model tends to over-predict the wellhead temperate. Although this may seem detrimental to the model, the difference is less than 1 K, which is within the the uncertainty of the field data and margin of precision of the models, as the sensitivity analysis will further demonstrate. Similar to the vertical well, the difference in predicted pressure appears to be an small offset in relation to the field data, indicating imprecision in the two-phase flow correlation used.

Also, in this first production interval, the largest deviations recorded between the field data and the models was 6.18 K for the pseudo steady-state model and 7.43 K for the Laplace model. These differences take place exactly at 18 hours of production; at that point, the temperatures predicted by the models are much lower than the field measurement. An explanation for this discrepancy may be linked to the flow rate used as input of the model. When analyzing the pressure (bottom most axis) in Figure 62, it

is clear that the flow from the well passes through at least 4 different plateaus in the region where the flow rate data are not known. Since the flow value is extrapolated at shorter times, and its average begins with smaller values, the flow estimate for the first day may be underestimated in certain regions and overestimated in others.

During the second interval of production, after the well stopped producing for two days, the Hybrid-Laplace presented a good performance. However, more importantly, based on the temperature behavior, it is clear that this approach based on average flow can achieve good precision even after a brief interruption in production. As predicted, the use of the average flow in this second interval led to a poor representation of the pressure profile, leading to a difference of 830 kPa.

Figure 65 presents the first 12 hours of production which have some peculiarities which will be tackled.

Figure 65 – TPT results on first 12 hours of production for EWT well

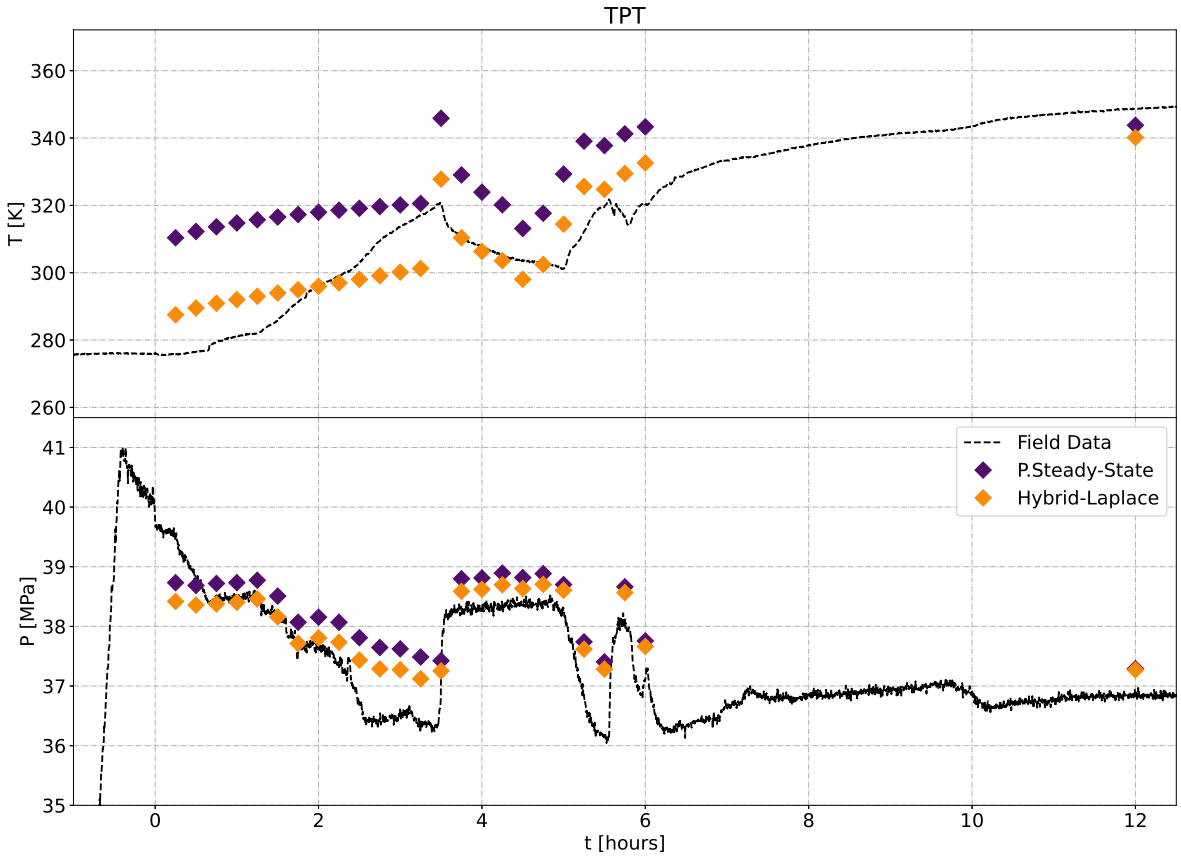

The general trends of the numerical results look very promising, as most of the characteristics of the field data were captured. Initially, both predicted temperatures are higher than the field data, of the order of 10 K for the Hybrid-Laplace model and 30 K for the pseudo steady-state. However, as the production continues, both models tend to estimate a slower growth rate for the temperature and, consequently, at about 2 hours of production the Hybrid-Laplace starts to under-predict the temperature. The pseudo

steady-state never gets to under-predict but, at 4 hours, it deviates by a small margin from the data.

Also, during the first 3 hours of production, both models managed to predict quite accurately the pressure behavior at the wellhead up to the point that, at 2 hours of production, the Hybrid-Laplace model managed to predict the wellhead pressure with a deviation of less than 10.95 kPa.

In the interval between 2 and 6 hours, the Hybrid-Laplace model managed to predict the wellhead temperature with the maximum deviation of 2 K. The pseudo steady-state, on the other hand, has a average deviation of 3.68 K, with the maximum deviation of 4.6 K.

The largest deviations from the field data, with regard to temperature, occur in the first two hours. In this region, a maximum deviation of 13.38 K for the Hybrid-Laplace model and 35.68 K for the pseudo steady-state model is perceived. Again, a simple explanation for this deviation is the lack of flow information, which is further confirmed by the fact that in regions where the flow measurement is more reliable, the predictions achieved better precision.

Of course, one could try to adjust the flow rate to better fit the data in the startup region. However, this adds little to the actual validation of the model, so the results will be analysed without any additional corrections. In sum, the results indicate that both models have problems when dealing with shorter time periods. However, even with these limitations, the results seems to indicate a better performance of the Hybrid-Laplace model in relation to the pseudo steady-state.

To improve the previous analysis, Figure 66 presents the deviation from the data measured in the TPT for both production intervals. It is clear to state that the deviations between the models and the field data for the wellhead pressure remain mostly below 1 MPa. Again, the region in which deviations are larger coincide with the start of production, where there is lack of flow rate data.

Figure 66 – Deviation from temperature and pressure at the TPT and the models for EWT well

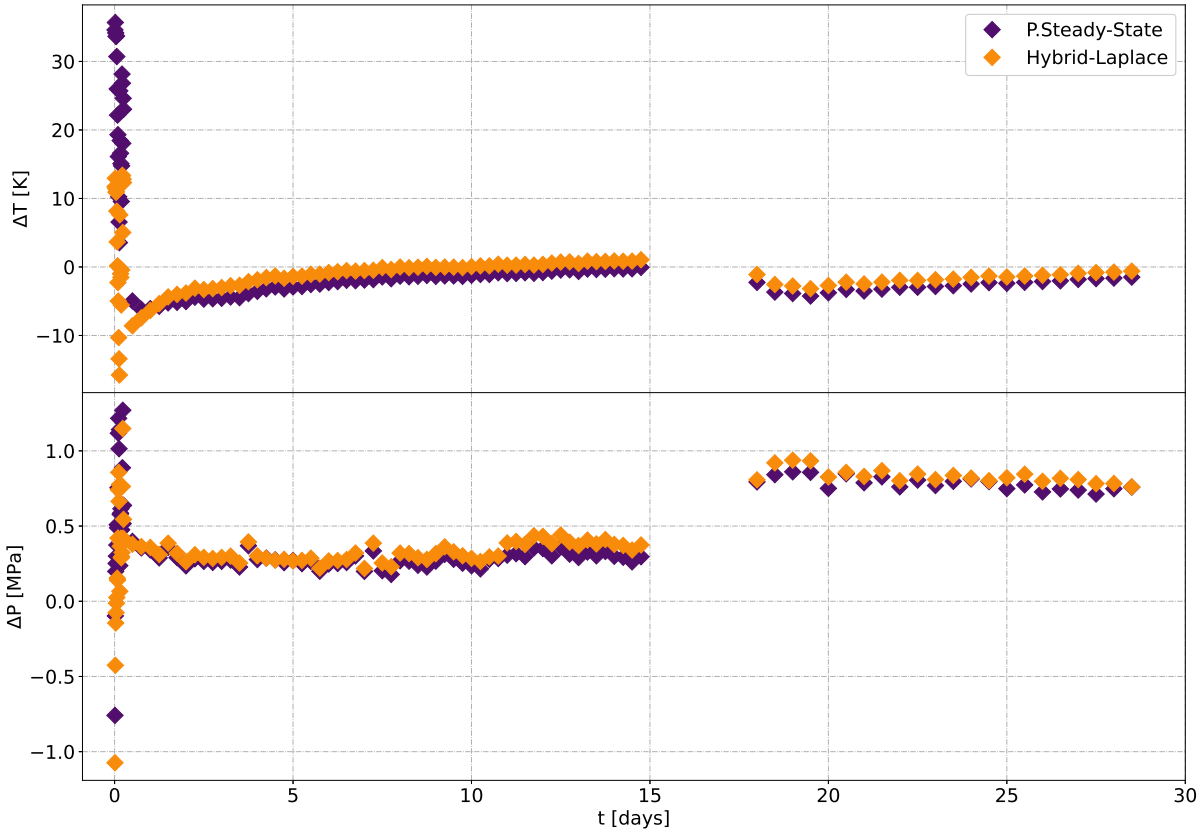

The main conclusion that can be drawn from the second production interval is that the approach of using an average flow rate to model wells, even after production interruptions, is a valid possibility for these models. Both models predicted very well the thermal behavior, which is an important requirement to estimate APB. However, a systematic error in relation to the pressure was identified at the wellhead. The mean temperature deviation measured at the wellhead in this period was 2.7 K for the pseudo steady-state model (0.78 MPa for pressure) and 1.72 K for the Laplace model (0.83 MPa for pressure).

In addition to this direct analysis with respect to the field data, a simple statistical analysis for the deviation can be used. Figure 67 shows the Average Absolute Deviation of these models in relation to TPT data. It is clear that, in general, the expected deviation for the measured pressure of both models remains close to 1.3%. For the temperature, on the other hand, there is a more notable difference between the the results, as the pseudo steady-state model reaches an expected average deviation of 2.2% while the Hybrid-Laplace model reaches 0.9%. Although this difference seems small, it occurs in relation to temperatures above 300 K, therefore, this difference may translate to more than 4 K in the predicted wellhead temperature. Despite being a small difference, the

sensitivity analysis will point out that such difference in wellhead temperature can lead to larger deviations in APB.

Figure 67 – AAD from temperature and pressure at the TPT for the EWT well

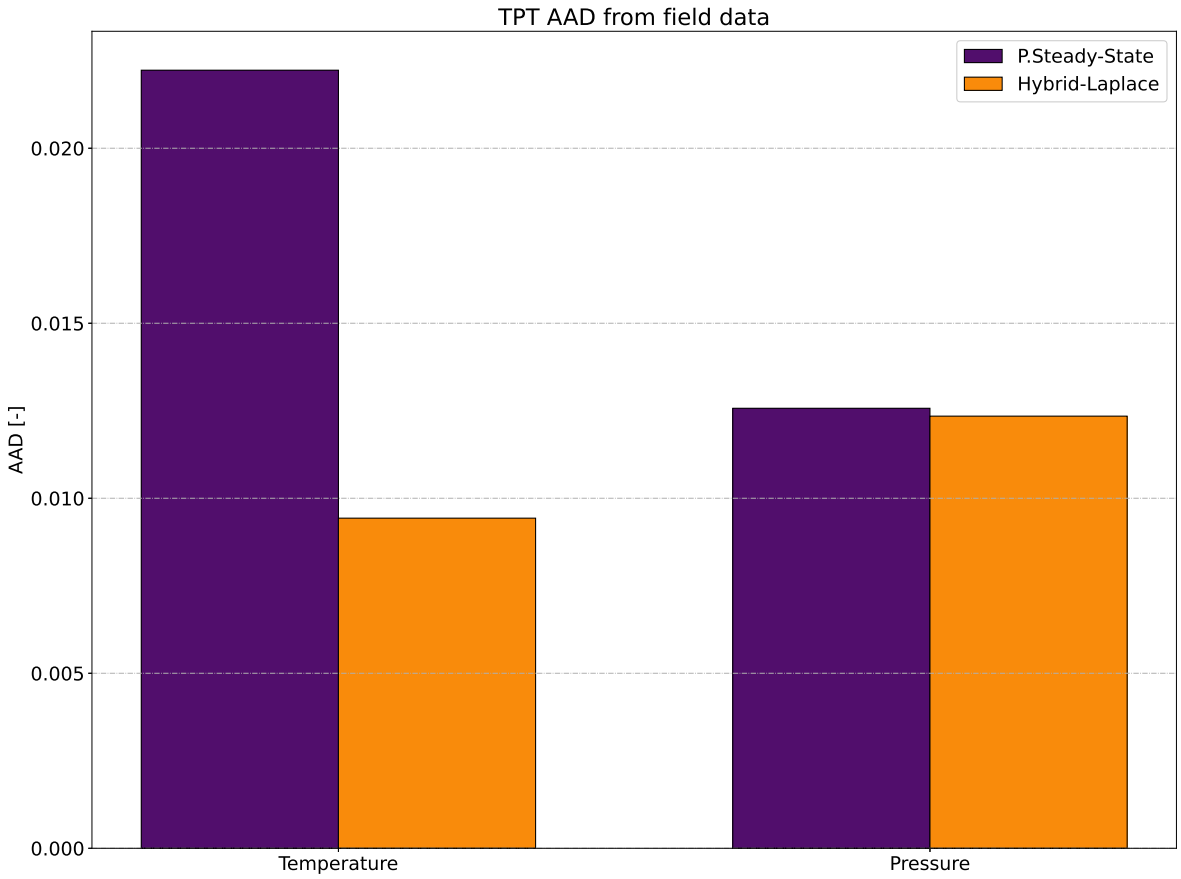

With the initial validation of both thermal models completed, it is possible to compare the physical behavior of their predictions. Firstly, Figure 68 presents the predicted temperature profile for each model at the first simulated time of 15 minutes. Contrary to what happened in the vertical analysis, here the effects of the capacitance are more pronounced, smoothing the thermal profiles at the annuli in the Hybrid-Laplace predictions. Also, the capacitance effects are more noticeable going up the well, such that shallow regions takes longer to detect the heating. This phenomenon is more perceptible when analysing annulus A, where the temperature increases first near the bottomhole. On the other hand, in annulus B, there is no perceptible heating using the Hybrid-Laplace model, with only an inperceptible variation of temperature in the bottom of the annulus. For the annulus C a more in-depth explanation is required due to the phenomena observed.

Figure 68 – Temperature profiles predicted for the EWT well at 15 minutes of production

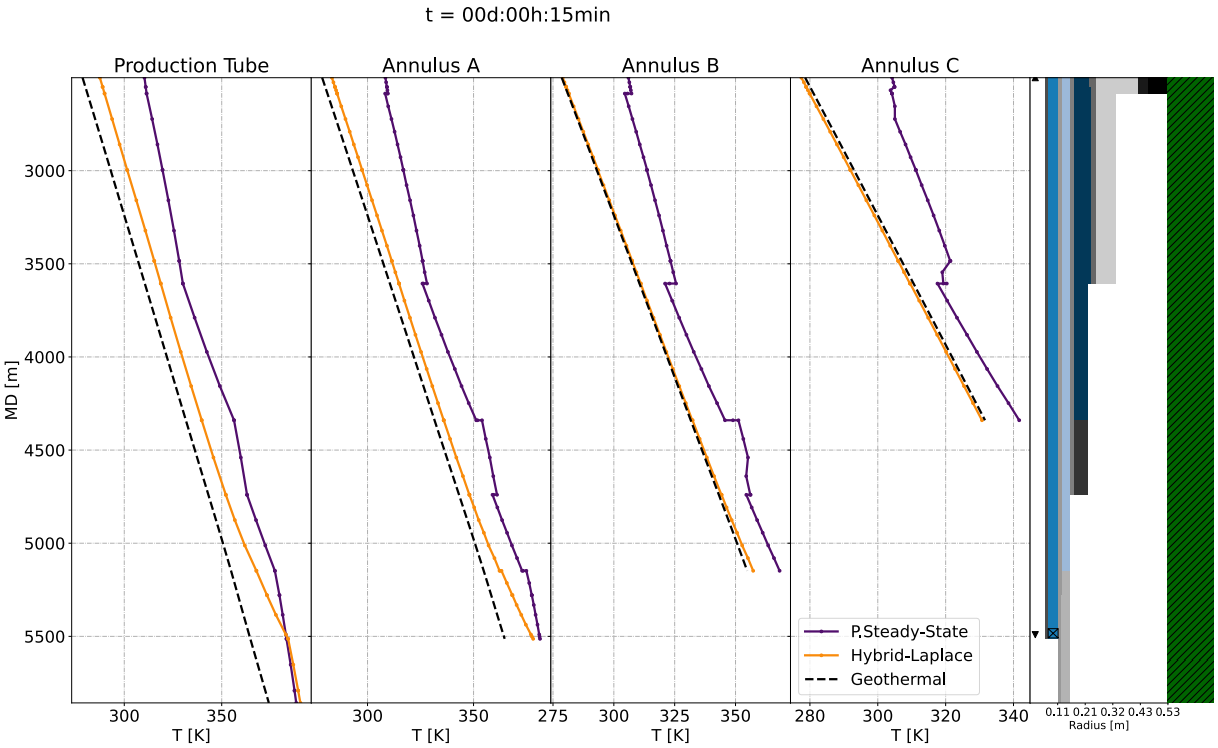

In the outermost annulus, annulus C, something that draws attention is the fact that the temperature slightly decreases in relation to the geothermal gradient, *i.e*, the initial temperature profile of the annulus. The average temperature drop was 1.05 K and, when analysing the reason for such a temperature drop, it was found to be related to the spatial discretization used. As the resistance-capacitance scheme is used it leads to a non-conservative solution of the heat equation. Thus, a small amount of energy is created and/or destroyed at each solution node of the thermal system. This fact leads to the temperature drop at the annulus under scenarios such as the one 15 minutes of production, where the heat front did not reach the annulus.

This phenomenon was first detected when, for shorter time simulations, the system became significantly unstable. The reason for that was exactly this reduction of temperature due to problems with the energy and mass conservation. During the iteration of the mass conservation, this reduction in temperature leads to iterations with larger steps, which causes the trial values for the iterative procedure to fall outside of the interpolation tables used. This was one of the greatest limitation of the Hybrid-Laplace method, as the stability of the mass conservation iteration may be compromised for shorter simulations.

Figure 69 depicts the temperature profiles at 12 hours of production. It shows that the annular volumes at deepest layers are already approaching the pseudo steady state, and only the layer surrounded by the cementation of the surface casing are still going through transient heating. The temperature difference between models is 3.63 K at the wellhead for the flowing fluid, while at the top of annulus A, the difference is 4.49

K.

Figure 69 – Temperature profiles predicted for the EWT well at 12 hours of production

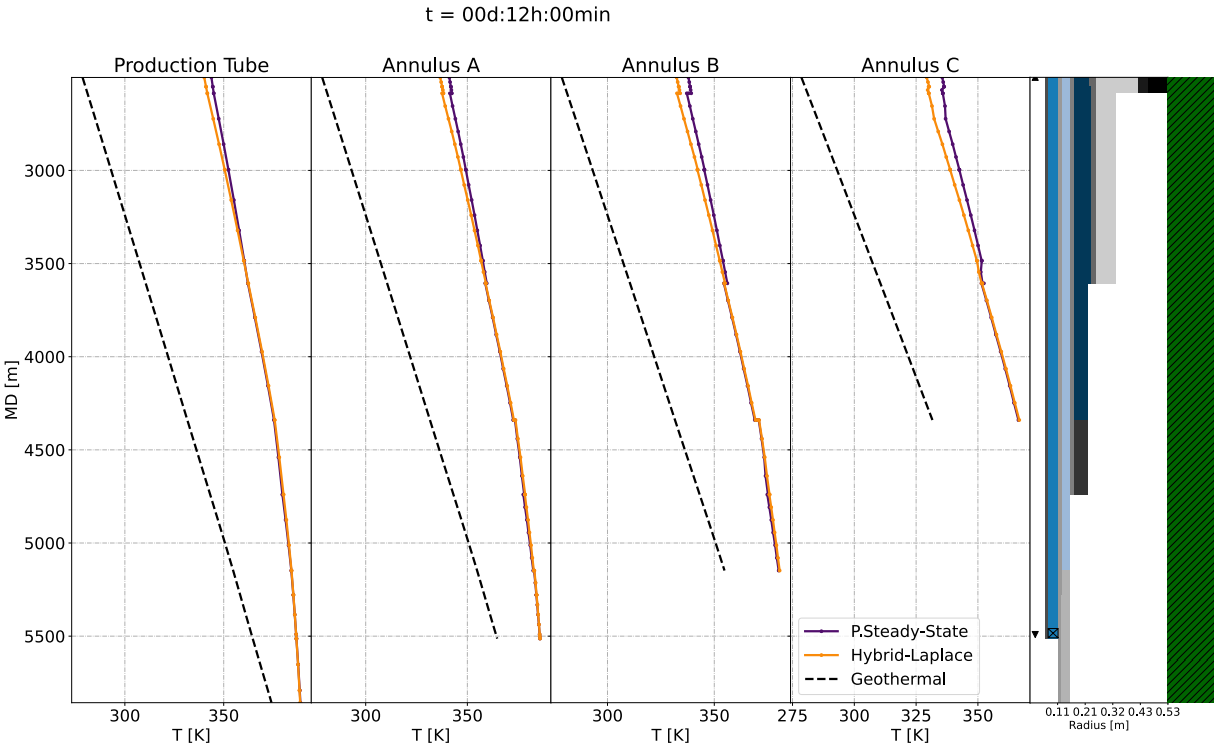

Given the speed under which the models reach the same solutions, it seems that before the end of the first day this well will already be operating under a pseudo steady-state condition for the annuli heating. To confirm this statement, it is possible to analyze the total heat transfer rate from the produced fluid shown by Figure 70. The heat transfer rate presented by both models is shown as a function of time and, as a result, it is clear that for 1 day of production the values of total heat transferred by the production fluid is similar in both models with a value of 1.32 MW. Also, as expected, the largest difference takes place at the start of heating process, before the first 6 hours of production.

Figure 70 – Total heat transfer rate from the produced fluid in the EWT well

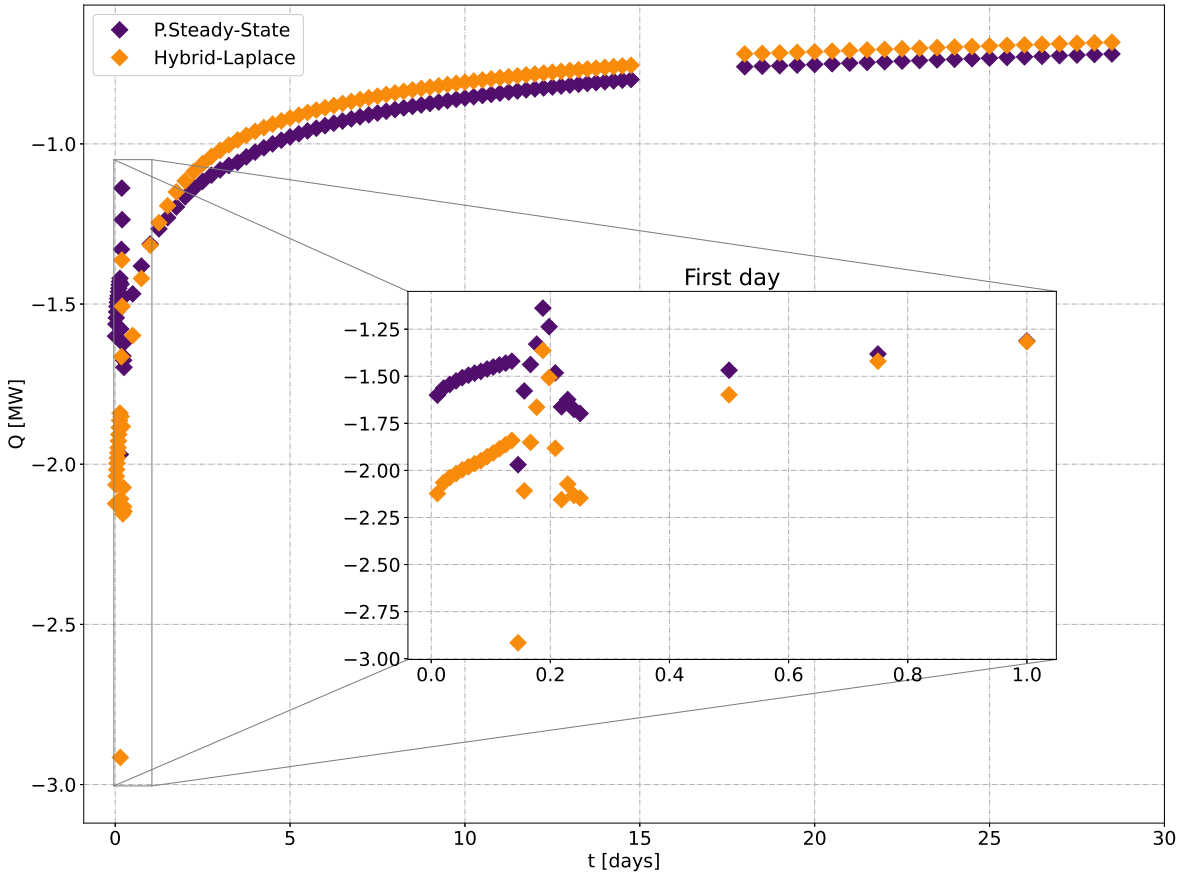

Figure 70 shows that, in the region where the flow rate is assumed constant (onset of production), the models predict a different behavior for the heat transfer. In this region, the idea that the Hybrid-Laplace model predicts higher (absolute values) heat transfer rates with a quicker decay is confirmed. After this point, the effects of fluctuations in flow rate affect each model differently, but the trend of higher transfer rates (in absolute terms), with a faster decay is recovered once the flow rate stabilizes at 12 hours.

After the first day, the pseudo steady-state assumption is already established, so analyzing the temperature profile from this point onward should return very similar curves with both models. This statement proved to be correct with Figure 71, where the temperature profiles are compared at 14 days of production.

Figure 71 – Temperature profiles predicted for the EWT well at 14 days of production

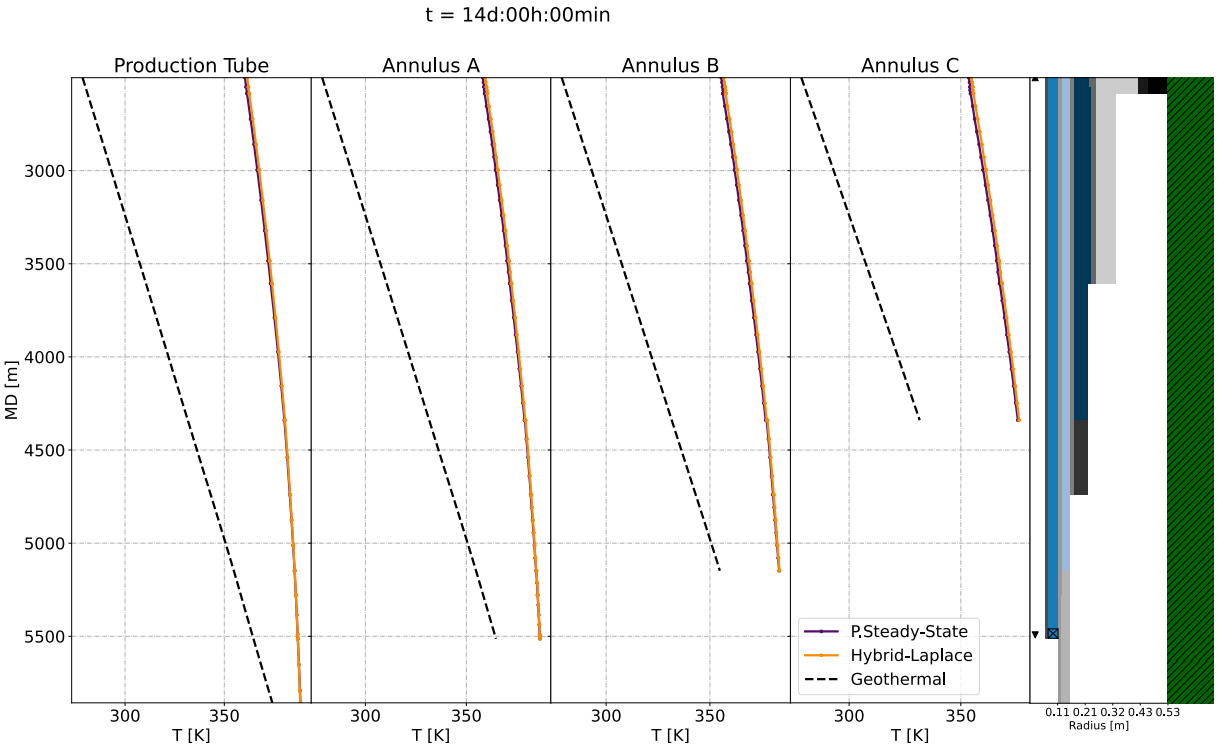

Once again, the temperature profile predicted by the Hybrid-Laplace model seems to be higher than the one predicted with the pseudo Steady-State model. Moreover, the agreement of both models is very good, again indicating that for sufficiently long times the Hybrid-Laplace model has a behavior similar to that of pseudo steady-state.

In terms of APB, this well does not have N_2 filling annulus A, so the expectation is that the models will return higher values of pressure increase in all three annuli. Also, due to the smaller compressibility of the fluid, the volume variation in annulus A will no longer be dominated by the neighboring annulus and by pressure effects in the production string, as was the case for the vertical well. In order to confirm these statements Figure 72 presents the APB in all annuli.

Figure 72 – APB predicted at each annuli for the EWT well by both proposed models

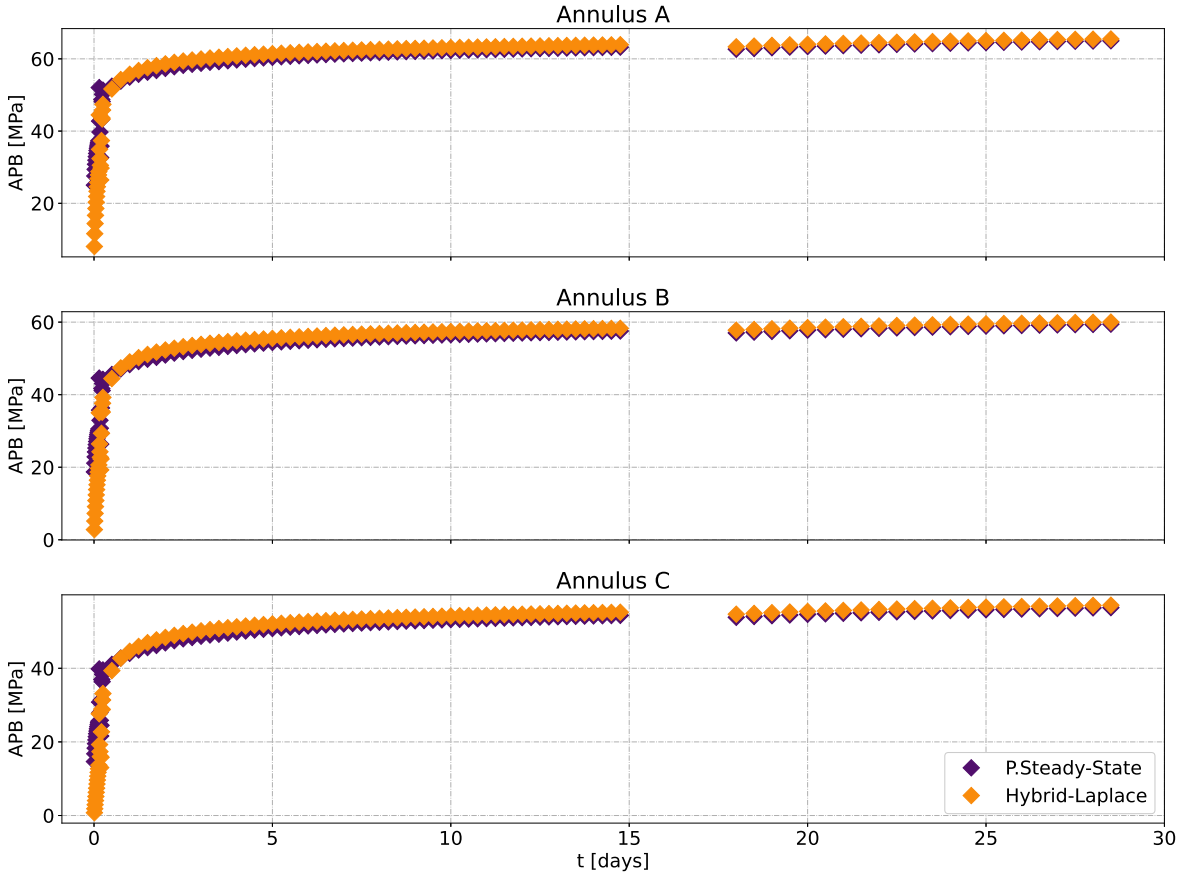

As indicated in figure, the pressure increase of annulus A was the highest among all annuli of this well. The predicted pressure increase reached its maximum value at the end of the second production interval, on the twenty-eighth day. The APB predicted in annulus A was 65.0 MPa by the pseudo steady-state model and 65.5 MPa by the Hybrid-Laplace model. In the other annuli, there is a slightly greater difference between the pressure increase predicted by the models with 59.34 MPa for the pseudo steady-state against 60.0 MPa for the Laplace model in the annulus B and 56.13 MPa for the pseudo steady-state against 57.14 MPa for the Laplace model in annulus C.

In order to better understand the difference between each model in shorter times, Table 5 presents the maximum difference of APB that the models presented in each annuli. In addition, it presents the moment when such difference was detected.

Table 5 – Maximum difference between the APB predicted by the models for each annulus, and the time at which the difference occurred

	Annulus		
	A	B	C
ΔAPB [MPa]	16.99	15.96	15.46
APB P.Steady-State [MPa]	25.03	21.12	19.52
APB Hybrid-Laplace [MPa]	8.04	5.16	4.05
Time of greater diff	15 min	30 min	60 min

This table shows that the speed of the pressure buildup is not equal in every annulus. As the maximum difference in pressure occurs at different times for each annulus, it makes clear that the capacitance term is acting in slowing the increase in pressure at the outer annuli.

This result is very important for this thesis, since one of the objectives in developing the Hybrid-Laplace model was to reduce the over estimation of the APB in the start of the production. Since the Hybrid-Laplace model considers the storage term in the heat equation for the annuli, the pressurization should tend to zero for very short times, as there is no time for the annulus to increase its temperature. This is confirmed for the outer annulus at 15 minutes of production, with the Hybrid-Laplace model predicting a APB of 2.80 MPa for annulus B and 0.76 MPa in annulus C. These values may still seem like a significant pressurization, however, when compared to the pseudo steady-state model, which predicted 18.71 MPa and 14.65 MPa respectively, it becomes clear that the new model does not suffer from the same high initial pressurization problem.

Figure 73 shows the volume variation of the annuli during production. As stated earlier, the volume variation of annulus A now follows the heating profile, more than the pressure effects in the production tube. Furthermore, as a consequence of the initial cooling predicted by the Hybrid-Laplace model, a small reduction in volume (0.022 m^3) was observed, contrary to the expansion predicted by the pseudo steady-state model (0.34 m^3).

Figure 73 – Volume variation in the annuli for EWT well

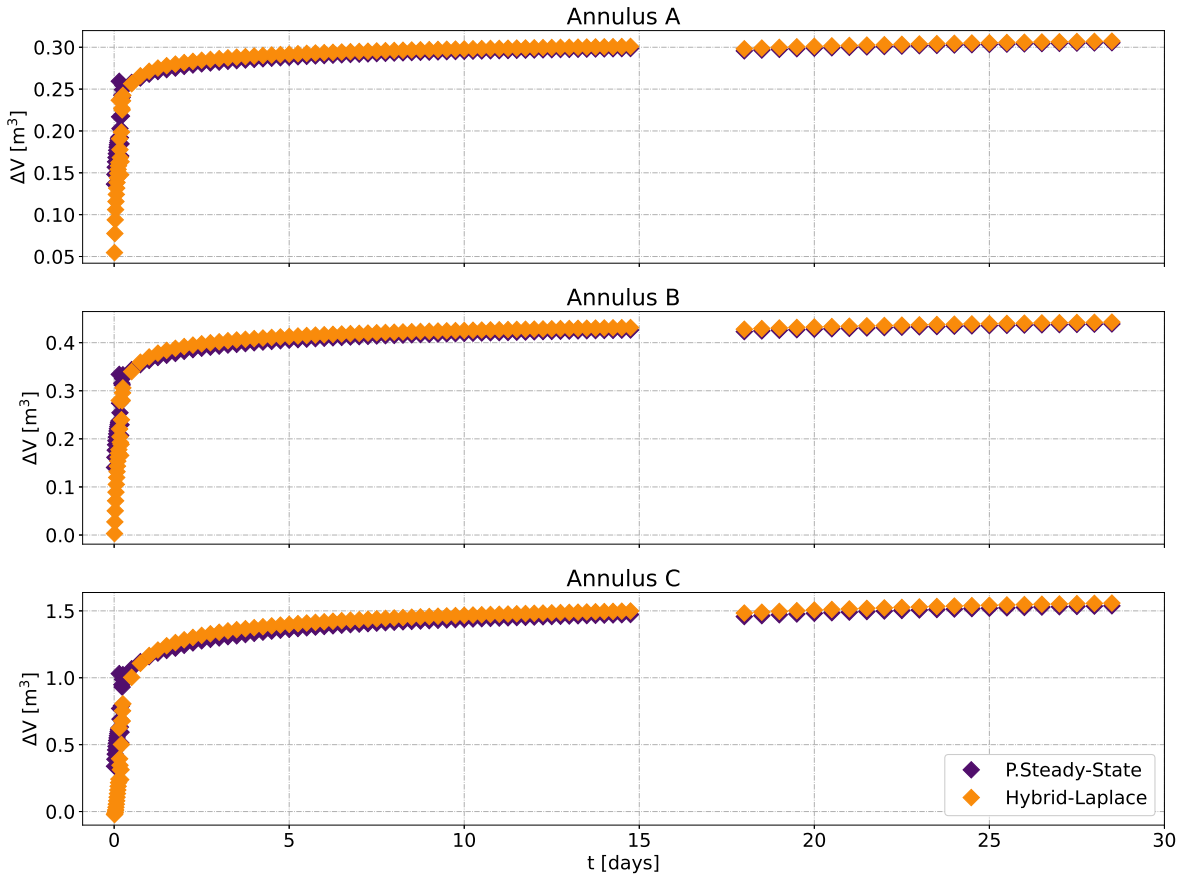

As the volume variation is a direct consequence of the deformation in casings and formation wall, Figure 74 presents the predicted strain of the EWT wellbore structure for 15 minutes of production.

Figure 74 – Strain profiles for 15 minutes of production in the EWT well

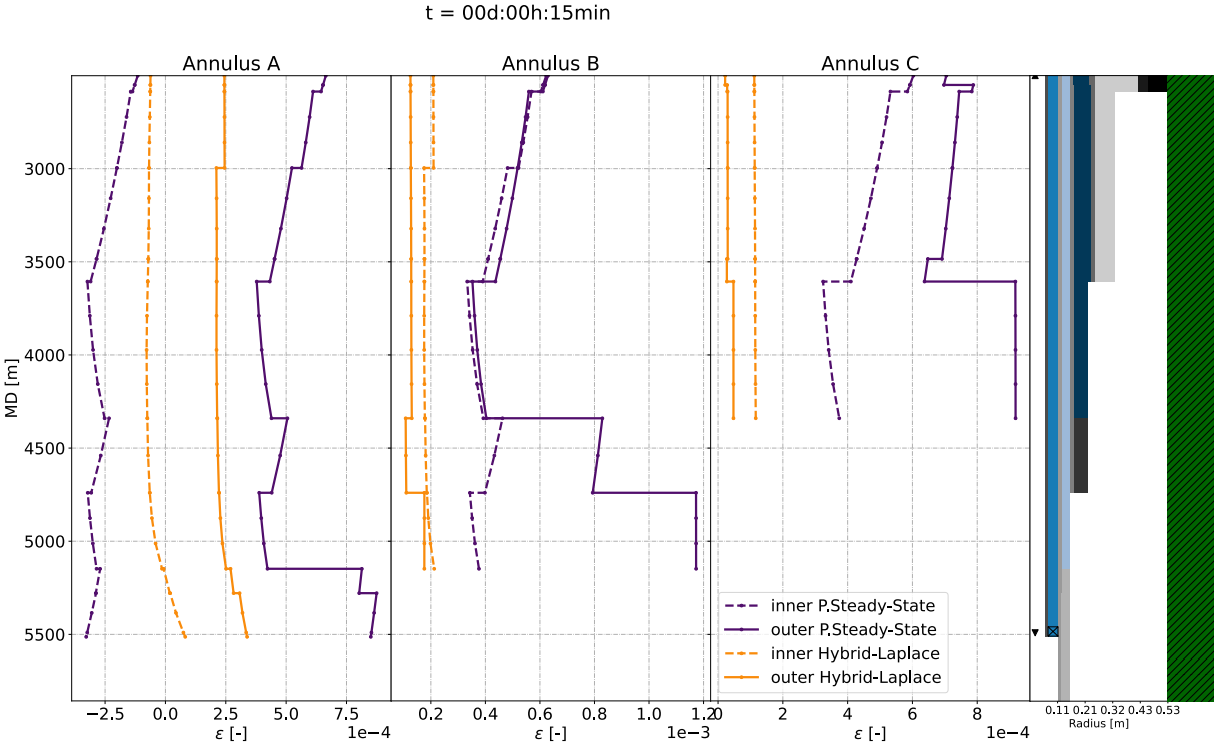

Once again, the inherent dependence of the strain model on the heat transfer at each layer is clear. However, contrary to what was detected in the first simulation of the vertical well, since this simulation is performed at shorter times, the discontinuities are not present in the results of the Hybrid-Laplace model. On the other hand, the pseudo steady-state already contains discontinuities related to the heat transfer in the wellbore. Another interesting aspect of using the Hybrid-Laplace model presented in this figure is the fact that, contrary to what is predicted by the pseudo steady-state, the strain of the first annulus seems to contract inward at certain depths. This interesting aspect indicates a completely different loading scenario for the casings, which should be taken into account for design purposes.

Beside this results, it is clear that, at least for the first 15 minutes, this well seems to stay within the 5% limit of strain. In order to ensure that this fact remains for longer times, Figure 75 presents the strain profiles for the 12^{th} hour of production.

Figure 75 – Strain profiles for 12 hours of production in the EWT well

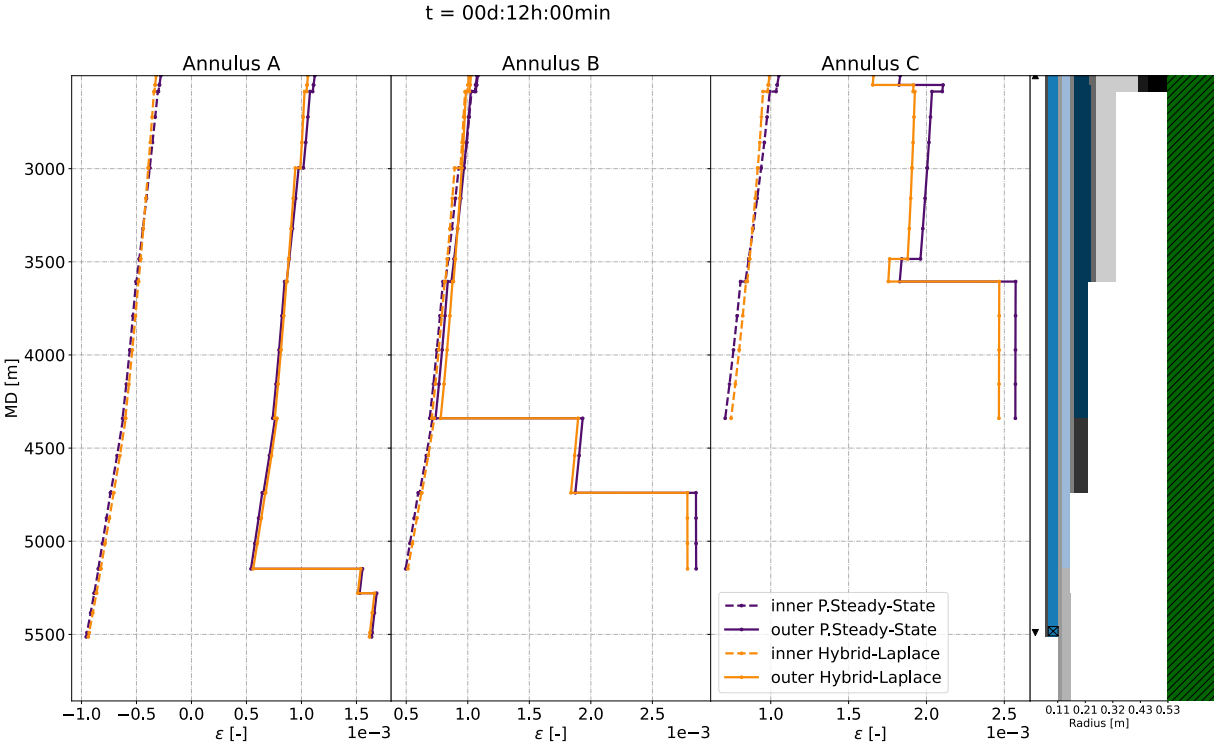

Similarly to the result presented in the temperature profiles at 12 hours of production (Figure 69), the main differences between the strains are located at annulus C.

Finally, Figure 76 presents the set of strains for 14 days of production. As can be seen, the two thermal models reach the same solution. In addition, even for 14 days of production, the strains are still within the safety margin.

Figure 76 – Strain profiles for 14 days of production in the EWT well

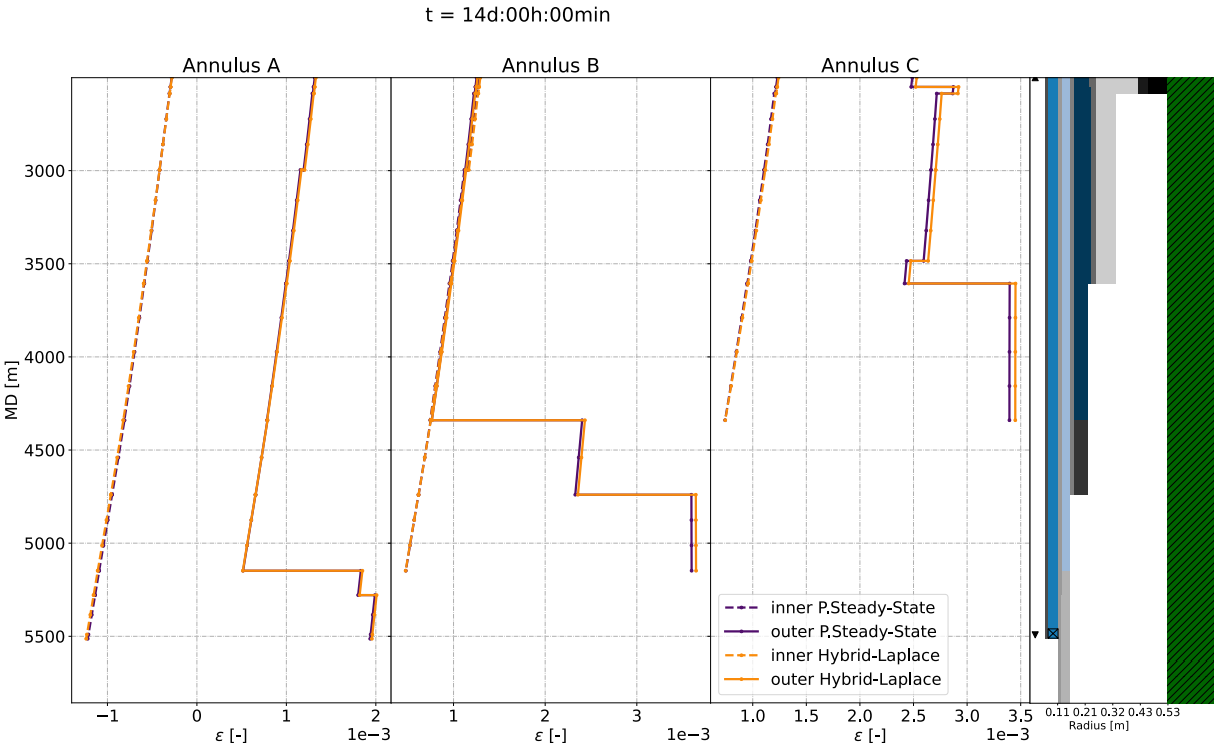

The results presented by the proposed models achieved good agreement with the field data for this new geometry. However, some unknowns still exist which may be significant and cannot be ignored. Next, a sensitivity analysis aiming to estimate the effects of such uncertainties in the models is presented.

5.2.2 Sensitivity analysis for EWT well

The sensitivity analysis initially focuses on the flow rate effects in the thermal models. This assessment is performed similarly to that carried out for the vertical well. Therefore, the same inputs will be used varying the flow rate within 60% of its original value.

Figure 77 shows the wellhead temperature variations for different flow rates, note that in this figure the *x-axis* represents the simulated time in which a set of comparisons is performed. The times were chosen to indicate different regions in the transient heating process, including some in which the pseudo steady-state assumption should not be valid, and others where the assumption is known to be valid. In this case, it is clear that for the first 15 minutes of production, even a reduction of 60% of the original flow rate would not be enough for the models to match the field data (see Figure 65). In this simulated time, the pseudo steady-state model overestimates the wellhead temperature by 34.60 K, so even in the most extreme scenario the deviation would still be around 19.0 K. For the Hybrid-Laplace model, the behavior is somewhat different, as the recorded deviation from the original field data was about 11.72 K. When carrying out

the study, it is noticed that for sufficiently short times the flow rate effect on temperature becomes very small when compared to the pseudo steady-state variations, so for 60% of reduction in flow rate the model would still deviate from the field data by 6.7 K.

Figure 77 – Flow rate effects on the temperature at the wellhead

(a) Pseudo steady-state model

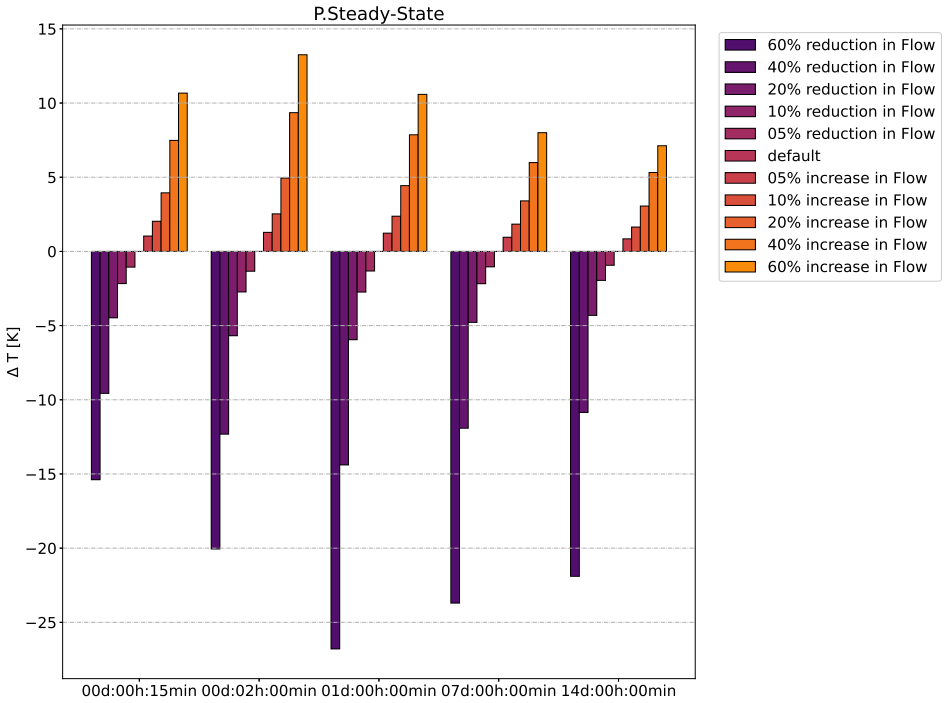

(b) Hybrid-Laplace

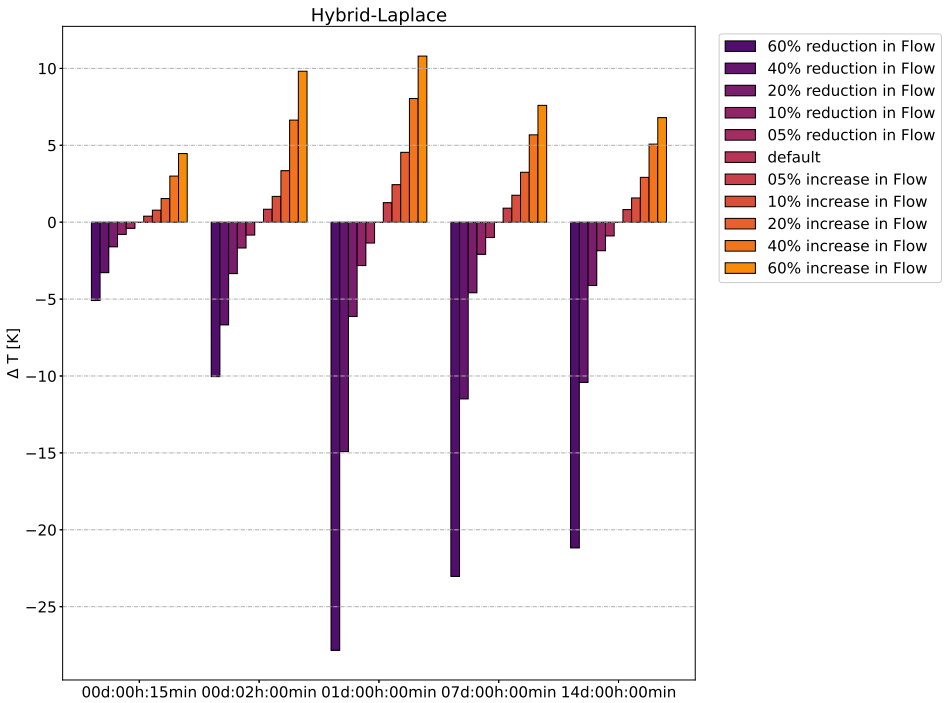

Also, in Figure 77, for 2 hours of production the effects of flow rate in the wellhead

temperature is more significant, up to the point that the data acquired at the TPT could be reproduced within this 60% margin of flow rate variation.

On the other hand, for one day of production a more complex phenomenon occurs. Similarly to what happened at 2 hours of production, the 60% variation of flow rate can reproduce the field data. The only problem in this statement is that, in order to reproduce the field data, the average flow rate should increase in relation to the original input used. This poses a problem, since in the previous comparison, a reduction in flow rate was required and, for the average flow approach, this meant reducing the flow rate, suggesting an inconsistency of the models. Therefore, it seems safer to state that both models have more difficulty in dealing with very short production times. Such a statement was already known for the pseudo steady-state model but it seems to be a common limitation for the Laplace model, even if on a smaller scale.

For longer times, such as past the 7^{th} day of production, both models manage to approximate the field data with higher accuracy. As a consequence, the real solution stays within a margin of 5% of variation in flow rate. For example, at 7 days of production a 5% increase in flow rate would actually make the pseudo steady-state outperform the Hybrid-Laplace method. For 14 days, on the other hand, this is inverted, as an reduction of 5% would lead to a better performance of the Hybrid-Laplace. As there are many unknowns in the measurement of the flow rate, as well as the associated GLR, it is difficult to indicate that a model is better than the other for longer simulation times.

Up this point, the focus of the sensitivity analysis remained within variations of flow rate, however, many approximations were made in order to describe the fluids of the wellbore. Barcelos (2017) analyzed the importance of accurately modeling the properties of the fluids. However, he did so by directly varying the concentration of the components used to model the drilling mud. This is surely a straightforward approach to better understand the effects of the drilling muds on the estimation of the APB. However, these fluids are complex and the real composition is not completely known. Therefore, in the present work, a new and more complete sensitivity analysis will be performed varying the properties directly. In other words, instead of varying the composition of the fluid, due to the complexity involved, the thermophysical properties themselves will be the focus of the sensitivity analysis.

Such analysis was performed considering the variation of the following properties: specific heat capacity, thermal conductivity, viscosity and base density. For the latter, it is important to explain that the expansivity and the compressibility remained constant. This is important since they are derived directly from the fluid density, which would lead to a more complex analysis for this property. Instead of varying all three variables simultaneously, this work will focus on the standard density of the fluid. The variations associated associated with each variable are calculated only for the standard values and are added to the tabulated values for each P and T pair used in the

interpolation tables.

Firstly, Figure 78 shows effects of uncertainties in specific heat on the results for wellhead temperature.

Figure 78 – Effects of c_P on wellhead temperature for EWT well

(a) pseudo steady-state model

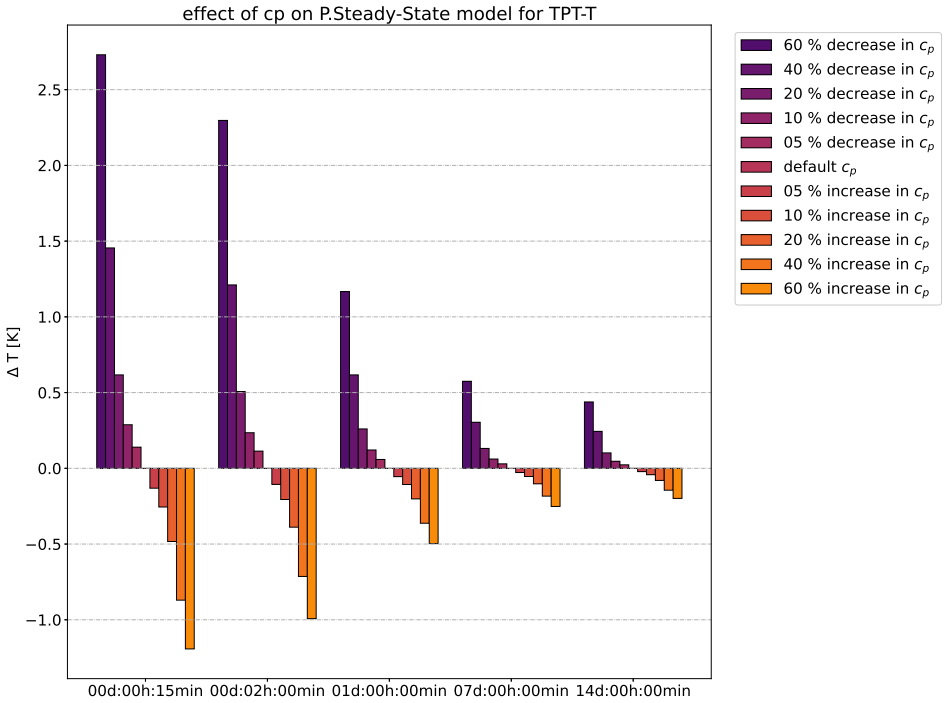

(b) Hybrid-Laplace model

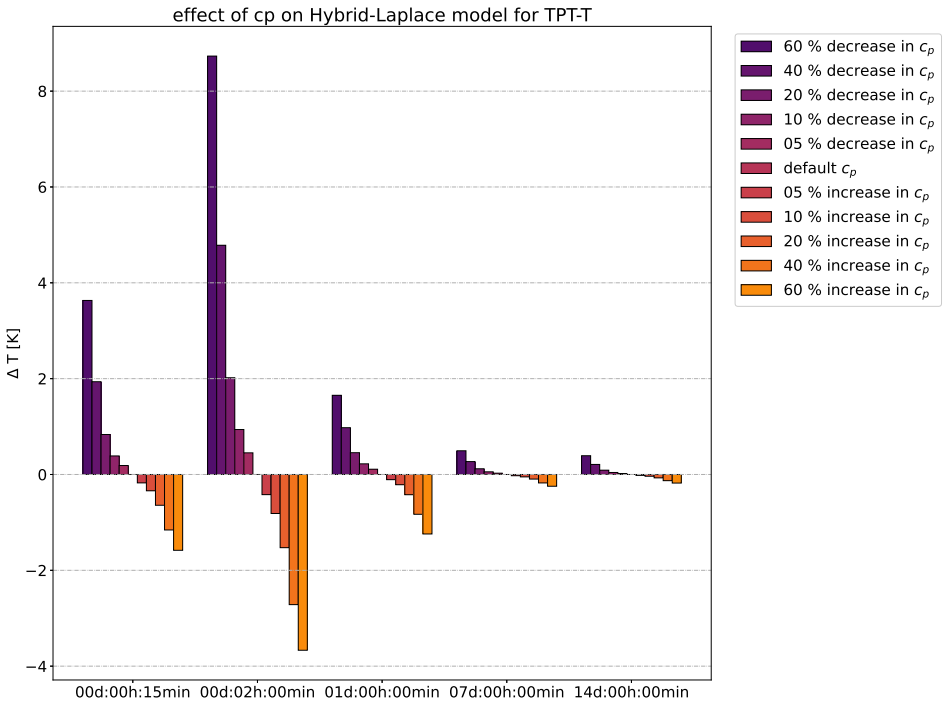

As the Hybrid-Laplace model considers the capacitance term in the heat transfer

at the annuli, this model has more pronounced effects of variations in the specific heat. In the pseudo steady-state approach, this variable only affects the *Ra* parameter for natural convection, so any variation in this variable is only perceived indirectly through the thermal resistances.

In relation to the results presented in Figure 78, an inversely proportional dependence between the heat capacity and the heating of the well becomes clear: for higher values of specific heat, colder temperatures are expected in the wellhead. In addition, it is noticeable that for long times the effect of this variable is reduced. In any case, the variation of c_p leads to small heating effects of the well, up to the point that a decrease of 60% in the value of this variable would have effects within a margin of 1 K in the wellhead temperature when the pseudo steady-state assumption is valid.

The effects of the specific heat of the drilling mud on the APB in the annulus A is shown in for the EWT well.

Figure 79 – Effects of c_P on APB on annulus A for EWT well

(a) pseudo steady-state model

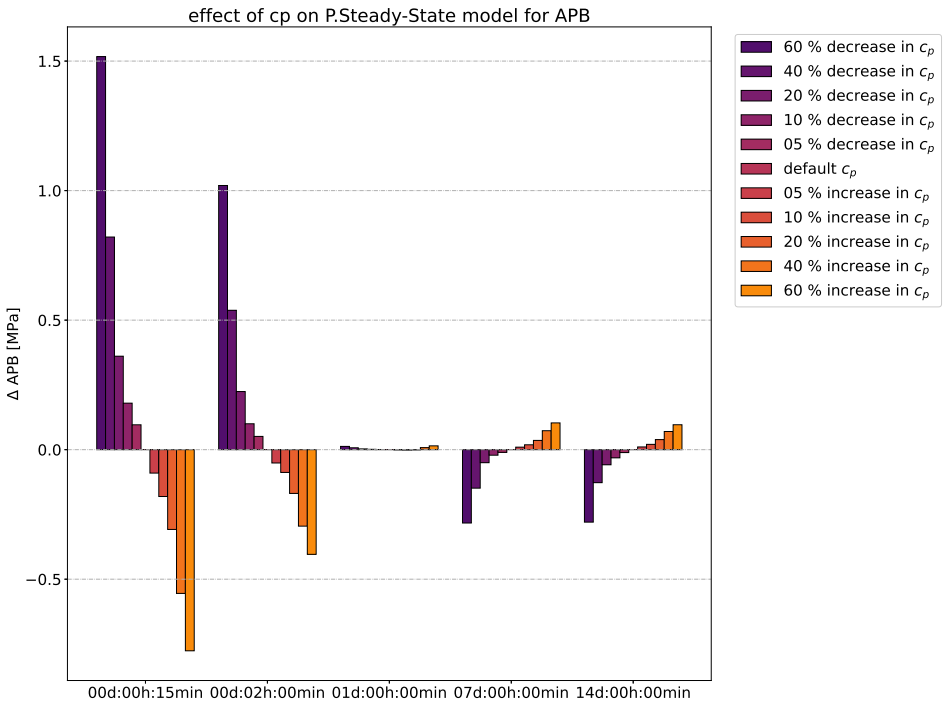

(b) Hybrid-Laplace model

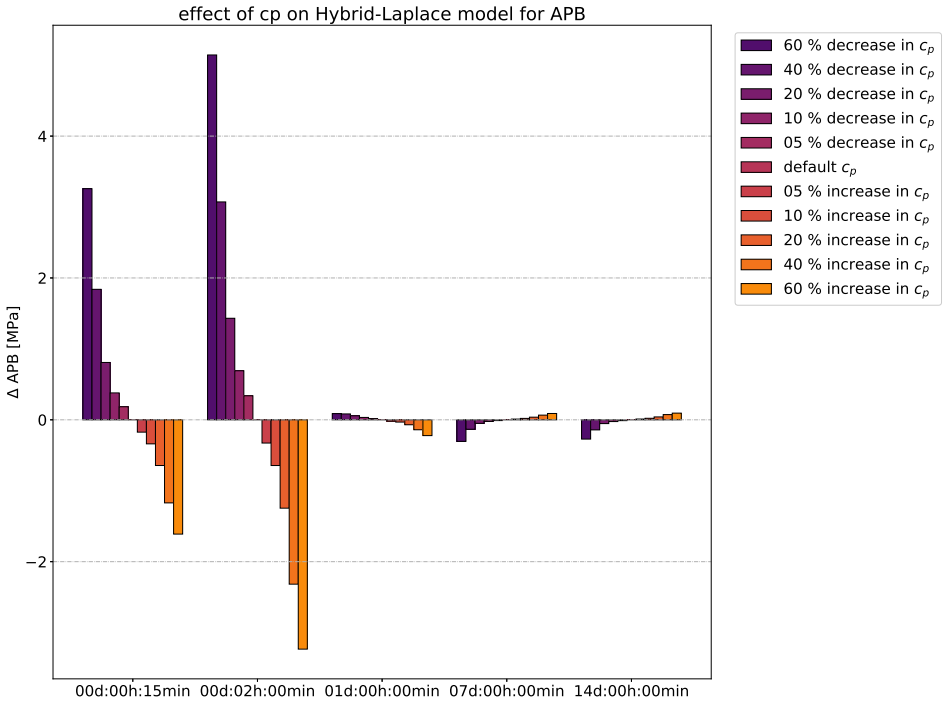

For shorter times (within hours of production), the effects of c_p are significant in the predicted APB, with a variation of 4.14 MPa for the Hybrid-Laplace model. In this initial time interval, the effects of c_p uncertainties and APB appears to be inversely proportional, however, after the annuli heats and the pseudo steady-state assumption is valid, this behavior appears to invert. But, for longer times, the effects of uncertainties

in c_p appears not to affect the APB significantly.

Figure 80 presents the variation in temperature at the wellhead of the EWT well for variations in the viscosity of the completion and drilling fluids.

Figure 80 – Effects of μ on wellhead temperature for EWT well

(a) pseudo steady-state model

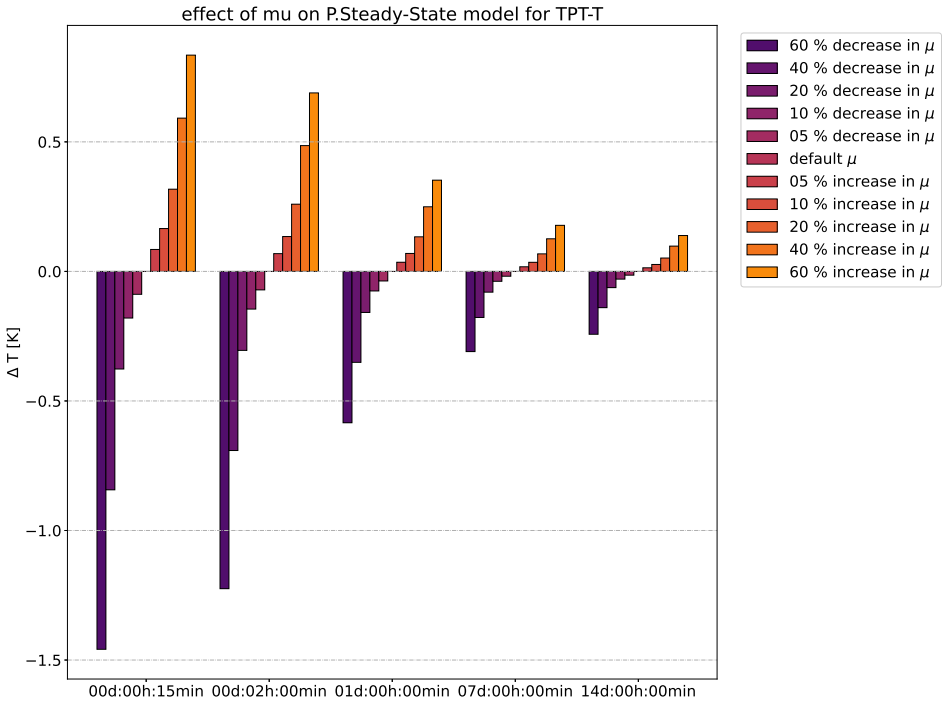

(b) Hybrid-Laplace model

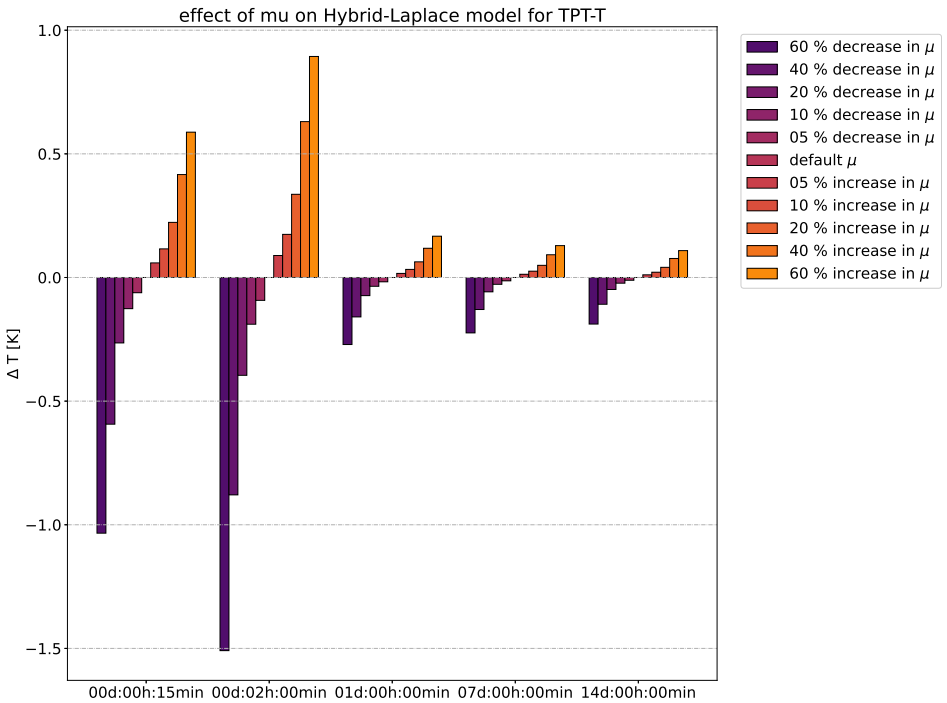

It is clear that, unlike with c_p, the relationship of wellhead temperature with vis-

cosity is directly proportional. This makes sense because when analyzing the terms necessary to calculate the thermal resistance by natural convection, the viscosity appears in the denominator of *Ra* number. In any case, the effects of viscosity are less pronounced than the effects of c_p for heat transfer, with a maximum difference detected of 1.51 K at 2 hours of production with the Hybrid-Laplace model.

In terms of APB, Figure 81 shows the effects of viscosity on the increase in pressure at annulus A.

Figure 81 – Effects of μ on APB for EWT well

(a) pseudo steady-state model

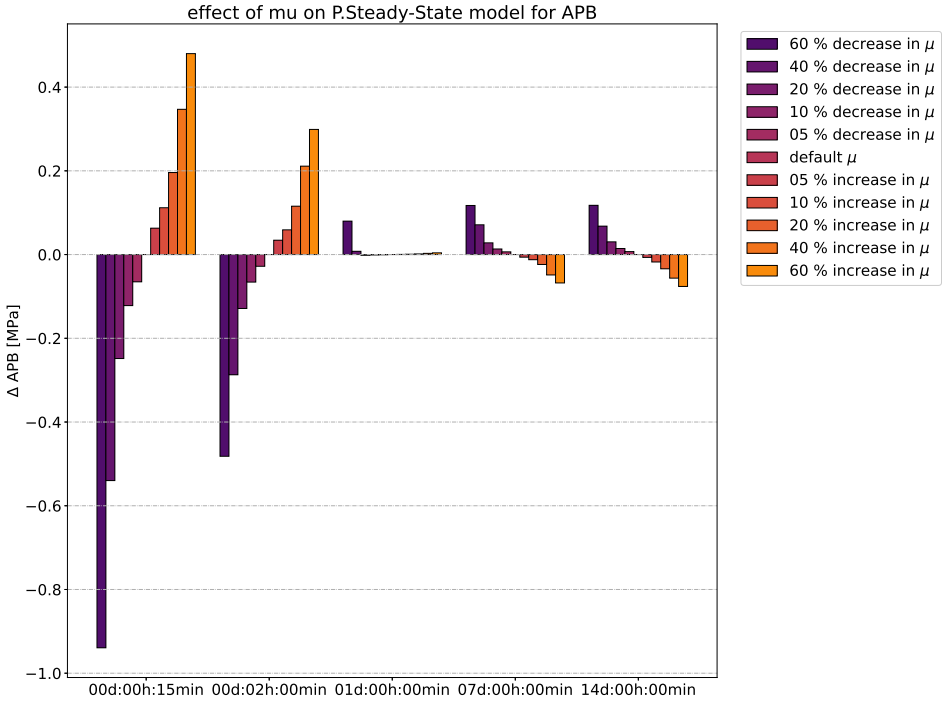

(b) Hybrid-Laplace model

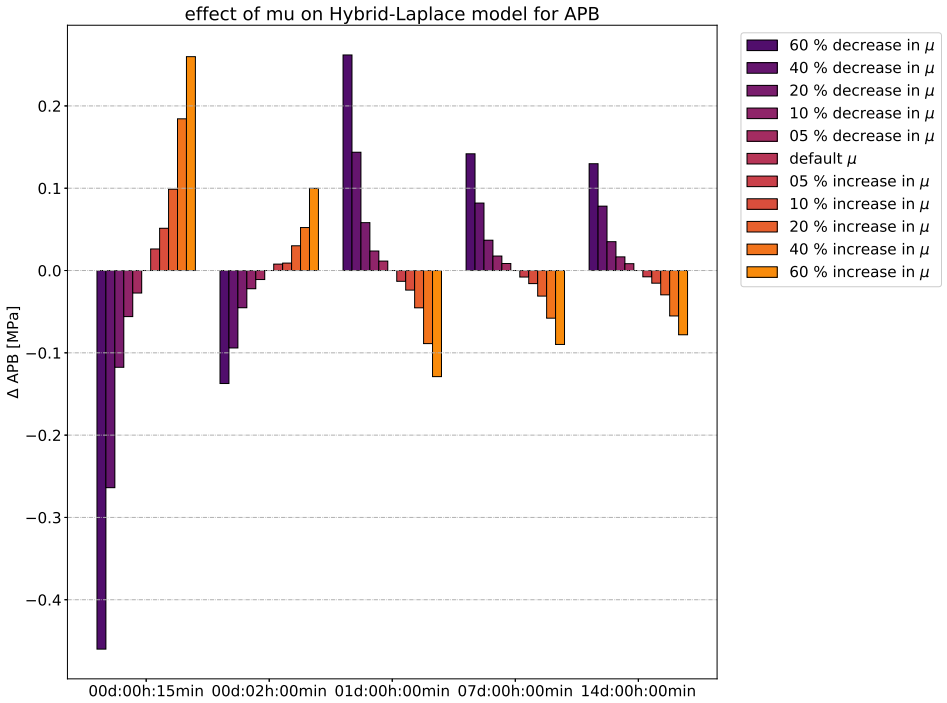

Compared to the c_p, the viscosity does not seem to affect the APB as drastically. The maximum variation detected was of 476 kPa at the first 2 hours of production with the pseudo steady-state model.

Here, the Hybrid-Laplace appears to be less affected by uncertainties in this variable than it was by uncertainties in the c_p. This makes sense as the viscosity

appears only in the thermal resistances, while c_p appears both in the resistance and in the actual energy conservation equation for the annuli (Equation 80).

Figure 82 shows similar comparisons in terms of temperature related changes as a function of thermal conductivity uncertainties.

Figure 82 – Effects of k on wellhead temperature for EWT well

(a) pseudo steady-state model

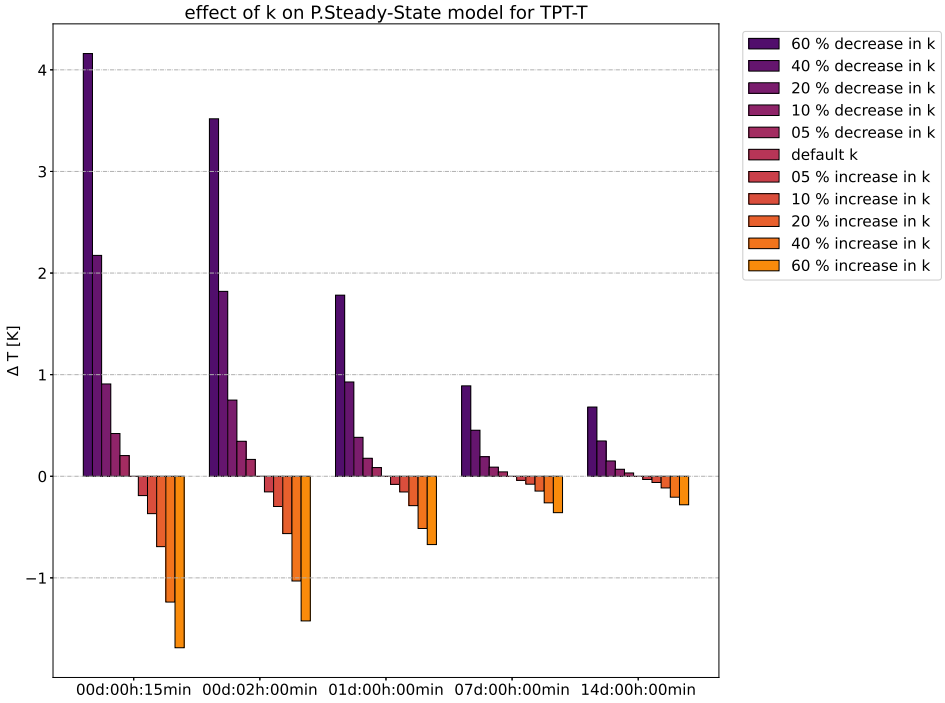

(b) Hybrid-Laplace model

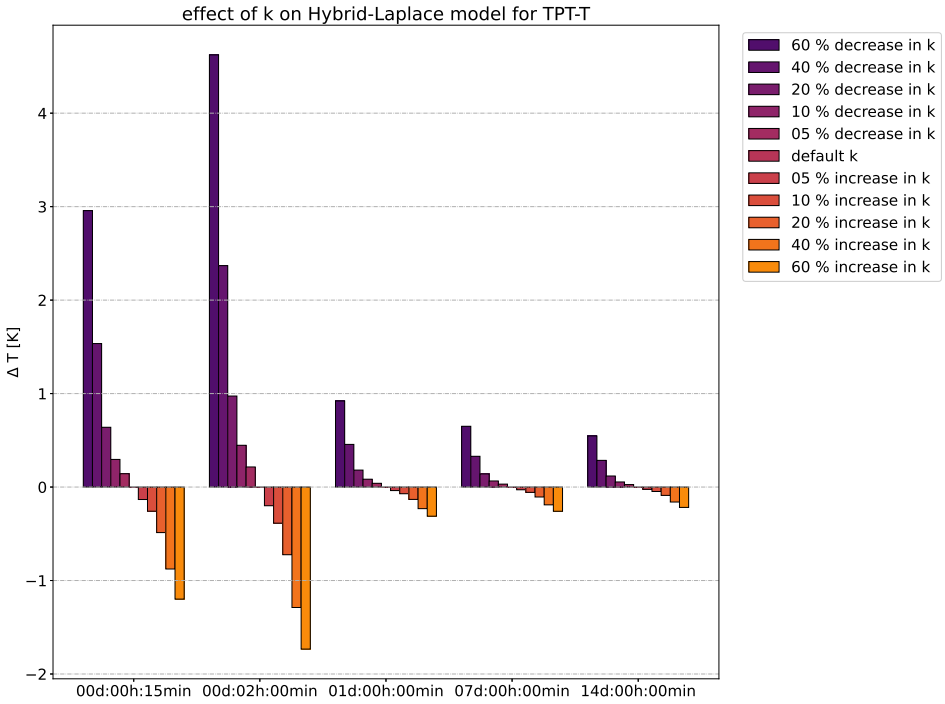

The thermal conductivity effects appear to be similar to those of c_p, with an inversely proportional dependence detected in the results. For shorter times, the effect of the thermal conductivity is stronger, decaying to a smaller dependency over time. In general, for longer simulations, the effects of variations in the thermal conductivity is less than 0.6 K.

Similarly to the viscosity, the thermal conductivity does not affect the APB significantly for longer times (see Figure 83). But, at the start of the production the effects this variable is more perceptible, especially with the pseudo steady-state model.

Figure 83 – Effects of *k* on APB for EWT well

(a) pseudo steady-state model

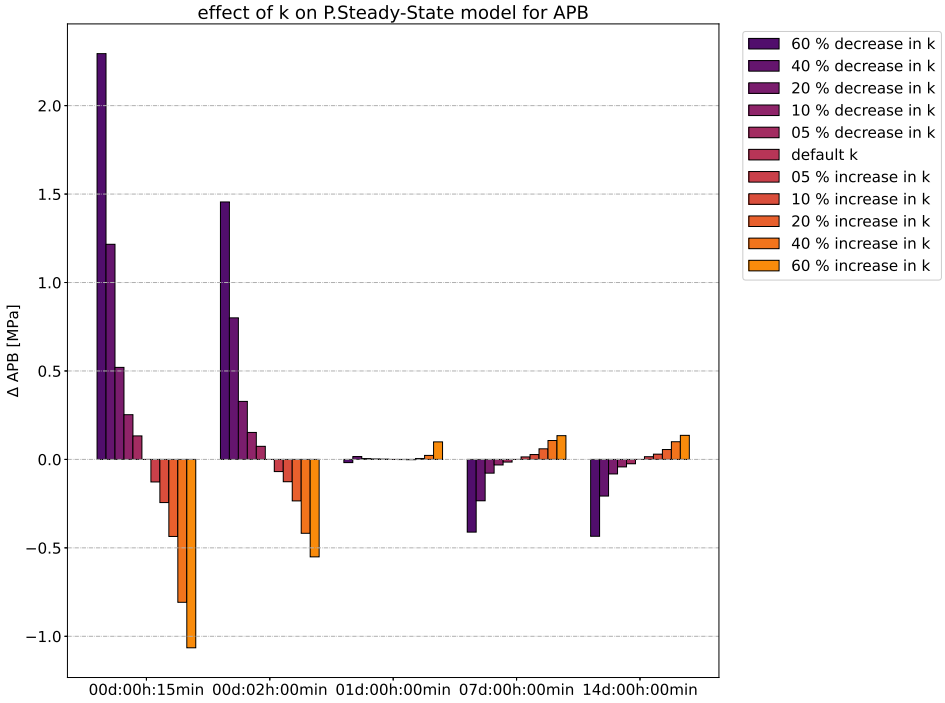

(b) Hybrid-Laplace model

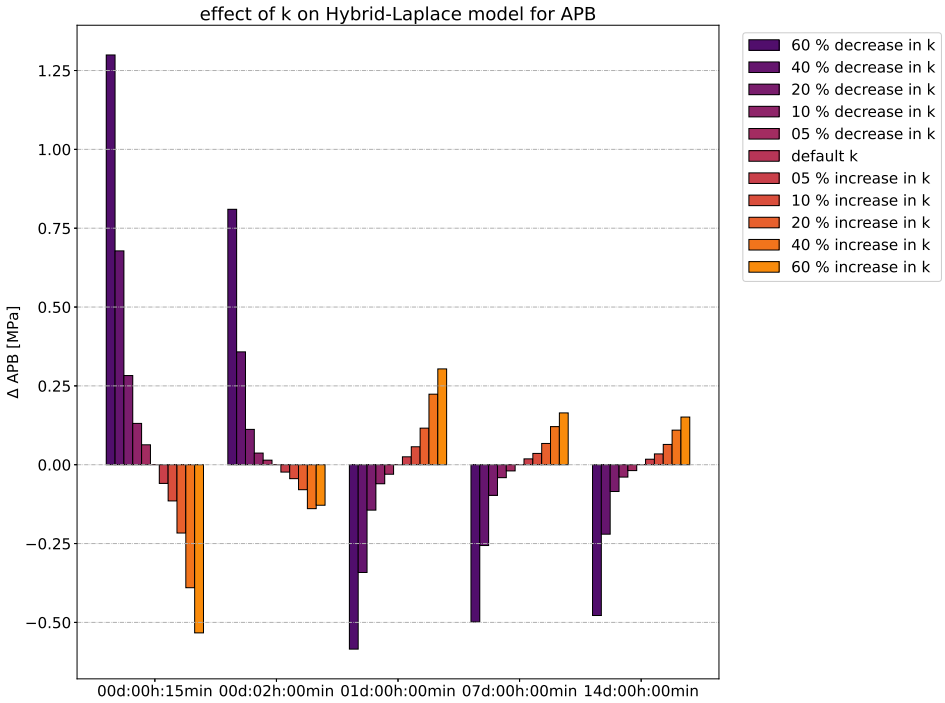

Once again, the strange behavior after the second day of production (inversion of dependency in the resulting APB) is observed. However, it is clear that, any of the studied variables can lead to a poor predictions of APB as a consequence of incomplete compositional characterization.

The last variable analysed was the base density of the mud and the completion

fluids. Figure 84 shows how the uncertainty in this variable translates to variation in the wellhead temperature.

Figure 84 – Effects of ρ on wellhead temperature for EWT well

(a) pseudo steady-state model

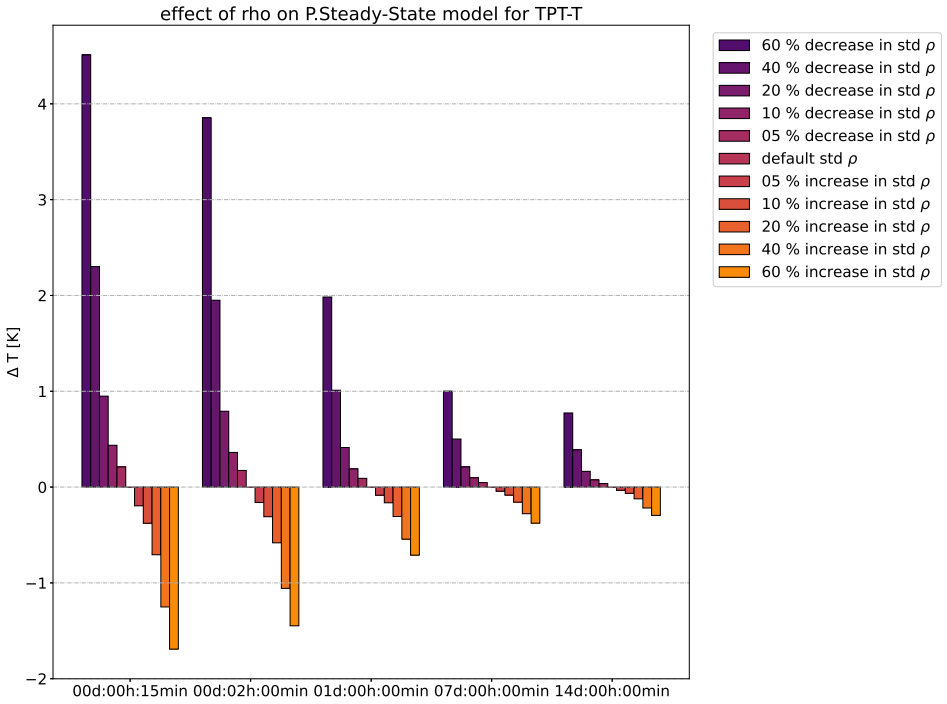

(b) Hybrid-Laplace model

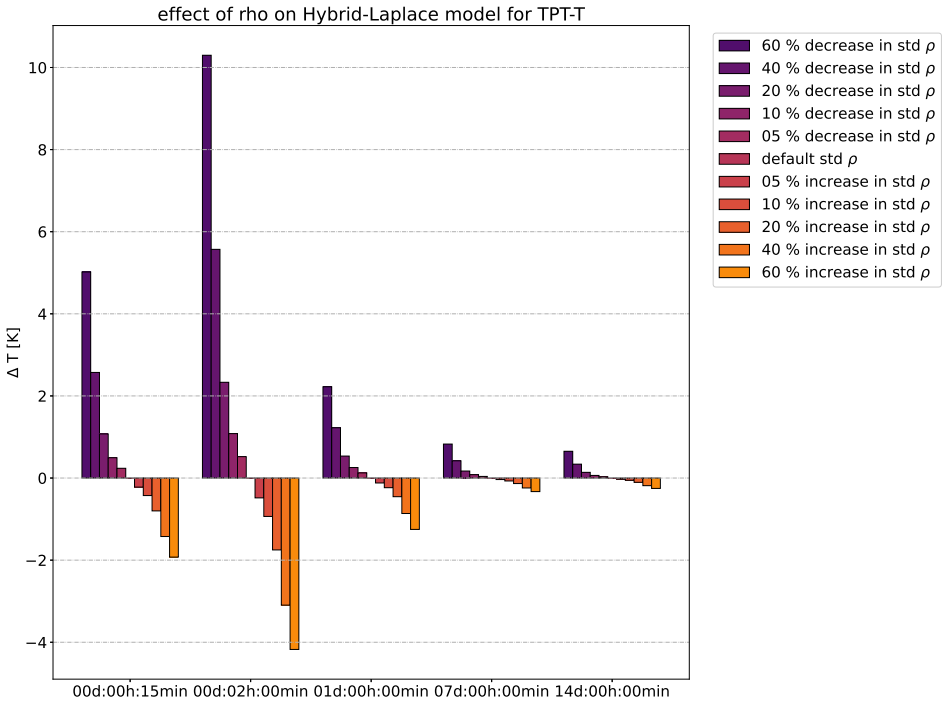

The effects of density in the wellhead temperature is similar to those of c_p, however, with slightly larger amplitude. This was expected as both ρ and c_p appear

together in the energy conservation, thus leading to a similar behavior. In addition, this figure shows that uncertainties in density are more significant than any other variable analysed.

This last statement is even more critical when the analysis is performed regarding the effect on APB for annulus A, presented by Figure 85. Since APB is a phenomenon dominated by the mass contained in each annulus, variations in density affects the initial condition of the problem. As a result, the pressure increase becomes much more pronounced even without taking into account the variations of the fluid expansivity and compressibility .

Figure 85 – Effects of ρ on APB for EWT well

(a) pseudo steady-state model

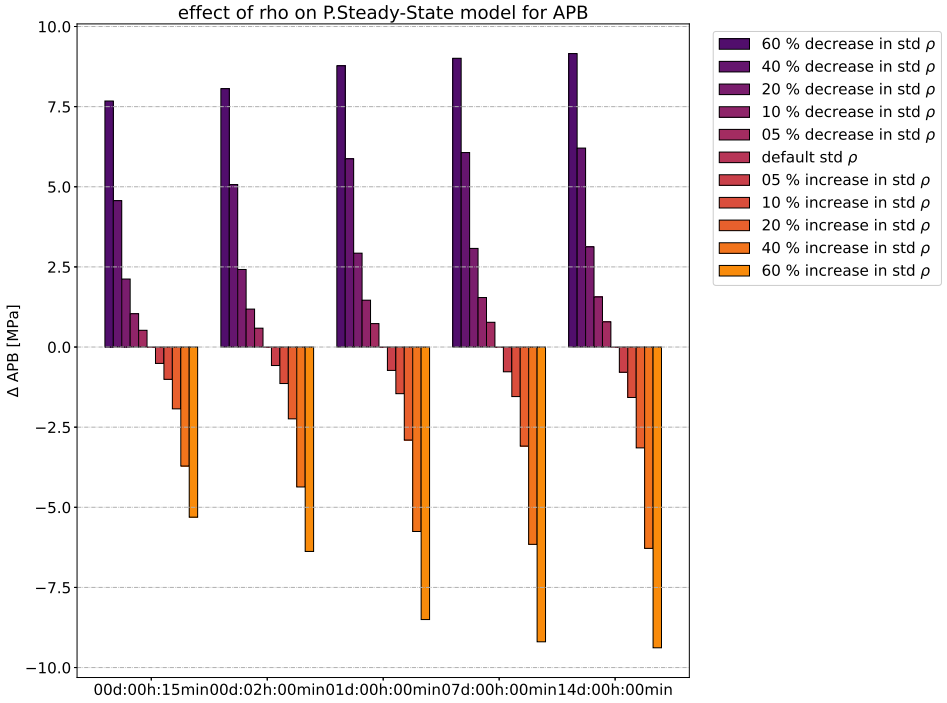

(b) Hybrid-Laplace model

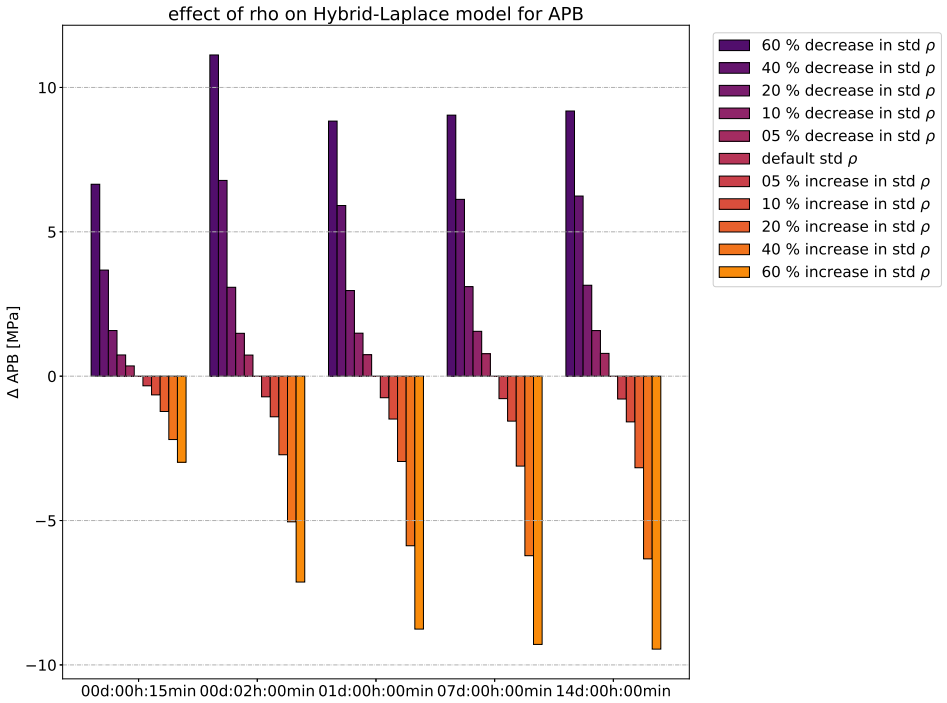

Notice that, especially at 2 hours of production, the predicted APB with the Hybrid-Laplace model can vary 11.06 MPa, which is a 47% variation with respect to the original estimation. Also, for both models, the effects of the density in the estimated APB increase over time. As the maximum APB during a production operation will occur at longer times, this indicates that the correct representation of the standard density is

required to properly model the phenomenon.

Also a last interesting result here is the fact that heavier fluids tend to lead to smaller APB. This, however, does not mean that the use of heavier fluids would lead to safer wells, as part of the casings resistances would be “consumed” by the initial loading, due to hydrostatic pressure. So a suggestion for future works is to study optimal weighting of both drilling and completion fluids in order to enhance safety factors considering APB.

5.2.3 Summary of results for EWT well

As with the vertical well, a brief summary of the main results of the studies with this well is now presented.

The EWT well is in a state which allows for better analysis, *i.e.*, starting its first production. Also, there is more information in relation to the field data for this well, with data for flow rate which can be used to improve the inputs of the simulation.

In order to take advantage of such information, some considerations can be made. Firstly, it was detected a perceptible lag in the flow rate measurements (28 minutes in relation to PDG data). Also, there is a region within the first 3 hours where the flow rate is not properly measured, so an extra treatment was necessary. Basically, for this initial region, a threshold value of 615 $m^3\,d^{-1}$ was extrapolated and, for the remainder of the simulated interval, a average flow function was used.

As a result of the well starting its production for the first time and the adoption of a new approach when dealing with provided data, the numerical results were promising. Both the pseudo steady state model and the Hybrid-Laplace model were able to predict with high accuracy the wellhead temperature and pressure during the production.

Disregarding a initial region of production, where the flow rate data had problems, both models were able to maintain deviations from the measurements from the TPT within 5 K and 500 kPa. When comparing the models, the Hybrid-Laplace model presented a greater precision against the pseudo steady-state, with an average of over 4 K in precision.

In terms of APB, unfortunately it was not possible to compare the predicted results with field data for the innermost annulus. However, as shorter times were simulated it was possible to compare the physical behavior of both models in regions where the pseudo steady state assumption is not suited. When doing so, it was possible to attest that the Hybrid-Laplace model has the characteristic of predicting zero APB for shorter times, this does not happen in the pseudo steady state model as was presented in Barcelos (2017).

From the sensitivity analyzes two major conclusions emerged. The first is that the inaccuracy of the results in the initial points simulated cannot be directly attributed to the lack of knowledge of the actual production flow rate data, this may indicate a

limitation of both models in modelling the initial production. In addition, among the properties analyzed, it is clear that from all the properties analysed, the density is the most crucial when modeling APB.

5.3 WELL WITH SALT LAYER

This well has a large layer of salt exposed to annulus B. Due to an incomplete data set, it will not be possible to carry out an analysis as complete as the one presented in the previous section, i.e., from the onset of production. In the present well, flow data are not known and the well underwent some operations prior to production, so thermal studies will be limited to comparing thermal models with each other without evaluating results with field data.

The proposed Salt Creep model is investigated in three fronts. The first, and most important, is the assessment, over long times, of the creep model coupled with the transient heat transfer model and its comparison with the purely elastic deformation model. Then a comparison is made between the creep formulation using the two different heat transfer models (Hybrid-Laplace and pseudo steady-state). This comparison is important because it reveals the importance of using transient models in this scenario. Finally, the thermal expansion module is activated. This case is analyzed separately because there is still no clear contribution in the literature that includes such terms; even in studies that consider the creep for modeling of APB do not take into account the thermal expansion (ALMEIDA, 2016).

As is often the case in real field data, the instrumentation in this well is not complete, so there is no pressure gauge installed in the second annulus. As a result, validation against field data is impossible for this model. In addition, as the available data were for an EWT scenario, there was no time for the creep induced annular volume variation to affect the APB significantly. Nevertheless, the comparisons are still useful to point out the importance of creep considerations in the design of the completion column.

The well geometry is presented in Figure 86. It consists of an offshore well under a water depth of 2333 m. Since the well goes through a layer of salt, it has a vertical inclination until it crosses such a layer. So, in this section, there is no differentiation between TVD and MD. However, as done with the previous vertical well, the inclinations terms will be used in the simulations. The completion of this well is extremely different from the previous ones due to an intelligent completion with two production zones. Because the program originally developed was not capable of modeling such a scenario, an approximation was made to consider that the well ends at the depth of the packer that seals the bottom of annulus A. As a result, all the lower layers of the well are disregarded for the study. It should me mentioned that such an approximation can be made because the PDG is located above the packer, and it does not affect the solution.

As seen in Figure 86 the entire exposed section of annulus B is assumed to be surrounded by Halite. This is, in fact, an approximation as other rock types may be present in the formation surrounding the actual well. However, because this is the most common evaporitic rock found in the Brazilian pre-salt, it is common practice to consider layers of salt as a single layer of Halite. Additionally, the figure shows the position considered to be bottomhole in 4956 m. This well also has two completion fluids in annulus A: down to a depth of 3386 m annulus A is completed with MEG, and below it the annulus is filled with brine. For the produced oil, the complete composition is presented in the Appendix B.

Figure 86 – Geometry of well with a salt layer

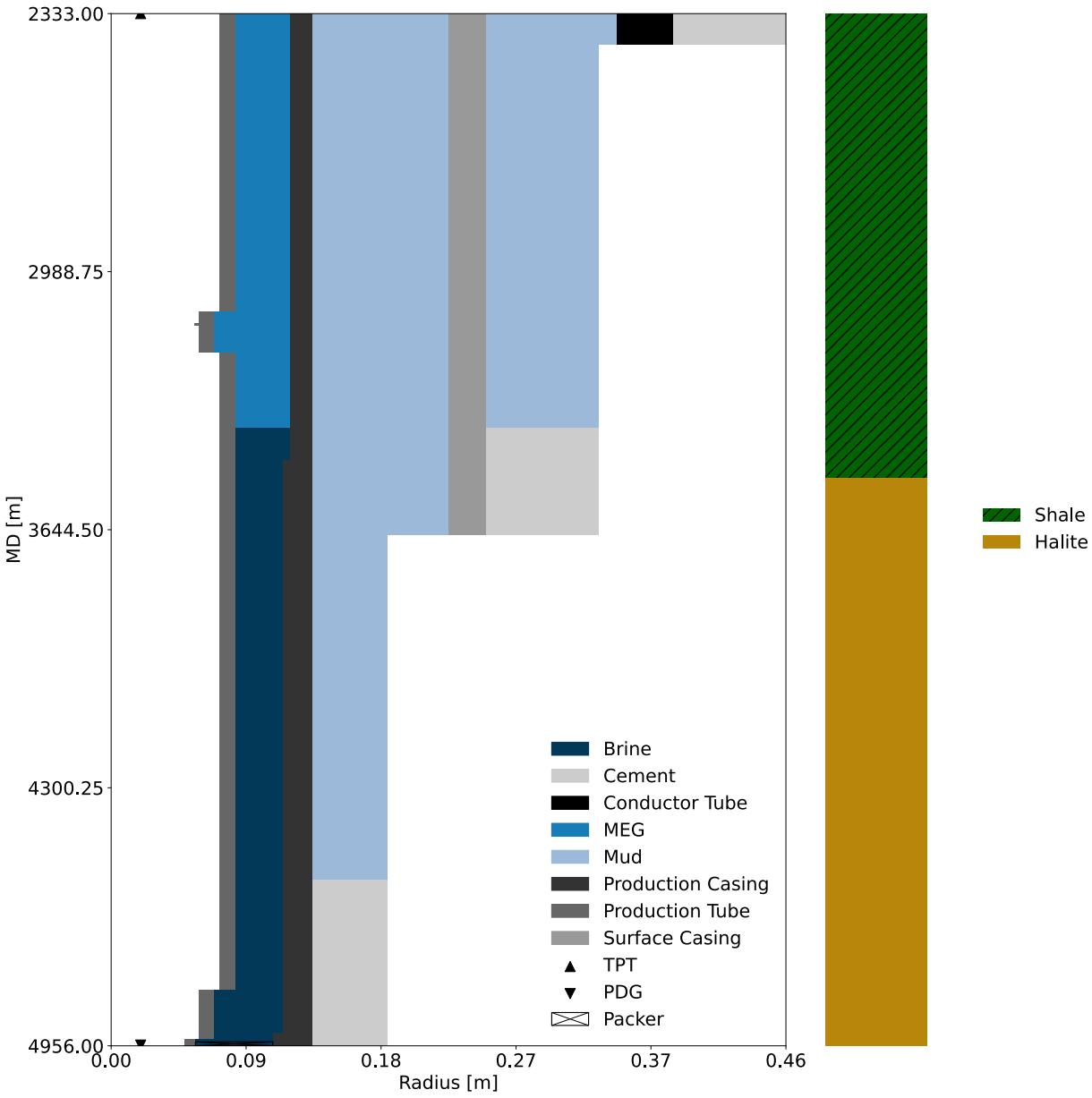

The PDG of this well is located at a depth of 4954 m. Since data from this meter were provided for some days of operation, an average of the pressure and temperature

was used, namely 55.01 MPa and 336.55 K. Also, it is known from the well operator that the flow rate was around 4747 $m^3\,d^{-1}$ at the beginning of its production life, so this value is adopted in the present study.

An important aspect to be discussed is the temporal discretization used in the salt creep model simulations. This was not an issue in the thermal models described previously, as history effects are not present in the purely elastic behavior attributed to the other wells. Here, due to the non-linearity of in the creep law, it is necessary to use a linearized approach to approximate the march in time. As a consequence, an appropriate temporal discretization is required in order to guarantee precision in the final solution. After testing some approaches, a simple mesh stretching formula was chosen, which guarantees the inclusion of simple parameters for calibration. The formula is given by Fletcher (1991):

$$s = \chi_1 \eta^* + (1-\chi_1)\left(1 - \frac{\tanh(\chi_2 - \chi_2 \eta^*)}{\tanh(\chi_2)}\right) \tag{139}$$

where s is the stretch factor for a given grid spaced in η^* domain. χ_1 and χ_2 are parameters related to the stretching.

In practical terms, once certain values appropriate for the stretching parameters are determined, the same time spacing is used for all subsequent studies. Their selection will be discussed in Section 5.3.2 along with the mesh convergence for the creep model.

Figure 87 shows the geothermal gradient for this well. Similar to the vertical well, there is a deviation in the gradient when crossing the saline region. As this layer is much longer than in the other well, it has a much more noticeable effect.

Figure 87 – Geothermal profile for well with a salt layer

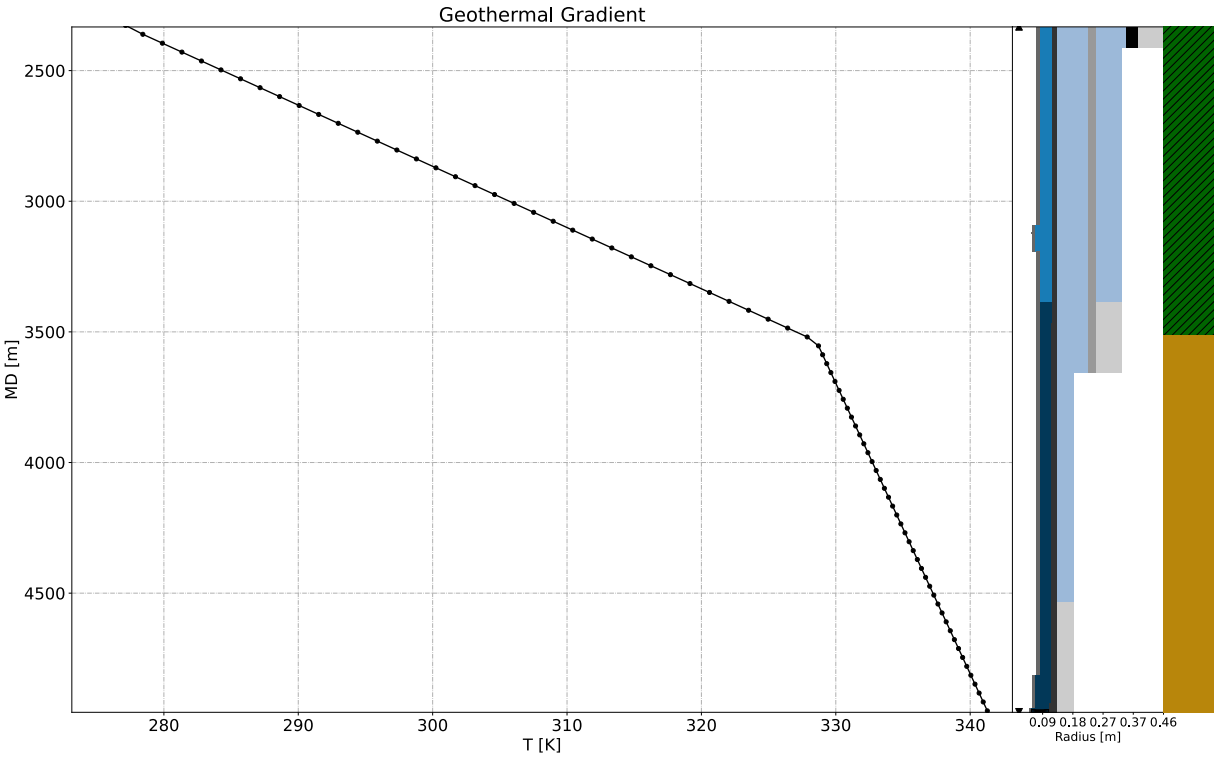

Another very important variable for the simulation of APB coupled with strain of salt layers is the overburden gradient. Figure 88 shows this gradient in its most usual form, equivalent to the density. This is in fact the most convenient form, as the salt deformation model is developed to receive this variable directly. To convert this gradient into the overburden stress itself, one may use Equation 95. However, in the algorithm, the linear interpolation as presented in the numerical model was used.

Figure 88 – Overburden gradient for well with a salt layer

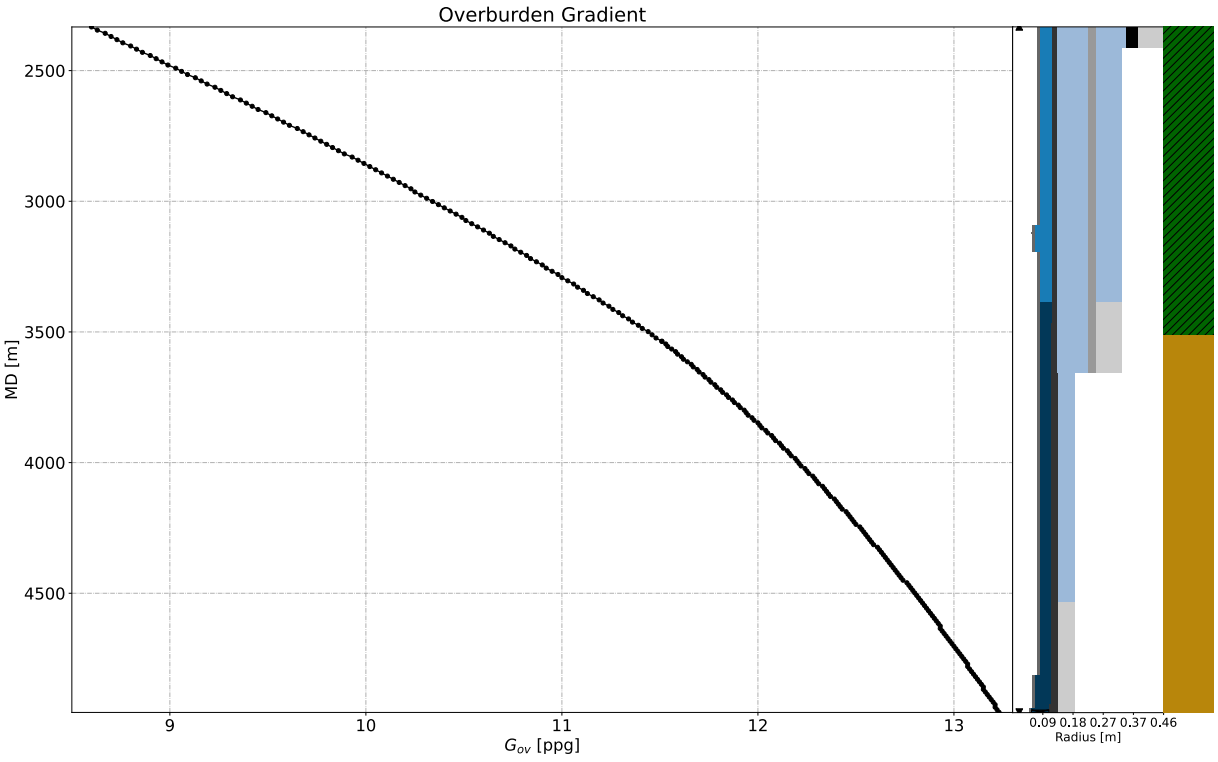

5.3.1 Thermal results

Contrary to the previously presented wells, in these simulations, the Hasan and Kabir (1991) time function was not used. As the temperature of the salt layer will be used later in the simulations of the creep displacement, it was opted to use Equation 7 with the numerical inversion algorithm. By doing so, the same kind of approximation of the formation interface is achieved, with the possibility of estimating the temperature in the salt layer when required.

As this well contains a salt layer, even in the purely thermal analysis, simulations as close as possible to the onset of production were carried out. However, none of the models were capable to simulate times shorter than half an hour. The reason was the same type of limitations mentioned in the EWT well for shorter simulations. Thus, in the simulation for a production time of 30 years, starting at 30 minutes of production, 125 intervals were used with the parameters $\chi_1 = 1.0 \times 10^{-5}$ and $\chi_2 = 9$.

Figure 89 shows the temperature increase at wellhead for the first 10 days of production. Note that this well undergoes a slower heating than the previous ones, with the Laplace model only exceeding the temperature predicted by the pseudo steady-state model after 3 days of production. At the first simulated point, 30 minutes, the temperature difference in the head is 4.46 K, which is the smallest difference between the models for all studied wells, even though it appears to be the well in which capacitance effects are observed for the longest time. The reason for this is the flow rate used in the study (4747 $m^3\,d^{-1}$), which is the largest value used in all three wells. As a

consequence the thermal resistance of the forced convection is reduced, thus leading to a higher heat transfer rate. This allows for the temperature inside the production string to settle quickly when compared to the annuli.

Figure 89 – TPT temperature for first 10 days of production in well with salt

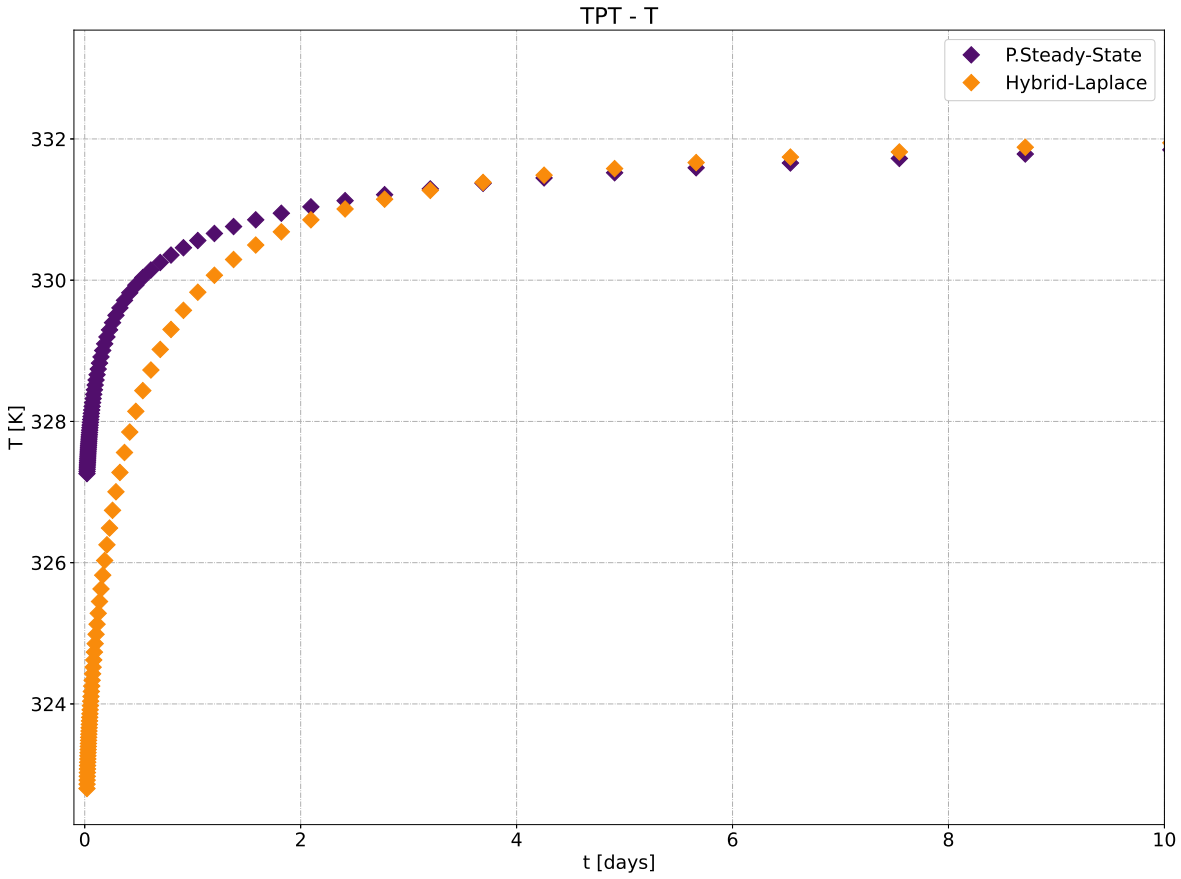

Figure 90 presents the temperature at the wellhead for the entire 30 years of production. Notice that the difference perceived in the first simulation point reduces with time, up to the point that at the end of the simulation this difference becomes 0.01 K. This value can be attributed to the tolerances used in the convergence of the thermal system.

Another interesting result is that the temperature increase seems to take place within the first couple years of production. At the end of the first year, the wellhead temperature is already close to 333 kelvin, and remains close to that until the end of the 30 years. At the last simulated time the value of the wellhead temperature is 333.02 K.

Figure 90 – TPT temperature for 30 years of production in the well with a salt layer

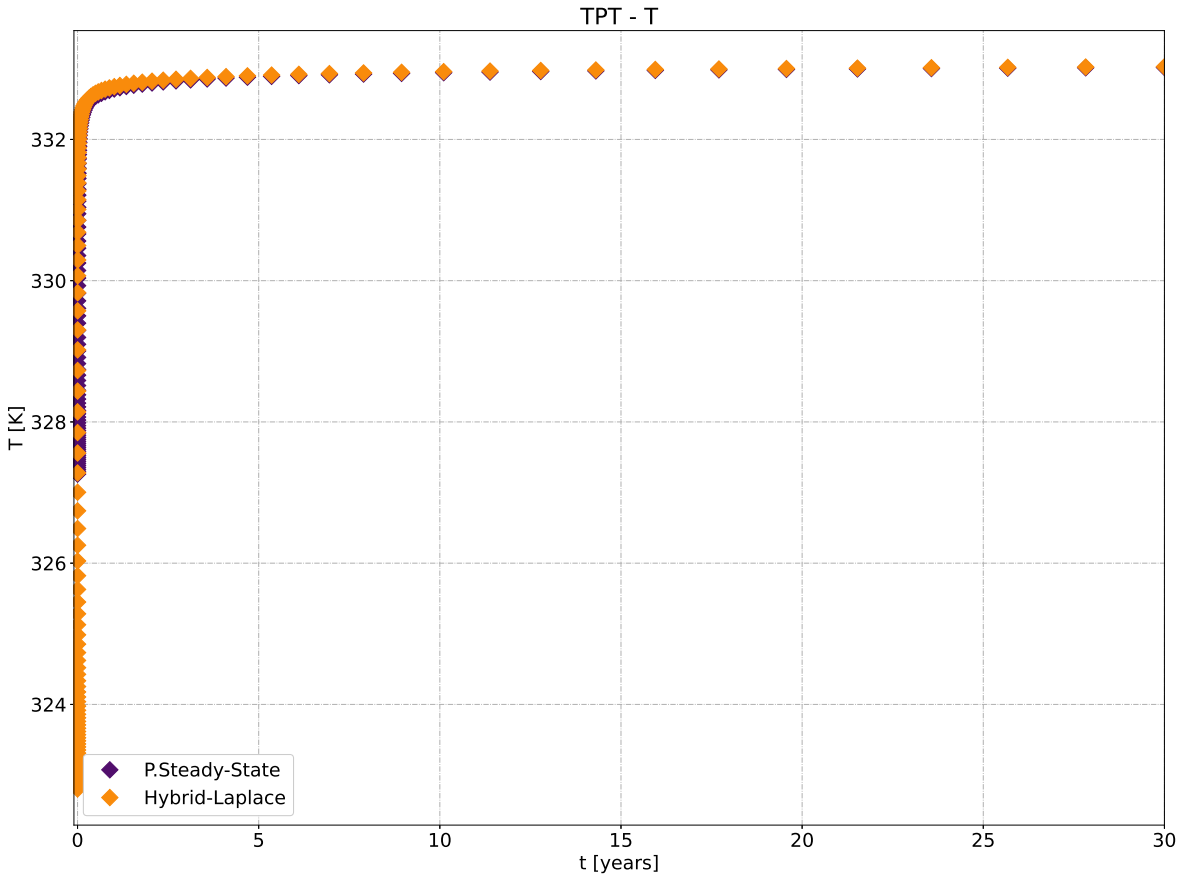

Figure 91 shows the temperature profile inside the well for half an hour of production, similarly to what happened with the previous wells, the pseudo steady-state model shows discontinuities associated with geometry variations. On the other hand, the Laplace model is smooth while still heating the outer annuli.

Figure 91 – Temperature profiles at 30 min for the well with a salt layer

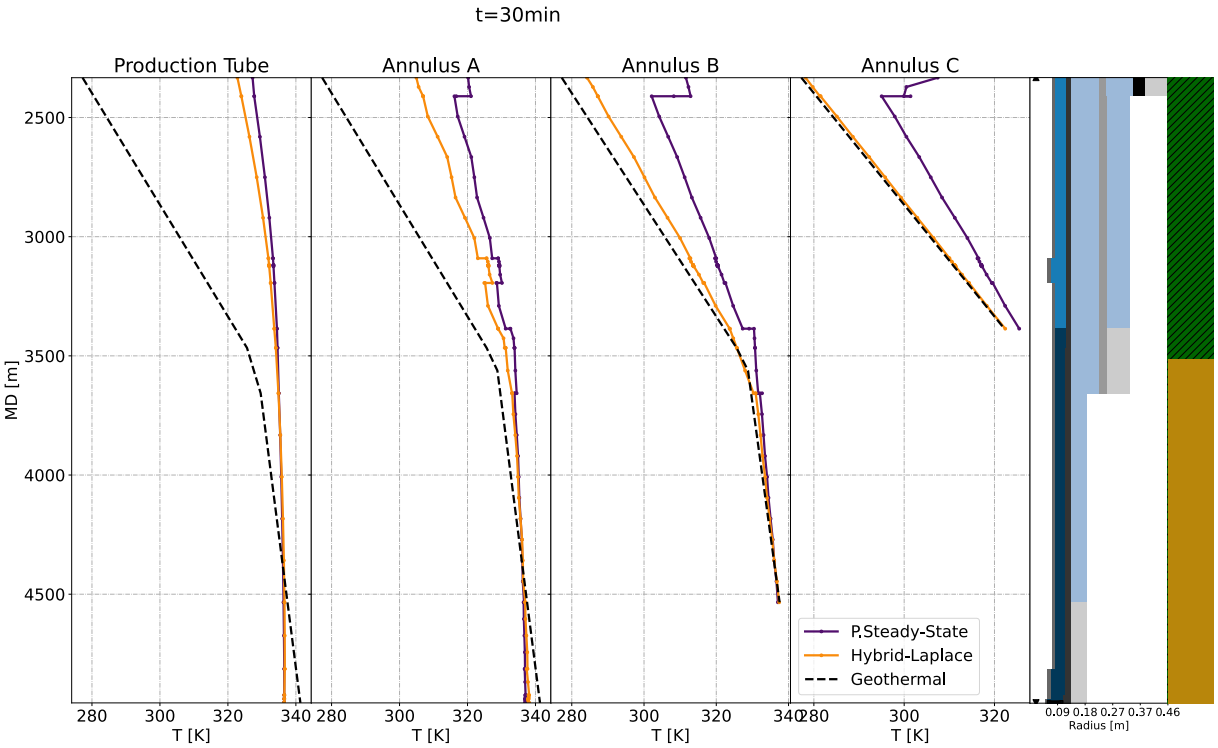

This figures also presents a problem related to the field data provided at the PDG. Notice that the bottomhole temperature is lower than the value indicated by the geothermal gradient. The most plausible explanation for this is that some operation has previously taken place and has cooled the reservoir before production. Thus, would allow cold fluid to enter the column. As the APB will not be compared with field data, this input will not be changed in the evaluation presented below.

Figure 92 presents the temperature profiles predicted in this well for the simulated time of 10 days, 1 hour and 25 minutes. This time is the closest to the mark of 10 days, and will be used to compare the results in a region where the pseudo steady-state assumption is considered valid. As can be seen, both models once again predict the same temperature results, indicating that Equation 7 is indeed close to the time function of Hasan and Kabir (1991). This conclusion is a consequence of the fact that in every other study, the Hybrid-Laplace model managed to achieve the same solutions predicted by the time function.

Figure 92 – Temperature profiles close to 10 days for well with a salt layer

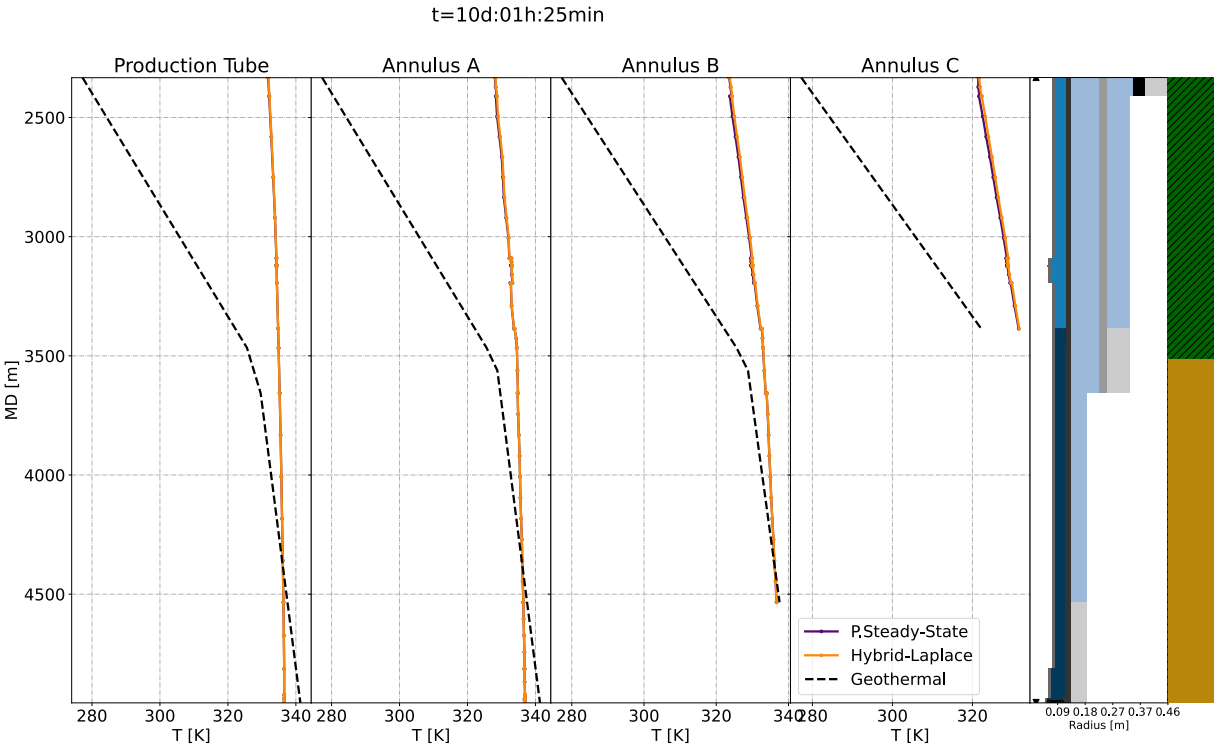

It is expected that these models will continue to show the same behavior for longer times and, to confirm this statement, Figure 93 presents the temperature profiles for 30 years of production (10950 days). It is clear that the models continue to predict the same results even for extremely long times. Thus, the Laplace model shows a very good behavior even in this scenario that has not been widely studied in the literature.

Figure 93 – Temperature profiles for 30 years in the well with a salt layer

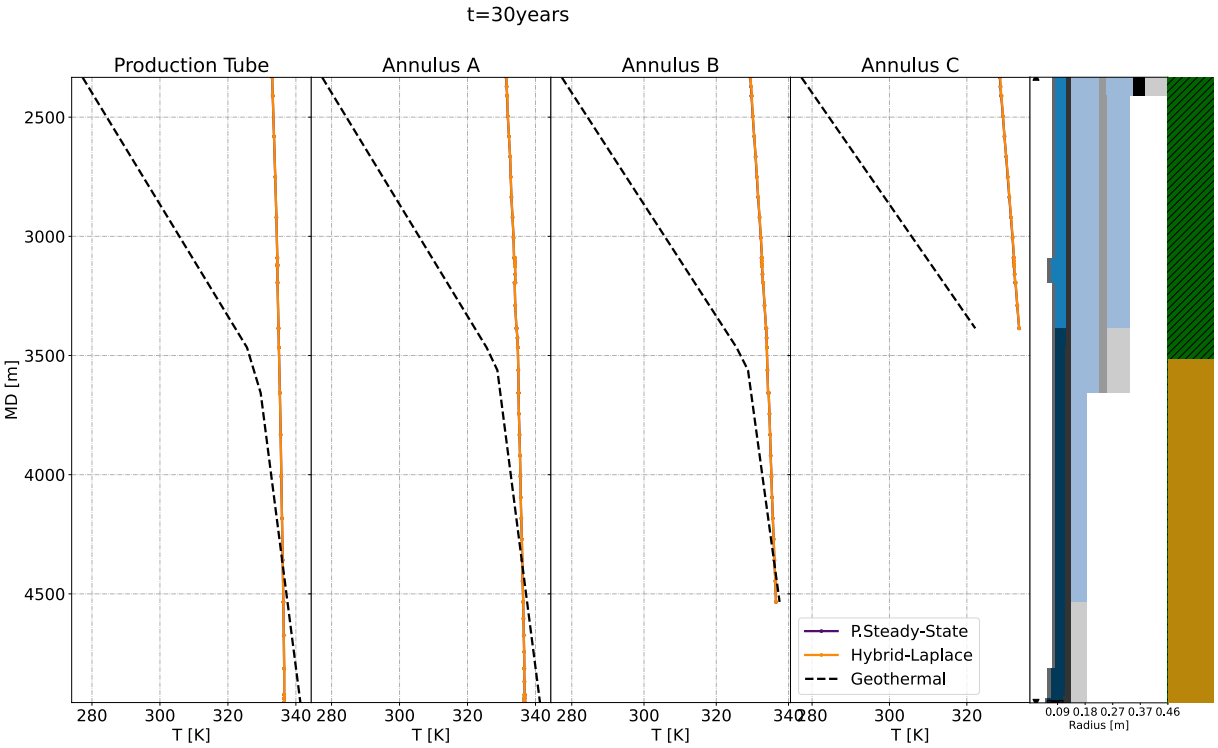

Another interesting result that emerged when analysing the long time behavior is related to the continuity of the temperature profiles. Note that most discontinuities tend to smooth out at this time scale. Besides, the temperature is nearly constant in the production string (336.5 K at the bottom and 330.0 K in the wellhead), so it is clear that with 30 years of, assumed constant, production, this well approaches a state where the heat exchanged will tend to zero. Actually, the Hybrid-Laplace model predicted a heat exchange rate of 79.5 kW, at the end of the thirtieth year of production, against the value of 1.39 MW at 15 minutes of production.

In terms of APB, Figure 94 shows the pressure increase at each annulus for the 30 years analysed. Based only on this figure, it is difficult to clearly compare the models due to the time scale. What is clear, however, are the magnitudes of APB at each annulus, as well as the fact that changes in pressure are mostly located within the first two years of production. After this point, the pressure stabilizes following the temperature profile at the wellhead.

Figure 94 – APB predicted in the well with a salt layer for the 30 years of production, without the creep module activated

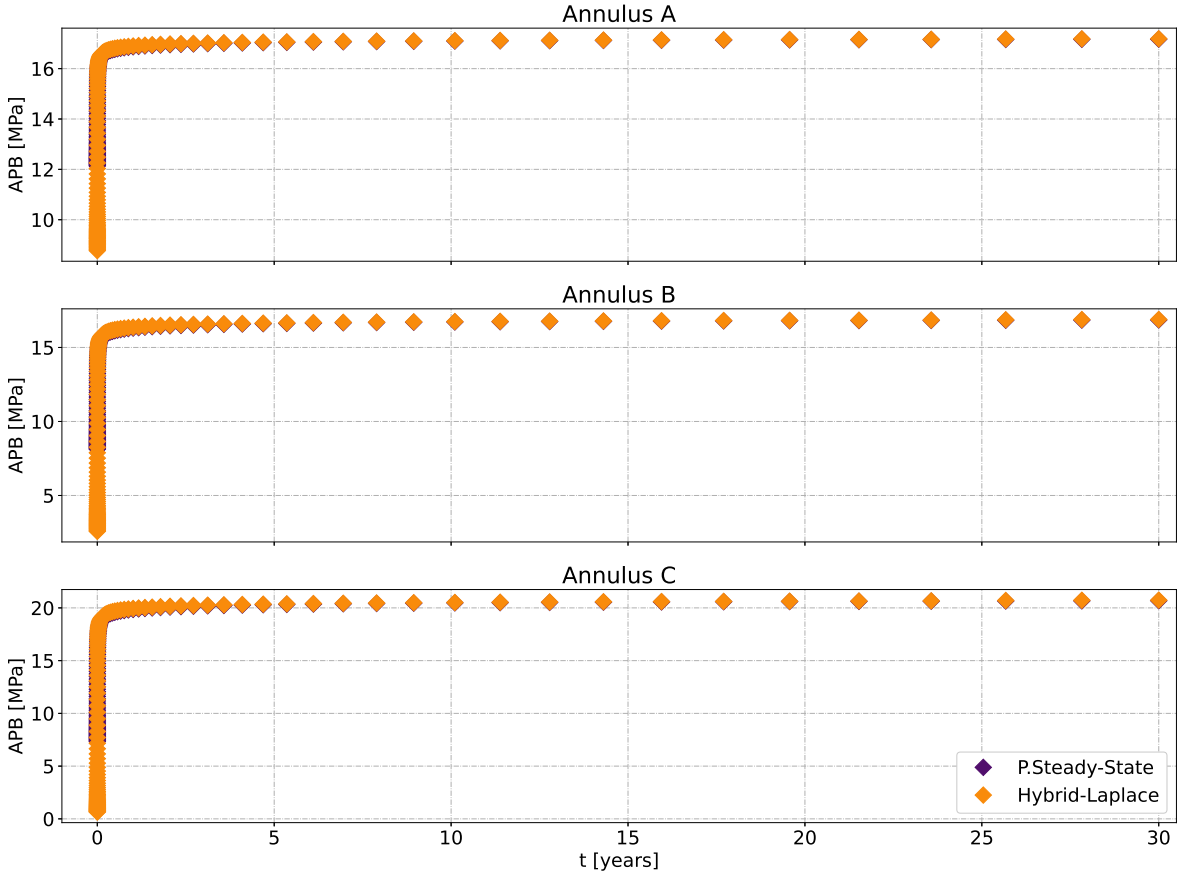

To better compare the models, Figure 95 shows APB for the first 10 days of production. In this region, the differences between models are clearer, with the Hybrid-Laplace model predicting smaller pressure increases, especially for the outer annuli, up to the 7^{th} day. For example, in annulus B at 30 minutes, the pseudo steady-state model predicts an APB of 8.12 MPa, whereas the Laplace model predicts a value of 2.58 MPa. Next to it, annulus C was predicted to face an APB of 7.32 MPa using the pseudo steady-state and 645.88 kPa using the Hybrid-Laplace model. As mentioned previously, the original planning accounted for simulations of even shorter times, of the order of 10 minutes. However, the thermal system became very unstable to generate meaningful results.

Figure 95 – APB predicted in the well with a salt layer for the first 10 days of production, without the creep module activated

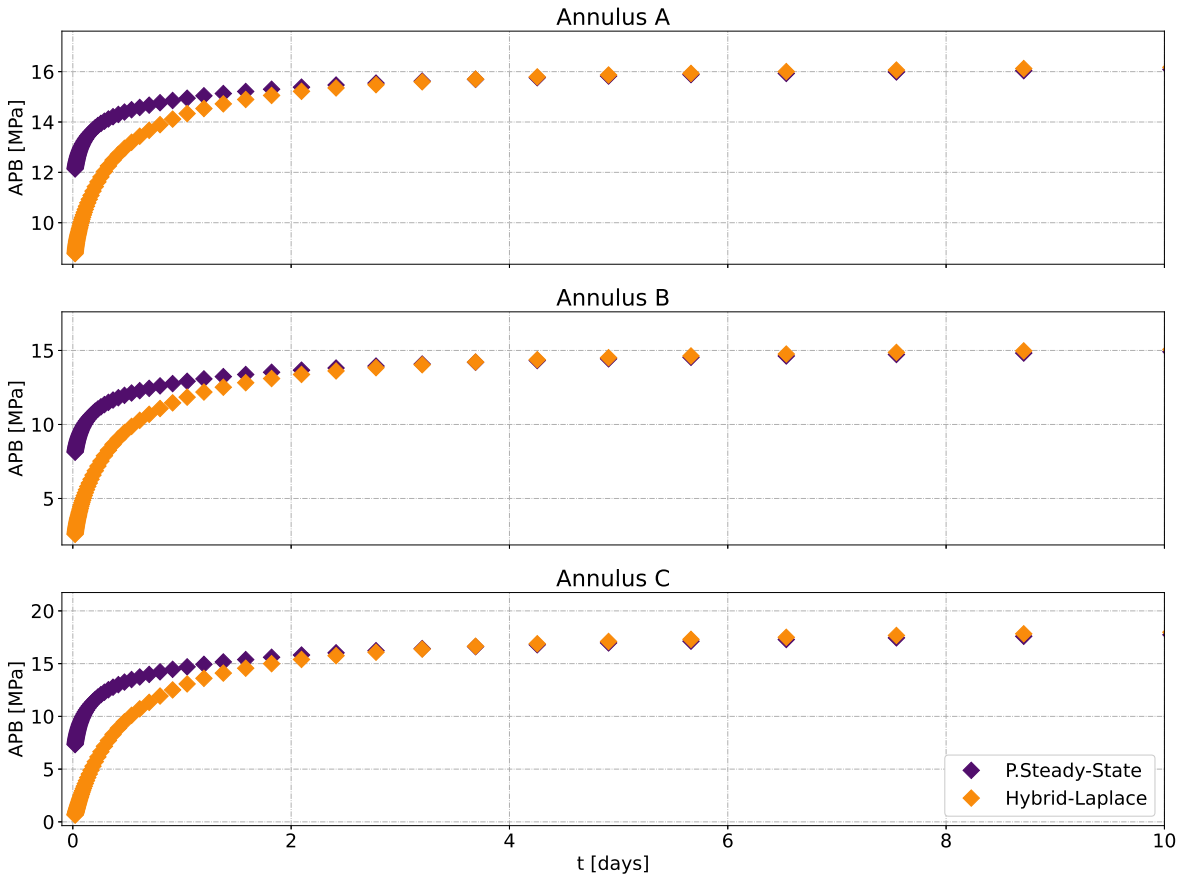

To assess how much the presence of salt can compromise the safety of this well, one can analyze the strain of the casings with and without the creep model activated. Figures 96, 97 and 98 show the behavior of the strain resulting from the traditional thermo-elastic model. As can be seen, no tubular approaches the 5% strain specification limit. In addition, the largest strains are detected in the formation exposed to annulus C.

Figure 96 – Strains at 30 minutes of production for the well with a salt layer without the creep model activated

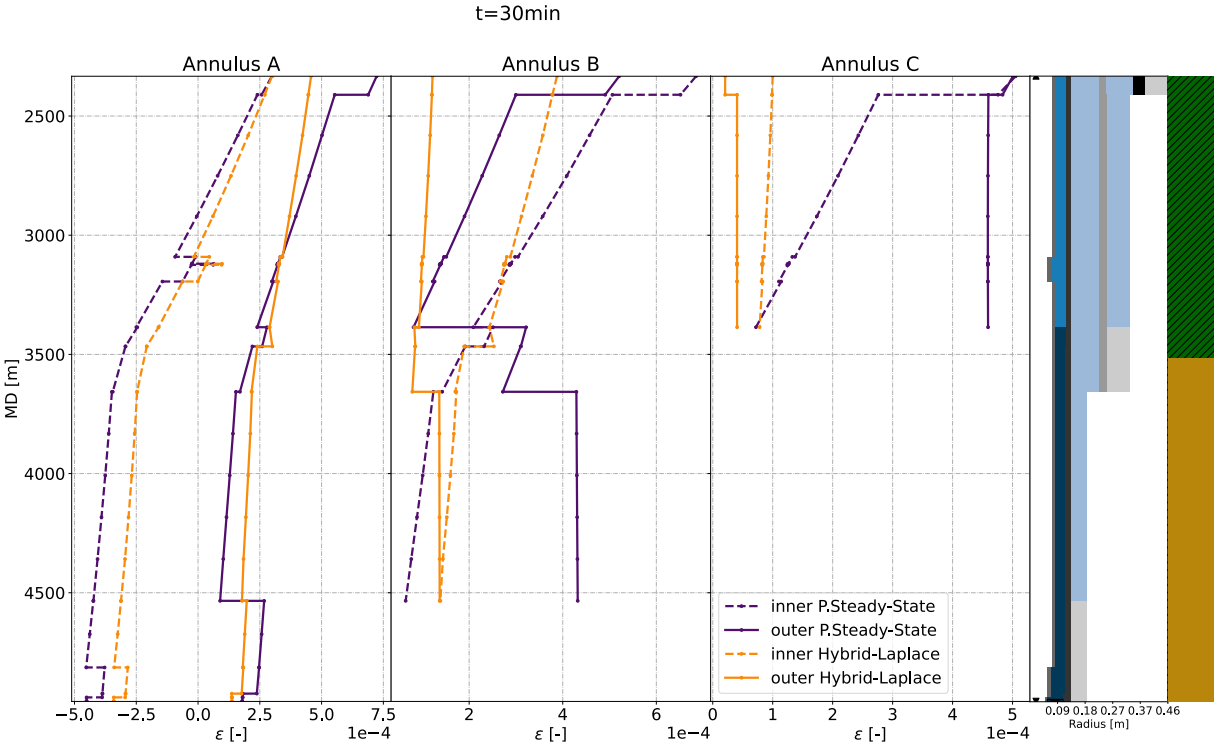

Figure 97 – Strains at 10 days and 1 hour of production for the well with a salt layer without the creep model activated

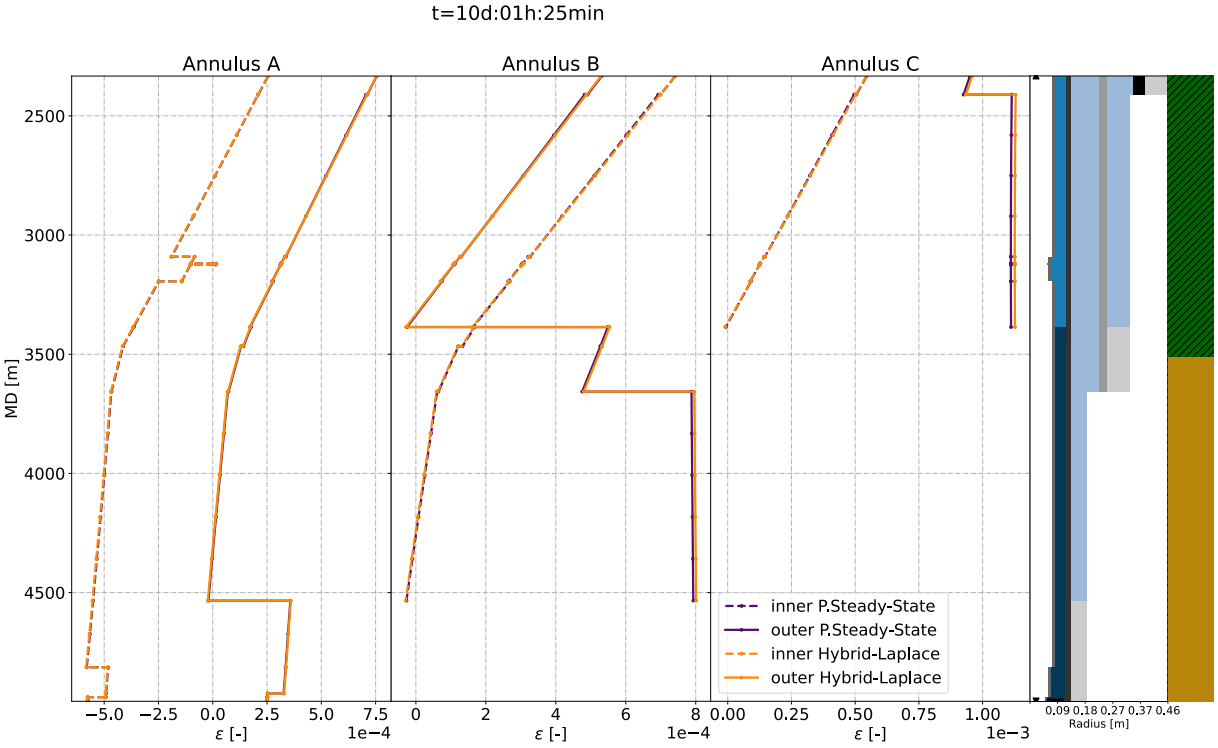

Figure 98 – Strains at 30 years of production for the well with a salt layer without the creep model activated

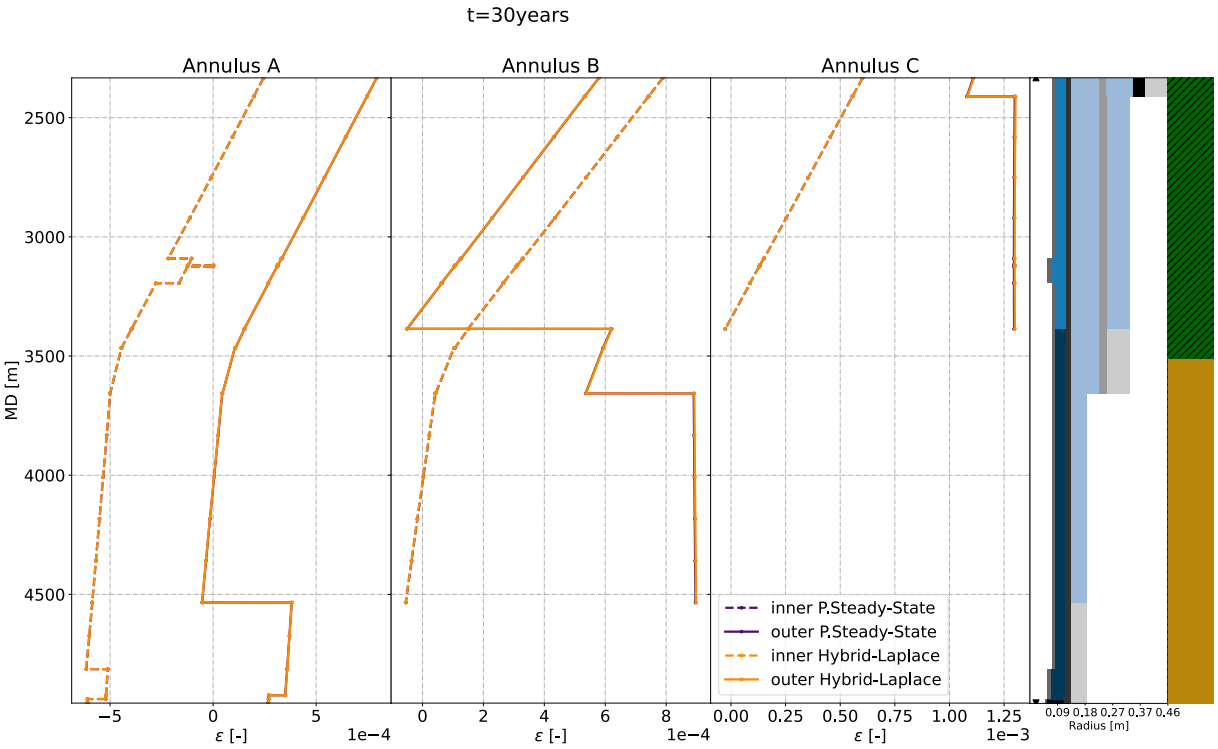

Note that, from the 10^{th} day of production, the annuli deform in larger scale within the first couple days of simulation. After this point, the strain is small when compared to previous simulations.

These results again reaffirmed the qualities of the Hybrid-Laplace model. Next, the analysis of the creep model for the strain of saline rock layers will be presented.

5.3.2 Salt model

First, before comparing the models, it is important to explain that the developed program was validated externally in a base case against standard structural simulation software (COMSOL, 2018). In the program, the creep law was implemented and tests of mesh convergence and comparative studies of the results were carried out. Once the creep simulation program was validated, it was integrated into the heat transfer and APB calculation program (pySAFE). The aforementioned preliminary validation is not included in the thesis. However, the subsequent validation steps which involved the coupling of the thermal and creep models are presented next, starting with the mesh convergence tests.

To determine the quality of the numerical meshes, a very simple procedure was adopted. Starting from a mesh with 2 × 8 elements, the APB simulations performed with progressively better meshes. This refinement was made by doubling the number of elements used to discretize independently each direction, until a total of 64 elements in each direction was used. So, in total, 24 tests were made. To determine the ideal

mesh for modeling APB coupled with salt layers displacements, the resulting values of APB in annulus B (the one in contact with the salt formation) were compared in order to detect at which point mesh configuration stopped affecting the calculation of APB. This analysis was carried out individually by comparing meshes in each direction, that is, a mesh would only be considered good if it met the convergence criterion in both the radial and axial directions. Such tolerance was chosen at 1%, since a difference of this magnitude in APB may be connected to different phenomena that are not particularly relevant to the present study.

In terms of the simulated geometry, Figure 86 shows that the salt layer consists of a cylindrical shell with an internal radius of 0.187325 m and a length of 873.82 m. As explained earlier, it is necessary to approximate the external boundary condition by truncating the domain at a point far enough. Almeida (2016) pointed to a distance of 10 inner radii to be sufficient, however, since thermal expansion effects are going to be studied, a distance of 100 internal radii will be used, leaving the condition of non-displacement external boundary located at 18.7325 m. Note that, as mentioned in Section 4.3, the radial discretization uses a geometric progression scheme, therefore, at each refinement of the grid, large amount of nodes will be added near the wellbore wall.

Figure 99 presents the results of the mesh convergence tests, which involved simulating the 30 years of production with the inputs used later in the final simulation. The converged criterion are simultaneously met in the 16 × 64 element mesh, which is the grid adopted in the simulations from this point on.

Figure 99 – Grid convergence for the salt domain simulations

(a) Convergence in the radial direction

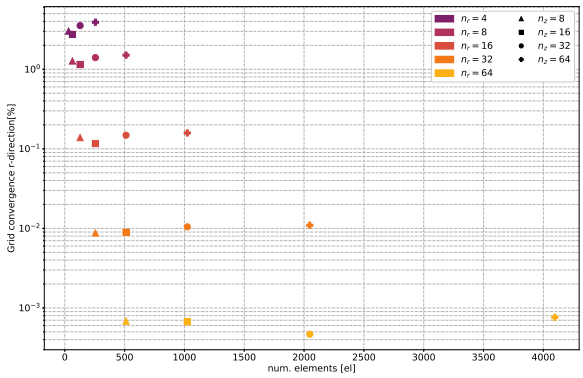

(b) Convergence in the axial direction

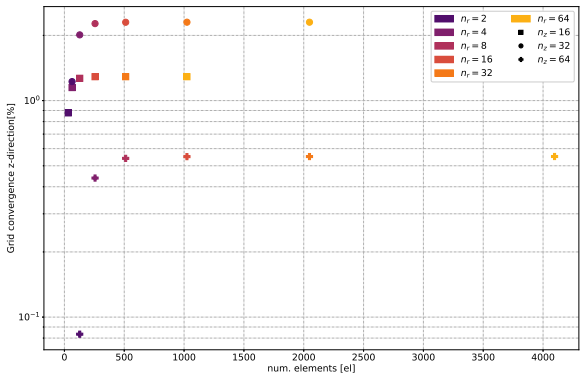

A mesh with 16 elements in the radial direction and 64 in the axial direction has a total of 1024 elements, with 4257 nodes, and each node with 2 degrees of freedom. In addition, since 9 integration nodes are used for each element, it is necessary to store extra information for the model in another 9216 integration nodes.

Regarding the time spacing used, it was attempted to determine the shortest possible first step of time without major instability in the system. The first point to be stable

in all tests, with different meshes, was the half hour time. Thus, the start and end point are 30 minutes and 30 years, respectively. To calibrate the parameters of Equation 139, a test similar to the previous one was carried out. As there are three parameters to be considered, the study is a little more complex. However, it was started with 100 spacing points with parameters $\chi_1 = 1$ and $\chi_2 = 1$. Once this was done, 25 points were added successively until 200 points were reached. Then, the same sequence was repeated, changing the values of χ_1 from 1, to 1E-3 and then to 1E-5. Subsequently, the value of χ_2 was changed from 1 to 3 and again to 9. Thus, in total, more than 45 simulations were run and the results were compared in terms of the APB predicted in annulus B.

Again, a tolerance of less than 1% was sought in the studied spacing. At the end of the study, it was determined that for any situation there is no significant gain when using more than 125 points in time spacing. In addition, the pair $\chi_1 = 1 \times 10^{-3}$ and $\chi_2 = 9$ proved to be the most suitable to be used in the simulations. So from this point on, this set of parameters are adopted for the time discretization.

In order to validate that the boundary conditions, as well as the coupled implementation, it is possible to take advantage of the first step of the program. It consists of calculating a purely elastic strain step that occurs supposedly during drilling. This is one of the major differences in the approach of this work to others that model APB in oil wells. Traditional programs for calculating such a variable operate by comparing the condition of the heated well with the non-deformed state. This proves to be a recurrent approach in the literature, especially in works that use the deformation models of Halal and Mitchell (1994). However, it is known that at the moment of drilling, as well as in the process of descending the casings, the solid materials will go through loading conditions that will cause strains. The proposed formulation tries to correct such considerations at least in the salt layer, using an elastic step which causes annulus B to have an initial volume different from that of the undisturbed geometry.

As the elastic strain and the geomechanical loads in a standard drilling operations can be modeled by simple analytical approximations, this step can be used in order to validate the boundary condition and communication of the different modules implemented work. The model used is similar to those proposed in Fjaer et al. (2008) and Jaeger, Cook, and Zimmerman (2007) for vertical perforation through elastic formations. Both authors present the set of boundary conditions and considerations required for the approach, such that, in the end, the basic formulation coincides with a plane stress with axisymmetric considerations. The governing equations can be derived by several means, but the most generic formulation is known as the Kirsch equations. These equations describe the stress state inside the formation and, by applying the linear elastic model, it is possible to reach an expression for the initial displacement.

With this model, using Equations 95 and 96, with the values of the overburden gradient provided in Figure 88, it is possible to determine the geomechanical stress

state in the rock. Thus, Figure 100 shows the behavior of initial state of stress in the formation in the undisturbed regions. As can be seen, even with the overburden gradient showing a very non-linear behavior, the resulting overburden stress exhibits a very linear aspect. This is an interesting feature for the model and, since elements with quadratic interpolation functions were used, adjustment to the data provided should not be a problem.

Figure 100 – Overburden stress and horizontal stress component estimation from field data in the salt layer

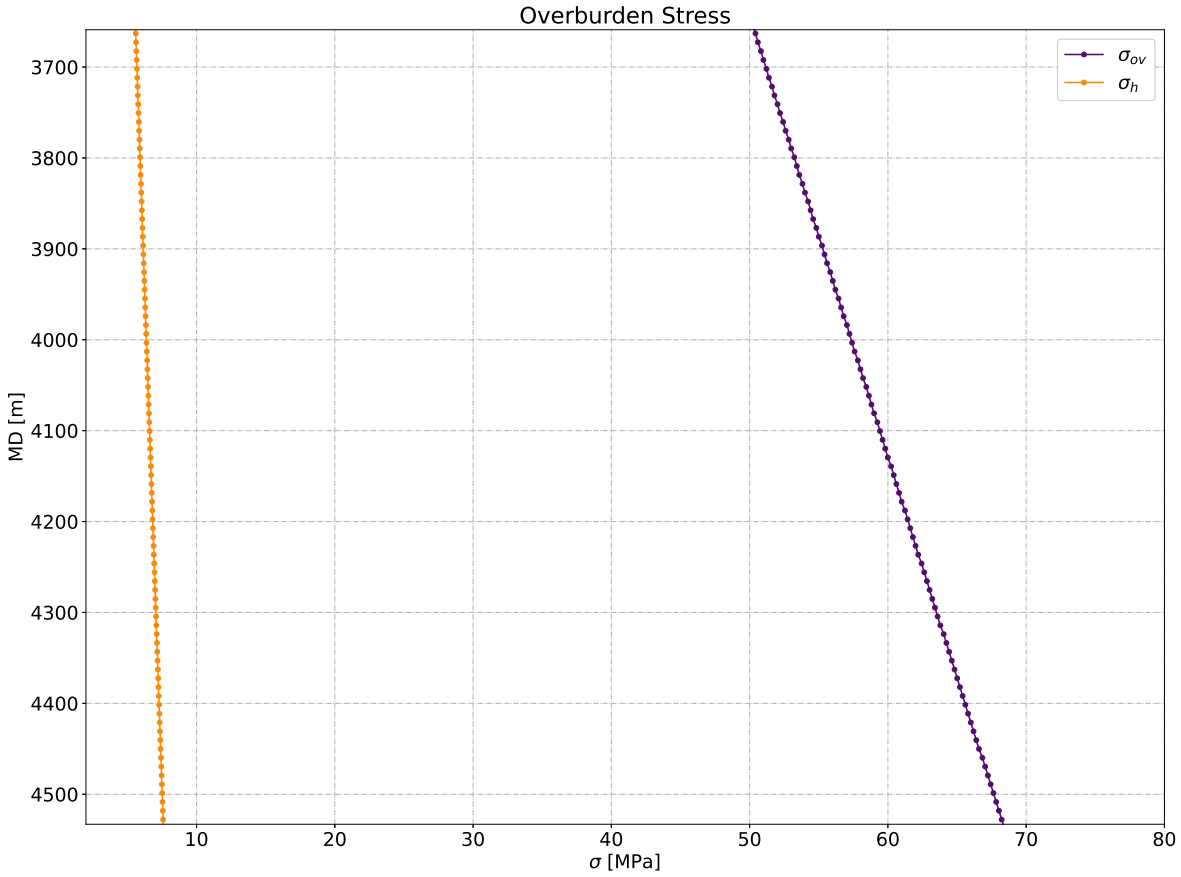

To confirm this last statement, Figure 101 presents the results of the stress state predicted by the FEM formulation, both for the vertical stress component and for the radial stress at the integration nodes furthest from the inner wall of the well. These nodes are positioned at 18.20 m from the center line of the well. Unfortunately for reasons of scale, the results overlapped in such a way that it becomes very hard to analyze the quality of the predictions. However, it is obvious that it was able to reproduce the basic trend with good accuracy.

Figure 101 – Comparison between the simple elastic model and the FEM program

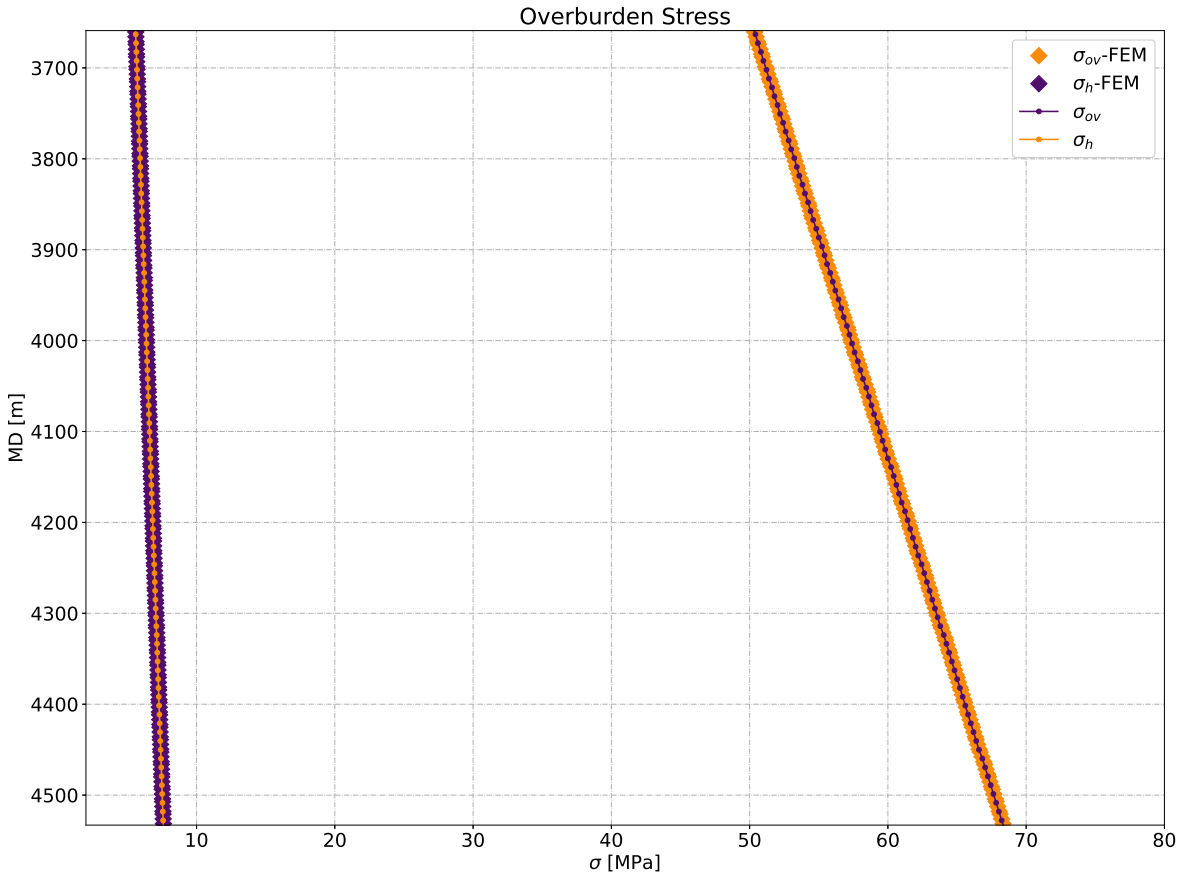

Figure 102 addresses this scale problem by presenting the relative deviation between the results of the FEM program and the geomechanical model. It is clear that both components of the stress state in the rock were predicted with high accuracy; for the axial component, the deviation is smaller than 0.002%. The only issue that appears in this graph are the high frequency oscillations.

Figure 102 – Relative deviations between the elastic steps of the FEM and geomechanical elastic models

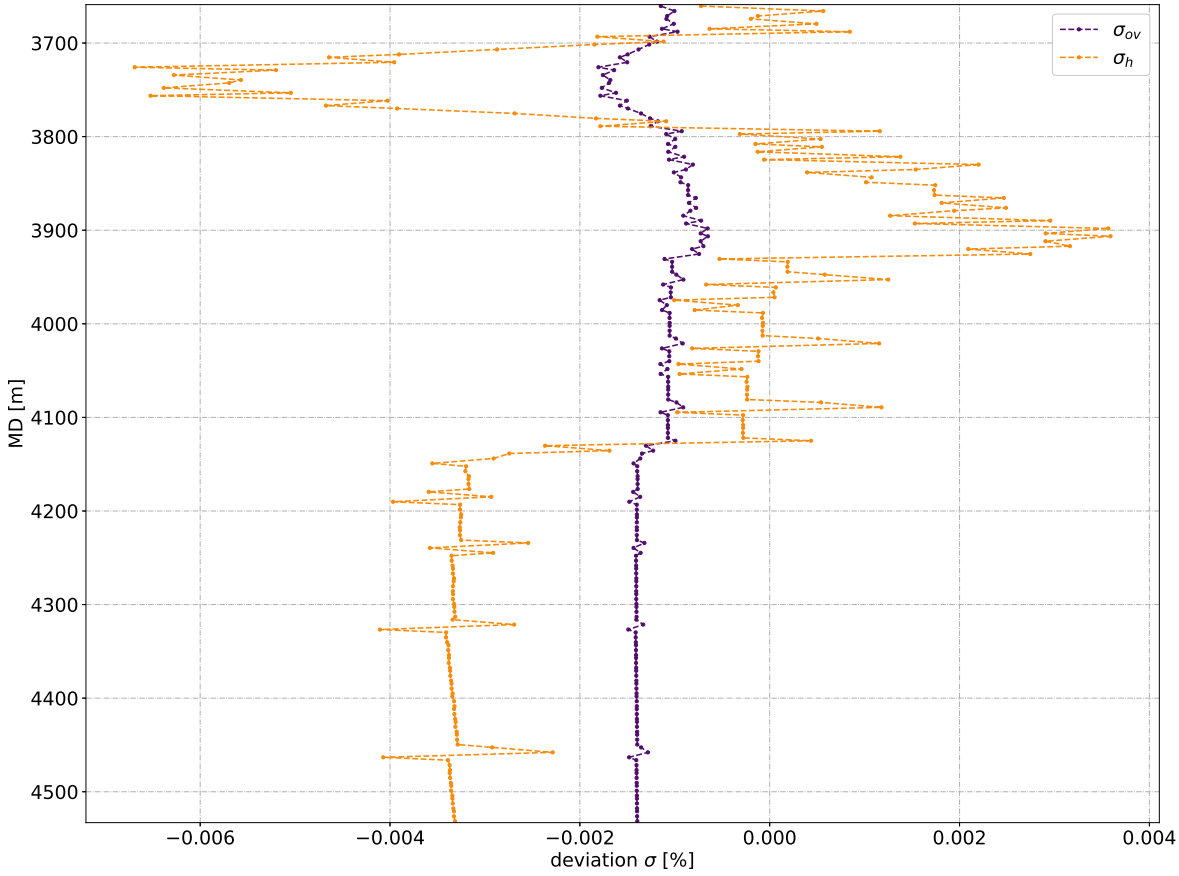

Investigations regarding the overburden stress data indicate the origin of such oscillations. As much as Figure 88 appears to represent a smooth profile for the overhead gradient, a low magnitude noise appears to be the cause of such an effect. This occurred because, as described in Equation 128, the calculation of the body force is done by means of the linearized overburden gradient and its derivative, so small oscillations tend to be smoothed out upon integration. To confirm this fact, Figure 103 presents the value of the derivative in the interpolator used to approximate this variable.

Figure 103 – Derivative of the overburden gradient in the salt layer

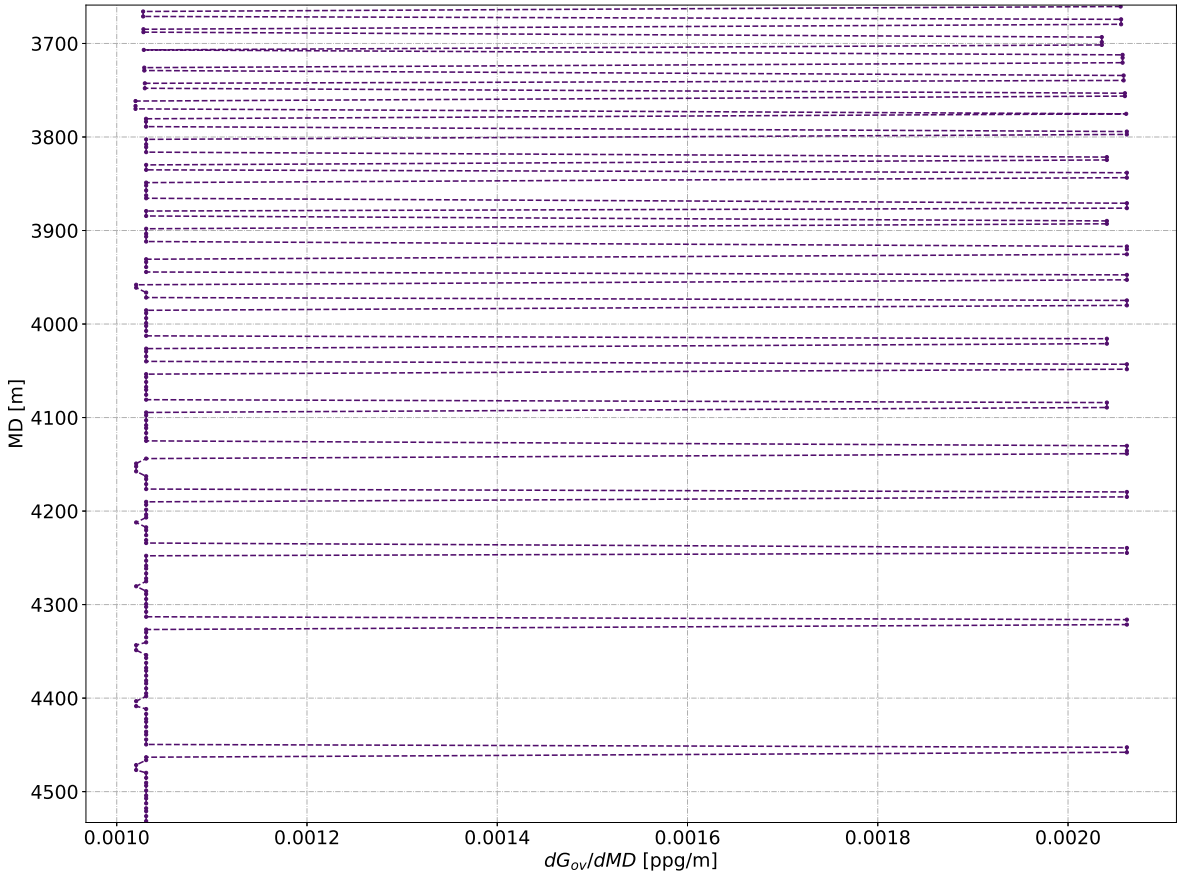

As the result is being compared to unfiltered data, the smoothing process which occurs in the integration step leads to the difference observed in Figure 102. Note that the oscillations present in Figure 102 occur at the same depths where there are discontinuities in the derivative of the overburden gradient. As the deviations detected in the original stress state of the rock are very small, this small difference will be considered acceptable without any extra treatment. However, for more critical studies, this question may be of significance and should be taken into account.

To further validate the model used, one can use Kirsch's equations for the plane stress in the rock. With these, it is possible to verify what happens with the stress field starting from the well wall toward more distant regions. These equations are given by:

$$\sigma_r = (\sigma_h - P_{\text{ann}}) \left(\frac{r_{\text{fm}}}{r} \right)^2 - \sigma_h \tag{140}$$

$$\sigma_\theta = (P_{\text{ann}} - \sigma_h) \left(\frac{r_{\text{fm}}}{r} \right)^2 - \sigma_h \tag{141}$$

Considering the vertical component, the overburden stress itself, it is possible to use these equations to evaluate the model along the radial direction. Figure 104 shows the comparison between Kirsch's equations and the results calculated by the FEM code in the final program in a radial section at a depth of 4102.92 m. As the functions are

inversely proportional to the square of the radial position, it was decided to only focus at a distance of 10 internal radii so that it is possible to visualize the gradient next to the wellbore wall without difficulties. The FEM model showed good agreement with the geomechanical model used. This indicates that the developed program managed to capture with fidelity the lithostatic stress at least for that depth.

Figure 104 – Comparison of the proposed model with Kirsch's equations for a depth of 4102.92 m

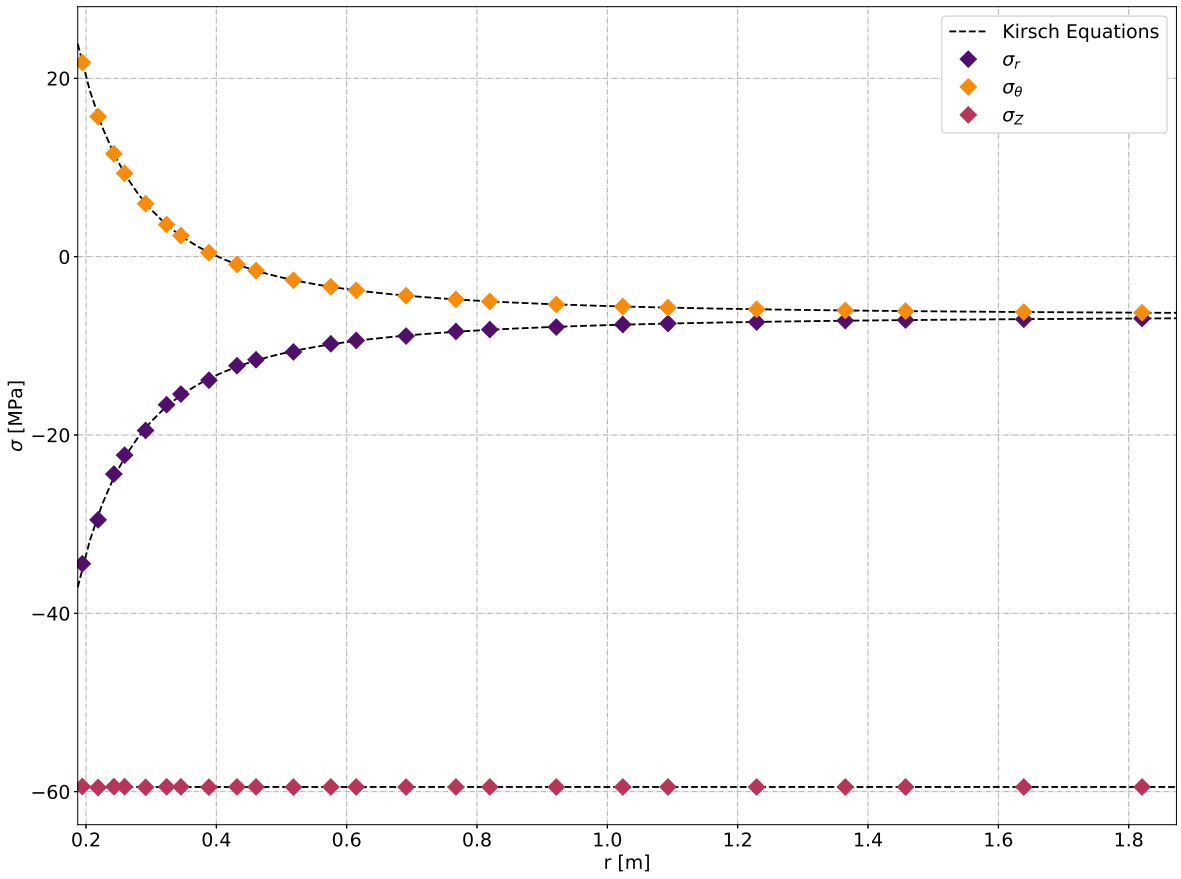

This plot is useful to validate the program at a given cross section, but to evaluate the entire salt layer, a more thorough analysis is necessary. For this purpose, the effective stress of the rock can be used. The choice of this variable is due to the fact that it groups all principal components of the stress tensor into a scalar, thus reducing the number of variables to be analyzed to only one, which is done at each integration node. For the Kirsch equations, the effective stress, calculated via the Von Mises criterion can be written as:

$$q = \sqrt{\frac{(\sigma_r - \sigma_\theta)^2 + (\sigma_r - \sigma_Z)^2 (\sigma_\theta - \sigma_Z)^2}{2}} \tag{142}$$

In order to compare the effective stress calculated by the model with this analytical expression, a contour of relative deviations is produced using the integration nodes.

These deviations are calculated using the same procedure of Figure 102, where the predicted values from the FEM program are compared with the geomechanical model. This contour is represented in Figure 105.

Figure 105 – Elastic effective stress deviation

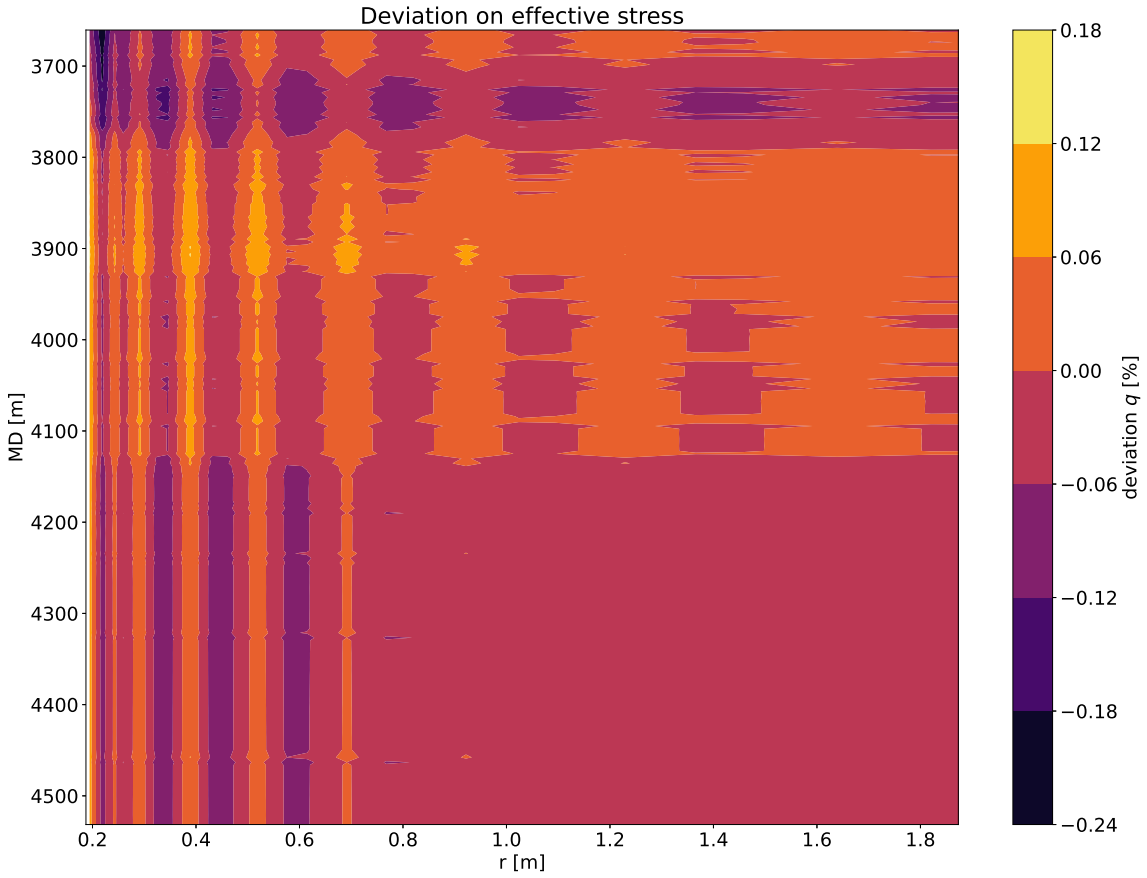

The results plotted in the figure show that there is a direct relationship between the oscillations detected in the overburden stress and the deviations in the effective stress in the domain. Despite this, the deviations have always remained below 0.25% when comparing the formulations, thus indicating a good quality of the program developed for representing the initial state of stress. The regions that experience the greatest deviations are close to the wall, in the zones with the greatest oscillations. In addition, something interesting that this result points out is an almost oscillatory characteristic that exists in the stress field radially. This occurs in the innermost nodes of the elements, indicating that such a phenomenon is related to the selected element (bi-quadratic). A possible correction could involve using different elements to try to eliminate such a phenomenon.

The results presented above validate the calculation of the stress fields. In order to complete the analysis, one must verify the behavior of the displacement. This is in fact the most important information, as it is directly related to the volume variation which affects the APB. Again, a comparison is made between the geomechanical model and

the code developed for validation. The following equation can be used to determine the displacement of the salt layer:

$$U_r = \frac{\sigma_h - P_{\text{ann}}}{2G} \frac{r_{\text{fm}}^2}{r} \tag{143}$$

Based on this equation, the comparison made for the stress states is repeated for the displacement at a depth of 4101.92 m, as presented in Figure 106. The finite element model was able to capture the radial displacement with great precision, especially near the well wall. In fact, an interesting behavior is that the model fits better near the inner wall than in the outer boundary condition. This is due to the non-displacement condition used in the geomechanical model, which assumes a non-displacement condition at an infinite distance from the well. The FEM formulation, on the other hand, assumes a non-displacement condition at a finite distance, leading to a smaller displacement in regions away from the well. However, even with this difference, the model managed to capture the displacement of the wall with great fidelity.

Figure 106 – Radial displacement from the elastic step at a depth of 4102.92 m

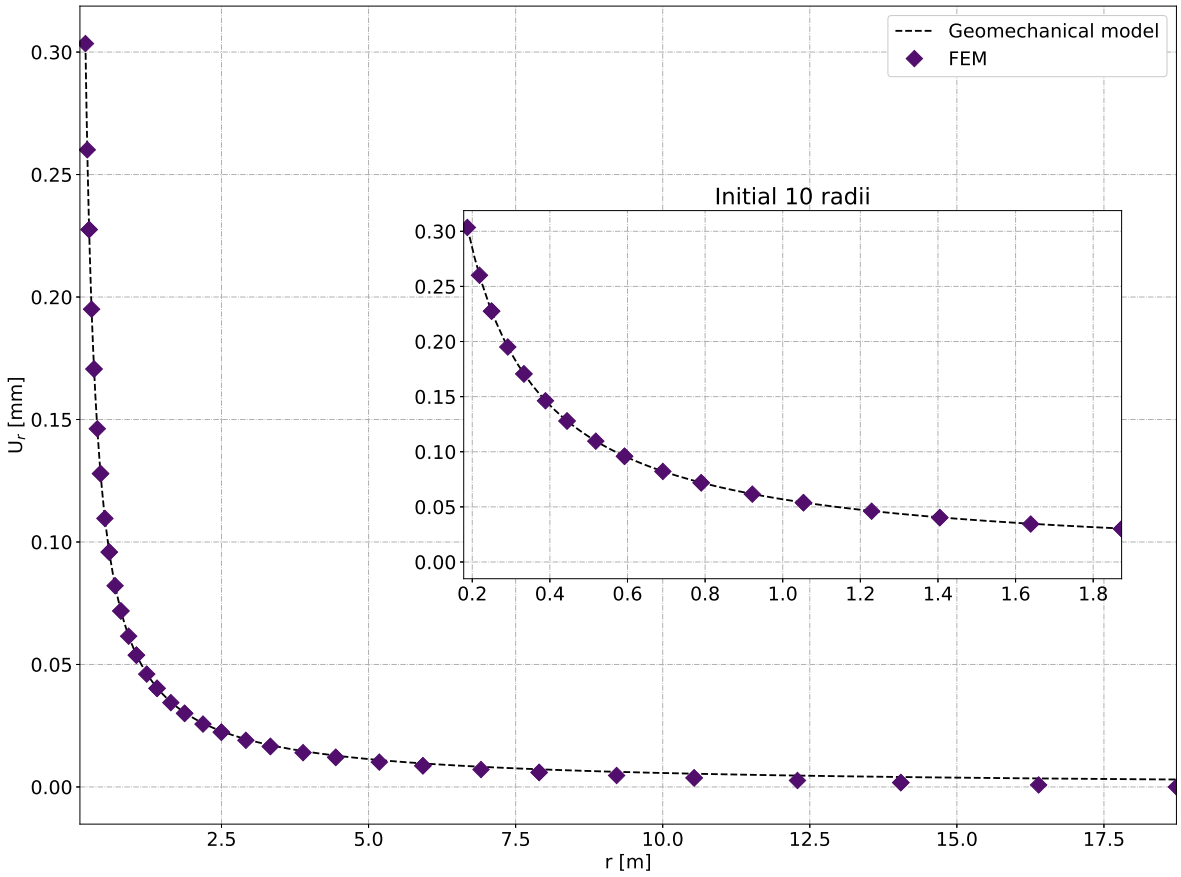

This figure guarantees the quality of the model for this particular depth, however, one needs to ensure the same performance along the entire well wall, as shown in Figure 107 for the complete displacement of the inner wall of the salt layer. As can be

seen, the geomechanical model and the FEM code predicted very close results, which is an indication of the validation of the model.

Figure 107 shows that the salt layer moves away from the well, increasing the volume of annulus B in relation to the reference volume. This creates a new possibility for analysis of APB in this case, since, with a higher initial volume it is expected that the thermal APB returns a smaller pressure increase compared to previous results of the standard thermal model.

Figure 107 – Elastic wall displacement of the salt layer

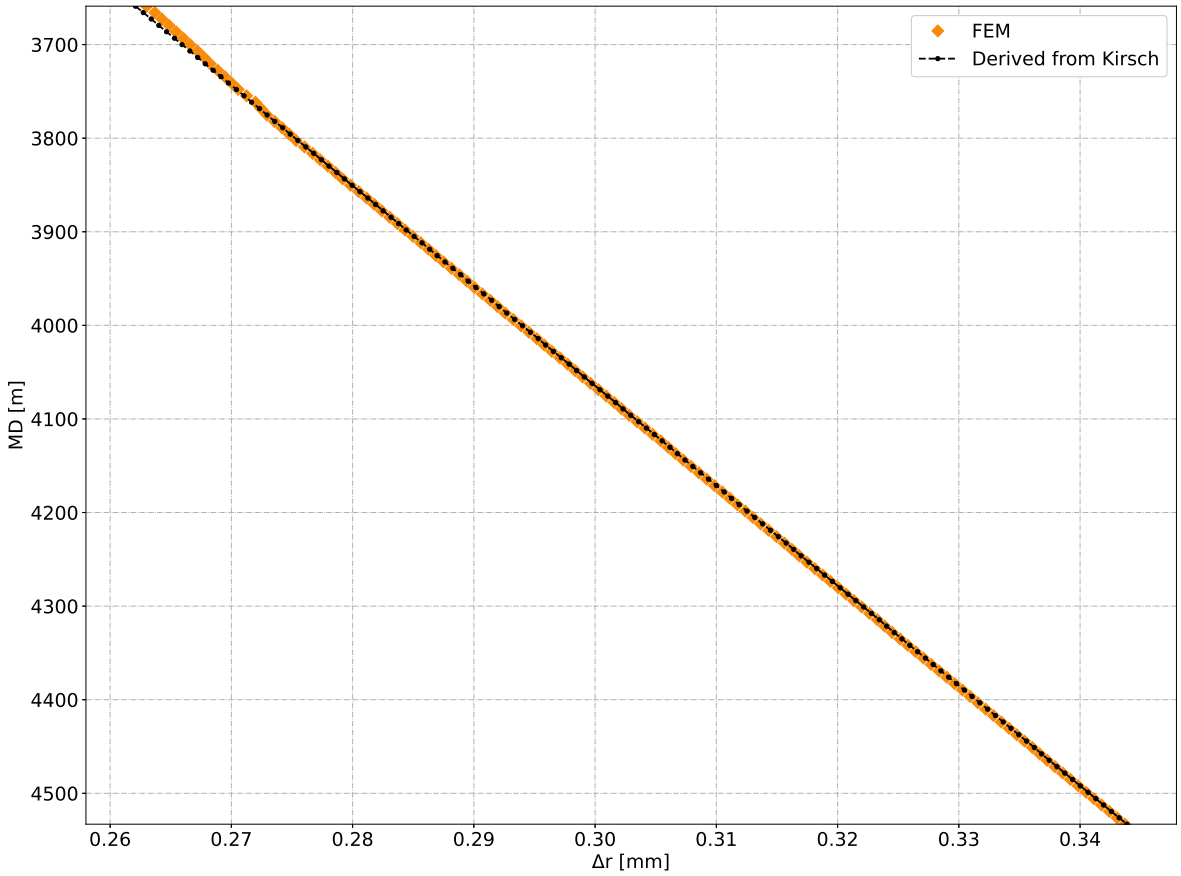

The undisturbed volume of annulus B is of 185.16 m^3. When considering the elastic displacement as the initial condition, a variation of 0.31 m^3, i.e., 0.16%, was detected. This directly affects the initial mass of the problem, which is a very important parameter, since it is the variable used to determine the convergence of the APB. Originally, the annulus was estimated to have 222.07 t of drilling mud. After considering this initial deformation, there was an increase of 228.55 kg, about 0.10% in mass in the annulus. This information is important because it is at the threshold value used for tolerance of the mass convergence iterations. Therefore, it is not certain that it will affect the final result, but it is important to take note that with only the displacement of a small part of the wellbore, the initial volume changed significantly.

Figure 107 also shows that the displacement of the well wall is larger at the bottom of the salt layer than at the top. This happens because the weight of the fluid column induces a pressure gradient in the annulus that creates a stress greater than the horizontal (σ_h) stress in the salt layer, resulting in greater displacements near the bottom.

With the initial elastic step validated, simulations are performed for the 30 years of production with the creep model activated. Contrary to the standard simulation, in which each simulated time took about 16 seconds on average to compute, the inclusion of the creep model increases the cost of each time step to the range from 40 seconds to 1 and a half minutes. In total, the simulation of the 30 years took 2 and a half hours to complete every 125 timesteps. The largest source of computational cost was related to the calculation of the temperatures at the location of each integration node of the creep model. Although the new Hybrid-Laplace model was developed in order to reduce computational cost, it still had to deal with a large number of calculation and ended up costing more than the Newton algorithm to solve the displacement of the salt layer.

As the prediction of APB is the most important result of this new formulation, its the starting point of the following analysis. Figure 108 presents the profile of APB in the three well annuli comparing the purely elastic model (standard method used up this point with the Hybrid-Laplace formulation) against the new creep model. It is important to explain that all the comparison will refer “Pure elastic” as the standard model, meanwhile “Salt creep” is the new creep model. As expected, the largest differences are predicted in annulus B. However, there is also a great effect in annulus A due to the strains of the production casing. Focusing on annulus B, the differences of APB start small and increasing over the years. At the end of the 30 years, this difference reaches the highest value with 2.55 MPa (approximately 15.1% of the original increase in pressure).

Figure 108 – APB comparison in the well with a salt layer

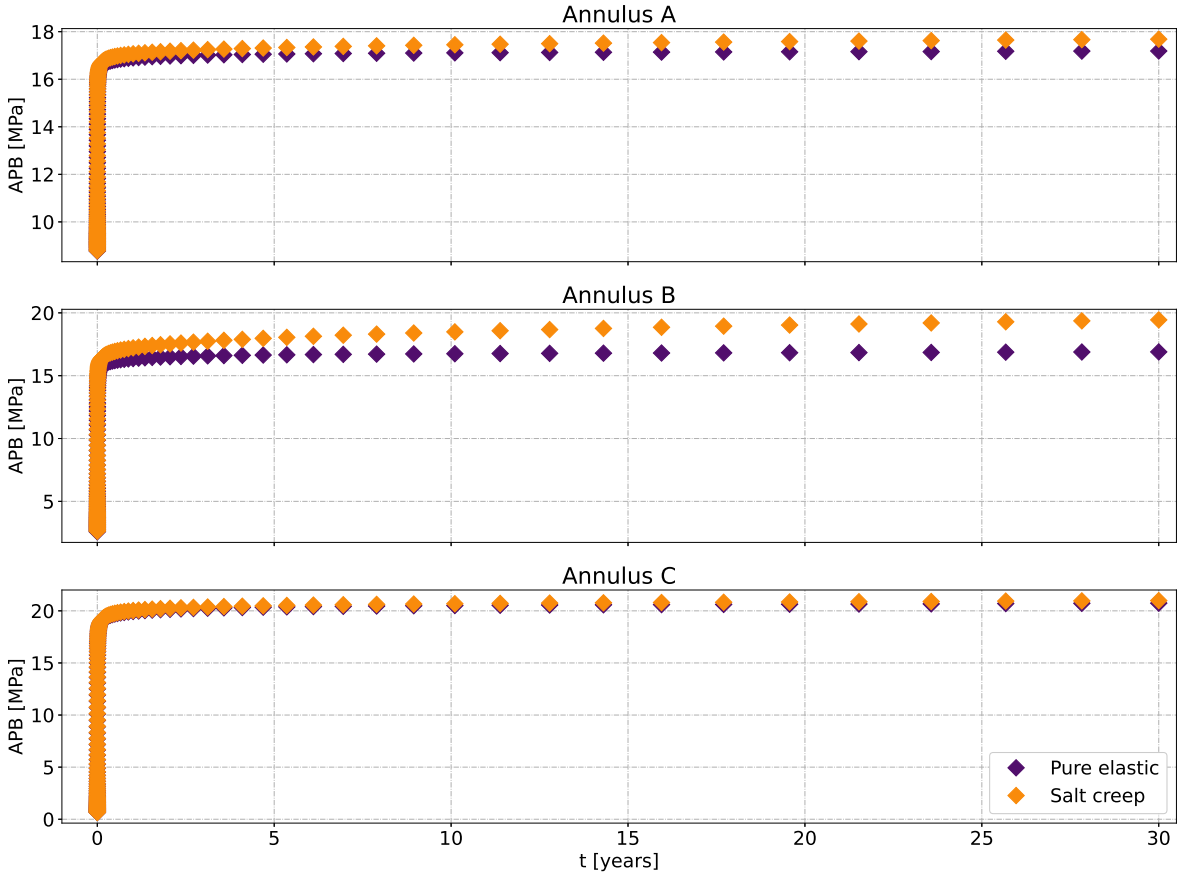

In order to facilitate the analysis of creep effects in the predicted APB, Figure 109 has two plots focusing on annulus B. The plot on the left shows the same result of the APB previously presented, while the one on the right presents the difference of predicted pressure increase. In the former, one can see that, initially, APB is a phenomenon dominated entirely by the thermal term. Thus, the beginning of pressure growths is very similar in both models. When analysing the second plot, it is clear that on can divide the differences in predicted pressure growth into three distinct stages.

Figure 109 – APB comparison with focus on annulus B

(a) APB on annulus B

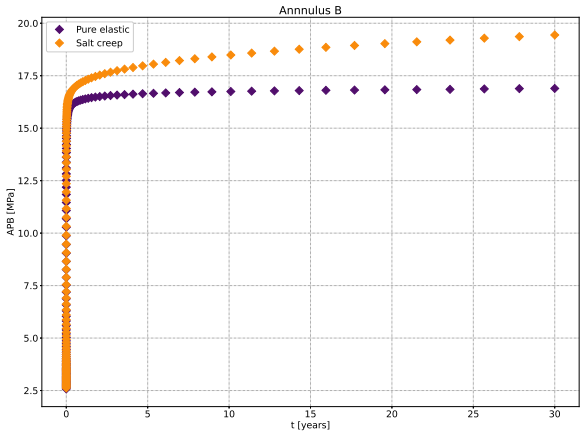

(b) Difference in APB

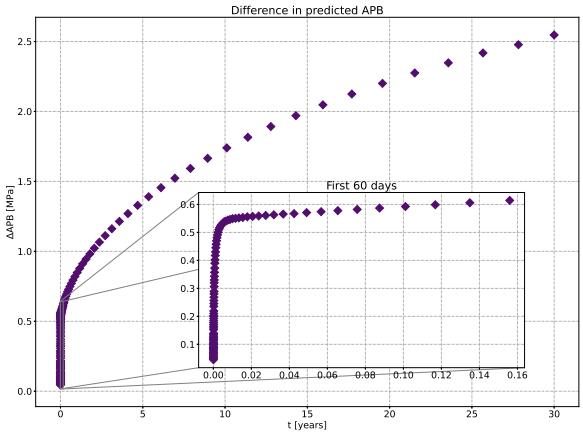

The first stage perceptible in the second plot involves the first couple days of production. In this region, the effective stress in the salt layer is at its highest values during the entire production, so it is expected that the creep rate will be the highest too, leading to higher creep. Past these initial moments, the differences between the models go through a short period when the difference remains almost constant (around 550 kPa). However, once the time steps start to increase in size, the difference goes back to increasing over time. By the end of the 30 years of production, it seems that this well still has a certain tendency to suffer from creep. However, since the expected production life of a well is around 30 years, there is no reason to expect the production to remaining for much longer, which will lead to a reduction in APB.

In order to explain the origin of the three distinct regions more clearly, Figure 110 shows the expected volume of annulus B. Note that this is the actual volume and not the volume variation. Firstly, in the first stage mentioned, the main difference is a direct result of creep. As the volume variation in the creep model is smaller than the one predicted in the pure elastic model, there is less final volume to accommodate the trapped fluid, leading to higher APB. For the second region mentioned, the reason for the constant difference in APB is made clear in Figure 110. This stage happens when, for the traditional models, the volume variation stabilizes, with smaller variations over time. This region occurs simultaneously with the moment when creep starts to dominate the volume variation of the annulus and begins to close the saline layer. During the period of change in direction, for a brief moment, the volume predicted by the creep model stabilizes and, as a result, the difference between the models is almost constant until the annular volume starts to fall. From this moment on, the volume reduction occurs at a high speed consistent with the pressure growth behavior.

Figure 110 – Volume of annulus B during 30 years of production, comparing the traditional formulation with the creep displacement consideration

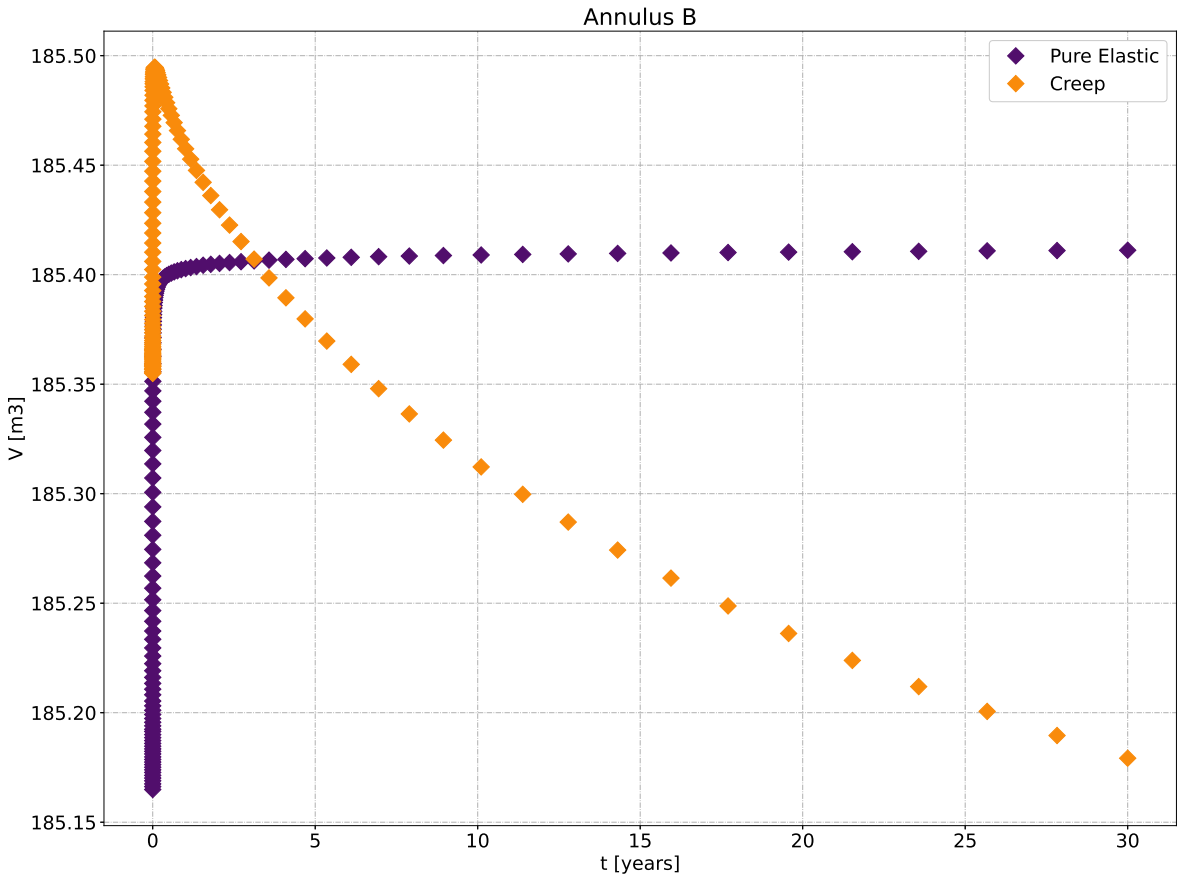

In order to better understand this volume variation, it is important to visualise the wall displacement in several stages of the production. Figure 111 presents the displacement profiles of the inner wall of the salt layer in the first 10 time steps simulated. Also, Figure 112 presents the displacement profiles of the points closest to 25%, 50%, 75% and 100% of the production time, thus allowing an analysis of the displacement in the several stages of production.

Figure 111 – Displacement of the salt layer wall for first 10 time steps

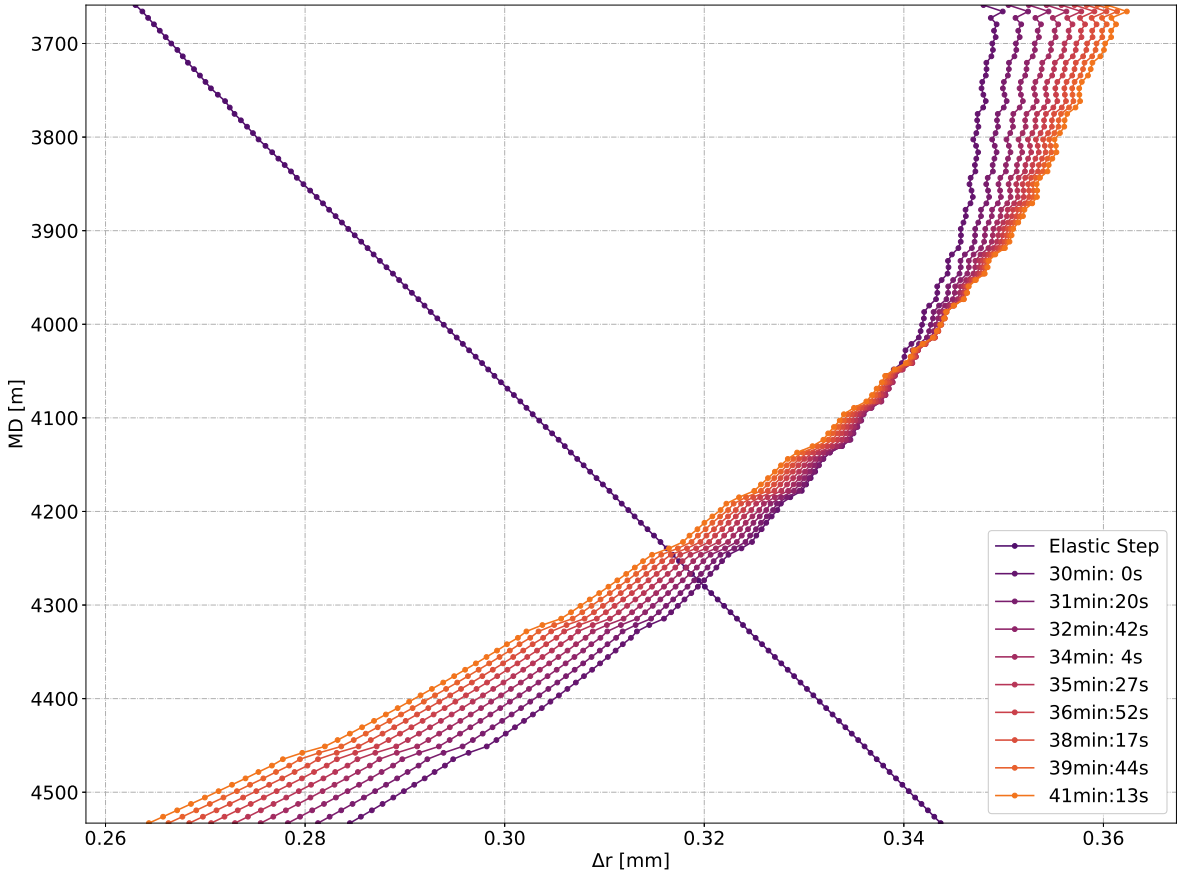

Figure 112 – Displacement of the salt layer wall with 25% spacing of total simulated time

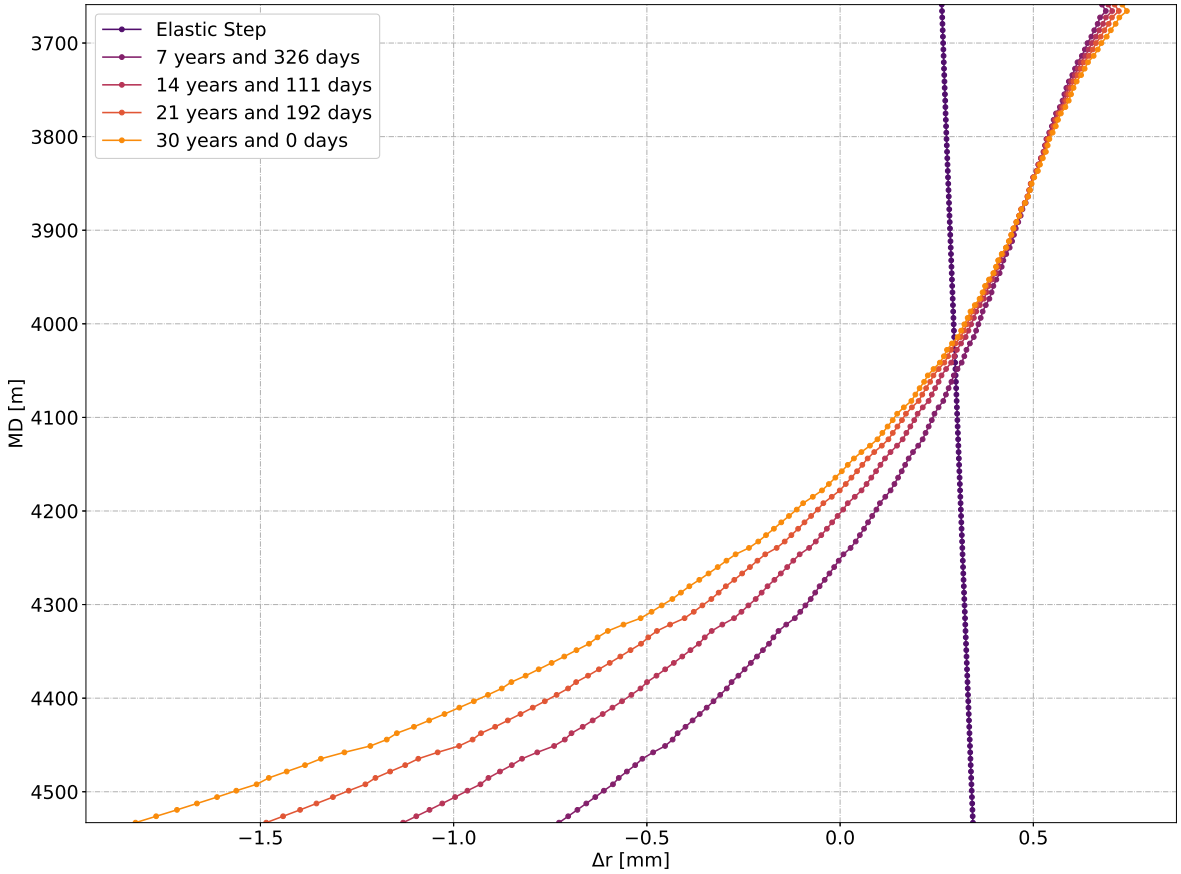

In both figures, the displacement profile of the elastic step was included, which enables comparisons with the creep effects. In the first figure, an interesting behavior already takes place, i.e., the increase in pressure appears to be acting against the creep. This stems from the fact that not only the displacement is slowing down but, over time, the wellbore radius starts to shrink at several depths within the salt layer. In the regions closer to the bottom, the creep affects more drastically, closing the annular space with a relatively high rate. This behavior causes the aspect of “X” detected in the figure. In the purely elastic step, the deeper layers tended to move further away from the well and, from the moment the creep started to act, they start to close.

As previously mentioned, it was not possible to perform a simulation with an initial time step of less than 30 minutes. However, this figure (Figure 112) makes it clear that it would be of great importance to have done so for a better understanding of the modeled phenomena, since this first step already experiences a shift due to the effects very high creep rates. It would be more interesting to run simulations with shorter times to be able to detect the moment when this “X” behavior occurs in addition to increasing the accuracy of the final solution.

Figure 112 shows that, for the first 25% of simulated time (7 years and 326 days),

the displacement is such that some of the bottom regions of the layer managed to shrink further than the non-deformed state, as indicated by the negative displacement. Also, this figure is useful to show that most of the creep takes place within the first 7 years of production. Compared, for example with the last step presented in Figure 111 (41 minutes and 13 seconds), an average displacement of 0.33 mm was predicted. On the other hand, for the first 25% of the simulated time, the predicted displacement is 0.15 mm. For the next 25% of the time (14 years and 111 days), the new predicted average displacement is of 0.06 mm, indicating that the process is slowing down significantly over time and confirming that most of the displacement occurred within the first 7 years of production.

To have a more continuous view of the wall displacement, Figure 113 presents a 3-D surface of the wall displacement over time. one axis presents the displacement as a function of depth and the other time. It is perceptible that at the top of the layer, the displacement seems to be accelerating in time. This is due to the APB itself, which is increasing the pressure of the annulus, pushing this layer away with extra force. In addition, the inflection point at which the creep changes direction seems to be rising over time, approaching the top of the salt column. This may be an important variable to be analyzed in well design, since it will determine a depth under which the volume starts to decrease.

Figure 113 – Displacement of the wall of the salt layer as a function of time

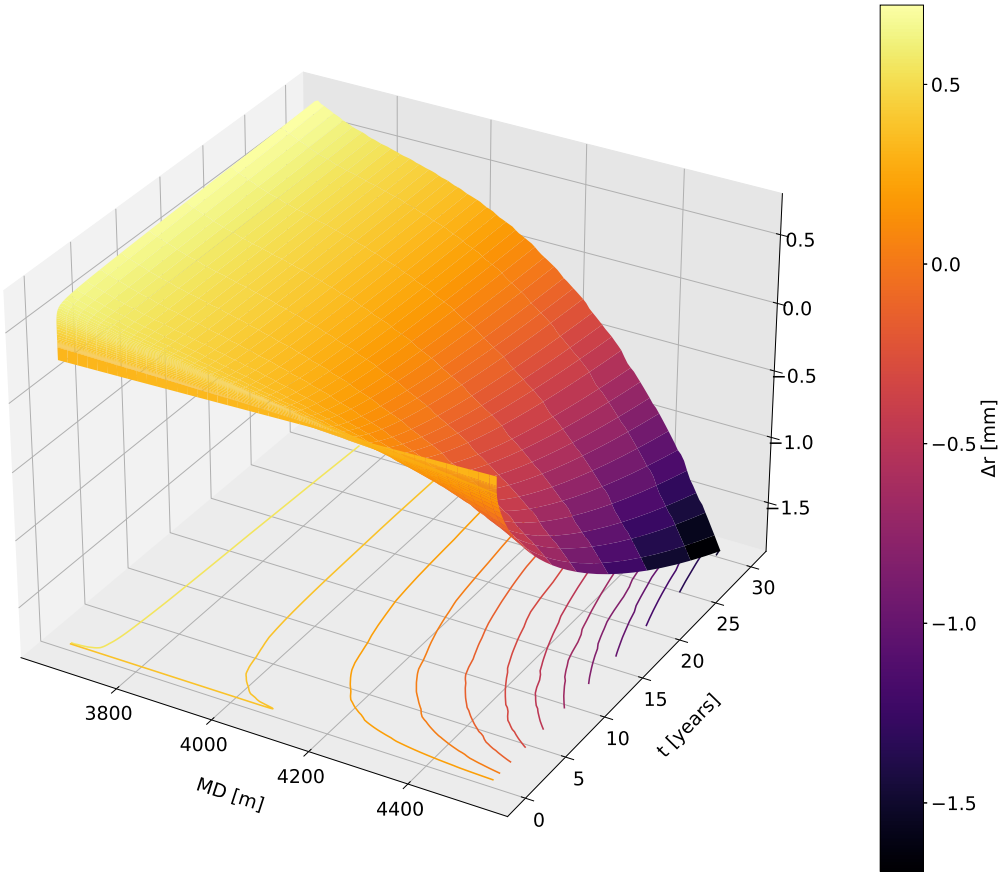

The wall displacement and the APB are important variables in the coupled solution. However, the creep model involves several internal variables, such as the strain itself and the creep amplitude. The behavior of these internal variables is discussed next.

To start this analysis, it is important to establish the behavior of the elastic step previous to the solution of the creep model. Figure 114 presents the four contours for the individual components of the Cauchy stress tensor.

Figure 114 – Stress field in salt layer during the elastic step

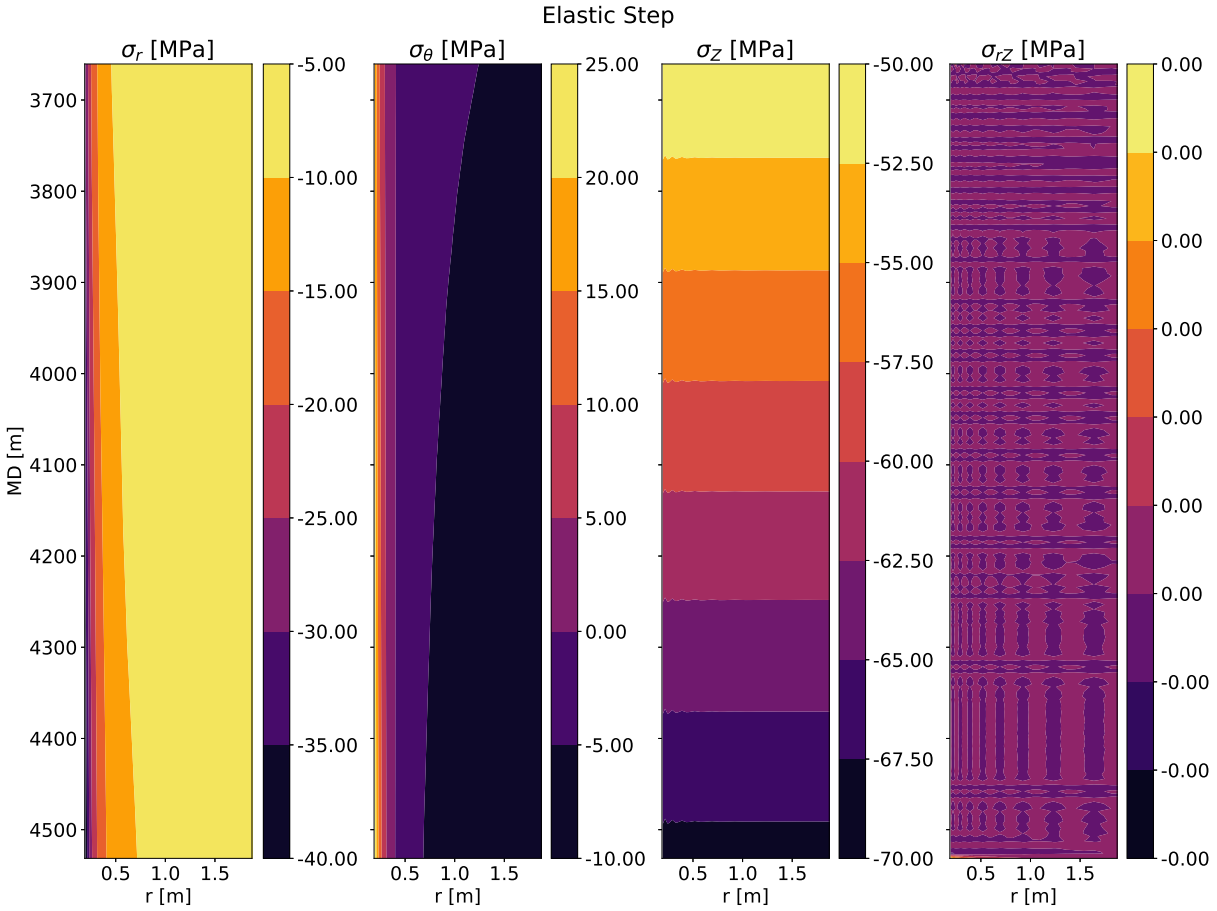

Figure 114 shows some characteristics of the numerical procedure. First, as much as the approach is two-dimensional, unlike the geomechanical model, the shear stress will still be basically null, consisting mostly of numerical noise. In addition, in the vertical stress term, there is a small perceptible oscillation near the wall. This was not captured in previous analyses because it was focusing on just one layer, something that masked the phenomenon. As much as it is visible in this contour, complementary studies indicated that better mesh refinements would be enough to eliminate this oscillation. However, as the effect is basically not felt in APB, it will not be treated as a problem that compromises the studies.

In addition, Figure 115 presents the contours of the effective tension for the elastic step, since this term is the driving force of creep, it will be a fundamental part of the comparisons as it should decrease in magnitude with time.

Figure 115 – Effective stress field during the elastic step

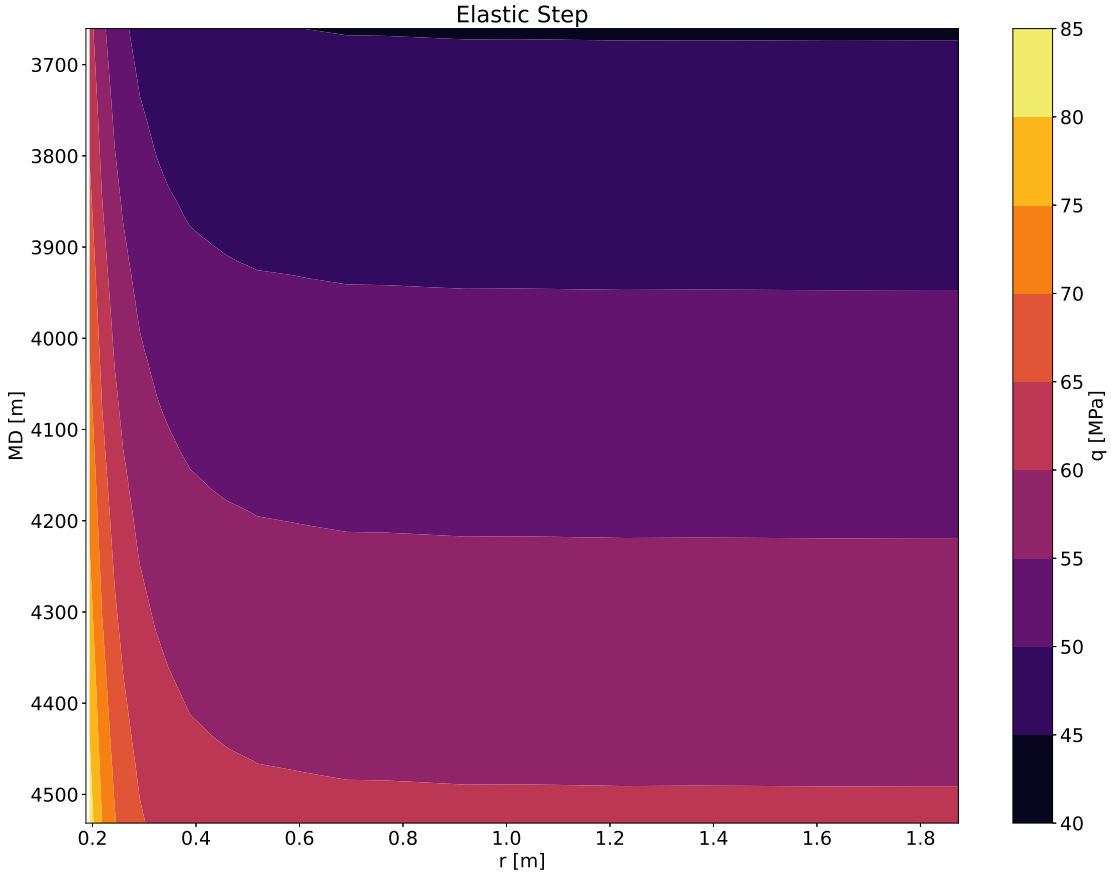

For other variables of the creep model, such as the creep amplitude (γ), they are set to 0 for the elastic step. Thus, at this point all variables for comparison have already been presented or defined so that it is possible to present the results of the creep model in terms of its internal variables.

The first variable to be analysed is the effective stress (q). Figure 116 shows the effective stress fields demonstrated with the same steps for times close to 25%, 50%, 75% and 100% of the simulated time. Note that, when comparing to Figure 115, it is possible to confirm the idea that most of the creep takes place within the first 7 years, with most of the effective stress being consumed in this period (around 95% of the original magnitude). Other than that, a interesting behavior is that the inflection region detected in the displacement occurs at the exact depths with the smaller effective stress, directly relating it to smaller creep strains.

Figure 116 – Evolution of the effective stress inside the salt domain at different times

(a) Effective stress field at 25% of simulation

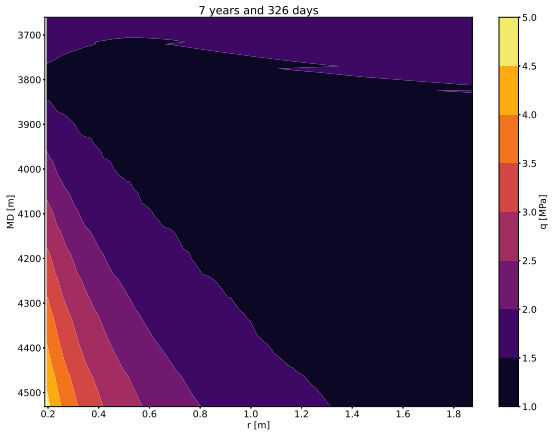

(b) Effective stress field at 50% of simulation

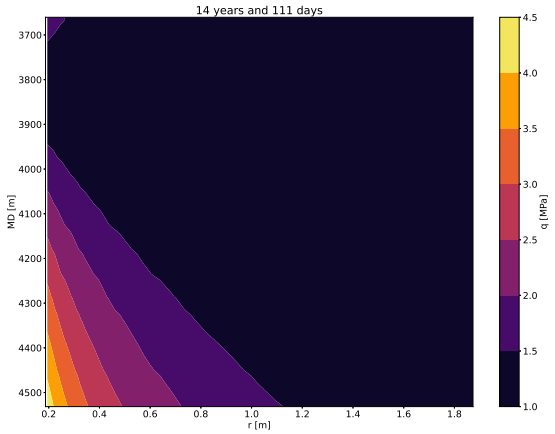

(c) Effective stress field at 75% of simulation

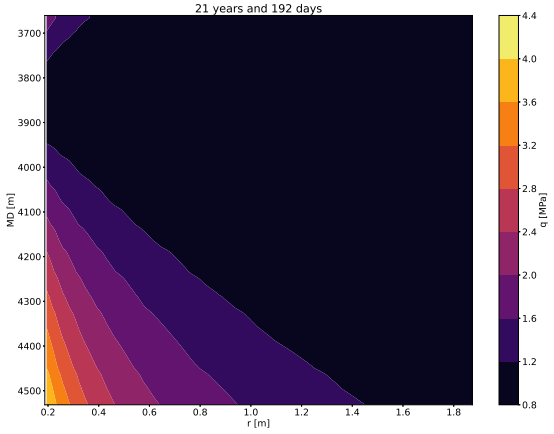

(d) Effective stress field at 100% of simulation

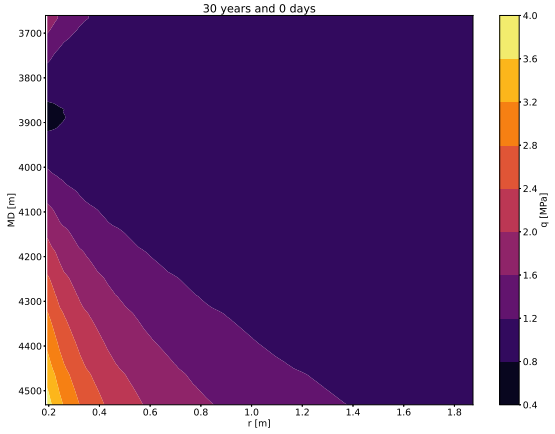

Figure 117 presents the creep strain for the same times presented previously. Note that most of the creep is concentrated near the well wall, with a behavior similar to the effective stress. Also, when analysing each component individually, for any of the analysed times, it is clear that the radial component of the creep strain is the largest, followed by the hoop component. Once again, the shearing component has the smallest magnitude, with 2 orders of magnitude lower in relation to the other components. Also, most of the creep strain seems to take place in the first 7 yeas. This is made clear by the fact that, within this time period, the strain in the radial direction, managed to achieve a magnitude of 7×10^{-3}. Meanwhile, for the rest of the 30 years, this strain only increased by 0.5×10^{-3}.

Figure 117 – Evolution of the creep strain (ε_{cr}) during simulation

(a) Creep strain (ε_{cr}) field at 25% of simulation

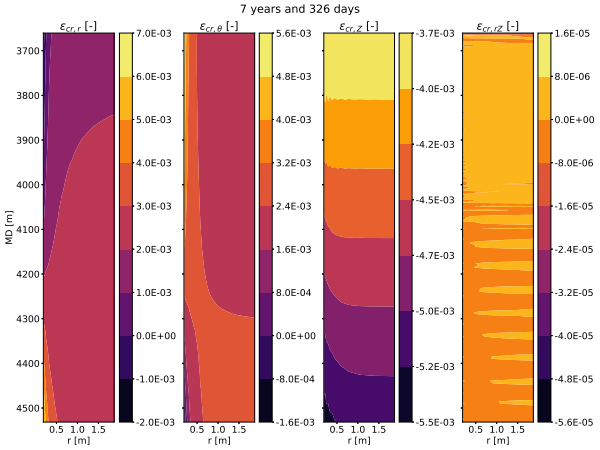

(b) Creep strain (ε_{cr}) field at 50% of simulation

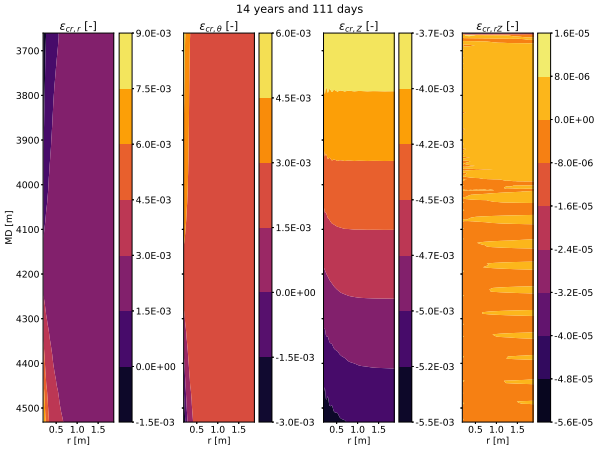

(c) Creep strain (ε_{cr}) field at 75% of simulation

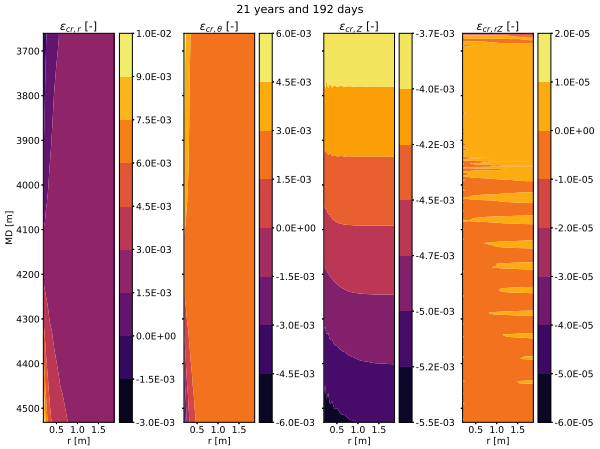

(d) Creep strain (ε_{cr}) field at 100% of simulation

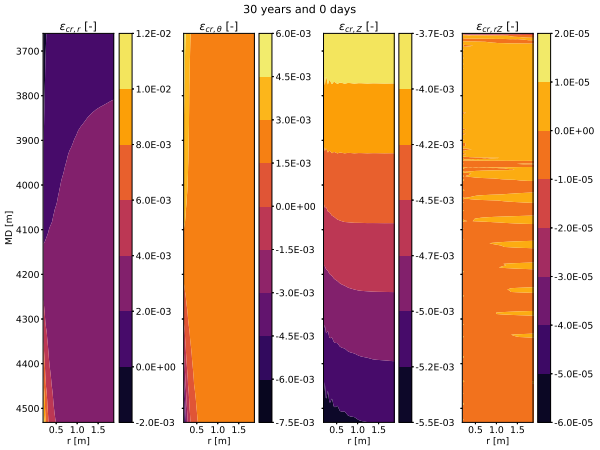

Another interesting result pointed out by these figures is the non-uniform strain of the salt layer in the vertical direction. Note that the creep strain in the Z direction tends to increase near the wellbore wall at the bottom of the salt layer. This indicates that regions near the wellbore would sink further than regions away from the well. In order to quantify this phenomenon, and better understand the effects of the creep in the total displacement of the salt layer, Figure 118 presents the resulting displacement in the salt domain for the same 25% time spacing.

Figure 118 – Evolution of the displacement (**U**) during simulation

(a) Displacement (**U**) field at 25% of simulation

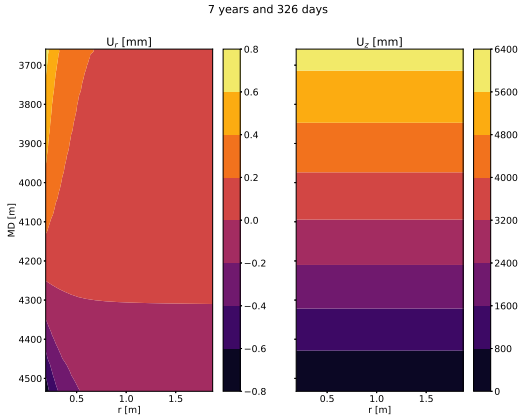

(b) Displacement (**U**) field at 50% of simulation

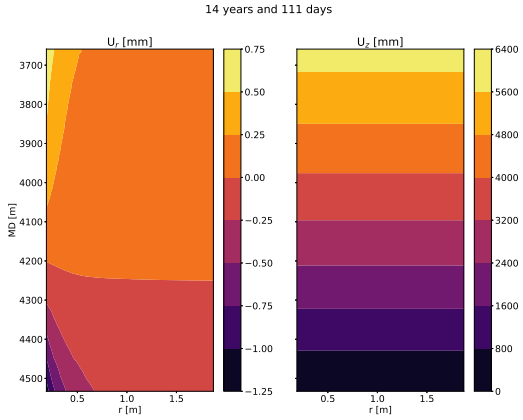

(c) Displacement (**U**) field at 75% of simulation

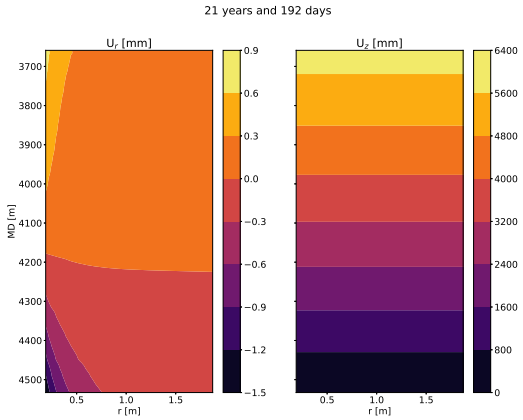

(d) Displacement (**U**) field at 100% of simulation

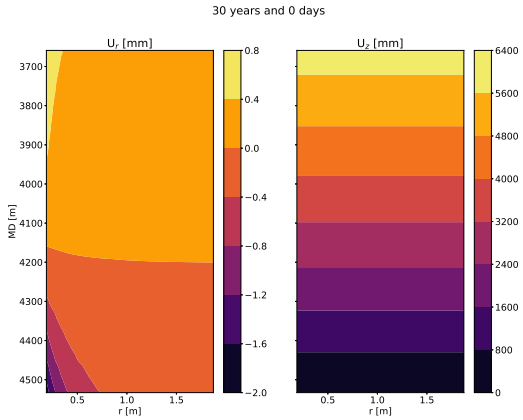

When analyzing the displacement fields in the salt layer, the concentration of the vertical strains near the wall is not so evident. However, since the model considers the two-dimensional displacement, the axial/vertical component can be quite significant, reaching up to 5.96 m. This leads to a small inconsistency in the computation of APB since this contribution is not taken into account anywhere else in the program, being present only as a closure for the equations. As mentioned before, some more complex models for computing the volume variation of the annulus take the axial strain as well as the radial displacement into account. In such a case, this variable would be important. However, for the present study, it is not used.

Besides this result, another conclusion is actually a confirmation of a consideration made by Almeida (2016) that the creep phenomena is concentrated in a region within 10 inner radii of the formation. In fact, these greater displacements are no longer perceptible for distances further than 1 m from the wall. This conclusion is important since it means that for simulations which would not take into account the thermal expansion of the salt layer, it is possible to reduce the simulated domain, leaving a larger margin for higher precision of the solution without increase in computational cost. For

the simulation presented, it is clear that the domain with a radial length of 100 radii is excessive. However, in the forthcoming study that investigates the effect of thermal expansion, it is important to keep the same domain for a fair comparison.

In order to verify the physical consistency of the developed program, it is important to check the transient behavior of the creep amplitude. Since this variable is defined as a monotonically increasing function, if it does not behave as such, it would mean that the developed program is not consistent. In order to analyze this variable, Figure 119 presents its contours at the same time steps shown for previous variables. First, contrary to previous variables analyzed, the creep amplitude tends to spread over the entire domain with the minimum value detected at 30 years of 0.038, located at the furthest integration node near the top of the layer. Even though the figure is not particularly clear, the numerical results show that the consistency criterion was met in the entire domain, a strong indication of proper implementation of the constitutive model. Once again, most of the creep was detect to occur on the first 25% of the simulation, with the remainder taking place at a much slower pace. Nevertheless, contrary to previous variables, the creep amplitude seems to spread along the domain, not necessarily concentrating near the inner wall. This is not to say that the magnitude of the creep is evenly spread, but when compared to the radial displacement, for example, the creep amplitude seems to be less concentrated near the inner wall.

Figure 119 – Evolution of the creep amplitude (γ) during simulation

(a) Creep amplitude (γ) field at 25% of simulation

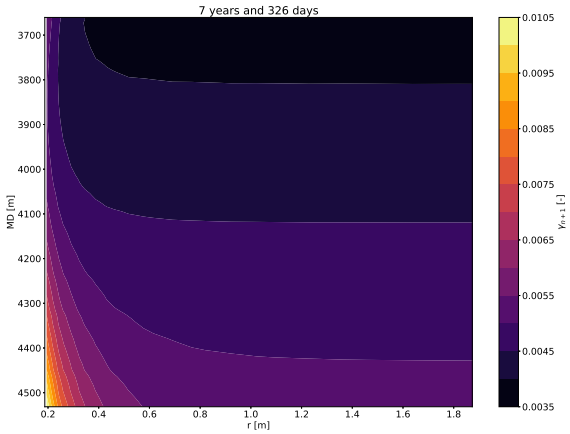

(b) Creep amplitude (γ) field at 50% of simulation

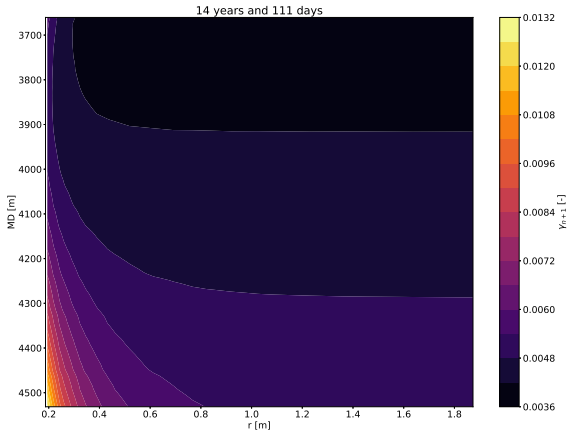

(c) Creep amplitude (γ) field at 75% of simulation

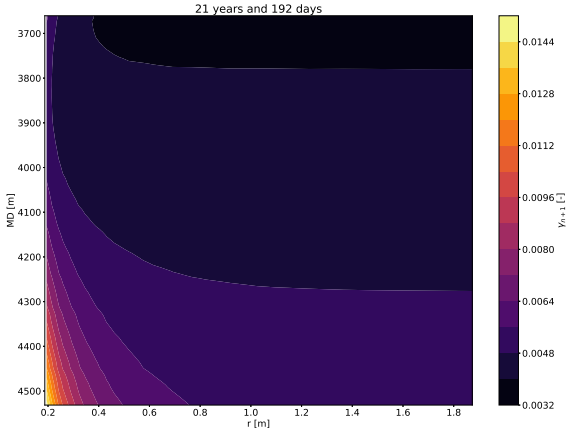

(d) Creep amplitude (γ) field at 100% of simulation

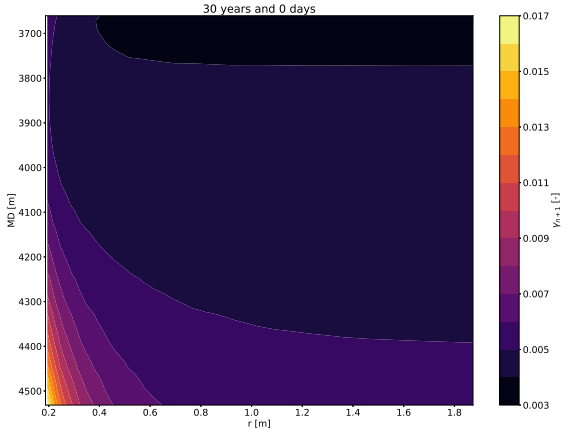

In order to properly monitor the evolution of the creep amplitude and the effective stress, a point was used in order to collect the data in every step of the simulation (a probe node). This point was located at $r = 0.1943$m and $MD = 4097.63$m in order to collect data at the middle horizontal line of the layer and near the wall. With the use of this probe, the data for both variables were collected and are presented in Figure 120.

Figure 120 – Transient behavior of probe node

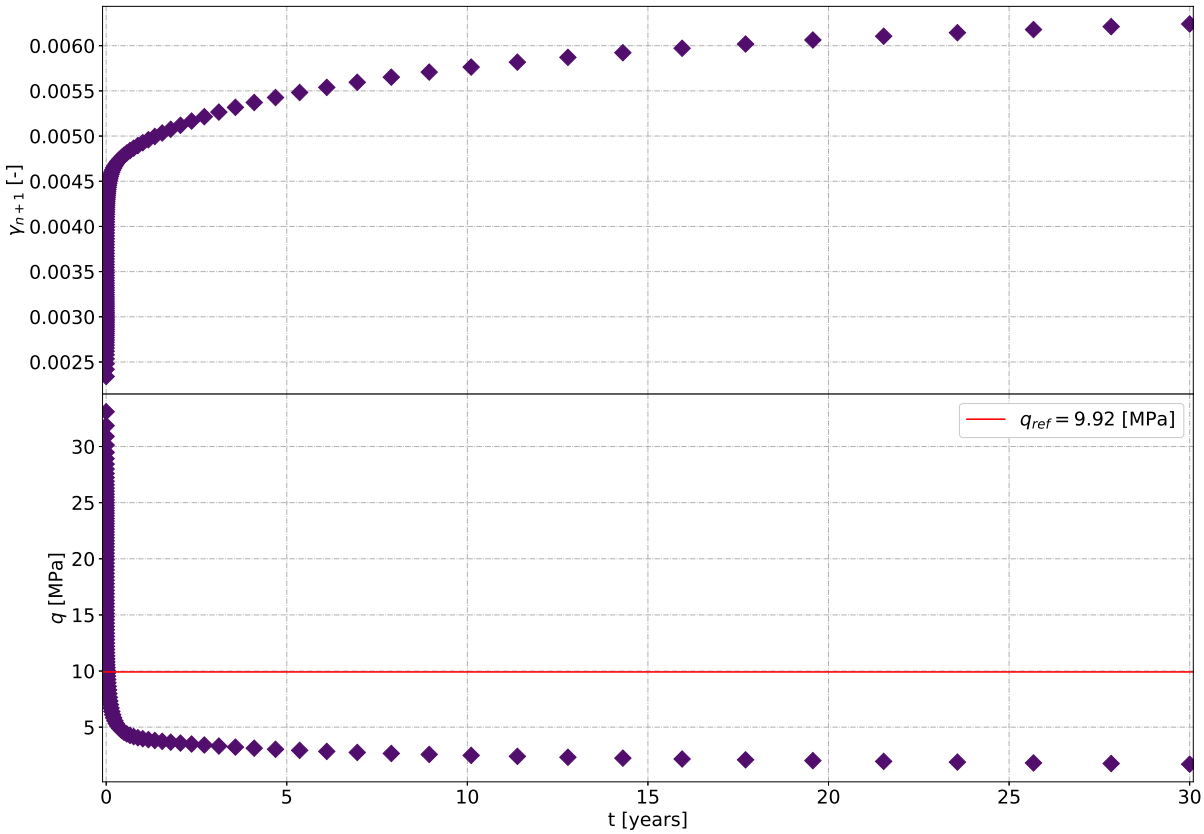

The figure shows that, in fact, the drop in the effective stress seems to occur in the region where the well is heated, that is, before the end of the first year of production. This phenomenon is simple to explain, as the source of the effective stress is a function of the difference of pressure in the annulus and the horizontal stress far from the well. Once the pressure starts to increase inside the annulus (APB), this difference rapidly decreases, reducing the effective stress and, as a consequence, the creep rate. In this initial region, there is even the moment when the effective stress crosses the reference state of the creep law. From this moment on, the creep rate decreases more quickly, something that ends up affecting the speed with which the deformation occurs.

Figure 120 also confirms a problem previously mentioned. Note that at the end of the simulation (30 years), the creep amplitude achieved a value of 0.0062. In the first time step, this variable is predicted to be 0.0022, which is about a third of the final value. So it is clear that most of the information resulting from the initial creep is lost due to lack of discretization at the start of the simulation. However, even with this detected phenomenon, the creep amplitude still kept the monotonic behavior during the entire simulation, once again suggesting that the constitutive model was correctly implemented.

As previously mentioned, the size of the simulated domains seems to be ex-

cessive, however, it was not reduced to ensure that the comparison with the thermal expansion is possible. Up to now, this term was disabled in the equations, however, it is possible to analyze the temperature increase over time inside the salt layer. Figure 121 shows the temperature in the formation. Note that the temperature appears to have a certain stepping behavior at specific depths, this is due to the interpolator used to inform the internal boundary condition of the interfacial temperature. This interpolator uses a very rudimentary interpolation technique, the “previous-value” approach. This was done due to the cementation present at the bottom of the layer, which caused some anomalies when using a linear interpolator. The main problem detected when using the linear interpolator was a prediction of temperatures colder than the initial condition in the salt layer, even for longer simulations. So, to avoid such a phenomenon, the interpolator was changed to the previous value, thus, taking the boundary condition from the point immediately above the MD of each integration node.

Figure 121 – Evolution of salt layer temperature (T) during simulation

(a) Salt layer temperature (T) field at 25% of simulation

(b) Salt layer temperature (T) field at 50% of simulation

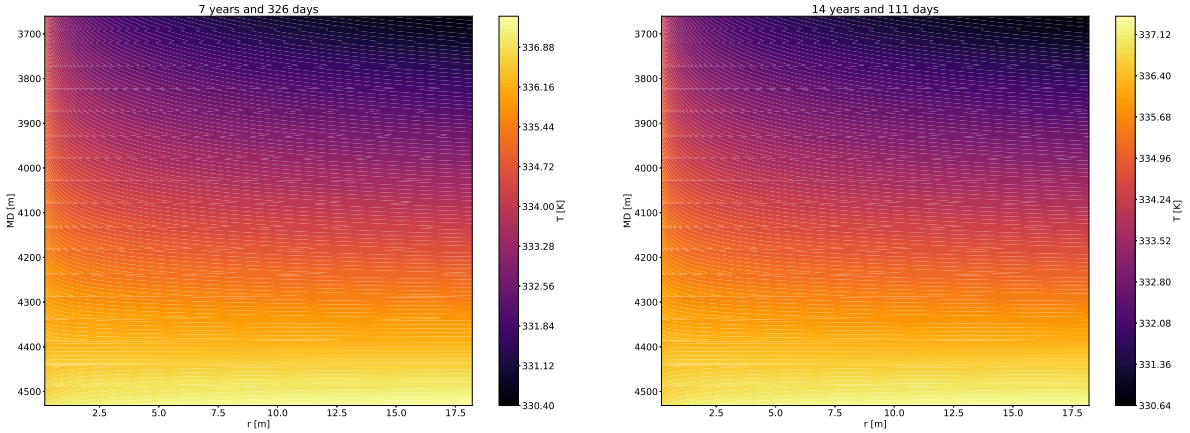

(c) Salt layer temperature (T) field at 75% of simulation

(d) Salt layer temperature (T) field at 100% of simulation

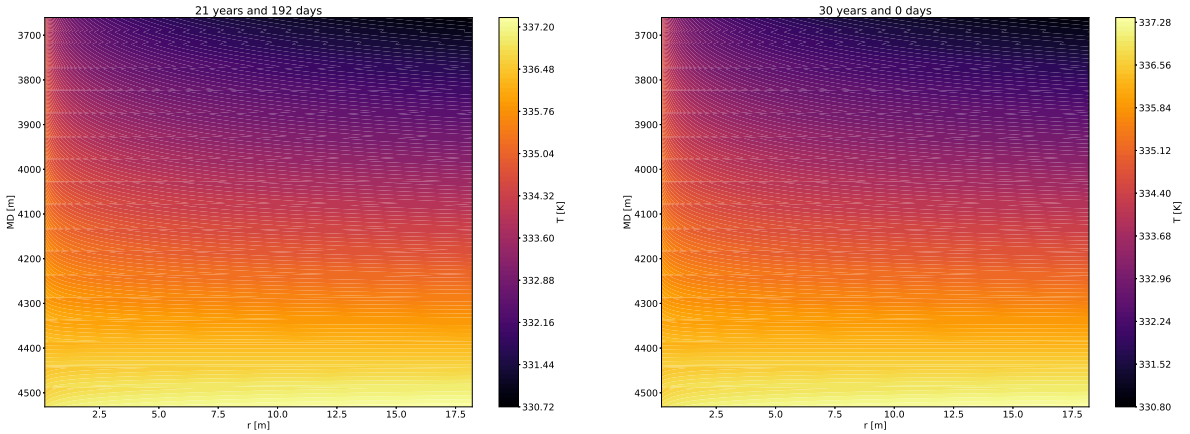

The figure also shows that the heat wave managed to advance far beyond the

distance of 100 inner radii. In addition, the heating (temperature increase), unlike the structural variables of the problem, is not concentrated near the wall, diffusing more evenly through the domain. Because of this, the decision to extend the domain even to excessively long distances seemed to be accurate.

The result of APB presented earlier shows that there is a potential for increasing the risk for this well. To check if this well is indeed at a risk of collapse, the following results evaluate the strains in the wellbore. So, Figure 122 shows the profiles of the strains at each casing and solid material. However, for annulus B, note that at the depth where the salt layer is located, the external strain of the annular model is set to zero. This, of course, is not the real result of the strain. However, when using the salt model, a null strain is imposed for the traditional approach, calculated via Halal and Mitchell (1994), so there would be no conflict between the two solutions. The strain in this region is directly inserted in the form of variation in the cross-sectional area for the calculation of the annular mass.

Figure 122 – Strain comparison for tubulars and elastic formation for well with a salt layer

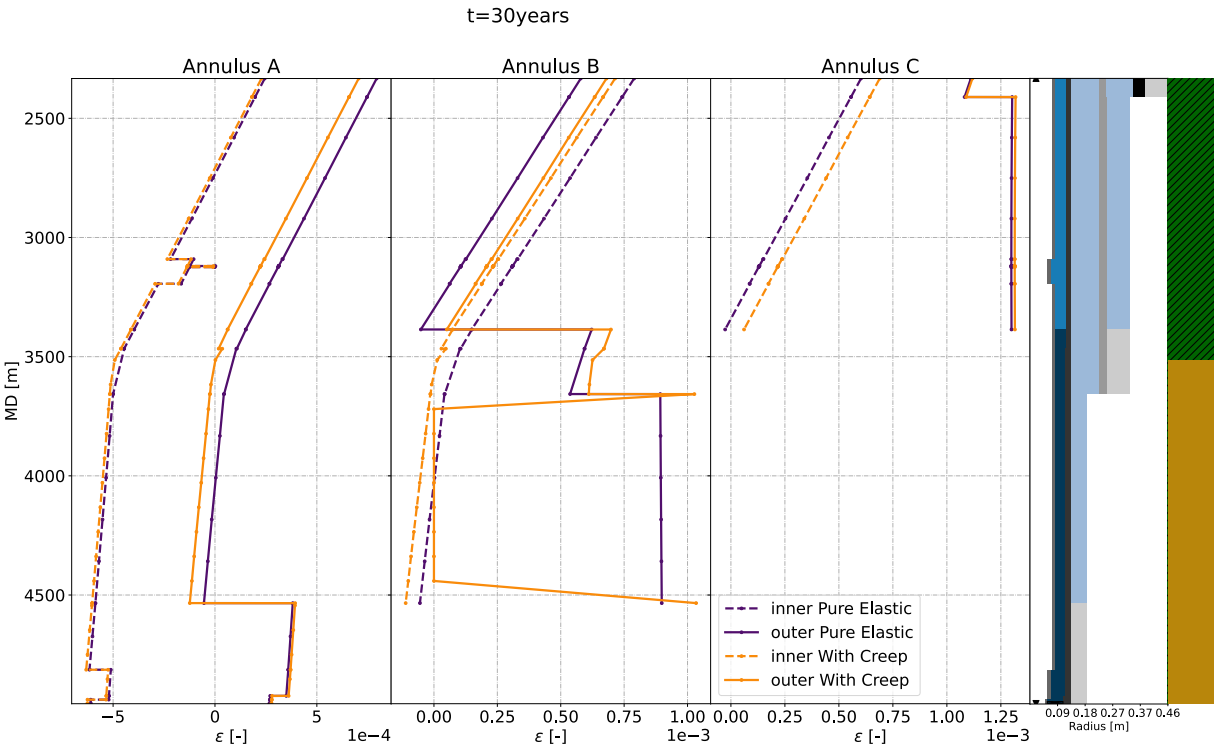

In this well, the salt does not seem to affect enough the APB so that the casings enter a risk region. In spite of this, the effects of variation on pressure due to creep are felt even in annuli other than annulus B. For example, annulus A feels large variations in strain of the production casing.

As can be seen, the model developed was able to deal with a real case without great difficulties; the only point that needs to be revised in the future is a way to allow simulations in shorter times. Even so, the results indicate that the model is able to

simulate the deformation of salt layers together with the thermal APB of oil producing wells. A brief analysis of two modifications in the model is presented next.

5.3.3 Comparisons with different formulations

The first comparison is between the thermal models used in conjunction with the salt model. As explained earlier, the development of Hybrid-Laplace model had as one of its objectives to allow more precise simulations in shorter times exactly because of the coupling with the salt formulation. Thus, a comparison in the resulting APB between the two considering while salt creep is also important in relation to the heat transfer model.

Figure 123 presents the APB in annulus B, initially the models start with a big difference as a direct consequence of the lack of capacitance slowing the heating of annulus B. As time progresses, the difference between the models drops. However, even for long times, a large difference in the results is apparent. Over the period of 30 years, the difference in the predicted APB is around 833.73 kPa. As the thermal APB resulting from the pseudo steady-state model in the first time steps of the simulation are greater than those predicted by Laplace model, the effective stress in the rock decreases at much higher rates. This causes creep to occur at lower magnitudes for longer times, thereby reducing its effects on the well.

Figure 123 – APB comparison with different thermal models for annulus B

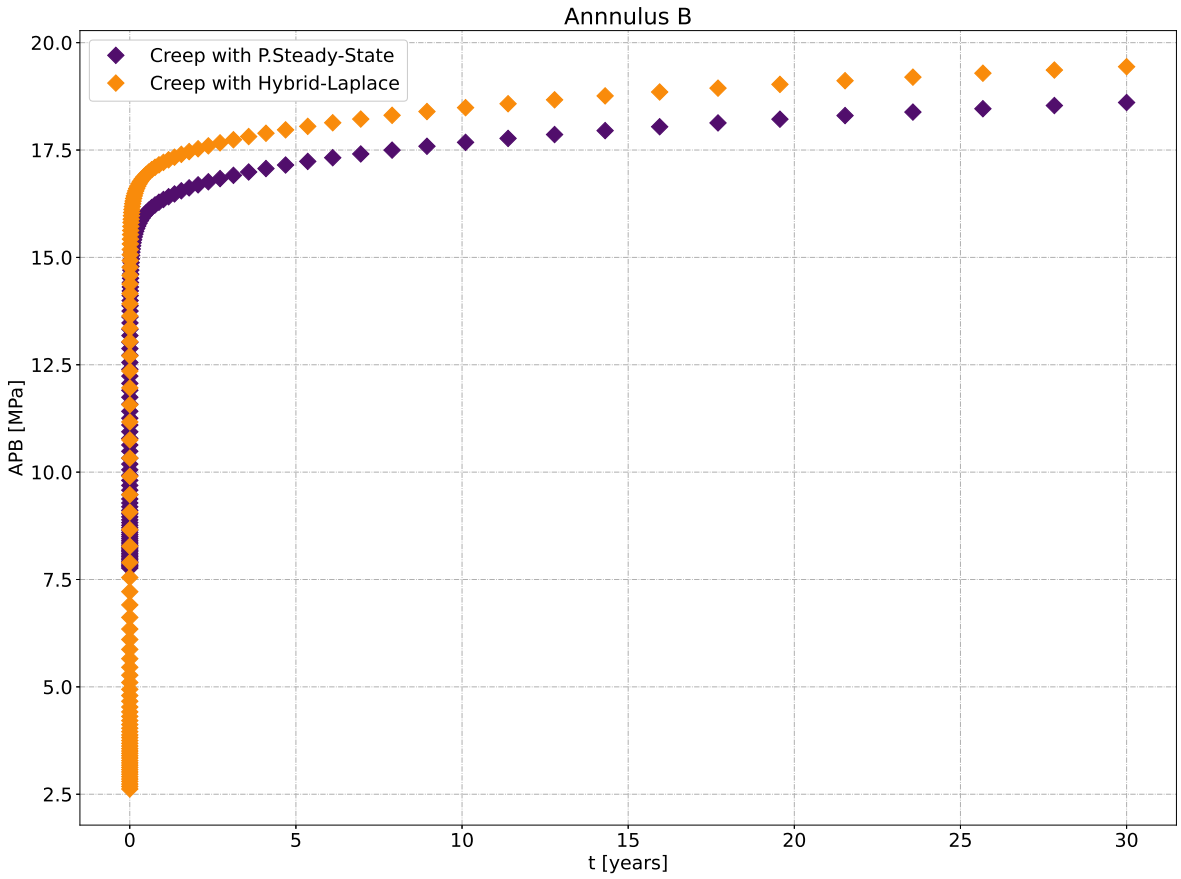

This result is interesting from two aspects. First, it confirms the importance of developing a new transient model to deal with the heat transfer in the annulus for shorter times. Also, it confirms the idea that studies involving shorter time are important to determine the final value of APB, since the model seems to be highly affected by the behavior of the effective stress for shorter times.

The second study involves activating the thermal expansion term in the mechanical balance equation of the salt layer. To do this, the thermal expansion value of the halite is included as $4.6 \times 10^{-6} K^{-1}$. Thus, the expansion term starts to affect the strain of the salt layer. As it is a purely volumetric term, it should not directly affect strains due to creep, however, if the effect on the annulus is sufficient, it can affect indirectly through the coupled pressure boundary condition.

Again, the analysis will be focused on the APB, as it is the most important variable studied. Figure 124 shows the APB comparatively between models.

Figure 124 – Comparison of the APB comparison on annulus B considering expansivity of salt layer

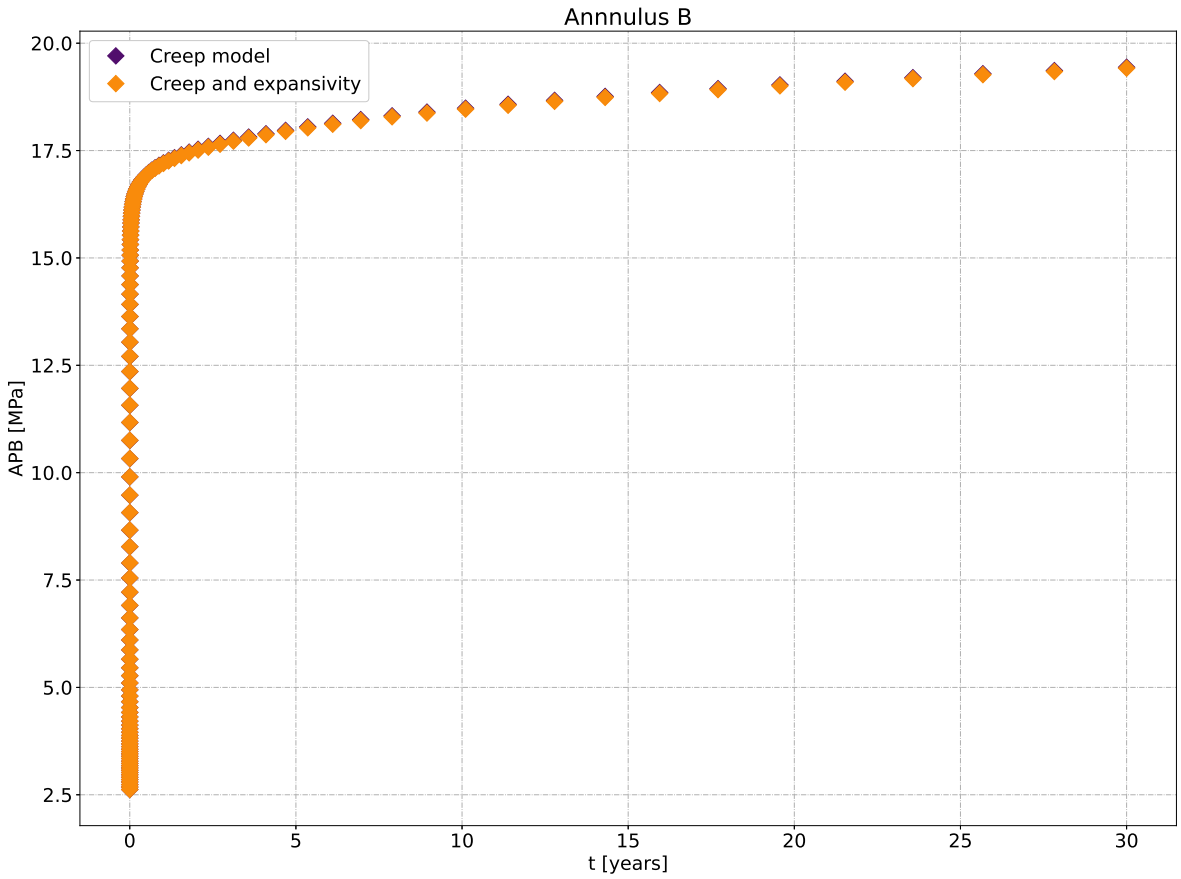

As can be seen, the effect of expansivity is minimal because of the very small absolute temperature increase in the salt layer. In fact, in 30 years of production the biggest difference in temperature perceived in an integration node, compared to the initial condition, was 4.64 K. Thus, the rock undergoes very little expansion, to the point of not even affecting the solution. This, however, should not be treated as an absolute result indicating that the effects of expansivity should not be taken into account in every scenario. It turns out that, for this well, the fact that the temperature provided in the PDG is lower than the temperature of the geothermal gradient causes a large section of the well to have a very small heat transfer, and the salt layer is within this region. For HP/HT producing wells, greater heating may occur and a simple analysis indicates that the expansion may indeed be significant.

In this case, from the results of Figure 117, the creep strain is of the order of 10^{-2}. With a simple calculation, one notices that for a temperature variation of 4 K, as predicted for the case studied, the expansion strain will be of the order of 10^{-5}, or three orders of magnitude smaller than the creep strain. However, when analyzing the heat exchange at the upper regions of the well, the temperature variation may exceed 30 K, so assuming that a strain of the order of 10^{-4} occurs is not an invalid hypothesis. For

this case, the order of magnitude of the strain increases, so it is difficult to assume that such a term is not important. In sum, it can be said that while for this case it may be discarded, it should not be extrapolated for every other well without considerations first.

The importance of this result is directly related to the computational cost of the code. Due to the process of solution of the mass conservation, when computing the displacement of the wellbore wall due to creep and thermal expansion, extra iterations are required to achieve convergence. As a consequence, the code jumped from an execution time of 2 and a half hours to over 5 hours. Thus, a suggestion for future studies involves detecting the order of magnitude of the thermal strain previously to define the possible contribution of it in the total strain, since using the term can result in a considerable increase in the computational cost.

Finally, Figure 125 shows the displacement of the inner wall of the salt layer to verify if there is any point with greater deviation resulting from the heating. It was found that the biggest differences occur near the top of the salt layer, which makes sense since the largest temperature increases occur the closer to the surface. This result confirms what was stated earlier, i.e., that these studies must be repeated in wells that undergo greater heating in the salt layers.

Figure 125 – Comparison of the wellbore wall displacement considering expansivity

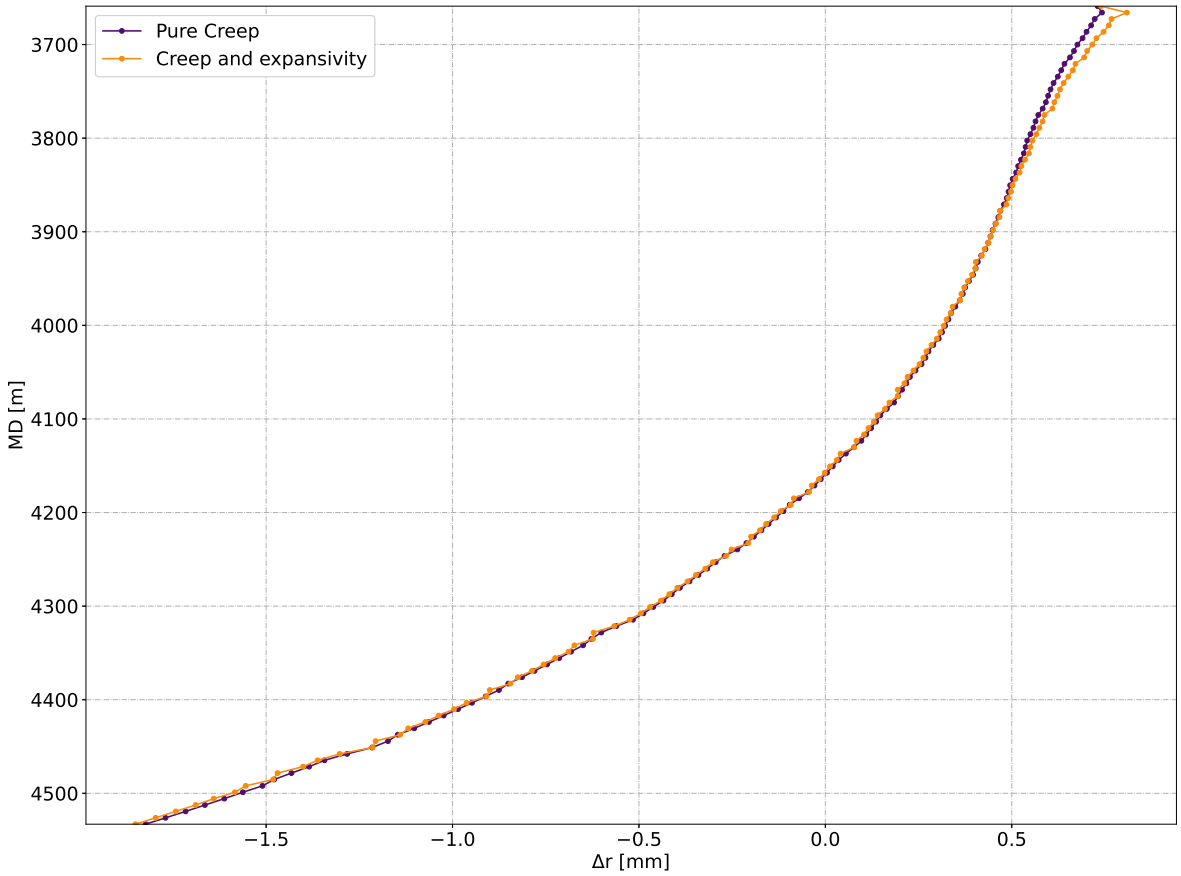

5.3.4 Summary of results in well with a salt layer

In this section it was possible to use a new geometry to study heat transfer in oil producing wells under new scenarios. First, it is the well with the largest flow rate within the ones used. This leads to a behavior in which the temperature difference from the predicted model start the smallest from all studied wells. Besides this behavior, this is also the well where the Hybrid-Laplace model takes the greater amount of time to settle in temperatures higher than the pseudo steady-state model.

This well was also the first to be used in order to evaluate the APB for what is equivalent to the lifespan of a well. This simulation, of 30 years, presents some interesting results about the time necessary to model the worst scenario for APB in a well, when considering steady production. For example, in this well the wellhead temperature settles around 2 years of production, so using this value to model heat transfer seems to be a safer estimate in order to model the worst scenario for the casings instead of values such as 7 or 10 days.

This is also the first real well with a salt layer in contact with an annulus to be analysed, so it is possible to use the new creep model to determine the effect of such a layer on APB. The study associated with the creep related model is split into some different section. To start, a brief grid convergence was performed, determining that a grid with a configuration of 16×64 elements are sufficient to model APB with the salt contribution. After this convergence test, the elastic step is used to validate the formulation against a geomechanical plane stress model.

After performing the complete simulation considering the creep effects, the contribution of the salt layer to the final APB is around 2.55 MPa. This value is over 10% of the estimated APB predicted by the traditional methods, indicating the importance to take this term into account for this simulation. As the main objective of this thesis was to propose a coupled model for simulating thermal APB and the creep displacement in salt layers, this is the main result presented.

Besides that, it was also confirmed the importance of developing the Hybrid-Laplace heat transfer model. The reason for such statement is connected to the comparison of the results of the creep model. When using the pseudo steady-state model instead of the new Hybrid-Laplace model, the results in APB were significantly different. And even more crucial, the difference when using the standard approach lead to a less severe APB. This is dangerous as can lead to an overestimation of the safety factors in the design of well.

Finally due to the information provided for the PDG, the heat exchange in the salt layer is not high, as a consequence the thermo-elastic expansion does not affect the APB prediction for this well. However, complementary results points that this term may be important depending on the simulated conditions and must be further investigated.

5.4 RESULT ANALYSIS

This section presents the main results in each individual studies pointing out the contributions of this thesis for the literature on APB simulation.

For the improved heat transfer model, a new formulation based on Laplace transforms was created to write a system of algebraic equations that represents the transient temperature profiles in the wellbore and formation. The analogy of thermal resistance and capacitances was adopted to approximate the heat transfer. The resulting system of algebraic equations was solved with the aid of a numerical framework (ABATE; WHITT, 2006), which used the weights and nodes according to the CME method (HORVÁTH et al., 2020).

To model the deformation of salt rocks, a formulation similar to that presented in Almeida (2016) was used, the main difference being the fact that the proposed model in this work was developed in-house to allow for a consistent coupling scheme with the thermal solver. The formulation and discritization are based on the two-dimensional axissymetric FEM, for materials with time-dependent deformation. The element selected to describe the domain was the biquadratic element, choice made in order to achieve higher accuracy with reduced computational cost. Finally, terms related to thermo-elastic deformation were added to the model, which allowed an analysis not yet made regarding the expansion salt layers due to heating.

In other points, the program uses features presented in Veiga et al. (2020), both the approach used to calculate the thermodynamic properties of the fluids (table interpolation), and the equations solved in the production tube (energy and momentum). In the used version of the program pySAFE it was possible to use the correlation of Beggs and Brill (1973) to calculate the pressure gradient in two-phase flow, as well as the correlations of Chen (1966) and the modification of Zhou (2013) were used for the forced and natural heat transfer coefficients respectively.

For validation, geometries of real producer wells, supplied by Petrobras, were used. The first one used was a well already analyzed in Barcelos (2017), so it can be applied to test new formulations developed in Veiga et al. (2020) against the original SAFE program as well as validate the application of the new Hybrid-Laplace model. Then, a well operating in EWT was used, thus allowing for more conclusive studies regarding shorter production times (less than 7 days). Finally, a geometry of a pre-salt well that has its annulus B exposed to a salt layer was provided, so that a comparative study could be performed to analyse the new creep displacement model for APB calculation.

The first analysis performed involved the vertical well and its first important result was the rapid convergence of the Laplace transform model, requiring 16 nodes for the numerical inversion. This result is important because it is the first time that this methodology has been applied to heat transfer in wellbores and, therefore, the convergence

requirement of the method was not known. The use of these 16 inversion nodes caused the proposed code to be 3 times slower than the original pySAFE, however as much as it may seem, in absolute time, the execution of a single time step still remained below 20 seconds, a very acceptable runtime for a large number of applications.

Regarding the physical results for this first case, it was possible to assert that the new pySAFE performed similarly to the original SAFE with regards to the results of Barcelos (2017). In addition, the new heat transfer model, based on the Laplace transform, had a accuracy at least similar to traditional models in the literature when compared to this well's field data. The main reason for such similarity is primarily due to the fact that both models are, in fact, very similar and the assumptions of Ramey (1962) prove to be very strong for long times. Therefore, since this specific well is in production for at least 90 days, an objective comparison of the models with the field data should favor models with pseudo steady-state assumptions.

To attest to this question, a brief sensitivity study was carried out using the well's production flow rate and comparing the results considering that the well maintained constant production for a period of 90 days. The conclusions of this study are simply that in fact the field data provided is too sensitive for the region studied, thus making the comparison less conclusive to which model obtained the best results.

In terms of APB, because of the differences in the studies developed here, it was possible to determine some interesting phenomena. First, due to the way boundary conditions were inserted in the model, using PDG instant information as opposed to the use of average, as done in Barcelos (2017), something interesting can be detected. Due to the presence of N_2 in the first annulus, both the APB and volume variation in this space have a direct relationship with the production pressure. This is not something that affects the general solution, since the variations were very small, but it is still interesting since it shows that for wells completed with N_2, the pressure of the production column is felt in the first annulus.

The results of both models implemented in pySAFE, when compared to commercial software, showed a very good performance, validating its application for estimating the APB in oil producing wells. In this comparison, there were still some questions that may come to indicate a possible path in relation to future studies. In this case, the commercial software estimated higher APB with less temperature increase. On explanation for this result is a different structural formulation which yielded different results. So, implementing new deformations models in the pySAFE for the casing could prove beneficial.

When analysing the data from the PT for this well (pressure at the top of annulus A), a pressure of 28.5 MPa was detected for the 10^{th} production day. When simulating the production, both models predicted a value of 26.9 MPa.This may be indicating that the mass conservation technique is not capturing the phenomenon well, however, it is

most likely that the lack of complete information from the history of production to be affecting the accuracy of the study. An example of this is the lack of certainty involving the initial pressurization of annulus A.

On the EWT well, a larger set of results were achieved. Firstly, as it is a well that started operating for the first time, the formation is not yet affected by a long production history, thus, favoring studies at shorter times. In addition, due to knowledge of flow behavior in this study, it is possible to develop a formulation based on average flows in order to improve the quality of the study surrounding thermal phenomenon in the well. This approach managed to create positive results for the prediction of temperature at the wellhead, however it came at the price of a greater deviation in relation to the field data for the pressure. As the APB is inherently a thermal driven problem, this result was considered positive for its high accuracy in predicting the wellhead temperature.

In order to achieve this high accuracy, an automated formulation for determining lag in data was used. In total a lag of 28 minutes was perceived in the flow rate data, in relation to the PDG measurement of pressure. In addition to this lag, a region with loss of data was detected, in order to fill the space a simple extrapolation of a threshold value was used. In the rest of the production region analysed, instead of using an average value for the production flow rate, a average flow function was used in order to approximate the transient behavior of the production.

In this well, the Hybrid-Laplace model presented better results than the traditional model, with an average of 4 K greater accuracy. This small difference of predicted temperature, when analyzed from the perspective of the sensibility analysis, proves to translate to larger values of APB, for example, the studies in the sensitivity analyses managed to detect variations of over 1 MPa, in APB, as a result of variations within 2 K in the wellhead. This is an important result, since a variation of 3 K can be expected due to imprecision of up to 10% in the flow used.

However, from the results presented for the TPT data, it appears that the Hybrid-Laplace model managed to outperform the traditional pseudo steady-state formulation.

As the annulus A of this well was ventilated, it was not possible to evaluate the accuracy of mass conservation approach for computing the APB. However, comparisons between models shows that both results are very similar, but the pressure growth was significantly slower in the Hybrid-Laplace model compared to the pseudo steady-state model. This difference is directly related to the capacitance of the annuli, which for this well was larger when compare to the previous vertical well.

Furthermore, since annular A is not completed with N_2, the direct relationship from the pressure in the production string was not perceptible in the final result. In this well, the APB, as a consequence of the fluid expansion, was higher than the one predicted for the vertical well, thus, the deformation term for annulus A was less perceptible.

On the results of the sensitivity analysis for the fluid properties, It is clear that for most of the properties analysed, the effects on the estimation of the final APB are minor. However, even for those, on shorter simulated times, the effects where more pronounced. In addition, among those analyzed, it was determined that there is a direct relationship to APB in thermal conductivity, in the other variables studied, or the relationship was inversely proportional or did not significantly affect the result.

Other than that, it was determined that the density is the most important variable in the study of APB. Thus, for works focusing on the development of thermodynamic libraries for fluids contained in the annuli, special attention must be paid to the treatment of this variable.

The study carried out did not include the effect of compressibility nor expanssivity of the fluids, however, this analysis should still be performed later. Even so, there is already a path of studies that can be taken from this analysis and is directly related to the behavior of APB. Note that the pressure increase was lower for heavier fluids, so studies can be developed in order to optimize the weight of the mud used during drilling planning in order to optimize the loads of casings according to APB.

The last well analyzed does not have a comparative study with field data. Thus, studies of this well were mainly comparative between the models. Unfortunately, it was not possible to attribute better results, however, it was still possible to draw important conclusions.

Firstly, the study was extended to 30 years of production. During this period of time, the fact that the Hybrid-Laplace model reproduces the results of traditional models with great fidelity was reaffirmed, to the point that for long times the results get even closer than in previous comparisons.

This well also has an extensive layer of salt around annulus B, thus, it was possible to compare the creep effect in the APB. For that purpose, the Maia C et al. (2005) creep law was used with code developed from FEM. A brief mesh convergence test was performed which determined that even a mesh with little refinement can converge to a good estimation of APB, possibly due to the choice of a higher order element. For this mesh, a comparison was also made with traditional geomechanical models of elastic deformation for the well wall and it was concluded that the implementation performed with good accuracy on the elastic step of the simulation. In addition to this validation, the result of the elastic step served to indicate the idea that models of APB should start from the elastic deformed condition and not from the non-deformed one, since this can represent a large change in the volume of the annular spaces.

Than the results of the models were compared considering creep for long simulations. In the studied scenario, a difference of 2.55 MPa (7.75%) is foreseen in APB for annulus B. Also, it was detected that the effects of this pressure variation could be felt in annulus A on a smaller scale.

Another important result was the capacity of dividing the increase in pressure into three dominant stages. The first dominated by the thermal phenomenon. The second in which temperature growth stabilizes, causing a slowdown in the volume increase due to elastic deformations, as a result of this rapid stage, the APB almost stabilizes around 0.55 MPa. Finally, creep begins to cause a large reduction in the volume of the annular space, which leads to proportional pressure increases.

It is also possible to infer from the results that most of the creep rate was "consumed" in the first 7 years of production. However, even after 30 years the displacement is not yet settled. So in order to estimate the worst case scenario even further simulations are recommended.

The major problem detected in this study was the inability to simulate less than half an hour of production. Thus, new techniques for numerical stabilization of the mass conservation algorithm must be developed to increase the precision of the simulation. In addition, it is recommended to test the incorporation of this algorithm in state-of-the-art codes for heat exchange modeling in wells, such an approach should have a very high computational cost, however, it may bring better knowledge about the studied phenomena.

This same study was repeated using the traditional model of heat exchange in oil wells. It was clear that there is a big difference in the final result due to the pseudo Steady-State assumptions for short times, affecting the creep rate exactly at the moments when it reaches its highest values. Thus, it can be said that outside of producing promising results to model heat transfer in wells, the Laplace model still proved to be of great importance for coupling the modeling of APB with the deformation of salt layers.

The last study performed analysed the effects of the thermal expansion acting. It was concluded that, for the tested well, the thermal expansion does not affect significantly the APB. However, it is not necessarily this way for every well. When analysing the results, it was clear that, as a consequence of the PDG data for the temperature, the model predicted almost none variation in temperature at the formation (with a maximum variation of 4 K). By applying a simple dimensional analysis one can conclude that for variations over 10 K, this term may be important. Thus, a new study with higher temperatures in the PDG is recommended to test the result again, in addition to a new methodology for reducing the computational cost of the program by checking the order of magnitude for thermal expansion, discarding the term for cases in which it is not significant.

6 CONCLUSION

In this master thesis, the program pySAFE was improved based on the version presented in Veiga et al. (2020). For this purpose, a new consistent methodology was developed for coupled calculation of heat transfer in oil producing wells. This new model was developed to eliminate the need for *ad-hoc* time functions while guaranteeing the application of a thermally consistent boundary condition. In addition, an innovative methodology was developed to simulate APB in producing wells coupled with the deformation of layers of evaporitic rocks susceptible to creep. In order to verify the quality of the new proposed models three real wells were used.

The first well analyzed was a vertical well which was already studied in previous works, therefore, its results were used to validate the new heat transfer model based on the Laplace Transform. In general the new model was able to reproduce the same behavior of the standard pseudo steady-state model for longer simulations (10 days). When comparing the results among models with the field data and a golden standard commercial software it is clear that this new formulation managed to improve on previous models, with results closer to the more sophisticated software and the field data.

In the second well, the one in EWT, the extra data provided for the studies allowed for a more in-depth analysis. From this, it was possible to confirm a better accuracy for the new heat transfer model proposed, it managed to better reproduce the wellhead temperature within 4 K when compared to the pseudo steady-state model. In order to better understand the heat transfer phenomena and the APB a sensitivity analysis was also performed, which pointed, mainly, for the fact that both models managed to reproduce the field data within a margin under which the deviations of the results could be explained by uncertanties presents in the models. Also, from the sensitivity analysis, it is shown that when studying heat transfer in a wellbores, specially with the focus on APB, the density of the fluids filling all annuli are the main parameter to be accounted in the model.

In the final well, due to a presence of a salt layer exposed to the second annulus, it was possible to apply the new model for calculating APB considering displacement induced by creep in rocks. For 30 years of production, the difference in APB for annulus B was of 2.55 MPa when comparing the simulated scenario without the creep consideration. Also, it was possible to determine that, for simulations with creep phenomenon coupled with the heat transfer, the use of transient thermal models is strongly recommended. Besides that, it was detected that for the case studied, effects of thermal expansions in the salt is not significant to the final APB, therefore, a simple dimensional criteria was proposed based on maximum the temperature variation predicted in the rock. Mainly, for the cases with variations in temperature within 10 K, this term can be

disregarded.

Thus, the main contributions that can be drawn from this work to the literature is a new methodology for calculating heat transfer in oil-producing wells that presented a performance marginally superior to traditional models. In addition, a tool that allows coupling between the APB calculation due to thermal phenomena and rock deformations due to creep was developed that can be used for further studies.

6.1 PROPOSALS FOR FUTURE WORKS

From the main results presented in this work a list of possible future works can be deduced. it is as follows:

1. Compare the new Hybrid-Laplace model to other state-of-the-art models;
2. Add considerations for non-constant resistances and capacitances in the Hybrid-Laplace model;
3. Improve stability of the mass conservation;
4. Develop tools for estimating an optimal mud weight taking into account the APB;
5. Implement a formulation for dealing with multiple salt layers in contact, as was studied in Barcelos (2017);
6. Redo the study of the salt layer with higher temperature in the PDG to analyse the effect of the thermal expansion;
7. Develop new models for deformation of the casings, considering the initial deformation and other mechanism, such as plasticity;
8. Perform more studies with the developed models on others geometries and field data.

REFERENCES

ABATE, Joseph; WHITT, Ward. A unified framework for numerically inverting laplace transforms. **INFORMS Journal on Computing**, v. 18, n. 4, p. 408–421, 2006. ISSN 10919856. DOI: 10.1287/ijoc.1050.0137.

ABDELHAFIZ, Mostafa M.; HEGELE, Luiz A.; OPPELT, Joachim F. Numerical transient and steady state analytical modeling of the wellbore temperature during drilling fluid circulation. **Journal of Petroleum Science and Engineering**, Elsevier B.V., v. 186, June 2019, p. 106775, 2020. ISSN 09204105. DOI: 10.1016/j.petrol.2019.106775.

AER, Alberta Energy Regulator. **Directive 010: Minimum Casing Design Requirements Minimum Casing Design Requirements**. [S.l.], 2009.

AGOSTINI, Cristiano Eduardo; ALMEIDA, Luiz Felippe Medeiros, et al. Salt Creeping Analysis on Deepwater Wells Submitted to Cooling Operations on Trapped Annular. In: OFFSHORE TECHNOLOGY CONFERENCE. OFFSHORE Technology Conference Brasil. [S.l.: s.n.], 2019. DOI: https://doi.org/10.4043/29764-MS.

AGOSTINI, Cristiano Eduardo; JÚNIOR, Nelson Moreira, et al. Thermal shock transient analysis for well integrity through operational envelope. **Proceedings of the Annual Offshore Technology Conference**, 2020-May, p. 1–11, 2020. ISSN 01603663. DOI: 10.4043/30719-ms.

ALMEIDA, Luiz Felippe Medeiros de. **Modelagem termo-mecânica do crescimento de pressão em anulares confinados , frente a formações salinas**. 2016. Dissertação – Pontifíca Universidade Católica do Rio de Janeiro.

ALVES, I.N.; ALHANATI, F.J.S.; SHOHAM, Ovadia. A Unified Model for Predicting Flowing Temperature Distribution in Wellbores and Pipelines. **SPE Production Engineering**, Society of Petroleum Engineers, v. 7, n. 04, p. 363–367, Nov. 1992. ISSN 0885-9221. DOI: 10.2118/20632-PA.

API. **API TR 5C3**. 7th editio. [S.l.]: American Petroleum Institute, 2018. P. 402.

BAHONAR, M.; AZAIEZ, J.; CHEN, Z. Two issues in wellbore heat flow modeling along with the prediction of casing temperature in the steam injection wells. **Society of Petroleum Engineers - 14th Abu Dhabi International Petroleum Exhibition and Conference 2010, ADIPEC 2010**, v. 1, n. 1962, p. 688–708, 2010. DOI: 10.2118/137134-ms.

BAKER, Ron. **A primer of oilwell drilling**. [S.l.]: Burgess International Group Incorporated, 1979.

BARCELOS, Johann Goethe Alrutz. **MODELAGEM MATEMÁTICA DO AUMENTO DE PRESSÃO NOS ANULARES (APB) EM POÇOS DE PETRÓLEO**. 2017. S. 166. PhD thesis – Universidade Federal de Santa Catarina.

BEERENDS, R. J. et al. **Fourier and laplace transforms**. [S.l.]: Cambridge University Press, 2003. P. 458. ISBN 9780521806893.

BEGGS, H Dale; BRILL, James P. A Study of Two-phase Flow in Inclined Pipes. **Journal of Petroleum Technology**, p. 10, May 1973. DOI: 10.2118/4007-pa.

BIRD, James M et al. Interpretation of Temperature Logs in Water-and Gas-injection Wells and Gas-producing wells. In: AMERICAN PETROLEUM INSTITUTE. DRILLING and Production Practice. [S.l.: s.n.], 1954.

BOURGOYNE JR., Adam T. et al. **Applied Drilling Engineering**. [S.l.]: Richardson, TX, 1991.

BOYCE, William E; DIPRIMA, Richard C; MEADE, Douglas B. **Elementary differential equations**. [S.l.]: John Wiley & Sons, 2017.

BRADFORD, D.W. et al. Marlin Failure Analysis and Redesign: Part 1 - Description of Failure. **SPE Drilling & Completion**, v. 19, n. 02, p. 104–111, 2004. ISSN 1064-6671. DOI: 10.2118/88814-pa.

BRILL, James P.; BEGGS, H Dale. **Two-Phase Flow in Pipes, 6th Edition**. [S.l.: s.n.], 1991. P. 640.

BROWN, Jeanna; KENNY, Neil; SLAGMULDER, Yves. Unique Cement Design to Mitigate Trapped Annular Pressure TAP Between Two Casing Strings in Steam Injection Wells. In: SPE Heavy Oil Conference and Exhibition. [S.l.]: Society of Petroleum Engineers, Dec. 2016. DOI: 10.2118/184102-MS.

BYROM, Ted G. **Casing and Liners for Drilling Second Edition**. [S.l.]: Elsevier, 2015. v. 1. ISBN 9780128005705.

CALLISTER, William D. (University of Utah). **Materials Science and Engineering: an introduction**. Ed. by Joseph Hayton, Ken Santor and Anna Melhorn. 7th. New York: John Wiley & Sons, 2007. P. 975. ISBN 978-0-471-73696-7.

CARCIONE, José M.; HELLE, Hans B.; GANGI, Anthony F. Theory of borehole stability when drilling through salt formations. **Geophysics**, v. 71, n. 3, f31–f47, 2006.

CARTER, N. L. et al. Rheology of rocksalt. **Journal of Structural Geology**, v. 15, n. 9-10, p. 1257–1271, 1993. ISSN 01918141. DOI: 10.1016/0191-8141(93)90168-A.

CHEN, Hun Taw; CHEN, Cha'o Kuang. Application of hybrid laplace transform/finite-difference method to transient heat conduction problems. **Numerical Heat Transfer**, v. 14, n. 3, p. 343–356, 1988. ISSN 01495720. DOI: 10.1080/10407788808913648.

CHEN, John C. Correlation for boiling heat transfer to saturated fluids in convective flow. **Industrial and Engineering Chemistry Process Design and Development**, v. 5, n. 3, p. 322–329, 1966. ISSN 01964305. DOI: 10.1021/i260019a023.

CHENG, Wen-long et al. A novel analytical transient heat-conduction time function for heat transfer in steam injection wells considering the wellbore heat capacity. **Energy**, Elsevier Ltd, v. 36, n. 7, p. 4080–4088, 2011. ISSN 0360-5442. DOI: 10.1016/j.energy.2011.04.039.

CHIU, K; THAKUR, SC, et al. Modeling of Wellbore Heat Losses in Directional Wells Under Changing Injection Conditions. In: SOCIETY OF PETROLEUM ENGINEERS. SPE Annual Technical Conference and Exhibition. [S.l.: s.n.], 1991.

COLEBROOK, C F. Correspondence. Turbulent Flow in Pipes, With Particular Reference To the Transition Region Between the Smooth and Rough Pipe Laws. (Includes Plates). **Journal of the Institution of Civil Engineers**, v. 12, n. 8, p. 133–156, 1939. ISSN 0368-2455. DOI: 10.1680/ijoti.1939.14509.

COMSOL, AB. Comsol multiphysics® v. 5.4 www. comsol. com. Stockholm, Sweden. **COMSOL AB**, 2018.

DE SOUZA NETO, E. A.; PERI, D; OWEN, D. R. J. **Computational Methods for Plasticity**. [S.l.: s.n.], 2008. ISBN 9780470694527. DOI: 10.1002/9780470694626.

DONG, Guangjian; CHEN, Ping. A review of the evaluation methods and control technologies for trapped annular pressure in deepwater oil and gas wells. **Journal of Natural Gas Science and Engineering**, Elsevier B.V, v. 37, p. 85–105, 2017. ISSN 18755100. DOI: 10.1016/j.jngse.2016.11.042.

DURRANT, A. J.; THAMBYNAYAGAM, R. K.M. Wellbore Heat Transmission and Pressure Drop for Steam/Water Injection and Geothermal Production: a Simple Solution Technique. **SPE Reservoir Engineering (Society of Petroleum Engineers)**, v. 1, n. 2, p. 148–162, 1986. ISSN 08859248. DOI: 10.2118/12939-PA.

ELLIS, R.C. et al. Marlin Failure Analysis and Redesign: Part 2 - Redesign. **SPE Drilling & Completion**, v. 19, n. 02, p. 112–119, 2004. ISSN 1064-6671. DOI: 10.2118/88838-pa.

ENGINEERING, Canuck. **Norman Wells to Zama Pipeline-Structural Analysis and Soil-Pipr Interaction Study**. NW, Canada, 1983.

FERREIRA, M. V.D.; SANTOS, A. R.; VANZAN, V. Thermally insulated tubing application to prevent annular pressure buildup in Brazil offshore fields. **Society of Petroleum Engineers - SPE Deepwater Drilling and Completions Conference 2012**, Figure 1, p. 288–297, 2012. DOI: 10.2118/151044-ms.

FERREIRA, Marcus Vinicius Duarte. **ESTUDO TERMO-ESTRUTURAL DE POÇOS EQUIPADOS COM TUBOS ISOLADOS A VÁCUO**. 2017. S. 255. PhD thesis – Universidade Federal de Santa Catarina.

FISH, Jacob; BELYTSCHKO, Ted. **A first Course in Finite Elements**. [S.l.]: Wiley, 2007. v. 17, p. 344. ISBN 978-0-470-03580-1.

FJAER, E. et al. **Petroleum related rock mechanics**. 2. ed. Amsterdam: [s.n.], 2008. v. 53, p. 514. ISBN 9780444502605.

FLETCHER, Clive A J. **Grid Generation**. 2. ed. [S.l.]: Springer, 1991. DOI: 10.1007/978-3-642-58239-4_3.

FOSSUM, A. F. et al. How should one-dimensional laboratory equations be cast into three-dimensional form? **Key Questions in Rock Mechanics**, p. 35–42, 1988.

GARIBOTTI, Cristiano Rodrigues. **Uma Metodologia de Volumes Finitos para a Simulação de Escoamentos Viscoelástico com Malhas não Estruturadas Híbridas**. 2014. S. 206. PhD thesis – Universidade Federal de Santa Catarina.

GOODMAN, M. A.; HALAL, A. S. Case study: HPHT casing design achieved with multistring analysis. **Proceedings - SPE Annual Technical Conference and Exhibition**, Delta, p. 63–77, 1993. DOI: 10.2118/26322-ms.

GOSCH, SW et al. Marlin failure analysis and redesign; part 3, VIT completion with real-time monitoring. In: SOCIETY OF PETROLEUM ENGINEERS. IADC/SPE Drilling Conference. [S.l.: s.n.], 2002.

GRIGGS, David. Experimental flow of rocks under conditions favoring recrystallization. **Bulletin of the Geological Society of America**, Geological Society of America, v. 51, n. 7, p. 1001–1022, 1940.

GUO, Boyun; LYONS, William C; GHALAMBOR, Ali. **Petroleum Production Engineering, A Computer-Assisted Approach**. [S.l.]: Elsevier Science, 2007. ISBN 0750682701.

HAFEMANN, Thomas Eduardt. **Modelagem do escoamento multifásico e transferência de calor em poços do pré-sal para a estimativa do APB (Annular Pressure Buildup)**. 2015. S. 147. PhD thesis – Universidade Federal de Santa Catarina.

HAGOORT, Jacques. Ramey's Wellbore heat transmission revisited. **SPE Journal**, v. 9, n. 4, p. 465–474, 2004. ISSN 1086055X. DOI: 10.2118/87305-PA.

HALAL, A.S.; MITCHELL, R.F. Casing Design for Trapped Annular Pressure Buildup. **SPE Drilling & Completion**, v. 9, n. 02, p. 107–114, 1994. ISSN 1064-6671. DOI: 10.2118/25694-pa.

HARRIS, F.J. (IEEE). On the use of windows for harmonic analysis with the discrete Fourier transform. **Proceedings of the IEEE**, v. 66, n. 1, p. 51–83, 1978. ISSN 0018-9219. DOI: 10.1109/PROC.1978.10837.

HASAN, A R; AMEEN, M M; WANG, Xiaowei. A Mechanistic Model for Circulating Fluid Temperature. **SPE Journal**, June, 1996.

HASAN, A. R.; IZGEC, B.; KABIR, C. S. Ensuring sustained production by managing annular-pressure buildup. **Society of Petroleum Engineers - EUROPEC/EAGE Conference and Exhibition 2009**, n. 1994, 2009. DOI: 10.2118/121754-ms.

HASAN, A. R.; KABIR, C. S. Aspects of Wellbore Heat Transfer During Two-Phase Flow. **SPE Production & Facilities**, August, 1994.

HASAN, A. R.; KABIR, C. S. Heat Transfer During Two-Phase Flow in Wellbores; Part I–Formation Temperature, p. 469–478, 1991. DOI: 10.2118/22866-ms.

HASAN, A. R.; KABIR, C. S. **Wellbore heat-transfer modeling and applications**. v. 86-87. [S.l.]: Elsevier B.V., 2012. P. 127–136. DOI: 10.1016/j.petrol.2012.03.021.

HORVÁTH, Gábor. **iltcme**. 2019. Available from: https://github.com/ghorvath78/iltcme. Visited on: 12 Mar. 2021.

HORVÁTH, Gábor et al. Numerical inverse Laplace transformation using concentrated matrix exponential distributions. **Performance Evaluation**, Elsevier B.V., v. 137, p. 102067, 2020. ISSN 01665316. DOI: 10.1016/j.peva.2019.102067.

HU, Xincheng et al. Numerical modeling of a coaxial borehole heat exchanger to exploit geothermal energy from abandoned petroleum wells in Hinton, Alberta. **Renewable Energy**, v. 148, p. 1110–1123, Apr. 2020. ISSN 09601481. DOI: 10.1016/j.renene.2019.09.141.

IFEACHOR, Emmanuel C.; JERVIS, Barrie W. **Digital Signal Processing**. [S.l.: s.n.], 1993. ISBN : 0-201- 54413-X.

INFOCHEM/KBC. **Multiflash™**. [S.l.: s.n.], 2019.

ISHIZUKA, Masaru et al. Application of thermal network model to transient thermal analysis of power electronic package substrate. **Active and Passive Electronic Components**, 2011. ISSN 08827516. DOI: 10.1155/2011/823654.

JAEGER, John Conrad; COOK, N.G.W.; ZIMMERMAN, R.W. **Fundamentals of Rock Mechanics**. 4. ed. [S.l.]: Backwell, 2007. P. 475. ISBN 978-0632057597.

JENYON, Malcolm K. **Salt tectonics**. [S.l.]: Springer, 1986.

LAKE, Larry W. **Petroleum Engineering Handbook: Vol. II - Drilling Engineering**. [S.l.: s.n.], 2006. v. II, p. 771. ISBN 9781555631222.

LEE, John; ROLLINS, John B.; SPIVEY, John P. **Pressure Transient Testing**. Richardson: Society of Petroleum Engineers, 2003. ISBN 1555630995.

LI, Gao; YANG, Mou, et al. Transient heat transfer models of wellbore and formation systems during the drilling process under well kick conditions in the bottom-hole. **Applied Thermal Engineering**, v. 93, p. 339–347, 2016. ISSN 13594311. DOI: 10.1016/j.applthermaleng.2015.09.110.

LI, Mengbo; LIU, Gonghui; LI, Jun. Thermal effect on wellbore stability during drilling operation with long horizontal section. **Journal of Natural Gas Science and Engineering**, Elsevier B.V, v. 23, p. 118–126, 2015. ISSN 18755100. DOI: 10.1016/j.jngse.2015.01.027.

LIU, Xiuquan et al. Multistring analysis of wellhead movement and uncemented casing strength in offshore oil and gas wells. **Petroleum Science**, v. 11, n. 1, p. 131–138, 2014. ISSN 16725107. DOI: 10.1007/s12182-014-0324-7.

MACKAY, F. et al. Geomechanical effects of a 3D vertical salt well drilling by FEA. **42nd U.S. Rock Mechanics - 2nd U.S.-Canada Rock Mechanics Symposium**, 2008.

MAIA C, A et al. Triaxial creep tests in salt applied in drilling through thick salt layers in Campos basin-Brazil. In: SOCIETY OF PETROLEUM ENGINEERS. SPE/IADC Drilling Conference. [S.l.: s.n.], 2005.

MATLAB. **version 7.10.0 (R2010a)**. Natick, Massachusetts: The MathWorks Inc., 2010.

MELO, D. D.E.F. et al. Finite Element analysis of casing-in-casing integrity due to annulus pressurization by means of Salt Creep. **49th US Rock Mechanics / Geomechanics Symposium 2015**, v. 1, Figure 1, p. 326–333, 2015.

MENDONÇA, Paulo de Tarso R.; FANCELLO, Eduardo Alberto. **O método de Elementos Finitos aplicado à Mecânica dos Sólidos**. [S.l.]: Orsa Maggiore, 2019. ISBN 978-85-907153-1-3.

MOE, GEORGE ROBERT; ERPELDING, Peter. **Annular Pressure Buildup: What it is and what to do about it.** [S.l.: s.n.], 2000. P. 21–23.

MOREIRA, Nelson et al. Structural analysis of thermal behavior on cooling trapped annular pressure in water and gas injection wells. **Offshore Technology Conference Brasil 2019, OTCB 2019**, p. 1–14, 2020. DOI: 10.4043/29832-ms.

MUNSON, Darrell E. Constitutive model of creep in rock salt applied to underground room closure. **International journal of rock mechanics and mining sciences & geomechanics abstracts**, v. 34, n. 2, p. 233–247, 1997. ISSN 01489062. DOI: 10.1016/S0148-9062(96)00047-2.

MUNSON, Darrell E. **Preliminary deformation-mechanism map for salt (with application to WIPP)**. [S.l.], 1979. P. 38.

MUNSON, Darrell E.; DAWSON, PR. **Constitutive model for the low temperature creep of salt (with application to WIPP)**. [S.l.], 1979.

NAUMENKO, Konstantin. **Modeling of High-Temperature Creep for Structural Analysis Applications**. 2006. S. 1–220. PhD thesis.

NIAN, Yong Le et al. Study on the effect of wellbore heat capacity on steam injection well heat loss. **Applied Thermal Engineering**, Elsevier Ltd, v. 70, n. 1, p. 763–769, 2014. ISSN 13594311. DOI: 10.1016/j.applthermaleng.2014.05.056.

NIKISHKOV, G.P. **Introduction to the Finite Element Method**. [S.l.: s.n.], 2004. P. 45.

OLIVEIRA, Danilo Bento. **Implementação Computacional de Modelos Elastoplásticos para Análise Fisicamente não Linear**. 2016. PhD thesis – Escola de Engenharia da Universidade Federal de Minas Gerais.

OUDEMAN, P; BACARREZA, L J. Field Trial Results of Annular Pressure Behavior in a High-Pressure/High-Temperature Well. **SPE Drilling & Completion**, 1995.

OUDEMAN, P; KEREM, M. Transient Behavior of Annular Pressure Build-up in HP / HT Wells. **International Petroleum Exhibition and Conference**, 2004.

PATTILLO, Phillip D; COCALES, Brett W; MOREY, Stephen C. Analysis of an Annular Pressure Buildup Failure During Drill Ahead. **SPE Drilling & Completion**, v. 21, n. 04, p. 242–247, 2006. ISSN 1064-6671. DOI: 10.2118/89775-pa.

PATTILLO, Phillip D; SATHUVALLI, Udaya Bhaskar R, et al. Mad dog slot W1 tubing deformation failure analysis. In: SOCIETY OF PETROLEUM ENGINEERS. SPE Annual Technical Conference and Exhibition. [S.l.: s.n.], 2007.

PEREZ, Hernan E E. SALT CREEP EFFECT IN APB OF SUBSALT WELL. In.

PETROBRAS. **Plano Estratégio 2021-2025**. [S.l.: s.n.], 2020. Available from: https://api.mziq.com/mzfilemanager/v2/d/25fdf098-34f5-4608-b7fa-17d60b2de47d/174ab356-7f22-96e7-6828-94b10fcb3349?origin=1.

POIATE, Edgard; MAIA, Alvaro; FALCAO, Jose. Well Design for Drilling Through Thick Evaporite Layers in Santos Basin—Brazil. In: February. PROCEEDINGS of IADC/SPE Drilling Conference. Miami: Society of Petroleum Engineers, Feb. 2006. DOI: 10.2523/99161-MS.

PRESS, William H. et al. **Numerical Recepies - The Art of Scientific Computing**. 3. ed. Cambridge: Cambridge University Press, 2007. ISBN 978-0-511-33555-6.

RAMEY !JR, J.H. Wellbore Heat Transmission. **J. Petrol. Technol.**, v. 14, n. 4, p. 427–435, 1962.

RENNER, JL. Volume VI–Emerging and Peripheral Technologies, 2007.

ROSSUM, Guido Van; DRAKE, Fred L. **Python 3 Reference Manual**. [S.l.]: CreateSpace Independent Publishing Platform, 2009. P. 242. ISBN 1441412697.

SAGAR, Rajiv; DOTY, D.R.; SCHMIDT, Zelimar. Predicting Temperature Profiles in a Flowing Well. **SPE Production Engineering**, v. 6, n. 04, p. 441–448, 1991. ISSN 0885-9221. DOI: 10.2118/19702-pa.

SANTOS, H. L. et al. APB mitigation techniques and design procedure. **OTC Brasil 2015: The Atlantic: From East to West - An Ocean of Innovation**, October, p. 1979–1991, 2015. DOI: 10.4043/26294-ms.

SATHUVALLI, U. B.; PAYNE, M. L., et al. Development of a screening system to identify deepwater wells at risk for annular pressure build-up. **SPE/IADC Drilling Conference, Proceedings**, p. 849–862, 2005. DOI: 10.2118/92594-ms.

SATHUVALLI, U. B.; PILKO, R. M., et al. Design and Performance of Annular Pressure Build-Up APB Mitigation Techniques. In: IADC/SPE Drilling Conference and Exhibition. [S.l.]: Society of Petroleum Engineers, Mar. 2016. DOI: 10.2118/178886-MS.

SATTER, Abdus. Heat Losses During Flow of Steam Down a Wellbore. **Journal of Petroleum Technology**, v. 17, n. 07, p. 845–851, 1965. ISSN 0149-2136. DOI: 10.2118/1071-pa.

SIEDER, E. N.; TATE, G. E. Heat Transfer and Pressure Drop of Liquids in Tubes. **Industrial & Engineering Chemistry**, v. 28, n. 12, p. 1429–1435, Dec. 1936. ISSN 0019-7866. DOI: 10.1021/ie50324a027.

STEHFEST, Harald. Algorithm 368: Numerical inversion of Laplace transforms [D5]. **Communications of the ACM**, v. 13, n. 1, p. 47–49, Jan. 1970. ISSN 00010782. DOI: 10.1145/361953.361969.

TAHERI, S. Reza et al. Investigation of rock salt layer creep and its effects on casing collapse. **International Journal of Mining Science and Technology**, China University of Mining and Technology, 2020. ISSN 20952686. DOI: 10.1016/j.ijmst.2020.02.001.

TIMOSHENKO, SP; GOODIER, JN. Theory of Elasticity, McGraw. **New York**, 1970.

VAN EVERDINGEN, A.F.; HURST, W. The Application of the Laplace Transformation to Flow Problems in Reservoirs. **Journal of Petroleum Technology**, v. 1, n. 12, p. 305–324, Dec. 1949. ISSN 0149-2136. DOI: 10.2118/949305-G.

VEIGA, Arthur Pandolfo da et al. Predicting Thermal Expansion Pressure Buildup in a Deep Offshore Well with an Annulus Partially Filled with Nitrogen Gas. Submitted to Journal of Petroleum Science and Engineering. [S.l.], 2020.

VIRTANEN, Pauli et al. SciPy 1.0: fundamental algorithms for scientific computing in Python. **Nature Methods**, v. 17, n. 3, p. 261–272, Mar. 2020. ISSN 1548-7091. DOI: 10.1038/s41592-019-0686-2.

WALT, Stéfan van der; COLBERT, S Chris; VAROQUAUX, Gaël. The NumPy Array: A Structure for Efficient Numerical Computation. **Computing in Science & Engineering**, v. 13, n. 2, p. 22–30, Mar. 2011. ISSN 1521-9615. DOI: 10.1109/MCSE.2011.37.

WANG, Han Yi; SAMUEL, Robello. 3D geomechanical modeling of salt-creep behavior on wellbore casing for presalt reservoirs. **SPE Drilling and Completion**, v. 31, n. 4, p. 261–272, 2016. ISSN 10646671. DOI: 10.2118/166144-PA.

WARPLNSKL, Norman R. Plastic and viscoelastic calculations of stresses in sedimentary basins. **SPE Formation Evaluation**, v. 4, n. 4, 1989. ISSN 0885923X. DOI: 10.2118/15243-pa.

XU, Zhengming et al. Development of a transient non-isothermal two-phase flow model for gas kick simulation in HTHP deep well drilling. **Applied Thermal Engineering**, v. 141, p. 1055–1069, 2018. ISSN 13594311. DOI: 10.1016/j.applthermaleng.2018.06.058.

YANG, Jin et al. Prediction model of casing annulus pressure for deepwater well drilling and completion operation. **Petroleum Exploration and Development**, Research Institute of Petroleum Exploration & Development, PetroChina, v. 40, n. 5, p. 661–664, 2013. ISSN 18763804. DOI: 10.1016/S1876-3804(13)60088-9.

YANG, Mou et al. Prediction of wellbore and formation temperatures during circulation and shut-in stages under kick conditions. **Energy**, Elsevier Ltd, v. 91, p. 1018–1029, 2015. ISSN 03605442. DOI: 10.1016/j.energy.2015.09.001.

YI, Liang Ping et al. Coupled calculation model for transient temperature and pressure of carbon dioxide injection well. **International Journal of Heat and Mass Transfer**, Elsevier Ltd, v. 121, p. 680–690, 2018. ISSN 00179310. DOI: 10.1016/j.ijheatmasstransfer.2018.01.036.

YOU, Junyu; RAHNEMA, Hamid; MCMILLAN, Marcia D. Numerical modeling of unsteady-state wellbore heat transmission. **Journal of Natural Gas Science and Engineering**, v. 34, p. 1062–1076, 2016. ISSN 18755100. DOI: 10.1016/j.jngse.2016.08.004.

ZHANG, Bo; GUAN, Zhichuan, et al. Trapped annular pressure caused by thermal expansion in oil and gas wells: A review of prediction approaches, risk assessment and mitigation strategies. **Journal of Petroleum Science and Engineering**, v. 172, p. 70–82, Jan. 2019. ISSN 09204105. DOI: 10.1016/j.petrol.2018.09.041.

ZHANG, Jincai; STANDIFIRD, William; LENAMOND, Chris. Casing ultradeep, ultralong salt sections in deep water: A case study for failure diagnosis and risk mitigation in record-depth well. **Proceedings - SPE Annual Technical Conference and Exhibition**, v. 1, p. 129–152, 2008. DOI: 10.2118/114273-ms.

ZHOU, Fuzong. **Research on heat transfer in geothermal wellbore and surroundings**. 2013. Doctoral Thesis – Technische Universität Berlin, Fakultät VI - Planen Bauen Umwelt, Berlin. DOI: 10.14279/depositonce-3861.

APPENDIX A – DETERMINATION OF MODELING EXPRESSIONS

This appendix is intended to assist in deducing parts of the mathematical models presented in Chapters 3 and 4.

A.1 LAPLACE BASED MODELS

The thermal models developed in the work relied on the application of the Laplace transform in several heat transfer equations, for reasons of simplicity the procedure of deduction were previously omitted, however now they will be presented in a more complete manner.

As previously mentioned, even for the solution nodes of the thermal network system in the well, there will be a process of dimensioning in relation to the formation properties. This is intended to make the Equation 3 homogeneous, allowing for the analytical solution of the problem. Now the dimensionless parameters will be applied as done previously, so that the set of equations can be obtained again as presented in section 3.3.

$$\begin{cases} \dfrac{\partial^2 T_{D,fm}}{\partial r_D^2} + \dfrac{1}{r_D}\dfrac{\partial T_{D,fm}}{\partial r_D} = \dfrac{\partial T_{D,fm}}{\partial \tau} & (144a) \\ T_{D,fm}(r_D, \tau = 0) = 0 & (144b) \\ \lim\limits_{r_D \to \infty} T_{D,fm}(r_D, \tau) = 0 & (144c) \end{cases}$$

Note that here the internal boundary condition has been omitted, as this will be decisive between the application of the prescribed flow model, used for the traditional models of Steady-State formulation, and for the new model of transient heat transfer. So that term will be dealt within its due time.

First, the following Laplace Transform properties will be presented as they will be very useful during the deduction process.

$$\begin{cases} \mathscr{L}\{f(t)\} = \dfrac{f}{s} & \text{if f is constant in relation to t} & (145a) \\ \mathscr{L}\{f(t) + g(t)\} = \mathscr{L}\{f(t)\} + \mathscr{L}\{g(t)\} & & (145b) \\ \mathscr{L}\{af(t)\} = a\mathscr{L}\{f(t)\} & \text{if a is constant in relation to t} & (145c) \\ \mathscr{L}\left\{\dfrac{\partial f}{\partial t}\right\} = s\bar{f}(s) - f(t=0) & & (145d) \end{cases}$$

Thus, the Laplace Transform can be applied to the dimensionless heat conduction equation. As there is a derivative term in relation to the Fourier time, the last property presented must be applied. Thus it is possible to write:

$$\frac{\partial^2 \overline{T}_{D,fm}}{\partial r_D^2} + \frac{1}{r_D}\frac{\partial \overline{T}_{D,fm}}{\partial r_D} - s\overline{T}_{D,fm} + T_{D,fm}(\tau = 0) = 0 \tag{146}$$

Applying the initial condition this equation is summarized in:

$$\frac{\partial^2 \overline{T}_{D,fm}}{\partial r_D^2} + \frac{1}{r_D}\frac{\partial \overline{T}_{D,fm}}{\partial r_D} - s\overline{T}_{D,fm} = 0 \tag{147}$$

This differential equation has a known analytical solution, it consists of the combination of the two modified Bessel functions of the first and second kind. Therefore, the temperature field in the formation should satisfy:

$$\overline{T}_{D,fm}(r_D, s) = AK_0\left(r_D\sqrt{s}\right) + BI_0\left(r_D\sqrt{s}\right) \tag{148}$$

Where A and B were determined by applying boundary conditions to the problem. Directly, from the external boundary condition, it is already possible to determine that one of these two constants will be null. As the first type Bessel function tends to infinity for long times, the second term of the equation should be 0. Thus the temperature field solution becomes:

$$\overline{T}_{D,fm}(r_D, s) = AK_0\left(r_D\sqrt{s}\right) \tag{149}$$

To determine the values of A that satisfy the heat transfer, it is necessary to choose how to treat, either the temperature of the interface or the heat transfer that passes through it.

For the case of prescribed heat flow condition, as necessary for the Steady-State annular, the heat flow is directly provided by the thermal network model, so the internal boundary condition for the formation is described by:

$$Q' = -2\pi k_{fm} r_{fm} \left.\frac{\partial T_{fm}}{\partial r}\right|_{r=r_{fm}} \tag{150}$$

With the use of dimensionless groups, this equation can be rewritten so that:

$$Q'_D = -2\pi \left.\frac{\partial T_{D,fm}}{\partial r_D}\right|_{r_D=1} \tag{151}$$

Thus, the Laplace transform can be applied in this boundary condition in order to find an expression that can be applied to find the last constant of the temperature profile.

$$\frac{Q'_D}{s} = -2\pi \left.\frac{\partial \overline{T}_{D,fm}}{\partial r_D}\right|_{r_D=1} \tag{152}$$

Thus, applying these conditions to Equation 149 it is possible to determine expression for the formation temperature profile.

$$\overline{T}_{\mathrm{D,fm}}(r_{\mathrm{D}},s)=\frac{Q'_{\mathrm{D}}K_0\left(r_{\mathrm{D}}\sqrt{s}\right)}{2\pi s\sqrt{s}K_1\left(\sqrt{s}\right)} \tag{153}$$

Note that this expression is the same as that presented in Equation 7, only with the difference that the heat transfer term has been removed from the transform. Thus, the Steady-State regime model is completely described.

For the transient annular model, an interfacial condition must be used between the ring and the formation. In this case, on the one hand, there must be continuity of the temperature profile, both from the side of the annular and from the formation, and continuity of the heat transfer. To apply such continuity, a temperature profile will be prescribed on the wall, which will be provided by the temperature from the last node in the thermal network, on the other hand the formation will deliver the heat transfer that satisfies this profile. So, the boundary condition used will be:

$$T_{\mathrm{D,fm}}(\tau,r_{\mathrm{D}}=1)=T_{\mathrm{D,Int}} \tag{154}$$

where $T_{\mathrm{D,i}}$ is the dimensionless temperature of the last node (interface with the formation) in the thermal system.

Now it is possible to take advantage that the thermal system solved with the Laplace Transformation by applying the Laplace transform to this last equation and than use the result to determine the heat flow compatibility condition. By applying this last boundary condition into Equation 149 the temperature profile is given by:

$$\overline{T}_{\mathrm{D,fm}}(r_{\mathrm{D}},s)=\frac{\overline{T}_{\mathrm{D,Int}}K_0\left(r_{\mathrm{D}}\sqrt{s}\right)}{K_0\left(\sqrt{s}\right)} \tag{155}$$

As mentioned, this equation is capable to model the temperature inside the formation provided the behavior of the temperature in the interface of the domain. However, this behavior appears from the heat compatibility flowing through this interface. To determine it one must apply the Fourrier law to this equation, such that:

$$\overline{Q'_{\mathrm{D,Int}}}(s)=\frac{2\pi\overline{T}_{\mathrm{D,Int}}\sqrt{s}K_1\left(\sqrt{s}\right)}{K_0\left(\sqrt{s}\right)} \tag{156}$$

Since the equation for the last node of the thermal system is written by:

$$C_iR_i\frac{\alpha_{fm}}{r_{\mathrm{fm}}^2}\frac{\partial T_{\mathrm{D,i}}}{\partial\tau}=-T_{\mathrm{D,i}}+T_{\mathrm{D,i-1}}-k_{fm}R_iQ'_{\mathrm{D,Int}} \tag{157}$$

applying the Laplace transform, a the equation for the last node coupled with the heat transfer in the formation is recovered:

$$R_iC_i\frac{\alpha_{fm}}{r_{\mathrm{fm}}^2}s\overline{T}_{\mathrm{D,i}}=-\overline{T}_{\mathrm{D,i}}+\overline{T}_{\mathrm{D,i-1}}-\frac{2\pi k_{fm}R_i\sqrt{s}K_1\left(\sqrt{s}\right)}{K_0\left(\sqrt{s}\right)}\overline{T}_{\mathrm{D,i}} \tag{158}$$

Note that this equation is just a rearrangement away from Equation 90c so this is the complete definition of the thermal system using Laplace model for the formation.

A.2 CONSTITUTIVE MODEL

From Section 4.2 the model developed did not include the procedure that led to Equation 111. To this end, this section of the Appendix will address this issue.

For that, the starting point of the deduction will be from the Equation 114. In addition, auxiliary variable y will be introduced in order to make it possible to find the desired terms. It will be used to make it possible to write:

$$\frac{\partial \boldsymbol{\sigma}_{n+1}}{\partial y} = \frac{\partial \boldsymbol{\sigma}_{\mathrm{n+1}}}{\partial \boldsymbol{\varepsilon}_{\mathrm{n+1}}} : \frac{\partial \boldsymbol{\varepsilon}_{\mathrm{n+1}}}{\partial y} \tag{159}$$

note that the first term on the right hand side of the equation is exactly the desired term in Equation 111. So, just find an expression similar to the one above to isolate the desired term.

For that, the derivative of Equation 114 is taken with respect to the auxiliary variable, such that:

$$\frac{\partial \boldsymbol{\sigma}_{\mathrm{n+1}}}{\partial y} = \frac{\partial \boldsymbol{S}^{\mathrm{tr}}_{\mathrm{n+1}}}{\partial y} - 2G\frac{\partial (\gamma_{\mathrm{n+1}} - \gamma_{\mathrm{n}})}{\partial y}\boldsymbol{N}^{\mathrm{tr}}_{\mathrm{n+1}} - 2G(\gamma_{\mathrm{n+1}} - \gamma_{\mathrm{n}})\frac{\partial \boldsymbol{N}^{\mathrm{tr}}_{\mathrm{n+1}}}{\partial y} + \frac{\partial p_{\mathrm{n+1}}}{\partial y}\mathbf{I} \tag{160}$$

To find the desired expressions, each term associated with the derivatives in the previous equation, this one will be separated and solved individually. Starting from the first term more to the left one can expand:

$$\frac{\partial \boldsymbol{S}^{\mathrm{tr}}_{\mathrm{n+1}}}{\partial y} = 2G\frac{\partial \mathrm{dev}\left(\boldsymbol{\varepsilon}^{\mathrm{tr}}_{\mathrm{n+1}}\right)}{\partial y} = 2G\frac{\partial \mathrm{dev}\left(\boldsymbol{\varepsilon}_{\mathrm{n+1}}\right)}{\partial y} - 2G\frac{\partial \mathrm{dev}\left(\boldsymbol{\varepsilon}_{\mathrm{n}}\right)}{\partial y} \tag{161}$$

Some considerations arising from the model used should be highlighted. A property that will be used a lot in the following deductions, due to the choice of a implicit method, all variables related to time steps other than $\mathrm{n}+1$ will, by definition, be constant for the current time step, therefore, derivatives taken on those will be null as a result. That is, this equation can be reduced to:

$$\frac{\partial \boldsymbol{S}^{\mathrm{tr}}_{\mathrm{n+1}}}{\partial y} = 2G\frac{\partial \mathrm{dev}\left(\boldsymbol{\varepsilon}_{\mathrm{n+1}}\right)}{\partial y} \tag{162}$$

The deviatoric operator has not yet been mathematically described in the work as it did not prove to play crucial role in understanding the basic procedure. However, it is now necessary to describe such an operator. So for a generic tensor $\boldsymbol{A}$:

$$\mathrm{dev}\left(\boldsymbol{A}\right) = \boldsymbol{A} - \frac{1}{3}\mathrm{tr}\left(\boldsymbol{A}\right)\mathbf{I} \tag{163}$$

Therefore, expanding the previous expression and applying basic properties of tensor calculations, we arrive at the following equation:

$$\frac{\partial \boldsymbol{S}^{\text{tr}}_{\text{n+1}}}{\partial y} = 2G\mathbb{P} : \frac{\partial \boldsymbol{\varepsilon}_{\text{n+1}}}{\partial y} \tag{164}$$

This expression will be kept in this form until the remaining terms are resolved. For the second part of the Equation 160, it is again possible to remove the creep amplitude term of previous time step, thus summarizing the derivative that needs to be determined. In addition, a question of notation that will be used assumes that because the stress state of the material is already known for time $t_{\text{n+1}}$, the creep law can be used in its non-conditional form, so a unique equation that groups the empirical exponents into just a single n can be used in the deduction process. This notation serves only to reduce the size of the calculated expressions and does not result from any approximation, because the value of n used will be the value defined for the known stress state. Therefore:

$$\frac{\partial \gamma_{\text{n+1}}}{\partial y} = \Delta t \dot{\gamma}_{\text{ref}} \exp\left(\frac{A}{R_{gas}T_{\text{ref}}} - \frac{A}{R_{gas}T}\right) \frac{\partial}{\partial y}\left[\left(\frac{q^{\text{tr}}_{\text{n+1}} - 3G(\gamma_{\text{n+1}} - \gamma_{\text{n}})}{q_{\text{ref}}}\right)^{n}\right] \tag{165}$$

Rearranging the terms of this equation and expanding the derivative on the right side it is possible to write:

$$\frac{\exp\left(\frac{A}{R_{gas}T} - \frac{A}{R_{gas}T_{\text{ref}}}\right)}{\Delta t \dot{\gamma}_{\text{ref}}} \frac{\partial \gamma_{\text{n+1}}}{\partial y} = \frac{n}{q_{\text{ref}}}\left(\frac{q^{\text{tr}}_{\text{n+1}} - 3G(\gamma_{\text{n+1}} - \gamma_{\text{n}})}{q_{\text{ref}}}\right)^{n-1}\left(\frac{\partial q^{\text{tr}}_{\text{n+1}}}{\partial y} - 3G\frac{\partial \gamma_{\text{n+1}}}{\partial y}\right) \tag{166}$$

It is at this point that the two variables in Equation 112 and Equation 113 are defined. Thus, recalling that:

$$\Gamma_0 = \frac{\exp\left(\frac{A}{R_{gas}T} - \frac{A}{R_{gas}T_{\text{ref}}}\right)}{\Delta t_{\text{n+1}} \dot{\gamma}_{\text{ref}}}$$

$$\Gamma_1 = \frac{n}{q_{\text{ref}}}\left[\frac{q^{\text{tr}}_{\text{n+1}} - 3G(\gamma_{\text{n+1}} - \gamma_{\text{n}})}{q_{\text{ref}}}\right]^{n-1}$$

Now, grouping the previous equation with these two variables, one can write:

$$\frac{\partial \gamma_{\text{n+1}}}{\partial y} = \frac{\Gamma_1}{\Gamma_0 + 3G\Gamma_1}\frac{\partial q^{\text{tr}}_{\text{n+1}}}{\partial y} \tag{167}$$

This expression is already close to the desired result, however the expression for the derivative of the trial effective stress needs to be worked on. First, it is necessary to go back on the definition of trial effective stress, that is:

$$q^{tr}_{n+1} = \sqrt{\frac{3}{2}} \| \boldsymbol{S}^{tr}_{n+1} \|$$

Using basic properties of tensor algebra this expression can be derived such that:

$$\frac{\partial q^{tr}_{n+1}}{\partial y} = \sqrt{\frac{3}{2}} \frac{\boldsymbol{S}^{tr}_{n+1}}{\| \boldsymbol{S}^{tr}_{n+1} \|} : \frac{\partial \boldsymbol{S}^{tr}_{n+1}}{\partial y} \tag{168}$$

This last derivative was already dealt with, so it is possible to use Equation 164 in this equation. Also, one can use the definition of the normal creep direction to reduce the number of terms.

$$\frac{\partial q^{tr}_{n+1}}{\partial y} = 2G \boldsymbol{N}^{tr}_{n+1} : \mathbb{P} : \frac{\partial \boldsymbol{\varepsilon}_{n+1}}{\partial y} \tag{169}$$

Than, by a property of $\boldsymbol{N}^{tr}_{n+1}$ and $\mathbb{P}$, more specifically that $\boldsymbol{N}^{tr}_{n+1} : \mathbb{P} = \boldsymbol{N}^{tr}_{n+1}$, the final expression for this term becomes:

$$\frac{\partial \gamma_{n+1}}{\partial y} = \frac{\Gamma_1}{\Gamma_0 + 3G\Gamma_1} 2G \boldsymbol{N}^{tr}_{n+1} : \frac{\partial \boldsymbol{\varepsilon}_{n+1}}{\partial y} \tag{170}$$

This done, now it is possible to perform similar procedure for the derivative of the normal creep flow direction. So, by the definition of the flow direction:

$$\frac{\partial \boldsymbol{N}^{tr}_{n+1}}{\partial y} = \sqrt{\frac{3}{2}} \frac{\partial}{\partial y} \left[\frac{\boldsymbol{S}^{tr}_{n+1}}{\| \boldsymbol{S}^{tr}_{n+1} \|} \right] \tag{171}$$

Using another property from tensor algebra, the derivative from the term on the right side can be expanded providing an expression closer to the desired result.

$$\frac{\partial \boldsymbol{N}^{tr}_{n+1}}{\partial y} = \sqrt{\frac{3}{2}} \frac{1}{\| \boldsymbol{S}^{tr}_{n+1} \|} \left(\mathbb{I} - 2\frac{2}{3} \boldsymbol{N}^{tr}_{n+1} \otimes \boldsymbol{N}^{tr}_{n+1} \right) : \frac{\partial \boldsymbol{S}^{tr}_{n+1}}{\partial y} \tag{172}$$

Once again, Equation 164 can be used to find the desired expression.

$$\frac{\partial \boldsymbol{N}^{tr}_{n+1}}{\partial y} = \frac{3G}{q^{tr}_{n+1}} \left(\mathbb{P} - \frac{2}{3} \boldsymbol{N}^{tr}_{n+1} \otimes \boldsymbol{N}^{tr}_{n+1} \right) : \frac{\partial \boldsymbol{\varepsilon}_{n+1}}{\partial y} \tag{173}$$

Now the last term required to be solved is more simple. In order to deal with it, one must start by applying the derivative to the definition of p_{n+1}, from that:

$$\frac{\partial p_{n+1}}{\partial y} = K \frac{\partial \mathrm{tr}(\boldsymbol{\varepsilon}_{n+1})}{\partial y} \tag{174}$$

From the definition of the trace operator it is easy to reach:

$$\frac{\partial p_{n+1}}{\partial y} = K \mathbf{I} : \frac{\partial \boldsymbol{\varepsilon}_{n+1}}{\partial y} \tag{175}$$

This is already the end procedure for this expression. Now by substituting Equations 164,170,173 and 175 into Equation 160 the following expression emerges.

$$\frac{\partial \boldsymbol{\sigma}_{n+1}}{\partial y} = 2G\mathbb{P} : \frac{\partial \boldsymbol{\varepsilon}_{n+1}}{\partial y} - 4G^2 \boldsymbol{N}^{tr}_{n+1} \frac{\Gamma_1}{\Gamma_0 + 3G\Gamma_1} : \frac{\partial \boldsymbol{\varepsilon}_{n+1}}{\partial y} \boldsymbol{N}^{tr}_{n+1} + \\ - \frac{6G^2(\gamma_{n+1} - \gamma_n)}{q^{tr}_{n+1}} \left(\mathbb{P} - \frac{2}{3} \boldsymbol{N}^{tr}_{n+1} \otimes \boldsymbol{N}^{tr}_{n+1} \right) : \frac{\partial \boldsymbol{\varepsilon}_{n+1}}{\partial y} + K\mathbf{I} : \frac{\partial \boldsymbol{\varepsilon}_{n+1}}{\partial y} \mathbf{I} \quad (176)$$

And finally, by rearranging this equation it is easy to reach:

$$\frac{\partial \boldsymbol{\sigma}_{n+1}}{\partial y} = \left\{ 2G \left(1 - \frac{3G(\gamma_{n+1} - \gamma n)}{q^{tr}_{n+1}} \right) \mathbb{P} + 6G^2 \left[\frac{\gamma_{n+1} - \gamma n}{q^{tr}_{n+1}} - \frac{\Gamma_1}{\Gamma_0 + 3G\Gamma_1} \right] \frac{\boldsymbol{S}_{n+1} \otimes \boldsymbol{S}_{n+1}}{\| \boldsymbol{S}_{n+1} \|^2} + K(\mathbf{I} \otimes \mathbf{I}) \right\} : \frac{\partial \boldsymbol{\varepsilon}_{n+1}}{\partial y} \quad (177)$$

And by using a simple analogy from Equation 159, the terms inside the braces are exactly the terms desired for Equation 111.

A.3 BIQUADRATIC ELEMENT

As presented in section 4.3, this work used elements of the Lagrangean biquadratic type to approximate the displacement field within the solid. This section aims to explain the format of these functions and some characteristics arising for application in the FEM method.

The procedure for determining the shape functions for FEM is well established in the literature, for a more detailed explanation it is recommended to read Fish and Belytschko (2007) or Nikishkov (2004). More specifically, isoparametric quadrilateral elements will be used, these are characterized by a change from the spatial base to an element reference base. The Figure 126 demonstrates this new parametrization of the coordinate system.

Figure 126 – Isoparametric conversion

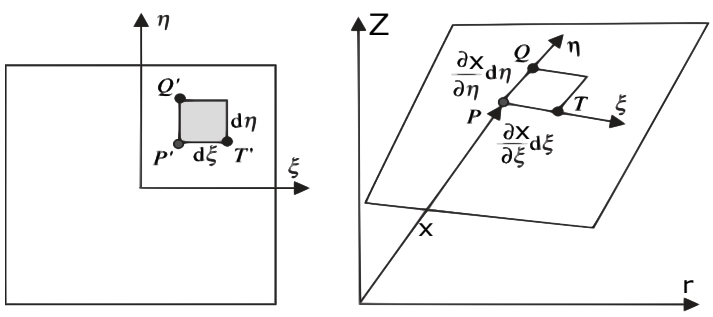

Source: Adapted from Fish and Belytschko (2007)

The variables ξ and η map the positions of the mesh described by *r* and *Z* within a given element. These variables range from -1 to 1, and for these values the position is at the limit of a given element. For the case of the two-way elements used, according to the convention presented in Figure 28, the points of the mesh will be allocated in the parameterized mesh so that:

$$\begin{bmatrix} \xi & \eta \end{bmatrix} = \begin{bmatrix} -1 & -1 \\ 1 & -1 \\ 1 & 1 \\ -1 & 1 \\ 0 & -1 \\ 1 & 0 \\ 0 & 1 \\ -1 & 0 \\ 0 & 0 \end{bmatrix} \tag{178}$$

where each line is related to a given node of the element.

Having done the traditional procedure to determine the shape functions for a Lagrangian biquadratic element, the following equation represents the resulting vector.

$$\mathbf{\Psi} = \begin{bmatrix} \frac{(1-\xi)(1-\eta)\xi\eta}{4} \\ -\frac{(1+\xi)(1-\eta)\xi\eta}{4} \\ \frac{(1+\xi)(1+\eta)\xi\eta}{4} \\ -\frac{(1+\xi)(1-\eta)\xi\eta}{4} \\ -\frac{(1-\xi^2)(1-\eta)\eta}{2} \\ \frac{(1+\xi)(1-\eta^2)\xi}{2} \\ \frac{(1-\xi^2)(1+\eta)\eta}{2} \\ -\frac{(1-\xi)(1-\eta^2)\xi}{2} \\ (1-\xi^2)(1-\eta^2) \end{bmatrix} \tag{179}$$

These shape functions, in this column vector representation, are able to map scalar functions to the domain using the values in the solution nodes. However, for the application for the displacements used, it is necessary to map vector fields. In order for these same shape functions to be used, the tensor $\mathscr{N}$ that was used previously in the work is defined.

$$\mathscr{N}^e = \begin{bmatrix} \Psi_0 & 0 & \Psi_1 & 0 & \Psi_2 & 0 & \Psi_3 & 0 & \Psi_4 & 0 & \Psi_5 & 0 & \Psi_6 & 0 & \Psi_7 & 0 & \Psi_8 & 0 \\ 0 & \Psi_0 & 0 & \Psi_1 & 0 & \Psi_2 & 0 & \Psi_3 & 0 & \Psi_4 & 0 & \Psi_5 & 0 & \Psi_6 & 0 & \Psi_7 & 0 & \Psi_8 \end{bmatrix} \tag{180}$$

This tensor has the property to interpolate values of the displacement field inside any given element. Another useful tensor is the one containing the derivatives of the

shape functions. In order define it, first it is presented the Jacobian of the parametrization.

$$\boldsymbol{J}^e = \begin{bmatrix} \frac{\partial r}{\partial \xi} & \frac{\partial Z}{\partial \xi} \\ \frac{\partial r}{\partial \eta} & \frac{\partial Z}{\partial \eta} \end{bmatrix} \tag{181}$$

So it is possible to define the derivatives from the shape functions in relation to the material grid by:

$$\begin{bmatrix} \frac{\partial \Psi}{\partial r} \\ \frac{\partial \Psi}{\partial Z} \end{bmatrix} = \left(\boldsymbol{J}^e\right)^{-1} \begin{bmatrix} \frac{\partial \Psi}{\partial \xi} \\ \frac{\partial \Psi}{\partial \eta} \end{bmatrix} \tag{182}$$

Now, to recover the definition of the $\boldsymbol{B}$, for the axyssimetric assumption, one can easily compute:

$$\boldsymbol{B} = \begin{bmatrix} \frac{\partial \Psi_0}{\partial r} & 0 & \frac{\partial \Psi_1}{\partial r} & 0 & \frac{\partial \Psi_2}{\partial r} & 0 & \frac{\partial \Psi_3}{\partial r} & 0 & \frac{\partial \Psi_4}{\partial r} & 0 & \frac{\partial \Psi_5}{\partial r} & 0 & \frac{\partial \Psi_6}{\partial r} & 0 & \frac{\partial \Psi_7}{\partial r} & 0 & \frac{\partial \Psi_8}{\partial r} & 0 \\ \frac{\Psi_0}{r} & 0 & \frac{\Psi_1}{r} & 0 & \frac{\Psi_2}{r} & 0 & \frac{\Psi_3}{r} & 0 & \frac{\Psi_4}{r} & 0 & \frac{\Psi_5}{r} & 0 & \frac{\Psi_6}{r} & 0 & \frac{\Psi_7}{r} & 0 & \frac{\Psi_8}{r} & 0 \\ 0 & \frac{\partial \Psi_0}{\partial Z} & 0 & \frac{\partial \Psi_1}{\partial Z} & 0 & \frac{\partial \Psi_2}{\partial Z} & 0 & \frac{\partial \Psi_3}{\partial Z} & 0 & \frac{\partial \Psi_4}{\partial Z} & 0 & \frac{\partial \Psi_5}{\partial Z} & 0 & \frac{\partial \Psi_6}{\partial Z} & 0 & \frac{\partial \Psi_7}{\partial Z} & 0 & \frac{\partial \Psi_8}{\partial Z} \\ \frac{\partial \Psi_0}{\partial Z} & \frac{\partial \Psi_0}{\partial r} & \frac{\partial \Psi_1}{\partial Z} & \frac{\partial \Psi_1}{\partial r} & \frac{\partial \Psi_2}{\partial Z} & \frac{\partial \Psi_2}{\partial r} & \frac{\partial \Psi_3}{\partial Z} & \frac{\partial \Psi_3}{\partial r} & \frac{\partial \Psi_4}{\partial Z} & \frac{\partial \Psi_4}{\partial r} & \frac{\partial \Psi_5}{\partial Z} & \frac{\partial \Psi_5}{\partial r} & \frac{\partial \Psi_6}{\partial Z} & \frac{\partial \Psi_6}{\partial r} & \frac{\partial \Psi_7}{\partial Z} & \frac{\partial \Psi_7}{\partial r} & \frac{\partial \Psi_8}{\partial Z} & \frac{\partial \Psi_8}{\partial r} \end{bmatrix} \tag{183}$$

So at the initialization of the program, the complete grid of is assembled with the shape functions defined and the required functions to compute its derivatives and to store information in the required nodes.

For a question of higher performance the code is designed to create grids with geometric spacing in the radial direction. This spacing is only related to the length of the element, in other words, the position of the nodes inside the elements are equally spaced. For example, the node 4 in the indexing system, is located at the bottom of the element, at the middle of the perimeter.

A.4 INTEGRATION NODES

As mentioned in section 4.3 the integration procedure follows the Gauss-Legendre method. This evaluates a function which will be integrated in certain points and, with the use of weights, estimates the integral.

For the biquadratic element, a total of 9 integration nodes are required for exact accuracy for linear problems (MENDONÇA; FANCELLO, 2019). Even though the problem solved is not linear, the 3 by 3 integration nodes will be used. This nodes are located as follows:

$$\boldsymbol{X_{int}} = \begin{bmatrix} -\sqrt{\frac{3}{5}} & -\sqrt{\frac{3}{5}} \\ \sqrt{\frac{3}{5}} & -\sqrt{\frac{3}{5}} \\ \sqrt{\frac{3}{5}} & \sqrt{\frac{3}{5}} \\ -\sqrt{\frac{3}{5}} & \sqrt{\frac{3}{5}} \\ 0 & -\sqrt{\frac{3}{5}} \\ \sqrt{\frac{3}{5}} & 0 \\ 0 & \sqrt{\frac{3}{5}} \\ -\sqrt{\frac{3}{5}} & 0 \\ 0 & 0 \end{bmatrix} \tag{184}$$

This are represented in the parametric space used in the isoparametric elements. For this set of 3 by 3 nodes used, the following weights for the integration are used:

$$\boldsymbol{W} = \begin{bmatrix} \frac{25}{81} \\ \frac{25}{81} \\ \frac{25}{81} \\ \frac{25}{81} \\ \frac{40}{81} \\ \frac{40}{81} \\ \frac{40}{81} \\ \frac{40}{81} \\ \frac{64}{81} \end{bmatrix} \tag{185}$$

This positions and weights are initialized simultaneously to the reaming terms initialized in the grid generation. This are pre-allocated for performance, since they are constants used during the entire simulation.

APPENDIX B – WELL GEOMETRIES AND FLUIDS

This appendix will contain the descriptions of the wells used in chapter 5 and the produced fluid in each one.

First each section will contain a table with the dimensions of the completion scheme. Following a table containing the data for inclination. Lastly a table with the molecular composition of the produced oil (if acctualy a real producing well)

B.1 VERTICAL WELL

Table 6 – Vertical well geometry

			MD [m]			
Name	Type	OD [in] ([cm])	TOP	BASE	CEMENT	Hole Size [in] ([cm])
Conductor	Casing	30 (76.2)	1412	1472.91	1412	36 (91.4)
Surface	Casing	20 (50.8)	1412	2040.40	1412	26 (66.0)
Intermediate	Casing	13 3/8 (34.0)	1412	3728.77	2060	16 (40.6)
Production	Casing	10 3/4 (27.3)	1412	4165.75	3825	14 3/4 (37.4)
Production	Liner	7 (17.8)	4040	4693.00	4040	8 1/2 (21.6)
Production	Tubing	6 5/8 (16.8)	1412	4040.00	-	-

Table 7 – Lithology of vertical well

Formation type	TVD top [m]	TVD base [m]
Shale	1394	2070
Marl	2070	2150
Sandstone	2150	2390
Marl	2390	2440
Calcilutite	2440	2460
Marl	2460	2600
Shale	2600	3040
Sandstone	3040	3230
Shale	3230	3380
Marl	3380	3730
Sandstone	3730	3800
Marl	3800	3900
Sandstone	3900	4100
Anhydrite	4100	4180
Limestone	4180	4500
Coquina	4500	4700

Table 8 – Inclination of vertical well

MD [m]	Angle [°]	Azimuth [°]	TVD [m]
1412	0	0	1412
1428.38	0.04	0	1428.38
1437.39	0.08	0	1437.39
1440.32	0.15	0	1440.32
1444.04	0.25	0	1444.04
1446.47	0.32	0	1446.47
1450.91	0.36	0	1450.91
1454	0.36	0	1454
1454.25	0.36	0	1454.25
1470.54	0.38	0	1470.54
1573.59	0.41	0	1573.59
1710.29	0.36	0	1710.28
1846.98	0.34	0	1846.97
1983.67	0.45	0	1983.66
2040.11	0.53	0	2040.09
2172.51	0.74	0	2172.48
2172.96	0.74	0	2172.93
2199.07	0.8	0	2199.04
2201.08	0.81	0	2201.05
2202.48	0.81	0	2202.45
2203.94	0.81	0	2203.91
2204.72	0.81	0	2204.69
2204.96	0.81	0	2204.93
2338.89	0.62	0	2338.85
2475.59	0.56	0	2475.54
2584.67	0.15	0	2584.62
2585.2	0.15	0	2585.15
2598.62	0.15	0	2598.57
2601.28	0.15	0	2601.23
2603.32	0.15	0	2603.27
2615.93	0.15	0	2615.88
2650.63	0.18	0	2650.58
2787.33	0.35	0	2787.27
2924.02	0.89	0	2923.96
2972.05	1.2	0	2971.98

Continued on next page

Table 8 – Continuation

MD [m]	Angle [°]	Azimuth [°]	TVD [m]
3108.74	1.37	0	3108.64
3245.43	1.23	0	3245.29
3382.13	0.21	0	3381.98
3518.82	0.12	0	3518.67
3655.52	1.26	0	3655.34
3670.48	0.84	0	3670.3
3728.28	0.7	0	3728.09
3788.78	0.3	0	3788.6
3808.14	0.2	0	3807.95
3821.52	0.14	0	3821.34
3823.36	0.12	0	3823.17
3824.61	0.11	0	3824.42
3888.43	0.31	0	3888.24
3890.22	0.33	0	3890.03
3891.34	0.35	0	3891.15
3892.79	0.37	0	3892.6
3905.83	0.44	0	3905.64
3908.64	0.39	0	3908.45
3927.84	0.06	0	3927.65
3948.3	0.14	0	3948.11
3950.29	0.16	0	3950.1
3951.69	0.17	0	3951.5
3953.18	0.18	0	3952.99
3979.24	0.64	0	3979.05
3980.43	0.67	0	3980.25
3989.22	0.78	0	3989.03
3990.58	0.79	0	3990.39
3994.51	0.79	0	3994.32
3995.75	0.8	0	3995.56
3997.46	0.8	0	3997.27
3999.71	0.8	0	3999.52
4005.49	0.82	0	4005.3
4030.79	0.66	0	4030.59
4030.93	0.66	0	4030.73
4036.2	0.64	0	4036.01
4038.94	0.63	0	4038.75

Continued on next page

Table 8 – Continuation

MD [m]	Angle [°]	Azimuth [°]	TVD [m]
4050.35	0.59	0	4050.16
4074.84	0.51	0	4074.64
4114.29	0.32	0	4114.09
4133.05	0.74	0	4132.85
4165.47	1.31	0	4165.27
4226.89	1.7	0	4226.67
4363.59	1.17	0	4363.32
4466.37	1	0	4466.08
4582.15	1.07	0	4581.85
4639.38	1.46	0	4639.06
4692.48	1.46	0	4692.14
4702.6	1.46	0	4702.26

Table 9 – Flash results for vertical well oil

Components	Dead Oil [%mol]	Flash Gas [%mol]	Reservoir Fluid [%mol]
CO_2	-	4.45	3.36
N_2	-	0.60	0.45
C_1	-	72.35	54.54
C_2	-	7.69	5.79
C_3	0.47	6.41	4.95
IC_4	0.25	1.26	1.01
NC_4	0.90	3.00	2.48
IC_5	0.72	0.92	0.87
NC_5	1.41	1.37	1.38
C_6	3.22	1.16	1.66
C_7	5.59	0.48	1.73
C_8	7.23	0.30	2.01
C_9	6.05	0.02	1.50
C_{10}	4.96	-	1.22
C_{11}	4.28	-	1.05
C_{12}	3.86	-	0.95
C_{13}	4.09	-	1.01
C_{14}	3.34	-	0.82
C_{15}	3.22	-	0.79
C_{16}	2.54	-	0.62
C_{17}	2.09	-	0.51
C_{18}	2.17	-	0.53
C_{19}	2.04	-	0.50
C_{20+}	41.58	-	10.24
Total Molar Mass	261.00 [g mol^{-1}]	24.8 [g mol^{-1}]	82.9 [g mol^{-1}]
Molar Mass C_{20+}	420 [g mol^{-1}]		
GOR at flash	243.65 [m^{3std}/m^{3std}]		
API	29.76 [°API]		

B.2 EWT WELL

Table 10 – EWT well geometry

			MD [m]			
Name	Type	OD [in] ([cm])	TOP	BASE	CEMENT	Hole Size [in] ([cm])
Conductor	Casing	36 (91.4)	2501	2586.05	2501	42 (106.7)
Surface	Casing	20 (50.8)	2501	3606.05	2501	26 (66.0)
Intermediate	Casing	13 3/8 (34.0)	2501	4739.95	4339.95	17 1/2 (44.4)
Production	Casing	9 7/8 (25.0)	2501	5857.16	5148	12 1/4 (31.1)
Production	Tubing	5 1/2 (14.0)	2501	558.17	-	-

Table 11 – Lithology of EWT well

Formation type	TVD top [m]	TVD base [m]
Shale	2476	6173

Table 12 – Inclination of EWT well

MD [m]	Angle [°]	Azimuth [°]	TVD [m]
2501.00	0	0	2501
2555.00	0.23	0	2555
2588.00	0.41	0	2588
2666.00	0.14	0	2666
2705.00	0.35	0	2705
2744.00	0.32	0	2744
2783.00	0.41	0	2783
2821.00	0.48	0	2821
2859.99	0.62	0	2860
2898.99	0.64	0	2899
2937.99	0.5	0	2938
2976.99	0.64	0	2977
3015.99	0.35	0	3016
3092.98	0.56	0	3093
3168.98	0.57	0	3169
3207.98	0.59	0	3208
3285.97	0.58	0	3286
3363.97	0.29	0	3364
3440.97	0.26	0	3441
3518.97	0.3	0	3519
3621.97	0.59	0	3622
3661.96	0.54	0	3662
3700.96	0.63	0	3701
3738.96	0.56	0	3739
3776.96	0.67	0	3777
3815.96	0.59	0	3816
3853.95	0.64	0	3854
3892.95	0.7	0	3893
3931.95	0.7	0	3932
3970.95	0.73	0	3971
4008.94	0.73	0	4009

Continued on next page

Table 12 – Continuation

MD [m]	Angle [°]	Azimuth [°]	TVD [m]
4048.94	0.68	0	4049
4087.94	0.73	0	4088
4125.93	0.79	0	4126
4164.93	0.7	0	4165
4203.93	0.76	0	4204
4241.92	0.74	0	4242
4279.92	0.82	0	4280
4318.92	0.78	0	4319
4357.91	0.88	0	4358
4396.91	0.96	0	4397
4435.90	0.98	0	4436
4473.90	0.93	0	4474
4512.89	1.02	0	4513
4550.88	1.02	0	4551
4589.88	1.23	0	4590
4667.86	1.21	0	4668
4707.85	1.16	0	4708
4726.85	1.16	0	4727
4750.84	1.2	0	4751
4790.83	1.26	0	4791
4830.82	1.21	0	4831
4868.81	1.25	0	4869
4908.80	1.34	0	4909
4946.78	2.9	0	4947
4983.70	4.28	0	4984
5022.54	6.12	0	5023
5061.25	8.23	0	5062
5099.75	10.21	0	5101
5137.95	12.98	0	5140
5174.58	17.7	0	5178
5208.70	19.53	0	5214
5246.40	19.53	0	5254
5283.14	19.6	0	5293
5319.89	19.58	0	5332
5355.76	18.99	0	5370
5391.69	18.96	0	5408

Continued on next page

Table 12 – Continuation

MD [m]	Angle [°]	Azimuth [°]	TVD [m]
5428.51	19.59	0	5447
5465.11	20.75	0	5486
5500.62	20.97	0	5524
5538.90	20.99	0	5565
5567.85	21.01	0	5596
5607.02	21.24	0	5638
5643.53	19.92	0	5677
5681.14	19.93	0	5717
5717.81	19.9	0	5756
5753.55	19.8	0	5794
5789.29	19.9	0	5832
5809.98	19.91	0	5854
5855.05	20.33	0	5902
5891.67	19.9	0	5941
5927.50	19	0	5979
5964.48	18.09	0	6018
6000.71	16.98	0	6056
6038.11	16.03	0	6095
6075.66	15.31	0	6134
6113.31	14.89	0	6173
6150.07	14.54	0	6211
6178.15	14.36	0	6240
6198.49	14.36	0	6261

Table 13 – Flash results for EWT oil

Components	Dead Oil [%mol]	Flash Gas [%mol]	Reservoir Fluid [%mol]
CO_2	-	1.05	0.87
N_2	-	0.56	0.46
C_1	-	75.80	63.00
C_2	-	9.14	7.60
C_3	0.36	6.10	5.13
IC_4	0.32	1.35	1.18
NC_4	1.02	2.55	2.29
IC_5	1.27	0.96	1.01
NC_5	1.54	0.88	0.99
C_6	4.17	0.83	1.39
C_7	9.24	0.55	2.02
C_8	11.96	0.22	2.20
C_9	9.43	0.01	1.60
C_{10}	7.50	-	1.27
C_{11}	5.73	-	0.97
C_{12}	4.70	-	0.79
C_{13}	4.80	-	0.81
C_{14}	3.79	-	0.64
C_{15}	3.75	-	0.63
C_{16}	2.85	-	0.48
C_{17}	2.57	-	0.43
C_{18}	2.53	-	0.43
C_{19}	2.35	-	0.40
C_{20+}	20.13	-	55.28
Total Molar Mass	215.75 [g mol^{-1}]	23.31 [g mol^{-1}]	55.28 [g mol^{-1}]
Molar Mass C_{20+}	491.00 [g mol^{-1}]		
GOR at flash	462.32 [m^{3std}/m^{3std}]		
API	36.15 [°API]		

B.3 WELL WITH SALT

Table 14 – Well with salt geometry

			MD [m]			
Name	Type	OD [in] ([cm])	TOP	BASE	CEMENT	Hole Size [in] ([cm])
Conductor	Casing	30 (76.2)	2325	2411	2322	36 (91.4)
Surface	Casing	20 (50.8)	2325	3683	3386	26 (66.0)
Production	Casing	10 3/4 (27.3)	2325	5090	4534	14 3/4 (37.5)
Production	Tubing	5 1/2 (14.0)	2325	5048	-	-

Table 15 – Lithology of well with salt

Formation type	TVD top [m]	TVD base [m]
Shale	2325	3513.59
Halite	3513.59	5025.56
Shale	5025.55	5698.54

Table 16 – Inclination of well with salt

MD [m]	Angle [°]	Azimuth [°]	TVD [m]
2327	0	0	2327
2415	0.28	131.05	2415
2497	0.49	129.68	2497
2538	0.59	139.5	2538
2622	0.28	117.75	2621.99
2663	0.4	83.43	2662.99
2746	0.49	111.85	2745.99
2788	0.46	85.99	2787.99
2827	0.55	104.08	2826.99
2868	0.53	113.34	2867.99
2909	0.72	128.43	2908.98
2950	0.77	141.63	2949.98
2991	0.98	149.54	2990.97
3032	1	162.28	3031.97
3073	1.03	173.38	3072.96
3157	1.28	180.12	3156.95
3198	1.39	188.14	3197.93
3239	1.51	191.1	3238.92
3281	1.57	199.53	3280.91
3321	1.82	206.18	3320.89
3363	1.9	215.82	3362.87
3404	2.2	226.83	3403.84
3443	2.75	232.52	3442.8
3528	3.64	235.93	3527.67
3570	4.14	234.45	3569.57
3612	4.52	235.37	3611.45
3652	4.91	235.68	3651.32
3721	3.64	231.66	3720.13
3762	1.97	236.14	3761.07
3803	0.78	233.19	3802.06

Continued on next page

Table 16 – Continuation

MD [m]	Angle [°]	Azimuth [°]	TVD [m]
3845	0.14	101.15	3844.06
3886	0.14	325.33	3885.06
3928	0.13	55.01	3927.06
3969	0.13	115.18	3968.06
4011	0.11	63.6	4010.06
4052	0.1	89.68	4051.06
4133	0.18	149.61	4132.06
4175	0.35	164.37	4174.06
4216	0.34	147.71	4215.06
4257	0.1	171.72	4256.06
4298	0.12	61.57	4297.06
4340	0.07	137.15	4339.06
4381	0.07	173.09	4380.06
4422	0.07	36.32	4421.06
4464	0.1	281.81	4463.06
4506	0.14	192.24	4505.06
4547	0.03	17.84	4546.06
4588	0.15	146.24	4587.06
4630	0.22	213.2	4629.06
4671	0.1	175.96	4670.06
4753	0.13	293.47	4752.06
4794	0.13	224.04	4793.06
4877	0.15	115.26	4876.06
4918	0.17	160.34	4917.06
4960	0.13	168.87	4959.06
5002	0.11	217.44	5001.06
5042	0.13	325.26	5041.06
5074	0.14	157.15	5073.06
5098	0.22	257.62	5097.06
5138	0.11	197.7	5137.06
5179	1.64	138.51	5178.05
5219	2.5	148.09	5218.02
5258	1.39	90.63	5257
5301	1.65	110.39	5299.99
5341	1.61	97.66	5339.97
5381	1.8	106.53	5379.96

Continued on next page

Table 16 – Continuation

MD [m]	Angle [°]	Azimuth [°]	TVD [m]
5403	1.63	98.64	5401.95
5443	1.64	70.25	5441.93
5485	2.31	52.17	5483.91
5526	3.2	34.96	5524.86
5567	3.34	22.08	5565.79
5609	3.22	11.88	5607.72
5650	3.74	5.99	5648.65
5676	3.76	1.41	5674.59
5700	3.76	1.41	5698.54

Table 17 – Flash results for well with salt oil

Components	Dead Oil [%mol]	Flash Gas [%mol]	Reservoir Fluid [%mol]
CO_2	-	26.42	19.68
N_2	-	0.41	0.30
C_1	-	52.44	39.07
C_2	-	8.07	6.01
C_3	0.22	6.26	4.72
IC_4	0.17	0.98	0.77
NC_4	0.77	2.59	2.13
IC_5	0.68	0.65	0.66
NC_5	1.44	0.99	1.11
C_6	3.33	0.71	1.38
C_7	6.18	0.31	1.81
C_8	7.70	0.15	2.08
C_9	5.93	0.01	1.52
C_{10}	4.90	-	1.25
C_{11}	4.36	-	1.11
C_{12}	3.92	-	1.00
C_{13}	4.08	-	1.04
C_{14}	3.56	-	0.91
C_{15}	3.26	-	0.83
C_{16}	2.39	-	0.61
C_{17}	2.08	-	0.53
C_{18}	2.30	-	0.59
C_{19}	2.07	-	0.53
C_{20+}	40.65	-	10.37
Total Molar Mass	282.60 [g mol^{-1}]	29.69 [g mol^{-1}]	94.20 [g mol^{-1}]
Molar Mass C_{20+}	479.00 [g mol^{-1}]		
GOR at flash	214.48 [m^{3std}/m^{3std}]		
API	26.94 [°API]		

APPENDIX C – SOLID MATERIALS AND FORMATIONS PROPERTIES

C.1 STEEL AND CEMENT PROPERTIES

Table 18 – Steel and Cement table of mechanical and thermal properties

Material	k [W/mK]	ϵ [-]	c_p [J/Kkg]	ρ [kg m^{-3}]	β_{lin} [K^{-1}]	E [GPa]	ν [-]
Cement	0.8	0.68	1200	2500	1.0E-6	10.0	0.21
Steel	16	0.68	800	7800	1.0E-5	200.0	0.9

C.2 ROCK PROPERTIES

Table 19 – Rocks table of mechanical and thermal properties

Material	k [W/mK]	ϵ [-]	c_p [J/Kkg]	ρ [kg m^{-3}]	β_{lin} [K^{-1}]	E [GPa]	ν [-]
Anhydrite	5.08	0.68	814	2780	-	67.1	0.315
Calcilutite	1.96	0.68	844	2644	-	1.5	0.35
Coquina	2.19	0.68	887	2540	-	45.0	0.68
Halite	6.21	0.68	880	2162	4.6E-5	20.7	0.10
Limestone	2.19	0.68	887	2540	-	45.0	0.68
Marl	1.38	0.68	1734	1970	-	37.5	0.15
Sandstone	2.50	0.68	737	2198	-	32.5	0.14
Shale	1.60	0.68	2151	2057	-	17.5	0.10

C.3 CREEP PROPERTIES

Table 20 – Creep law properties

Material	$\dot{\gamma}_{\text{ref}}$ [s^{-1}]	q_{ref} [MPa]	n_1 [-]	n_2 [-]	A [kJ mol^{-1}]	T_{ref} [K]
Halite	5.22×10^{-10}	9.92	3.36	7.55	12.0	359.15

Source: Almeida (2016)